From Gas and Dust to Protostars:
Addressing the Initial Stages of Star Formation Using Observations of Nearby Molecular Clouds

by

Steve Mairs
B.Sc., University of British Columbia - Okanagan, 2012

A Dissertation Submitted in Partial Fulfillment of the
Requirements for the Degree of

DOCTOR OF PHILOSOPHY

in the Department of Physics and Astronomy

From Gas and Dust to Protostars:
Addressing the Initial Stages of Star Formation Using Observations of Nearby Molecular Clouds

by

Steve Mairs
B.Sc., University of British Columbia - Okanagan, 2012

Supervisory Committee

Dr. Doug Johnstone, Co-Supervisor
(Department of Physics and Astronomy)

Dr. Falk Herwig, Co-Supervisor
(Department of Physics and Astronomy)

Dr. Charles Curry, Outside Member
(School of Earth and Ocean Sciences)

ABSTRACT

Though there has been a considerable amount of work investigating the early stages of low-mass star formation in recent years, the general theory is only broadly understood and several open questions remain. Specifically, the dominant physical mechanisms which connect large-scale molecular cloud structures, intermediate-scale filamentary gas flows, and small-scale collapsing prestellar envelopes in the interstellar medium are poorly constrained. Even for an individual forming protostar, the evolution of the mass accretion rate from the envelope onto the central object is debated with little observational evidence to help guide the theoretical framework. In addition, with the development of new technology such as the continuum imaging instrument in operation at the James Clerk Maxwell Telescope (JCMT), the Submillimetre Common User Bolometer Array 2 (SCUBA-2), the best practices for data reduction and image calibration for ground-based, submillimetre wavelength observations are still being investigated.

In this dissertation, I address facets of these open questions in five main projects with an overarching focus on the flow of material from the largest to the smallest scales in a molecular cloud. By performing synthetic observations of a numerical simulation of a turbulent molecular cloud, I investigate the nature of prestellar envelopes and find evidence of larger mass reservoirs that form filamentary structures and feed cluster formation. Then, after robustly investigating and suggesting improvements for ground-based, submillimetre data reduction techniques, I continue to probe the connection between larger and smaller scales by characterising structure fragmentation in the Southern Orion A Molecular Cloud from the perspective of 850 μm continuum data. Finally, I follow star forming material to even smaller scales by exploring the evolution of the mass accretion rate onto individual protostars. This examination has required designing and implementing unprecedented spatial alignment and flux calibration techniques at 850 μm. Using these newly calibrated images, I am able to identify several candidate sources that show evidence for submillimetre variability, suggesting changes in protostellar accretion rates over several year timescales.

Contents

List of Tables

List of Figures

ACKNOWLEDGEMENTS

Where to begin? I suppose with my family, by blood or otherwise, for all of their incredible support in getting me this far. There are three people I'd especially like to highlight. First, my wife, Desirée. Though so many times I got caught up in computer screens and publications, she has never allowed me to forget about the wondrous beauty above our heads and why I set out to study astronomy in the first place. Second, Reg Keown for his insight, his ability to challenge me to think outside the box (I'm not sure he is aware a box exists), and most of all his friendship. Third, I'd like to thank Kite from the bottom of my heart for making clear the path before me and for reminding me to look up when it was dark outside.

Next, I want to underscore that the quality and the breadth of this dissertation could never have been achieved without the guidance of my fantastic supervisor, Dr. Doug Johnstone. He has been the most incredible mentor. He was always patient, he pushed me when I needed to be pushed, and he taught me to approach star formation in innovative and fresh ways. It is my goal, lofty as it is, to one day have the same kind of intuition, knowledge, and passion he has for astronomy.

I would also like to extend my gratitude to Dr. Helen Kirk, Dr. Gregory Herczeg, and to the members of my committee, Dr. Falk Herwig and Dr. Charles Curry and to my external examiner, Dr. Lee Hartmann for their encouragement, support, and comments, which have undoubtedly strengthened this body of work.

Additionally, I would like to acknowledge the useful discussions and support I've received from the UVIC graduate student community as a whole. You have all made my time in Victoria an adventure to remember and I'm honoured to know each of you. I'm especially grateful for my coffee sessions with Mike Chen as they have reminded me of the greater context of all our work.

Finally, I would like to thank the people of Hawaii who have allowed us to build telescopes on their sacred mountain, Maunakea. We are very fortunate to be able to commune with the heavens in our own way from this site and I so appreciate the welcome I have received whenever I have visited your shores.

"Even after all this time, the Sun
never says to the Earth 'You owe me'.
Look at what happens with a love like that.
It lights the whole sky..."
∼Hafiz

DEDICATION

For Desirée.
All the stars in the sky pale in comparison to the light in your heart.

Chapter 1

Introduction

"Like when the mother met the father,
Kissed the horizon, and gave birth to stars..."
-Nahko Bear, I Mua

Deep within the cold dust and gas which resides in our Milky Way Galaxy, a dramatic story is unfolding: the birth of stars. Understanding the formation and evolution of stars is not only quintessential to describing the visible universe but it is also important for recognising and appreciating our origins. The Sun and planets did not always exist and it is through comparing careful observations of our solar neighbourhood to cutting-edge theoretical simulations that we are able to investigate our cosmic history and perceive our solar system in the broader context of the Galaxy and, indeed, the universe.

An individual star may take several million years to fully form (Dunham et al., 2014, 2015), so we are unable to witness this entire event from beginning to end. By observing thousands of nearby stars at different stages of their formation along with their nascent environments, however, astronomers have begun piecing together a general story which is by no means complete (see reviews by Di Francesco et al., 2007a; Ward-Thompson et al., 2007a; André et al., 2014; Hubber, 2014). This story is dynamic. Shockwaves of gas and dust collide in the space between the stars (Pon et al., 2012a) while gravity must overcome opposing thermal, turbulent, and magnetic pressures (Kirk et al., 2007; Pattle et al., 2015) to create the right conditions for the ignition of nuclear fusion in the heart of a forming star (Sadavoy et al., 2010b). Powerful jets and energetic winds released by young stars shape the surrounding gaseous material like wind across the desert and subsequently prompt further generations of

stars to begin forming (Appenzeller & Mundt, 1989). Despite what we've already learned, each chapter of this story requires far more study as many details are just beginning to emerge.

Throughout this dissertation, I explore various facets of low-mass star formation from large-scale gas flows that bring together the stellar building blocks to the assembly of individual stars, probing the physics which governs and connects these phenomena. Here, a typical low-mass star has approximately the same mass as our Sun. I will also focus on image creation and processing techniques for observations taken using the James Clerk Maxwell Telescope, the facility which was used to collect the majority of the data presented in this work. I will begin, however, with a general introduction to the formation of stars, highlighting the prominent issues I address in later chapters.

1.1 Star Formation

The space between the stars is not empty. In fact, the **interstellar medium**[1] (ISM) is a vibrant and physically interesting laboratory comprised of gas and dust spanning different temperatures and densities that enables us, among a slew of broader goals, to study stellar birth (Lada, 1978; Benson & Myers, 1989; Di Francesco et al., 2007a; André et al., 2014). Though extraordinarily sparse when compared to atmospheric densities on the Earth, the coldest (10 K) and densest ($>$100 cm^{-3}) regions of the interstellar medium are referred to as **molecular clouds** owing to the fact that they are mostly comprised of molecular Hydrogen (H_2) (Dobbs et al., 2014). These molecular clouds are the large-scale (tens to hundreds of parsecs), massive (10^2 to 10^7 $M_\odot$) structures inextricably associated with the formation of stars and so they form the basis of observational targets for understanding, in greater detail, the processes involved in transforming gas and dust into solar systems. Fundamentally, piecing together the holistic picture of star formation relies on observing and characterising the flow of matter from the largest scales, through its various intermediary structures, to its eventual accretion onto individual stars and planets.

The basic description of how a low mass star is formed is summarised in Figure 1.1. In the top left panel, a molecular cloud (or, dark cloud) forms and develops overdensities which are shielded by the cloud itself from the **interstellar radiation**

[1]Terms which appear in bold are defined in Appendix A, the Glossary, for your reference.

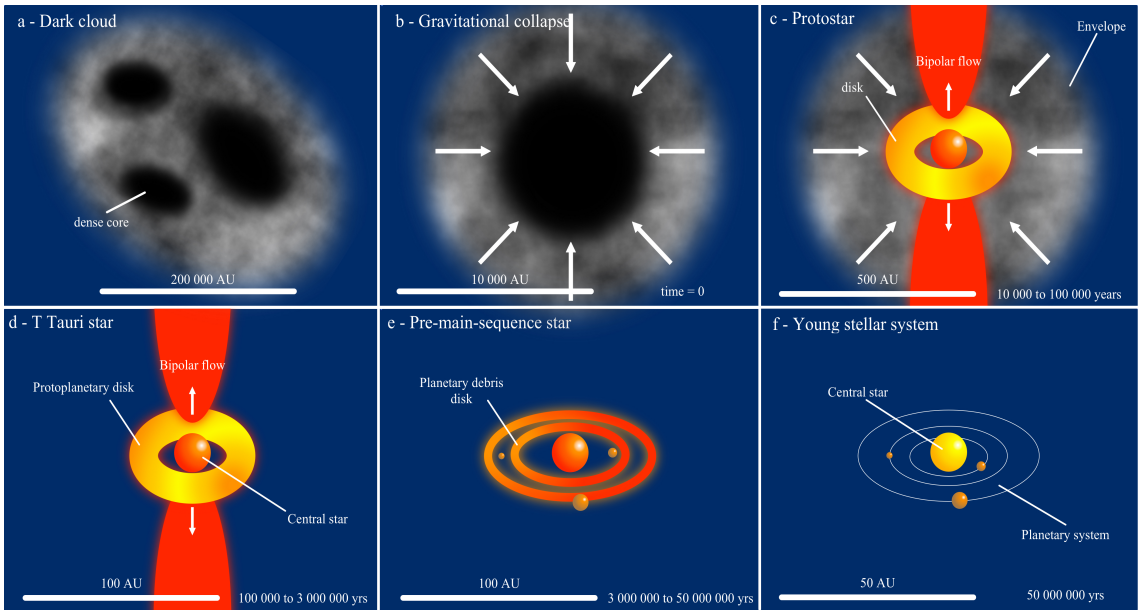

Figure 1.1 An overview of the low mass ($\sim 1\,M_{\odot}$) star formation process. Each panel represents a burgeoning field of research with the advent of new results from instruments such as the James Clerk Maxwell Telescope, the Atacama Large Millimetre/submillimetre Array, the *Spitzer Space Telescope*, and the *Herschel Space Observatory*. This diagram is based on a Figure presented by André (2002). Figure Credit: Sébastien Lavoie.

field, the radiation field present throughout the interstellar medium that is generated by a variety of physical processes such as the energy output of stars, the thermal emission from dust grains, the cosmic microwave background, and extragalactic x-ray and gamma ray sources (see Mezger, 1990). There are several proposed formation mechanisms of molecular clouds in the literature which all involve convergent flows of gas initiated either by the rotation of the galaxy or by more localised events such as supernovae or stellar winds (for a comprehensive review, see Dobbs et al., 2014). Further, the lifetimes of molecular clouds are under active debate with estimates ranging from upper limits of 10 Myr in solar neighbourhood clouds based on stellar populations (Hartmann et al., 2001) to 100 Myr in extragalactic observations based on large-scale galactic dynamics (Koda et al., 2009), with several groups concluding an average lifetime of 20-30 Myr (Kawamura et al., 2009; Murray, 2011; Miura et al., 2012; Meidt et al., 2015). The lifetimes of molecular clouds are difficult to study as these clouds cover such a wide range of densities and sizes. The eventual disruption of these objects, however, depends on the larger-scale environments, the strength of the primary support mechanisms against gravitational collapse (such as magnetic field pressure and turbulence; Shu et al. 1987; Krumholz et al. 2006; Klessen & Hennebelle 2010) and their drivers, as well as the amount of radiative feedback generated around massive, young stars (Krumholz et al., 2014). For the purposes of this discussion, however, I treat a molecular cloud as a formed object, though perhaps continuing to assemble, with a lifetime long enough to produce stars.

The smaller-scale overdensities seen in Figure 1.1 (top left), often called **clumps**, develop via a combination of gravitational collapse and converging flows (see also the discussion on filamentary structure in Section 1.2). The manner in which this proceeds is governed by the strength of pressure support mechanisms such as thermal energy, turbulent energy and magnetic field pressure. Depending on the mass and the size of these clumps, they may fragment into smaller structures called **cores**, the basic object of interest that will go on to form a star (top, middle panel of Figure 1.1). At this stage, a core can be *starless* (not gravitationally collapsing, or associated with forming stars) or *prestellar* (bound and expected to gravitationally collapse and form stars). Due to inherent measurement uncertainties and the sensitivities required to observe the low luminosity protostars which are deeply embedded within a core, these physical definitions are, in practice, difficult to determine.

Beginning with some simple assumptions about its environment, we can derive, for instance, the size of a prestellar core in hydrostatic equilibrium, beginning with

the standard hydrostatic equilibrium equation

$$\frac{dP}{dr} = -\frac{\rho G M(r)}{r^2}, \tag{1.1}$$

where P is the internal pressure counteracting gravitational collapse, r is the radial distance from the centre of the core, ρ is the density of the core, G is the gravitational constant, and M is the mass of the core. If one assumes that the central pressure, P_c is much larger than the pressure outside the core, P_0, this equation can be approximated as

$$\frac{P_c - P_0}{R} \approx \frac{P_c}{R} \approx -\frac{\rho G M}{R^2}, \tag{1.2}$$

where R is the outside radius of the core (defining some density threshold to be the "edge" of the core). By applying the ideal gas law $P = c_s^2 \rho$, where c_s is the sound speed, we find that

$$c_s^2 \approx \frac{GM}{R}, \tag{1.3}$$

where I have dropped the negative sign to indicate that these are scalars rather than opposing force vectors. By assuming a typical core mass of 1 $M_\odot$, at a typical temperature of 10 K, in a medium where the typical sound speed is 200 m/s, the radius of a prestellar core is approximately 0.11 pc. Taking these quantities and a mean molecular weight of $2.3 m_H$ (where m_H is the mass of hydrogen; a common value for the interstellar medium assuming it is comprised of 90% molecular Hydrogen and 10% Helium by mass), the number density within such a core is $\sim 1 \times 10^4$ cm^{-3}.

Shu (1977) presented the seminal work on how an isolated prestellar core undergoes gravitational collapse by modelling it as a singular isothermal sphere (SIS). Such a sphere has a radial density profile

$$\rho(r) = \frac{c_s^2}{2\pi G r^2}, \tag{1.4}$$

(see also Chandrasekhar, 1939; Bodenheimer & Sweigart, 1968). In Shu's model, a core collapses from the "inside out" until a hydrostatically supported, central object called a **protostar** forms[2] (top, right panel of Figure 1.1). To make this more clear,

[2]In reality, the central region first becomes sufficiently dense to briefly halt the collapse of the core. At this stage, the object is called a **first hydrostatic core**. Collapse will resume when the central temperature rises to ~ 2000 K (Larson, 1969) and H_2 molecules begin to dissociate. This dissociation and the subsequent ionisation of Hydrogen and Helium alter the opacity and allow

consider that the centre of a prestellar, singular isothermal core in hydrostatic equilibrium is perturbed in some fashion (Shu suggests molecule formation). Since the freefall time is proportional to $\rho^{-1/2}$, the higher density central region will collapse faster than the outer layers, diminishing the pressure support which is necessary to keep the core stable. Consider the infinitesimal change in mass, dM, within the infalling radius, r, over time

$$dM = 4\pi r^2 \rho(r) dr. \tag{1.5}$$

Note that the speed at which the radius of the collapsing zone will expand is the sound speed of the medium; it increases in size linearly with time, $r = c_s t$. In this case, an infinitesimal change in infalling radius can be expressed in terms of time $dt = dr/c_s$. Then,

$$dM = 4\pi (c_s t)^2 \rho c_s dt. \tag{1.6}$$

Substituting in Equation 1.4 for ρ, we find

$$dM = 4\pi (c_s t)^2 \frac{c_s^2}{2\pi G (c_s t)^2} c_s dt. \tag{1.7}$$

Simplifying, we find that the mass accretion rate is

$$\frac{dM}{dt} = \frac{2c_s^3}{G}. \tag{1.8}$$

The mass accretion rate is constant, so the stellar mass grows linearly over time. To analyse this collapse in further detail, Shu (1977) went on to show by numerically solving his derived, self-similar solutions that nearly half ($0.975 c_s^3/G$) of this infalling material is added to the central protostar while the other half is added to the infalling envelope. Thus, the steady-state accretion rate onto the central protostar is

$$\frac{dM_{protostar}}{dt} \sim \frac{c_s^3}{G}. \tag{1.9}$$

Of course, this solution is an approximation as singular isothermal spheres are not physical. Improvements can be made by changing the boundary conditions such that there is an external pressure which alters the density profile of the central region of a core so that it flattens rather than increases toward infinity. Objects in this

radiative energy to escape so the contraction continues towards a protostar.

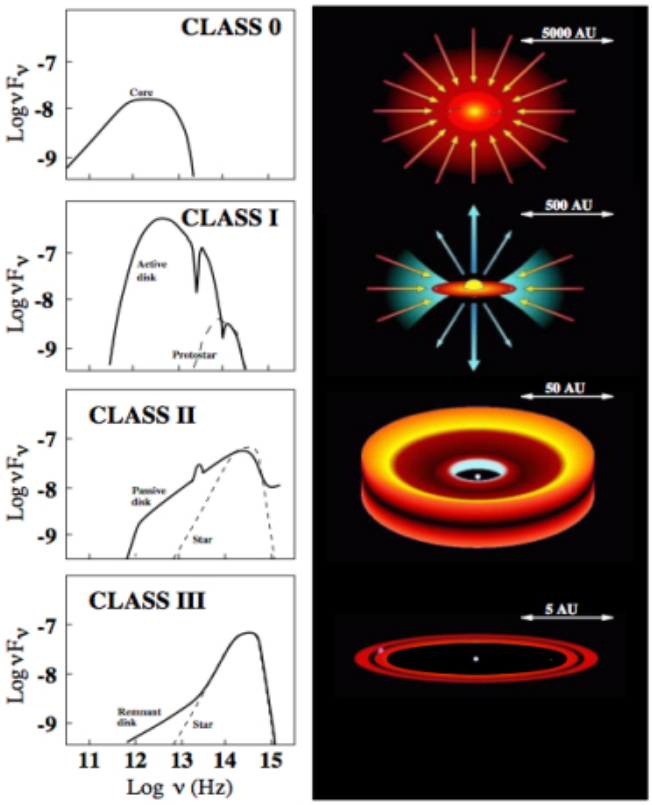

Figure 1.2 A summary of the different classes of young stellar objects. YSO classes are defined by the steepness of their spectral energy distribution at infrared wavelengths. Figure Credit: van Boekel (2004).

family of models are referred to as **Bonnor-Ebert spheres** (see Ebert 1955; Bonnor 1956 and the infall models of Henriksen et al. 1997). In addition, there are models which predict "outside-in" collapse (see, for examples, Bodenheimer & Sweigart, 1968; Larson, 1969; Penston, 1969; Safier et al., 1997; Gong & Ostriker, 2011), but for the sake of this discussion I will focus on the "inside-out" collapse presented above.

Before a protostar forms, a core is optically thin at far IR and submillimetre wavelengths and isothermal. Once a protostar is established, the energy produced at the centre causes this region to become opaque at these wavelengths of interest and the energy must be absorbed and re-emitted throughout the envelope. At this state, this dense central object along with its envelope is referred to as a *protostellar core* and it continues to undergo collapse, allowing material to accrete in a steady state from the envelope onto the central source. While the nascent envelope is more massive than the protostar, the **spectral energy distribution** (SED) of the object peaks

at submillimetre wavelengths and has very little emission at wavelengths less than 10 μm (see Figure 1.2). The submillimetre peak is a consequence of the reprocessing of high energy photons which cannot escape the very dense medium. At this stage, the protostar is referred to as a "Class 0" **young stellar object** (YSO; Lada 1987; Andre et al. 1993). Though the original definition of different classes of YSOs was based on the overall shape of the SED while Class 0 sources were defined by their relatively strong submillimetre luminosities, it is now common practice to separate each class by the steepness of the slope of their SED at infrared wavelengths (see, for example, Dunham et al. 2015).

Throughout the collapse of a protostar, while accretion is still ongoing, the conservation of angular momentum dictates that the rotational velocity of the material must increase, eventually resulting in the formation of a circumstellar disc (see, for example, Terebey et al. 1984). In addition, the magnetic fields present in the forming star and disc interact with the infalling, rotating material through processes still under investigation (see, for example, Shu et al., 2007) to form collimated, bi-polar outflows known as **stellar jets** (e.g. Bally, 2016, and references therein). These features allow for the dissipation of angular momentum as the protostar continues to collapse. In Section 1.3, I discuss in more detail the pivotal importance of understanding how this disc plays a role in the protostellar mass accretion process and how submillimetre observations of outbursts likely caused by instabilities in the disc are adding complexities to our current understanding of the star formation process.

The outflows and the continued accretion of interstellar material work to dissipate the natal envelope. Once the mass distribution in the core evolves such that the protostar is approximately more massive than its surrounding envelope, the SED is described by two components: a blackbody which peaks at approximately 5 μm, tracing the central protostellar region, and an "infrared excess" component which is visible at longer, submillimetre wavelengths, tracing the disc and remnant envelope (Figure 1.2). The protostar is then referred to as a "Class I" YSO (Lada, 1987).

When the envelope is completely dispersed and consumed, the protostar becomes a "Class II" source (Lada, 1987) (commonly referred to as a T-Tauri type object, see the bottom left panel of Figure 1.1) and the SED peaks at $\sim$1 μm (tracing the now exposed protostar) with a diminishing infrared excess disc component which still extends into the submillimetre wavelengths (Figure 1.2). Note that there is also an observed transitionary state between a Class I and a Class II source commonly referred to in the literature as a "Flat Spectrum" YSO owing to the flattening of its

SED as it evolves (Greene et al., 1994).

Due to the combination of entrainment and evaporation caused by the outflows, the final stages of accretion, energetic photons from the protostar, and strong solar winds, the disc vanishes and the protostar becomes a "Class III" source (the left over debris from the disc is where planet formation may continue, see Section 1.2; for an overview of each class, see McKee & Ostriker, 2007b) (bottom, middle panel of Figure 1.1). At this stage, the SED has very little emission at wavelengths longer than 100 μm (Figure 1.2). Finally, when the central temperature of the protostar is high enough to ignite the fusion of Hydrogen atoms into Helium atoms, the source arrives on the main sequence of the Hertzsprung-Russell diagram where it is finally a star by definition (bottom, right panel of Figure 1.1).

Of course, the overview of a forming, low-mass star presented above is overly simplistic and many important questions throughout this process remain. For instance, the mechanisms for the formation of molecular clouds and the processes which connect large-scale and small-scale structures are still debated (Dobbs et al., 2014), differentiating gravitationally unstable cores from other overdensities which will not go on to form stars is an inherently complicated problem that is under investigation (Pineda et al., 2009a), the effects of thermal energy, turbulence, and magnetic fields in preventing gravitational collapse are questioned (Sadavoy et al., 2010b), the dominant physical processes which govern the fragmentation of large structures into multiple star-forming components need to be addressed (Kainulainen et al., 2013), and the time dependency of material accreting onto the central protostar is poorly constrained (Kenyon et al. 1990, Evans et al. 2009a, Enoch et al. 2009, Dunham & Vorobyov 2012).

In this dissertation I will address several of these issues. Since this work focuses on the earliest stages of star formation when protostars are still deeply embedded in gas and dust, the submillimetre regime of the electromagnetic spectrum contains the most useful information I seek to investigate. Shorter wavelengths such as optical and UV light cannot penetrate through the high column densities of material which surround stars. To this end, I have obtained and used data taken by the **James Clerk Maxwell Telescope** (JCMT; see Figure 1.3) situated on Maunakea, Hawaii, USA. The JCMT is a 15 metre dish sensitive to submillimetre radiation (for more information, see Section 1.4).

Figure 1.3 The James Clerk Maxwell Telescope. Stars form in heavily extincted regions of gas and dust where the optical depth at visible wavelengths is too high to discern the important information necessary to study cores. Thus, astronomers studying the earliest phases of star formation use light with longer wavelengths (infrared, submillimetre, and radio) to see behind this high column density veil. Figure Credit: Steve Mairs.

The theory of star formation is only very broadly understood; many of the details are just beginning to emerge. New advances in technology coupled with innovative, large-scale surveys are challenging the current paradigm and rapidly leading to a more complex and exciting view on how material transfers from the dynamic environment to a forming protostar. In the following introductory sections, I describe recent developments and focus on the main challenges which will be addressed in Chapters 2 through 6.

1.2 Connecting Large and Small Scale Structures in the Interstellar Medium

In the previous section, I presented a simple overview of how a single star is formed in an isolated environment within a molecular cloud. A fundamental understanding of the dominant physical processes that are important for the formation of stars, however, also rests in our knowledge of the connection between the large-scale molecular cloud structure and the small-scale, localised core and protostellar disc structure. Classifying and analysing the dominant structures and how they evolve and connect on a variety of scales is quickly becoming the focus of this discipline.

In reality, molecular clouds are not as they are portrayed in Figure 1.1. Improvements in technology along with the development of innovative analysis techniques in recent years have complicated this picture by a significant degree. Figure 1.4 shows a combined optical and infrared image taken by the *Hubble Space Telescope* of the highest density region of the Orion Molecular Cloud as an example of the complicated morphology and physical characteristics of structures this large (the image is 3.4 pc on a side assuming a distance of 388 pc to the Orion Molecular Cloud; Kounkel et al. 2017), especially when massive stars produce high energy radiative feedback. This image traces the warm, diffuse gas that enshrouds the colder, star forming gas we seek to study.

Recently, surveys such as the Herschel Infrared Galactic Plane Survey (Hi-GAL, Molinari et al. 2010) and the Herschel Gould Belt Survey (André et al., 2010a) using the *Herschel Space Observatory* have revealed the "ubiquitous" networks of filamentary gas and dust structures found within molecular clouds (see Figure 1.5, for exam-

Figure 1.4 A combined optical/infrared image of the highest density region of the Orion Molecular Cloud taken using the *Hubble Space Telescope*. The image covers an area of $30' \times 30'$. Figure Credit: NASA, ESA, M. Robberto (Space Telescope Science Institute/ESA) and the Hubble Space Telescope Orion Treasury Project Team.

ple). Although star formation experts have been interested in filamentary structure for nearly forty years (Schneider & Elmegreen, 1979a; Bally et al., 1987; Johnstone & Bally, 1999), the prevalence of this type of structure has only recently been made definitive (André et al., 2014; Könyves et al., 2015). **Filaments** have therefore become a main focus in the recent literature (both observational and theoretical) to attempt to explain the shape of the **initial mass function** (IMF) (André et al., 2014), describe accretion modes (Kirk et al., 2013a), measure the effect of turbulence and magnetic fields on gas and dust structures (Kirk et al., 2015), analyse timescales for the gravitational collapse of non-spherical structures (Pon et al., 2012b; Freundlich et al., 2014; Clarke et al., 2017), and investigate the fragmentation of these larger objects into clumps and cores (Hartmann 2002; Kainulainen et al. 2013; Contreras et al. 2016). Observationally, it has become clear that material flows along filaments (McCutcheon et al., 1982; Miettinen, 2012; Kirk et al., 2013a; Friesen et al., 2016; Klassen et al., 2017). Indeed filaments are now thought to be the primary structures responsible for channeling interstellar material (Myers, 2009a) from molecular cloud scales (tens of parsecs) to star-forming core scales (tenths of a parsec); the connection which makes a holistic view of star formation possible.

The manner in which filaments form is an active topic in the current literature which I will not address here in detail (for a review, see André et al. 2014). The most likely scenario is a combination of turbulent, converging shock flows (e.g. Padoan & Nordlund, 2002; Pudritz & Kevlahan, 2013) and gravitational infall (Heitsch, 2013). The role of magnetic fields in the formation of filaments is still unclear, though there is evidence that it is dynamically important in at least some regions (e.g. Panopoulou et al., 2016). Once formed, these filaments are inextricably linked to the formation of individual stars as well as clusters. It is known that most stars appear to form in clustered environments (Lada & Lada 2003; see also Lane et al. 2016) and Myers (2009a) shows that young clusters are associated with regions of filamentary intersection, so-called "hubs". Infalling material from larger mass reservoirs, channeled through filaments, could provide the necessary mass to form such clusters (see Kirk et al. 2013a and Chapter 2). In addition to the convergence and interaction of multiple filaments to initiate dense enough media to form stars, there is also active research into the stability of a single filament and whether or not it fragments into prestellar cores along its length (Stodólkiewicz, 1963; Ostriker, 1964; Curry, 2000; Pon et al., 2012b; André et al., 2014). This is a complex issue which requires detailed knowledge of the interplay of gravity, and the three main support mechanisms: thermal pressure,

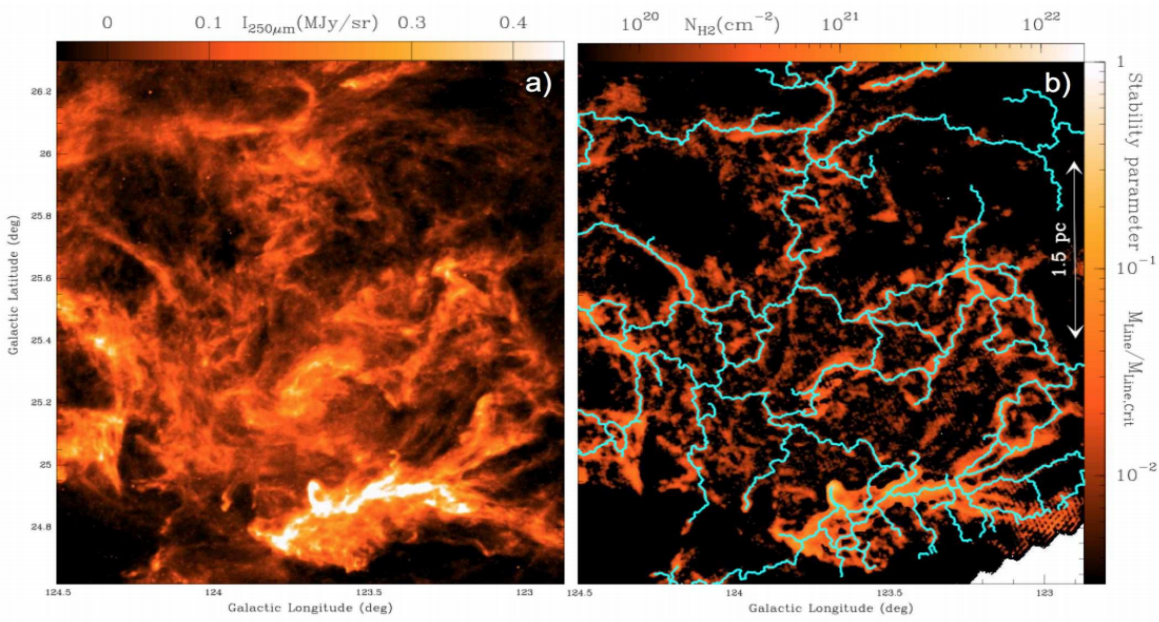

Figure 1.5 An example of the "ubiquitous" filamentary structure seen throughout several star forming regions in the Milky Way. The left panel shows a Herschel Space Observatory (250 μm) dust continuum map of the Polaris Flare. The right panel shows the corresponding column density map. The blue lines trace the main filamentary structure observed. Figure Credit: André et al. (2014).

turbulence, and magnetic field pressure.

Assuming only thermal support, the critical mass per unit length, M_{crit}, of a filament is given by

$$M_{crit} = \frac{2c_s^2}{G}, \tag{1.10}$$

where c_s is the sound speed and G is the gravitational constant (Stodólkiewicz, 1963; Ostriker, 1964). Therefore, a filament with a mass per unit length greater than M_{crit} is supercritical and unstable to collapse or fragmentation. The large majority (>70%) of dense, prestellar cores are found to be associated with supercritical filaments (Polychroni et al., 2013; André et al., 2014; Könyves et al., 2015) and the formation of dense cores may be primarily due to the fragmentation of these structures (see Figure 1.6).

One of the ongoing efforts in the field is to connect the **core mass function** (CMF), the distribution of the number of prestellar cores with a given mass, to the IMF, the distribution of the number of stars with a given mass when they arrive on the main sequence, to determine if the number of stars we observe of a given mass results directly from the physics which governs their primordial state. There is evidence in the literature that the CMF and the IMF have a similar shape (see, for examples, Motte et al. 1998, Johnstone et al. 2000b, Sadavoy et al. 2010a, and André et al. 2010a; see also Figure 1.7), but this is complicated by the variety of chosen methods of differentiating between observed structures and measuring masses (see Chapters 2 and 4).

Analysis of new observations of multiple molecular clouds across the Milky Way obtained through programs such as the **Gould Belt Survey** at the JCMT (GBS; Ward-Thompson et al., 2007c) are presenting researchers with the opportunity to independently derive the characteristics of cores (Pattle et al., 2015; Pattle, 2016) and compare them between different environments. Furthermore, the growing set of submillimetre observations across known star forming regions in our Galaxy is helping put constraints on simulations seeking to derive the origin of the IMF and question its universality (see, for example, Offner et al. 2014).

One of the main themes of this dissertation is performing analyses across large regions while probing even smaller scales by using synergistic datasets such as YSO catalogues produced with the *Spitzer Space Telescope* (e.g. Megeath et al., 2012; Dunham et al., 2015) and the *Herschel Space Observatory* (e.g. Stutz et al., 2013) in conjunction with the submillimetre dust data. These infrared wavelength surveys have

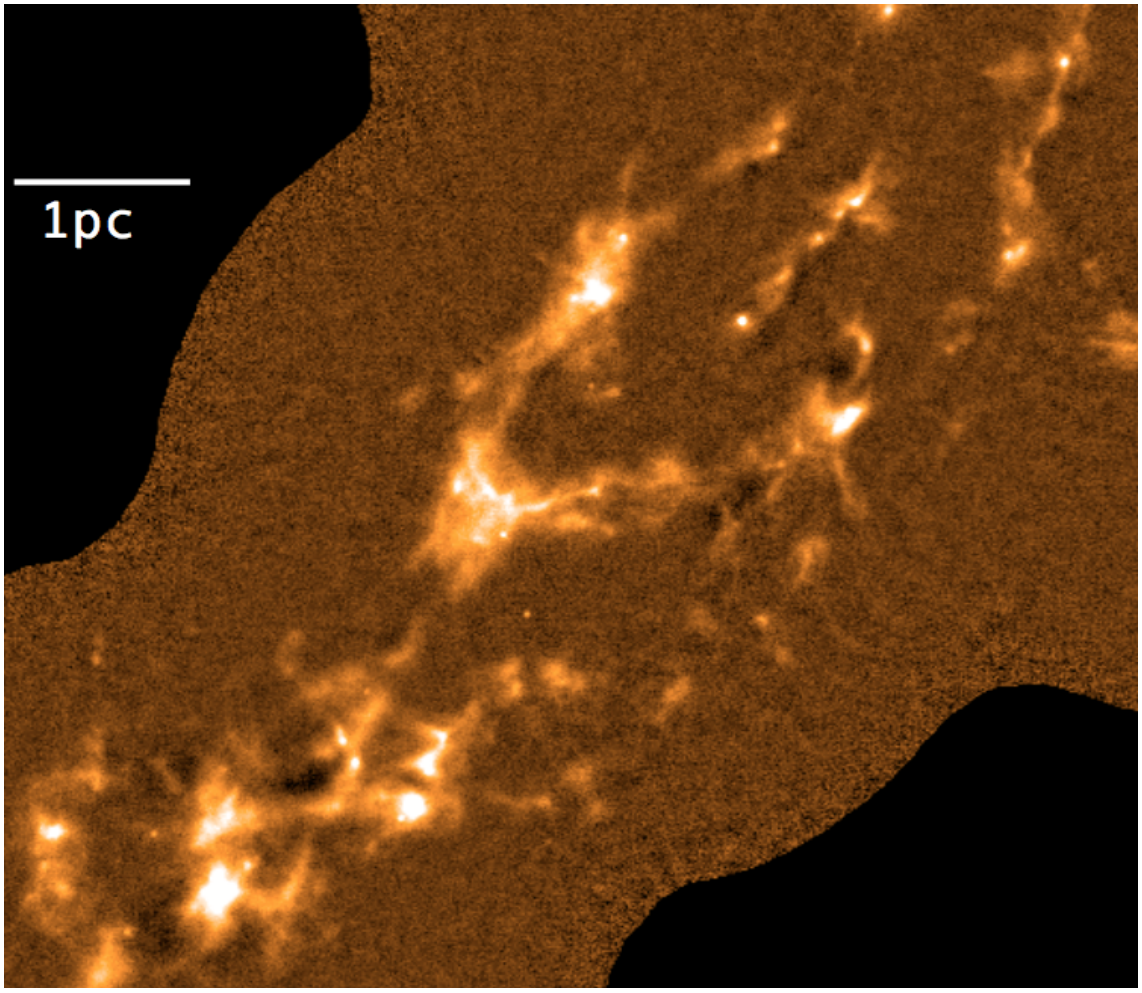

Figure 1.6 A portion of the Orion Molecular Cloud shown at 850μm, observed using the James Clerk Maxwell Telescope. The bright, compact emission sources are cores, preferentially lying along filamentary structure. A large majority of the filamentary structure itself is filtered out of this image due to submillimetre image processing practices (see Section 1.4).

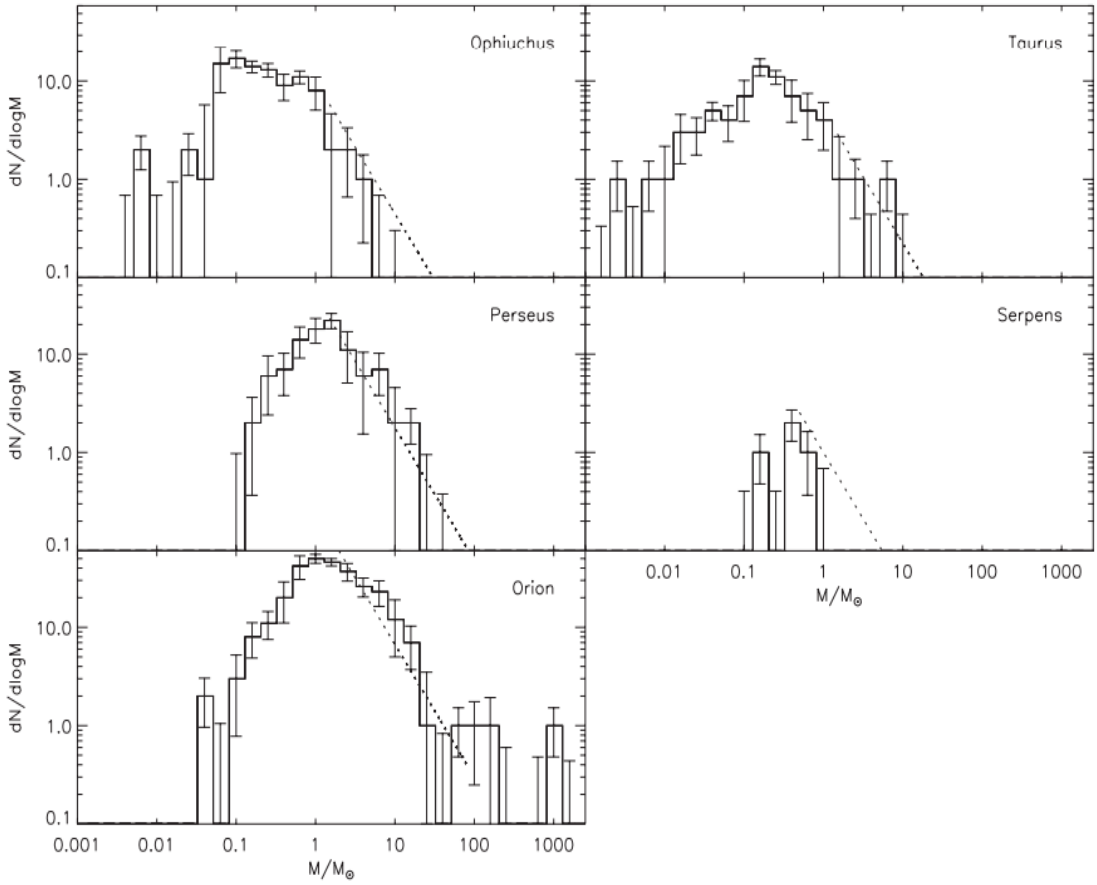

Figure 1.7 A series of core mass functions observed in a variety of star-forming regions. The dashed line represents a Salpeter power-law slope $dN/d(log\, m) \propto m^{-1.35}$. Figure Credit: Sadavoy et al. (2010a).

uncovered thousands of deeply embedded protostars across several molecular clouds like Orion, Taurus, Perseus, and Ophiuchus. By collating the positions of known protostars with dense cores, the population can be separated (with some difficulty due to inherent uncertainties in the measurements) into *starless* and *protostellar* categories and gravitational stabilities along with other physical properties of the cores can be separately addressed.

Finally, observationally probing the smallest scales is possible by using powerful interferometers like the Atacama Large Millimetre Array (ALMA). Undoubtedly, the disc which surrounds a forming star (see bottom, middle panel of Figure 1.1) is a significant zone of mass transfer from the surrounding envelope to the central protostar, though this connection is poorly understood (for a review of accretion onto forming stars, see Hartmann et al. 2016). ALMA allows us to detect these **protoplanetary discs** around forming stars with unprecedented resolution and sensitivity. Figure 1.8 shows one such disc surrounding a T Tauri star called *HL Tau*. The gaps in disc's material are thought to be carved by the formation of planets (ALMA Partnership et al., 2015). Observations of young discs with gaps and rings and discs with complicated substructures suggests that the physics within these discs is quite complex. Thus, transporting material from the envelope, through the disc, to the central protostar is likely to be non-steady.

1.2.1 A Note on the Analysis of Dense Cores

Throughout this dissertation, I mainly present data and analyses on the intermediate-scale dense, prestellar cores based on submillimetre data obtained using the James Clerk Maxwell Telescope (see Figure 1.3) so I summarise, here, the important aspects determining the physical properties of these dust emission structures in this context.

The thermally radiating dust we observe at submillimetre wavelengths can be described as a modified blackbody curve (greybody). Beginning with the radiative transfer equation (neglecting the absorption term):

$$I_\nu = B_\nu(T_d) \times (1 - \exp^{-\tau_\nu}), \tag{1.11}$$

where I_ν is the intensity at frequency ν, τ_ν is the optical depth at frequency ν, and $B_\nu(T_d)$ is the blackbody function at dust temperature T_d. In the optically thin limit

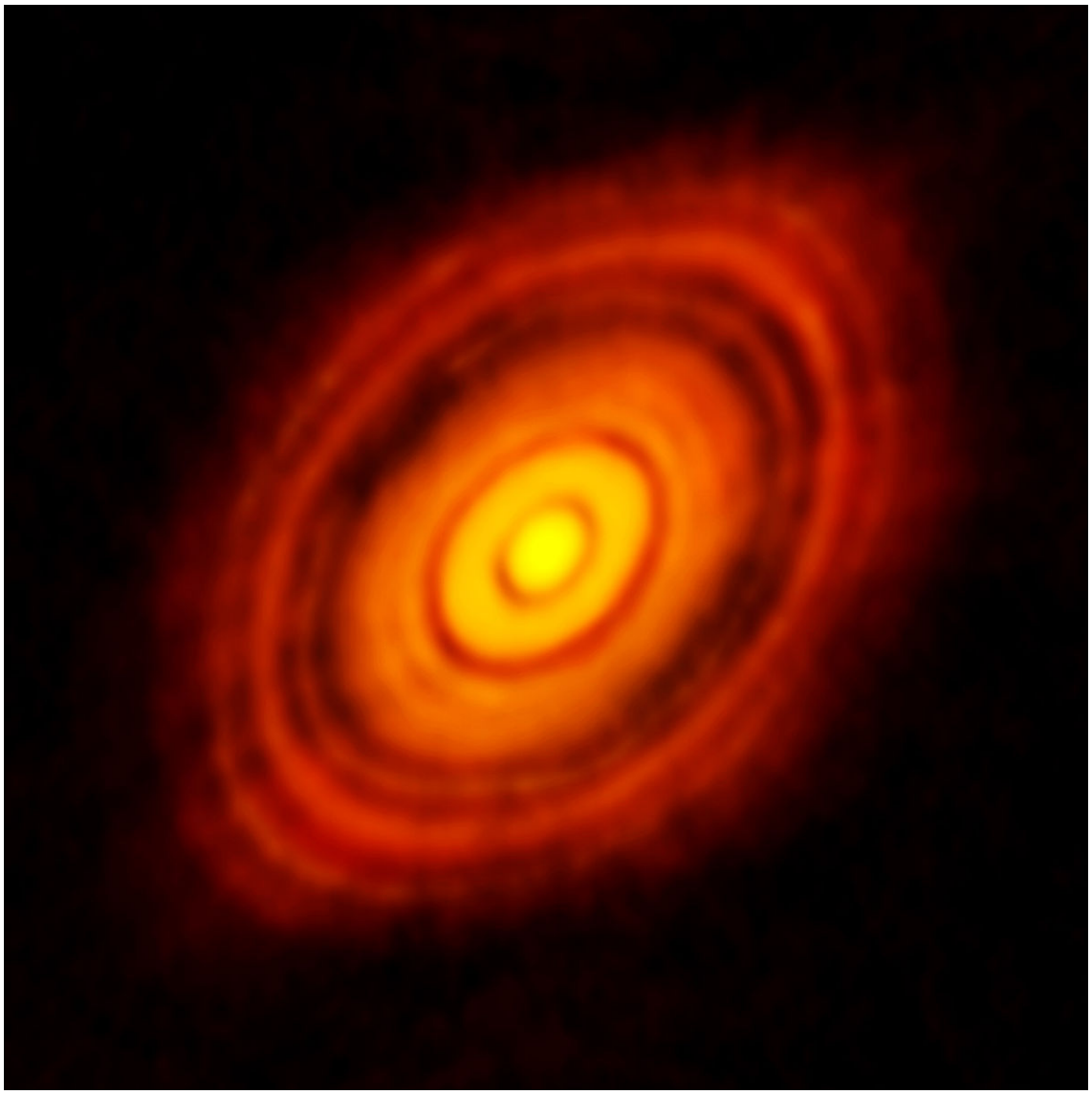

Figure 1.8 A protoplanetary disc surrounding the T Tauri star HL Tau observed using the ALMA interferometer. The gaps creating a ring-like structure are thought to be caused by the formation of planets. Figure Credit: ALMA (ESO/NAOJ/NRAO).

($\tau_\nu << 1$), the exponential term can be approximated as $\exp^{-\tau_\nu} \simeq 1 - \tau_\nu$. Then,

$$I_\nu \simeq B_\nu(T_d)\tau_\nu. \tag{1.12}$$

The optically thin assumption holds for the Rayleigh Jeans tail of a dense core's spectral energy distribution. In this regime, the optical depth can be described as a power law with frequency where the dust emissivity spectral index, β, is the exponent (see, for examples, Friesen et al. 2005; Chen et al. 2016). This can be represented by the ratio of the optical depth at the frequency of interest, ν, to the optical depth at a reference frequency, ν_0:

$$\frac{\tau_\nu}{\tau_{\nu_0}} = \frac{\nu}{\nu_0}^{\beta}. \tag{1.13}$$

Then, the intensity at a frequency of interest, ν, can be re-written in terms of this power law:

$$I_\nu = \tau_{\nu_0}(\nu/\nu_0)^\beta B_\nu(T_d) \tag{1.14}$$

Once the significant cores in a given continuum map are identified, we can calculate their physical properties and connect those quantities to the presence or absence of young, forming stars. Assuming a dust temperature and emissivity, we can use Equation 1.14 to derive quantities such as the mass (M), the column density (N), the **Jeans mass** (M_J, the maximum mass that can be thermally supported in a spherical configuration before undergoing gravitational collapse), and the "concentration" (or, "peakiness"). Beginning with Equation 1.14, the mass of a core can be expressed and calculated in the following way (see Hildebrand 1983, Sadavoy et al. 2010a, and Chapters 2 and 4),

$$M_{850} = 2.62 \left(\frac{S_{850}}{\text{Jy}}\right) \left(\frac{d}{450\text{ pc}}\right)^2 \left(\frac{\kappa_{850}}{0.012\text{ cm}^2\text{g}^{-1}}\right)^{-1}$$

$$\times \left[\frac{\exp\left(\frac{17\text{ K}}{T_d}\right) - 1}{\exp\left(\frac{17\text{ K}}{15\text{ K}}\right) - 1}\right] M_\odot, \tag{1.15}$$

where S_{850} is the total flux density of the observed emission structure at 850 μm, d is the distance to the star forming region, κ_{850} is the dust opacity at 850 μm, and T_d is the isothermal dust temperature. The value of 17 K in the exponential term is merely a result of the fundamental constants found in Planck's law: $\frac{hc}{k_B\lambda} = 17K$, where h is Planck's constant, c is the speed of light, k_B is Boltzmann's constant, and

$\lambda = 8.5 \times 10^{-4}$ m is the wavelength. Factored into our definition of κ is an assumed standard gas to dust mass ratio of 100 (e.g. Ossenkopf & Henning, 1994).

The Jeans mass of a core can be rewritten in terms of its temperature and radius (see Sadavoy et al. 2010b),

$$M_J = 2.9 \left(\frac{T_d}{15\,\mathrm{K}} \right) \left(\frac{R}{0.07\,\mathrm{pc}} \right) M_\odot, \tag{1.16}$$

where R is the core's projected circular radius. By calculating the ratio between the core mass and its associated Jeans mass (assuming spherical geometry and only thermal pressure support), one can identify objects that are unstable to gravitational collapse; a gravitationally unstable object has a ratio of $M/M_J \geq 1$. Taking into account the potential turbulent and magnetic pressure support, however, requires additional data sets to fully account for the smaller contributions to the binding energy budget (see, for example, Pattle et al. 2015)

From the scales of molecular clouds to protoplanetary discs, understanding the complex environment which informs the formation of stars and, indeed, planets is a multi-scale, multi-physics problem which requires the use of a variety of different instruments and analysis methods. In this dissertation, I focus primarily on the intermediate scales where filaments and cores define the dominant physics (see, especially, Chapters 2 and 4). In Section 1.3 and Chapters 5 and 6, I will show how observations of dust emission from cores can help constrain models of mass accretion rates which involve transferring mass through the envelope, to the disc, and finally on to the central protostar.

1.3 The Luminosity Problem: Variability of Young Protostars

In the previous section, I outlined the general manner in which material is transferred from large-scale mass reservoirs down to individual forming stars. At the smallest scales I consider throughout this work, however, there is much to be done in understanding how a protostar physically assembles, especially with regard to the rate

of accretion. Assuming all protostars undergo steady-state, inside out collapse (described in Section 1.1 and derived by Shu 1977; Equation 1.9) leads to a discrepancy between the expected and the measured luminosities of observed protostars. This is known as **The Luminosity Problem** and it has existed in the literature for nearly thirty years (Kenyon et al., 1990) though it has been recently revisited and exacerbated by the enhanced statistics on protostars provided by the *Spitzer Space Telescope* (Evans et al., 2009b; Enoch et al., 2009; Dunham et al., 2015).

Simply stated, The Luminosity Problem is that the median protostellar luminosity is measured to be approximately an order of magnitude less than the luminosity generated by the expected steady-state accretion value. For low mass stars, the accretion luminosity dominates the energy output. The expected accretion luminosity, L_{acc}, is calculated assuming that gravitational potential energy is converted into radiation; it can be written

$$L_{acc} = f_{acc}\frac{Gm\dot{m}}{r} = 3.9 f_{acc}\left(\frac{m}{0.25M_{\odot}}\right)\left(\frac{2R_{\odot}}{r}\right)\left(\frac{\dot{m}}{10^{-6}\ M_{\odot}\mathrm{yr}^{-1}}\right)L_{\odot} \qquad (1.17)$$

(McKee & Offner, 2011a), where f_{acc} is the fraction of the accretion energy which contributes to the radiation (assumed to be 1), r is the radius of the protostar, m is the mass of the protostar, and $\dot{m}$ is the accretion rate onto the protostar. To form an average star (of mass 0.5 $M_{\odot}$; note that the mass of a protostar, m, is taken to be half of the final stellar mass), McKee & Offner (2011a) suggest that a protostar will have representative values of $r = 2\ R_{\odot}$ (see, also, Stahler 1988), and $\dot{m} \sim 2.5 \rightarrow 5 \times 10^{-6}\ M_{\odot}\mathrm{yr}^{-1}$ assuming a Class 0+I lifetime of 0.1 to 0.2 Myr (Kenyon et al., 1990) This implies that the luminosity of a protostar should be $10 \rightarrow 20\ L_{\odot}$ but the observed values are closer to $1 \rightarrow 2\ L_{\odot}$ (Kenyon et al., 1990; Dunham et al., 2010, 2015). The two main solutions to the Luminosity Problem addressed in the literature are: (1.) Protostars gain mass over much longer timescales, suggesting the accretion process is slower, or (2.) The accretion does not occur at a constant rate but it occurs during episodic events, punctuated by long quiescent periods.

Considering the first scenario requires an evaluation of the most recent, robust calculated lifetimes of protostars. For Class 0 and I sources, the generally accepted lifetimes are calculated by comparing the number of detected sources to the number of disc objects (Class II sources), then multiplying by the half-life of a disc source (see, e.g. Evans et al., 2009a; Dunham et al., 2015). The half-life of disc sources is

derived by determining the fraction of young stellar cluster members with discs and comparing it to the age of the cluster (e.g. Ribas et al., 2015).

There are many uncertain factors in estimating YSO lifetimes (for a review, see Soderblom et al. 2014). For instance, young stellar cluster ages themselves are highly uncertain (Hillenbrand, 2008), not all disc sources will have the same rate of dispersal with different surveys biased towards shorter and longer lived discs (Evans et al., 2009a), an extinction correction must be performed to properly identify the number of sources in different classes (Dunham et al., 2015), and background galaxy contamination in YSO catalogues can be significant (see Heiderman & Evans 2015 and Chapter 4).

Recently, Dunham et al. (2015) analysed *Spitzer Space Telescope* data taken across 18 molecular clouds across the Gould Belt and performed a protostellar lifetime analysis on the nearly 3000 confirmed YSOs. Assuming the disc half-life to be 2-3 Myr based on previous observational and theoretical work, and testing the inclusion of differing fractions of Class III objects along with the Class II objects in the reference sample of disc sources, they determined the Class 0+I protostellar lifetimes to be 0.46→0.72 Myr. If we input, instead, mass accretion rates of $\dot{m} \sim 0.7 \rightarrow 1 \times 10^{-6}\ M_{\odot}\mathrm{yr}^{-1}$ to form a $m = 0.5\ M_{\odot}$ star in 0.5→0.7 Myr into Equation 1.17, we find that $L_{acc} = 2.7 \rightarrow 3.9\ L_{\odot}$. This value is still higher than the median observed protostellar luminosity. The YSO lifetime results of Dunham et al. (2015) agree with and extend the *Spitzer Space Telescope* c2d (From Molecular Cores to Planet-forming discs; Evans et al. 2009a) survey, leading to the conclusion that mass accumulation onto young protostars indeed happens over timescales too short to fully solve the Luminosity Problem. One complication, however, is that this argument assumes a steady accretion rate throughout a protostar's formation. The accretion rate may subside as the protostellar mass increases (see, for examples, Kenyon et al. 1990; Dunham & Vorobyov 2012), resulting in the protostar gaining most of its mass during the earliest stages of its formation while it is still deeply embedded. In this way, the timescales of mass assembly could remain short and the majority of protostars would be observed while their accretion rates are lower than expected.

In recent years, evidence has been growing for the second scenario, episodic accretion, to resolve the Luminosity Problem as protostars undergoing luminosity outbursts have been observed by several groups (see, for examples, Fischer et al. 2012, Dunham et al. 2014, Audard et al. 2014, Safron et al. 2015, Hunter et al. 2017). In addition, several stars in the later stages of formation are known to undergo accretion burst

phases (for example, **FUors** and **EXors**; see for examples Hartmann & Kenyon 1985; Reipurth 1990; Hartmann & Kenyon 1996; Lorenzetti et al. 2012) and the processes which drive these outbursts may begin at earlier stages of their evolution. The accepted reason an accreting protostar undergoes an outburst is due to instabilities which arise in the protoplanetary disc orbiting the central source.

As briefly introduced in Section 1.1, this protoplanetary disc forms around an accreting protostar. This is the result of a combination of magnetic fields and rotation which cause anisotropies in the otherwise symmetrically infalling material. Therefore, a majority of the mass will first accrete onto the disc before being transferred to the protostar (for a review on pre-main sequence accretion, see Hartmann et al. 2016; also see Hartmann et al. 1998). The rate of mass transport through the disc is not well constrained and is likely variable due to gravitational (at outer disc radii; Vorobyov & Basu 2005, 2006) and/or **magnetorotational** (at inner disc radii; Armitage et al. 2001; Zhu et al. 2009) instabilities as well as the presence of larger-scale, viscous structures. The angular momentum and mass transport can be further complicated by rotation (Hartmann et al., 1986; Costigan et al., 2014; Venuti et al., 2017) the formation of giant planets in the disc (see, for example, Nayakshin & Lodato 2012 and Figure 1.8) and stellar encounters (e.g Forgan & Rice, 2010).

There have been several models developed which describe the variable accretion rate onto a protostar over time (see, for examples, Bell & Lin 1994, Vorobyov & Basu 2005, Rice et al. 2010, Dunham & Vorobyov 2012, Bae et al. 2014, and Vorobyov & Basu 2015) and very few observational constraints to help guide these models. Since the observed submillimetre emission is a result of the reprocessed energy produced by the central protostar, changes in the accretion rate will directly map to emission. In this way, observing variability in the emission is a direct proxy for understanding the underlying accretion variability. Figure 1.9 shows the fractional accretion variation expected from the models of Bae et al. (2014) (red, initially flatter lines) and Vorobyov & Basu (2015) (green, initially steeper lines) versus the time lag between observations. The former includes instabilities driven by the presence of a magnetic field while the latter relies on larger-scale gravitational instabilities in the circumstellar disc to generate episodic mass infall. The expected frequency of outburst strengths between the two models is markedly different over relatively short (observable) timescales (note, however, that both models are presented over timescales ranges shorter than their respective optima).

In order to advance our understanding of how a protostar assembles its mass,

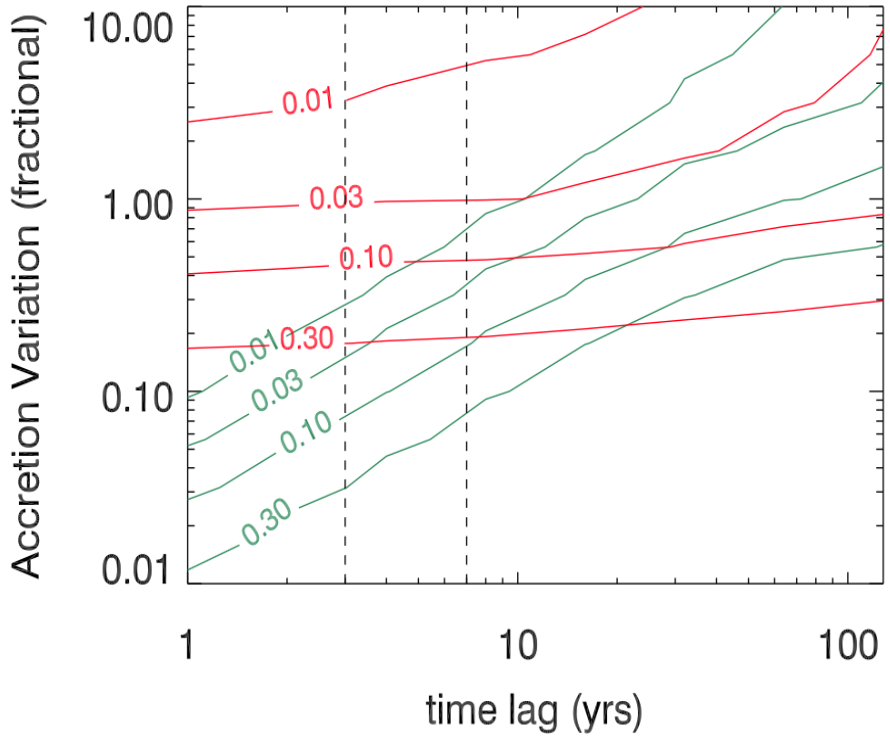

Figure 1.9 A comparison between the expected fraction of time (contours) that two theoretical models predict an amplitude variation greater than the specific amount indicated as a function of the time lag between observations. Green contours (initially steeper) show results from Vorobyov & Basu (2015), where accretion variability is driven by large-scale modes within the unstable disc. Red contours (initially flatter) show results from Bae et al. (2014) where accretion variability is driven by the inner disc. Figure Credit: Herczeg et al., Submitted.

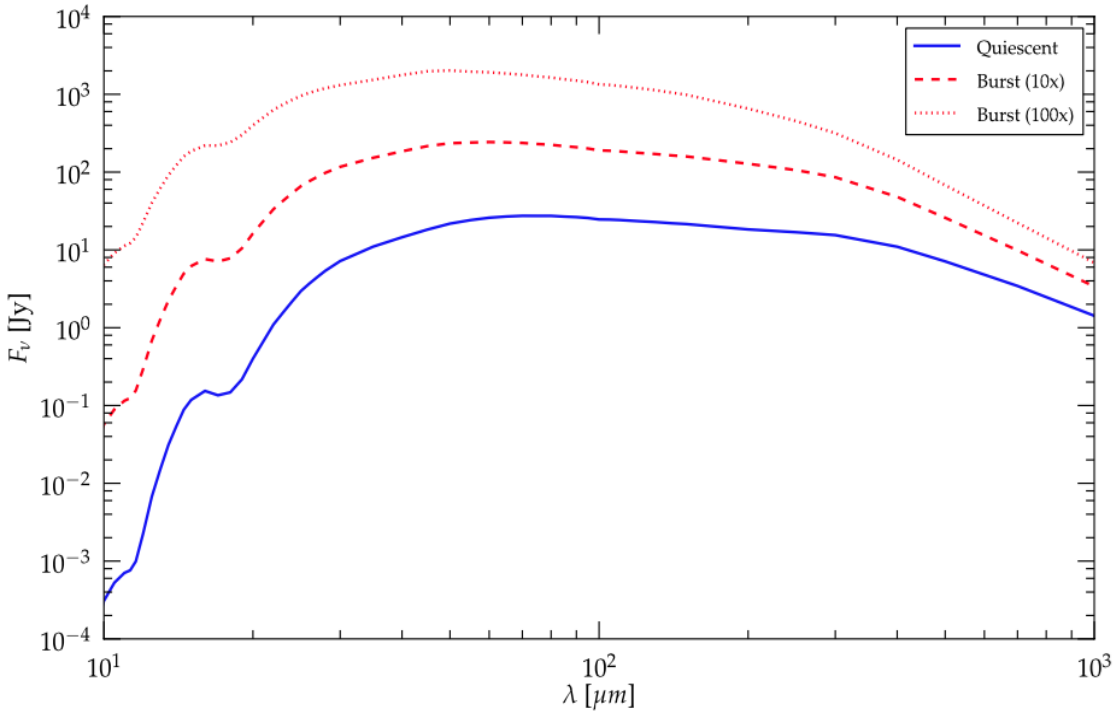

Figure 1.10 The modelled spectral energy distribution of a deeply embedded protostar in its quiescent state (solid line) and in a burst state where the total luminosity (the luminosity of the protostar and the accretion luminosity) increases by a factor of ten (dashed line) and by a factor of 100 (dotted line). Figure Credit: Johnstone et al. (2013).

we require careful and consistent observations over many different star forming regions such that we can determine how often these episodic accretion bursts occur and if different environments lead to different event frequencies. To determine the best observational approach, Johnstone et al. (2013) modelled the SED of a protostar deeply embedded in its nascent envelope undergoing burst events of different strengths (see Figure 1.10) and analysed the fractional brightness increase expected across infrared and submillimetre wavelengths. While the strongest signal occurs at infrared wavelengths, at present the observational potential is limited since there are very few instruments currently available to carry out dedicated, repeated observations as these need to be performed from space.

Depending on the strength of the signal, however, observing an accretion burst is also possible at submillimetre wavelengths (see, for example Safron et al., 2015; Hunter et al., 2017). The increase in the submillimetre continuum brightness is caused by the efficient thermal re-radiation of light due to the dusty envelope surrounding the

protostar. Interstellar dust has a low heat capacity per unit mass, so the envelope quickly achieves thermal equilibrium while the gas takes much longer (owing to its higher heat capacity and the relative inefficiency of gas-to-dust coupling; see Johnstone et al. 2013). Therefore, the timescales for detecting a submillimetre outburst corresponding to a significant variable accretion event are governed by the light crossing time of a typical protostellar envelope. Taking the outer shell of a typical envelope to have a radius of $R \sim 10^3 \rightarrow 10^4$ AU, Johnstone et al. (2013) calculate the light crossing time, $t_{cross} = 2R/c$, to be on the timescale of weeks to months.

Consequently, to further understand variable accretion from an observational perspective, The JCMT Transient Survey was designed to observe eight nearby (<500 pc from the Sun) star-forming regions (see Figures 1.11 and 1.12) at a one month cadence over a period of three years. Observations began in December 2015 and have already produced the deepest submillimetre maps available for some of these eight regions (for a complete overview of the survey, see Herczeg et al., submitted). In addition, after developing robust data reduction, image alignment, and flux calibration techniques (see Section 1.4 and Chapter 5), the survey is expected to uncover significant variable accretion events by detecting flux variation levels of 10% or greater (with an expected corresponding accretion rate increase of 2-4 times this amount; see Johnstone et al. 2013) and there have already been notable detections (see Yoo et al. submitted and Chapter 6). These observations will help constrain the current models of protostellar mass assembly on several year timescales, offering insight into the dominant physics which governs the time lag between accretion bursts.

To help resolve *The Luminosity Problem* and to understand accretion process in general, a wide range of consistent observations focussed on a variety of star-forming environments is necessary to constrain theoretical models of protostellar mass assembly. In Chapters 5 and 6, I describe the methodology and a subset of the first results from the JCMT Transient Survey, the program developed to offer these necessary data.

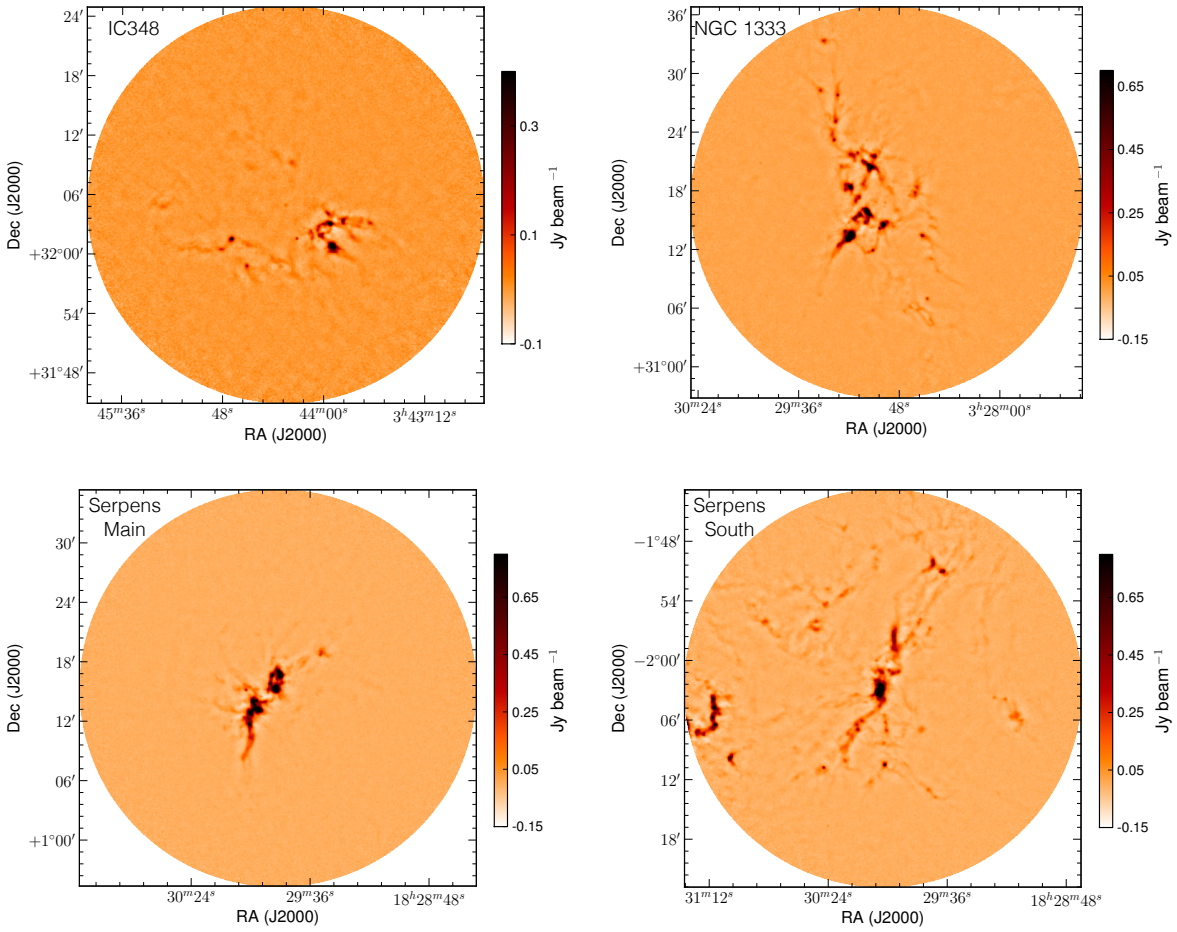

Figure 1.11 Four of the eight JCMT Transient survey regions. Each image was produced by co-adding ten 850 μm observations.

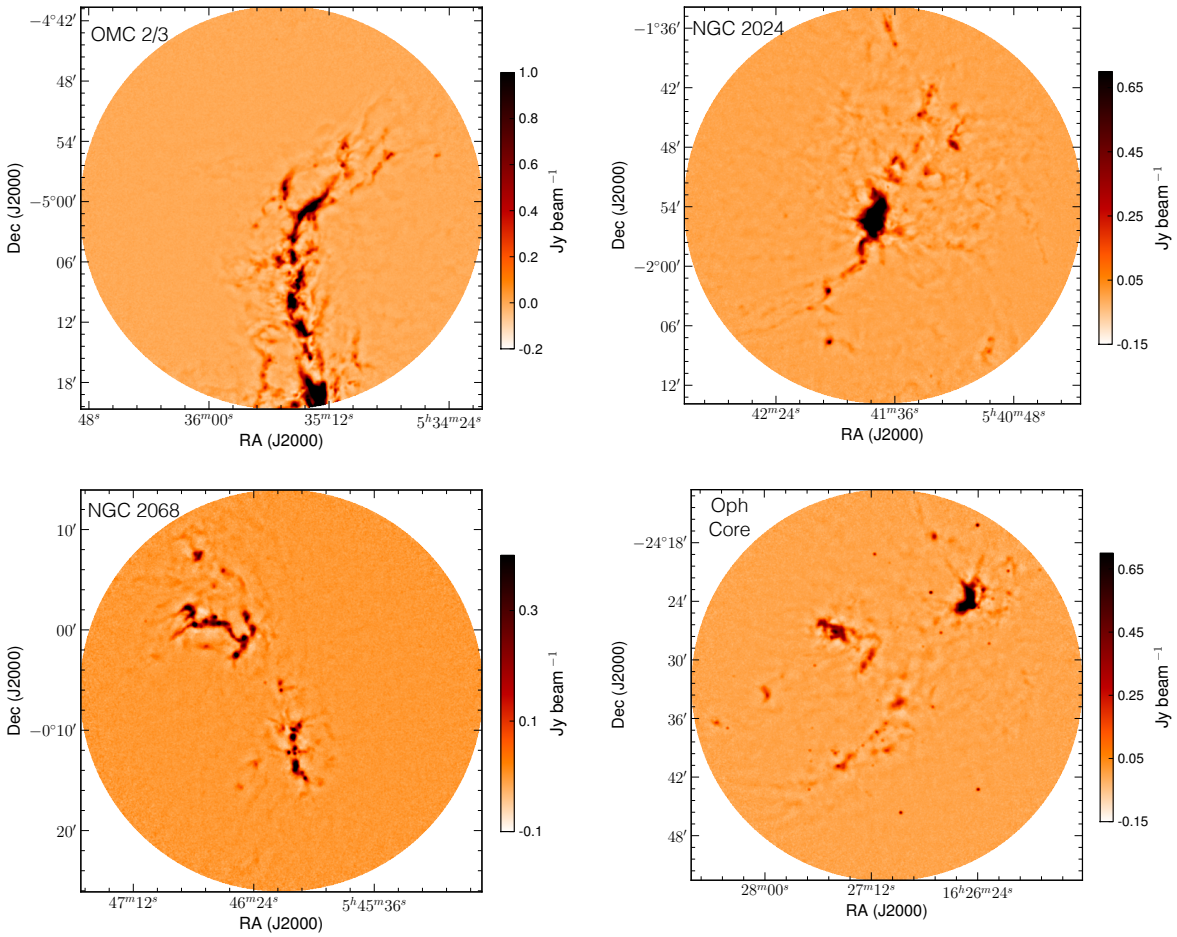

Figure 1.12 Four of the eight JCMT Transient survey regions. Each image was produced by co-adding ten 850 μm observations.

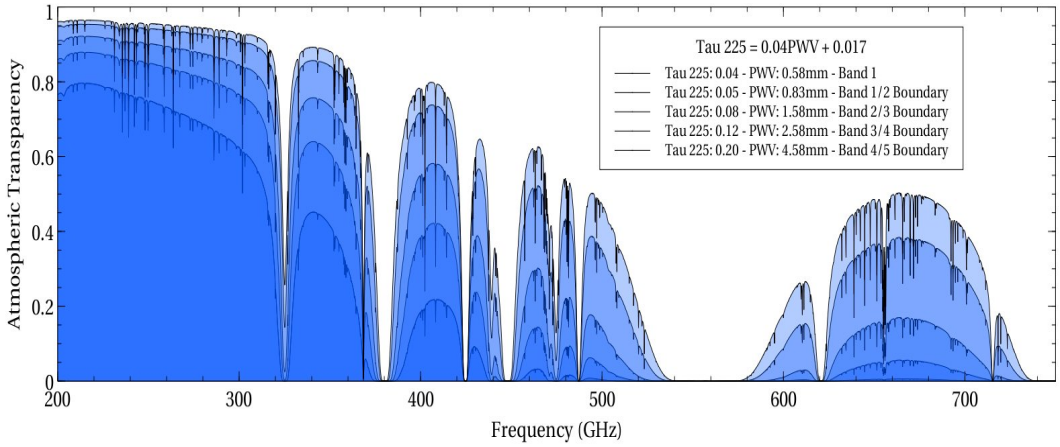

Figure 1.13 The atmospheric transparency at the site of the James Clerk Maxwell Telescope in five different weather bands. The weather bands are based on the amount of precipitable water vapour in the sky with Band 1 being the most ideal weather and Band 5 being the worst weather. Figure Credit: East Asian Observatory.

1.4 Observations at Submillimetre Wavelengths

Throughout the last few sections, I have broadly introduced the theory of star formation and have brought up several topics on which we are currently lacking understanding. There is, however, one underlying challenge that is necessary to address in order to put the observations presented in this dissertation in context. To further our investigation of star forming regions in the Milky Way, we must rely on ground-based submillimetre telescopes such as the JCMT (Figure 1.3). Thus, we are subject to the limitations of relatively narrow atmospheric transparency windows (see Figure 1.13) and we must develop and use robust methods of recovering the astronomical signal we seek to study in light of the atmosphere's emission and absorption. A central theme of this thesis is to develop and improve data reduction and image calibration best practices (see Chapters 3 and 5), specifically regarding the **Submillimetre Common-User Bolometer Array 2** (SCUBA-2; Holland et al. 2013), the work horse continuum observation instrument in operation at the JCMT. Here, I introduce the basics of how this camera operates and what a robust data reduction procedure seeks to accomplish (for further information, see Holland et al. 2013; Chapin et al. 2013; Dempsey et al. 2013).

SCUBA-2 collects continuum data at 450 and 850 μm simultaneously with half-power bandwidths of 32 and 85 μm, respectively. For each wavelength, the detectors are comprised of 4 subarrays of 40×32 **bolometers** which allow for fast, wide-field

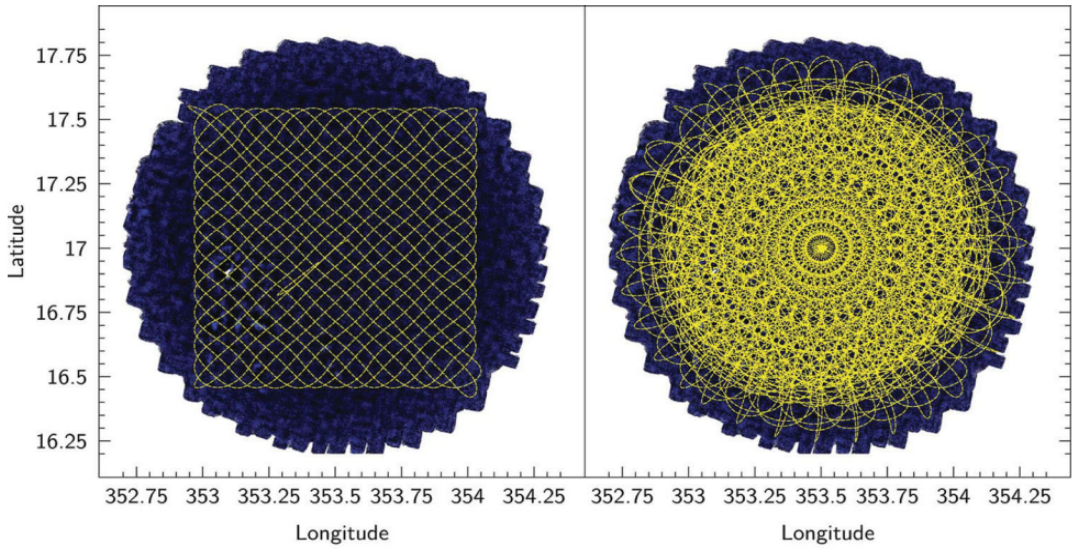

Figure 1.14 A typical *Pong observation* pattern. The blue circular area represents a region of the sky which is being observed. The yellow lines indicate the motion of the telescope across the sky, scanning across a 30′ diameter until the area is consistently sampled. Figure Credit: Holland et al. (2013).

continuum imaging (increasing the number of detectors its predecessor, SCUBA, was equipped with by more than two orders of magnitude). The bolometers are an alloy of Molybdenum mixed with Copper cooled to ~ 60 mK known as **transition edge sensors**. When submillimetre radiation is absorbed by these devices, their resistance dramatically changes and the corresponding change in output current is converted into a power received based on calibration images taken nightly.

In a typical observation of the type presented in this dissertation, the telescope continuously scans across a circular region of the sky, 30′ in diameter. Whenever the telescope reaches the boundary of this footprint, it changes direction, scanning across the same areas of the sky from multiple position angles until the desired region is consistently sampled to a required depth (see Figure 1.14). This scan pattern is called a **pong observation** after the video game which its motion resembles. The data received are measurements of power throughout the duration of the observation and these can be transformed into an image, with signals appearing for short timescales corresponding to smaller-scale structures and signals appearing for longer timescales corresponding to larger-scale structures.

At any given time, t, the power received by the bolometer, $b(t)$, is given by

$$b(t) = f \times [e(t) \times a(t) + n(t)], \tag{1.18}$$

(Chapin et al., 2013) where f is the flux conversion factor from power units to flux units, $e(t)$ is the extinction through the atmosphere, $a(t)$ is the astronomical signal we seek to study, and $n(t)$ is the noise which is comprised of three sources:

1. Uncorrelated white noise.
2. Atmospheric signal.
3. $1/f$ noise (pink noise) introduced by the instrumentation.

The goal of data reduction and image recreation is to model and eliminate the sources of noise such that the astronomical signal can be recovered. In the case of ground-based submillimetre astronomy, the most challenging issue to address is that of the atmospheric signal. This is the reason that the telescope scans continuously across the sky, revisiting each area from several different position angles. The time varying atmosphere which mimics large-scale structure will appear differently with each pass whereas the astronomical signal will remain steady and this allows us to partially disentangle the signals. If a significant fraction of bolometers receive the same, low frequency signal over time, this is referred to as a *common mode* source of noise (dominated by atmospheric fluctuations) and it is removed from the data. This means that large-scale, astronomical structures ($\sim 600''$) cannot be recovered by SCUBA-2 and further information must be gathered from other telescopes and similar wavelengths (see Section 1.2 for a discussion on analysing star formation at different scales).

In addition to the atmospheric emission, there is also an extinction correction that must be calculated and applied (see Figure 1.13 and Equation 1.18). At the JCMT, this calculation relies on measurements taken by the Precipitable **water vapour monitor** (WVM) in operation at the telescope (Dempsey & Friberg, 2008). This device measures three points of the 183 GHz water line (the peak and the two wings of the profile) in order to fit the broad feature and characterise the amount of precipitable water vapour in the atmosphere.

For the work presented here, SCUBA-2 is an excellent choice of instrument (due to the relatively small beam size of $15''$ at 850μm, the sensitivity that allows us to probe ideal mass ranges, and the necessary subtraction of larger scale atmospheric

structure) which provides information on the imperative intermediate scales involved in the theory of star formation such as prestellar cores and their connection with young stellar objects (see Chapter 4 for an example of combining SCUBA-2 data with larger-scale information provided by the 2 Micron All Sky Survey and smaller-scaler information provided by the *Spitzer Space Telescope* and the *Herschel Space Observatory*).

Analysing ground-based submillimetre data in the most robust manner possible is heavily reliant on the data reduction process and, thus, it should be studied and understood in order to recover the most useful images for analysis. Chapters 3 and 5 describe, in detail, the work I have completed to investigate these procedures and derive best practices for a variety of scientific goals.

1.5 Dissertation Overview

In this dissertation, I build on the knowledge presented in the previous introductory sections by offering new insights organised into five main projects:

1. In Chapter 2, I examine core formation in a numerical simulation, analyse the associations between identified cores and simulated protostellar objects, investigate mass flow from larger to smaller scales, and discuss observations which can be performed to obtain a more complete picture of the substructure present in cores at small scales. The contents of this chapter are published in The Astrophysical Journal (Mairs et al., 2014).

2. In Chapter 3, I investigate both the successes and limitations of astronomical signal recovery using two prominent reduction methodologies as case studies by introducing simulated emission sources with known properties into raw 850 μm, SCUBA-2 data. In this way, I quantify the reliability of the Gould Belt Survey reduction recipe used for more than 10 papers. I then offer suggestions for improving these methods such that the most robust signal is consistently recovered. The contents of this chapter are published in the Monthly Notices of the Royal Astronomical Society journal (Mairs et al., 2015).

3. In Chapter 4, using the 850 μm continuum maps of the southern extent of the Orion A molecular cloud obtained using SCUBA-2, I calculate masses, sizes, column densities, and concentrations of identified emission sources. I then discuss fragmentation in terms of a Jeans instability analysis and highlight interesting structures as candidates for follow-up studies. Furthermore, I associate the detected emission with young stellar objects identified by the *Spitzer Space Telescope* and the *Herschel Space Observatory* and construct a simple model to examine the spatial distribution of these YSOs with respect to the dense structures observed using SCUBA-2. The contents of this chapter are published in the Monthly Notices of the Royal Astronomical Society journal (Mairs et al., 2016).

4. In Chapter 5, I develop methods that use the properties and locations of bright, compact emission sources fitted with Gaussians to decrease the uncertainties in SCUBA-2 measured fluxes by an unprecedented factor of 3 for a wide range of consistent observations spanning eight different star-forming environments. This chapter presents the detailed ground work necessary in order to study the evolution of the mass assembly rate onto a forming protostar (Chapter 6). The contents of this chapter are presented in The Astrophysical Journal (Mairs et al., 2017).

5. In Chapter 6, I use the data reduction and calibration methods outlined in Chapter 5 to investigate variability at the earliest stages of low-mass star formation, which is fundamental in understanding how a protostar assembles mass. I compare 850 μm JCMT Transient Survey data with archival JCMT Gould Belt Survey data to investigate signatures of variability over 2-4 year timescales. Throughout this work, I identify 7 robust candidates for variability across 8 different molecular cloud regions in the Gould Belt and measure their fractional brightness changes over time to better understand submillimetre signatures of changing mass accretion rates. The contents of this chapter have been submitted to The Astrophysical Journal for publication.

Finally, in Chapter 7, I summarise the results of each project and provide concluding remarks. A glossary of commonly used terms and acronyms is provided in Appendix A.

Chapter 2

Synthetic Observations of a Simulated Turbulent, Star-Forming Region

"You should see the stars tonight.
How they shimmer, shine so bright.
Against the black they look so white.
Coming down from such a height
To reach me now..."
-David Crowder, Stars

2.1 Foreword

At the heart of science is the comparison between observational data and theoretical predictions. A question is posed, a model is constructed, and observational constraints guide and motivate further refinements to that model. One of the most direct ways this exercise unfolds is by post-processing theoretical models (simulations) with all of their known physics through the same procedure as data obtained using a telescope such that the final images can be analysed and directly compared to observations (see, for examples, Malinen et al., 2011; Duarte-Cabral & Dobbs, 2016). By convolving the simulations to the same resolution as observed data, observing only projections of three dimensional simulated image cubes, and, in the case of ground-based sub-millimetre observations, removing large-scale structures to recreate the subtraction

The material presented in this chapter (excluding the foreword) has been published in the Astrophysical Journal: Mairs et al. 783, 60, 2014. DOI: 10.1088/0004-637X/783/1/60.

of atmospheric signal (see Section 1.4 and Chapter 3), the same analysis techniques used by an observer can be directly applied to theoretical predictions where useful physical insights can be derived.

One of the prominent goals regarding the formation of stars that can be approached by synthetically observing simulated data is determining the dominant sources of pressure support against gravitational collapse within a prestellar core or filament. We expect that thermal pressure plays a large role; in fact, the Jeans mass (the maximum mass an object or a given size can achieve before gravitational collapse is inevitable) of dust emission structures is generally calculated assuming only thermal pressure support (see Equation 1.16). There are, however, other potential support mechanisms such as magnetic field pressure and non-thermal, turbulent motions. The relative contributions of these support pressures are still debated and are likely largely influenced by the individual star-forming environments (for a review, see André et al., 2014).

The project I present in this chapter was largely motivated by recent studies indicating that there are cores which have masses calculated to be several times their Jeans masses yet show no obvious signs of protostellar associations (for example, Sadavoy et al., 2010b). Deemed "Super-Jeans starless cores", these objects gained considerable interest in the community. Are they prestellar cores that had not yet initiated collapse? What additional support along with thermal pressure might aid in preventing gravitational collapse? Are these cores, in fact, associated with protostars which are too deeply embedded in their dusty envelope to be unambiguously detected and therefore, they are misclassified?

To address this problem, my collaborators in the following paper (Mairs et al., 2014) ran simulations of a turbulent molecular cloud (Offner et al., 2013) and post-processed them to look like data obtained by the James Clerk Maxwell Telescope. I then led an analysis on column density maps generated at different time snapshots throughout the evolution of the simulated, star-forming molecular cloud in an effort to uncover evidence of Super-Jeans starless cores to gain insight as to the potential importance of turbulence as an additional support mechanism alongside thermal pressure. In the process of investigating this question, I compared initial core masses to final protostar masses and realised that there was an important connection between large-scale mass reservoirs (structures which were subtracted from the simulation due to the post-processing) and small-scale cores. Following this assembly of cores further, I produced and analysed additional post-processed observations of the simulation this

time approximately recreating data as they might be obtained by the Atacama Large Millimetre/submillimetre Array (ALMA) which has a much higher resolution than the JCMT.

This work has provided an important point of comparison to other simulations (Frimann et al., 2016), informed predictions for what is possible with ALMA (Bradshaw et al., 2015; Dunham et al., 2016; Kirk et al., 2017), and provided additional evidence for mass flow along filamentary structures in the interstellar medium (e.g. Johnstone et al., 2017).

Abstract

Interpreting the nature of starless cores has been a prominent goal in star formation for many years. In order to characterise the evolutionary stages of these objects, we perform synthetic observations of a numerical simulation of a turbulent molecular cloud. We find that nearly all cores that we detect are associated with filaments and eventually form protostars. We conclude that observed starless cores which appear Jeans unstable are only marginally larger than their respective Jeans masses (within a factor of 3). We note single dish observations such as those performed with the JCMT appear to miss significant core structure on small scales due to beam averaging. Finally, we predict that interferometric observations with ALMA Cycle 1 will resolve the important small scale structure, which has so far been missed by mm-wavelength observations.

2.2 Introduction

A core, as defined in this work, is an object which has a relatively small mass and will form at most a few stars. Distinguishing "starless" cores from "protostellar" cores is the first step to answering several open questions in the field of star formation. For example, many starless cores have been measured to have masses several times that of their "Jeans mass" (Sadavoy et al., 2010a), the limit at which thermal pressure alone can provide adequate support against the self gravity of the object (Jeans, 1902). One possibility is that there are poorly understood non-thermal support mechanisms, such as magnetic fields or turbulence, preventing the collapse of these cores. Another likely possibility, however, is that the cores have been misclassified as starless when in fact they are collapsing and dim protostars lie hidden within their dusty envelopes. In fact, there is strong evidence from recent interferometric observations (Schnee et al. 2012a; Enoch et al. 2010; Dunham et al. 2011; Pineda et al. 2011) that many cores classified as "starless" actually harbour Very Low Luminosity Objects (VeLLOs, objects with luminosities $\lesssim 0.1\ L_{\odot}$; see Young et al. 2004; Kauffmann et al. 2005; Di Francesco et al. 2007a; Dunham et al. 2008).

Another avenue of study which relies on an accurate classification of starless and protostellar cores is the effort to link the prestellar Core Mass Function (CMF) to the stellar Initial Mass Function (IMF) (for example, Nutter & Ward-Thompson 2007; Enoch et al. 2008; Könyves et al. 2010; Alves et al. 2007). It appears that more massive cores are typically found to harbour protostars (see, for example, Sadavoy

et al. 2010a and Ragan et al. 2012). As a result, if protostellar cores have been misclassified as starless and if the misclassification is more likely for particular masses, then any attempt to compare the observed starless CMF with the IMF is problematic.

Finally, as Kirk et al. (2005) describe, the lifetime of the subset of starless cores that will go on to form stars can be determined by comparing the relative number of starless cores and protostellar cores. Similarly, the number of protostars relative to more evolved young stars is proportional to the protostellar lifetime (Evans et al., 2009a).

The most common method to classify cores as starless or protostellar is to identify cores via their dust continuum emission by using catalogues such as the "Submillimetre Common-User Bolometer Array (SCUBA) Legacy Survey" (Di Francesco et al., 2008a) and then attempt to identify embedded sources using infrared data (e.g. Jørgensen et al. 2007; Sadavoy et al. 2010a) such as the "Molecular Cores to Planet Forming Disks Catalogue" (c2d; Evans et al. 2003, Evans et al. 2009a). Due to the high optical depth of these dusty envelopes, however, extinction can obscure and even completely hide dim protostars in the centre of these structures leading to errors in the core classification. In an attempt to explore the veracity of the non detections of embedded infrared objects, recent studies have utilised interferometric spectroscopy of a variety of protostellar and outflow tracers such as CO, SiO (2-1), HCO^+, and N_2H^+ (Pineda et al., 2011; Schnee et al., 2012a,b).

In order to gain further insight into the misclassification of starless cores while investigating the effectiveness of observational techniques, we compare starless and protostellar cores observed in the controlled environment of a simulated turbulent molecular cloud. We analyse the formation and evolving properties of dense structures in the same manner as real observations taken with SCUBA at the JCMT with the added benefit of knowing precise locations and masses of forming protostars. This analysis concentrates on the observed stability of a given object, as defined by the Jeans mass, near the time in which collapsing regions begin to form.

This paper is organised as follows: Section 2.3 describes the numerical simulation. Section 2.4 outlines the methods we use to simulate observations and describes our method to identify objects and derive their stability. We present the bulk properties of the observed objects and their general evolution including stabilities, densities, and protostar/envelope relationships as "observed" by SCUBA in section 2.5. Section 2.6 gives the results of the simulated interferometric observations. In section 2.7, we discuss the results. Section 2.8 presents concluding remarks.

2.3 Simulations

In this paper, we analyse a series of snapshots from a hydrodynamic simulation of a turbulent molecular cloud that is forming stars. This simulation was previously presented in Offner et al. (2013) (simulation Rm6), in which it was used to study the chemical distribution in molecular clouds. We briefly summarise the numerical procedure and parameters below.

The simulation was performed with the ORION adaptive mesh refinement (AMR) code (Truelove et al., 1998; Klein, 1999), and it includes large-scale driven turbulence, self-gravity, and sink particles (Krumholz et al., 2004). The simulation was first driven for two crossing times without gravity and then evolved for a global free-fall time with gravity. Sink particles were inserted at the finest AMR level when the local density violated the Truelove criterion for $J = 0.25$[1] (Truelove et al., 1997). This corresponds to a mass density of 4.6 x 10^{-16} g cm^{-3} ($n_{\rm H} = 1.2$ x 10^{8} cm^{-3}). Throughout this work, the terms "sink particle" and "protostar" will be used interchangeably when discussing the simulation. The basegrid is 256^3 cells and the run has 4 AMR levels.

The bulk properties of the simulation were chosen to represent a typical Galactic low-mass, star-forming region. The simulation domain has a length of 2 pc and contains $\sim$600 $M_\odot$, which corresponds to an average number density of $n_{\rm H} = 1300$ cm^{-3}. The Mach number, $\mathcal{M}_{\rm 3D}$=6.6, was set so that the simulated cloud is approximately virialised and satisfies the linewidth-size relation (e.g., McKee & Ostriker 2007a).

The simulation was run for one global free-fall time of 0.95 Myr. At the final time, the cloud contains 88 protostars and has a star formation rate per free-fall time of 0.18[2]. Since the simulation does not include magnetic fields or stellar feedback, the sink particles represent an upper limit on the true star formation (Offner et al., 2009a; Commerçon et al., 2011; Hansen et al., 2012). Since the collapse has not been followed down to the sizes of individual protostars, and feedback such as outflows is not included, the sink particles likely over-estimate the stellar mass by a factor of ~ 3 (Matzner & McKee, 2000; Enoch et al., 2007; Alves et al., 2007). The most massive sink particle formed throughout the simulation is 8.5 $M_\odot$.

[1] Where J is the ratio of the cell size to the Jeans length.

[2] Including the mass of the protostars and their envelopes, see Figure 2.3.

2.4 Synthetic Observation Methods

2.4.1 Single Dish Synthetic Observations

The simulation was placed at a distance of 250 pc to represent the Perseus molecular cloud as this region has been well-studied by c2d (Evans et al., 2003, 2009a) and other surveys (Kirk et al., 2006a; Hatchell et al., 2005; Sadavoy et al., 2010a). At this distance, 2 pc corresponds to 1650″. We analyse column density maps integrated along each of the x, y, and z directions. Each integrated image was gridded to 512 x 512 square pixels 3.22″ on a side.

For the optically thin case, as we have here, it is simple to convert from column density, N, to flux, S_ν:
$S_\nu = N\kappa_\nu B_\nu$, where B_ν is the Planck function and κ_ν is the opacity calculated at frequency ν. The flux can then be related to the core mass via Equation 2 in Sadavoy et al. (2010b) (modified for a typical core temperature of 10 K):

$$\frac{S_{345}}{\mathrm{Jy}} = 0.48 \left(\frac{M_c}{M_\odot}\right) \left(\frac{d}{250\ \mathrm{pc}}\right)^{-2} \left(\frac{\kappa_{345}}{0.01\ \mathrm{cm^2\ g^{-1}}}\right) \times \left\{ \frac{\exp\left[1.7 \left(\frac{10\ \mathrm{K}}{T_d}\right)\right] - 1}{\exp(1.7) - 1} \right\}^{-1} . \quad (2.1)$$

Here, S_{345} represents the flux received at 345 GHz (850 μm), M_c is the core mass, $d = 250$ pc is the distance to the source, κ_{345} is the opacity at 345 GHz (see below), and $T_d = 10$ K is the isothermal dust temperature.

We adopt an opacity value appropriate for a dusty protostellar core at 230 GHz, $\kappa_{230} = 0.009$ cm^{2}g^{-1} (Ossenkopf & Henning, 1994), in accordance with previous observations (e.g. Schnee et al. 2012a). This value assumes MRN grains with a thin ice mantle for a core with a density of 10^6 cm^{-3} which is typical in nearby star forming regions (see Johnstone et al. 2000c, Schnee et al. 2012a, Sadavoy et al. 2010a).

By assuming a spectral index, β, where $\kappa_\nu \propto \nu^\beta$, one can extrapolate to other frequency values. For $\beta = 2.0$, which we adopt here, $\kappa_{345} = 0.0202$ cm^{2}g^{-1}.

The flux maps are smoothed to 20″ to compare against the smoothed SCUBA catalogues[3]. Then, to further match the observations, we remove large-scale structure by smoothing the same images by 120″ and subtracting this smoothed map from the

[3]The JCMT beam is 15″ but the SCUBA observations to which we are comparing were smoothed to 20″ (Di Francesco et al., 2008a).

former 20″ maps (see also Kirk et al. 2006a). In total, we analyse 68 simulation outputs distributed between $t = 0 - 1t_{\rm ff}$. For each of these outputs, we consider each projection separately. Note that the mass of each core changes depending on the projection (see Section 2.4.2 below) but, if detected multiple times, each detection will be considered as an individual core. The sink particle masses remain unchanged over each projection.

2.4.2 Core Definition

To extract the bulk properties of the core population and analyse their time evolution, we use the automated routine CLFIND2D (Williams et al., 1994).

The lowest flux level which defines the boundary of an observed core is 0.09 Jy/beam set by comparison with the observations. This threshold is defined by the opacity and, assuming the material is isothermal, it is equivalent to the mass depth to which we are sensitive (see Equation 4.1). Thus, the choice in our opacity value sets our scaling between the observations and the simulation.

Each core's radius is then compared to the full width at half maximum (FWHM) of the smoothed 850 μm SCUBA observations, 20″. If the core is smaller than this, it is deemed spurious and removed from the analysis (since it might be noise). For the non-spurious cores, we convert the measured flux into a mass by inverting Equation 2.1.

Once the mass is attained, an object's stability can be analysed using simple assumptions. We estimate the Jeans mass, $M_{\rm J,c}$, of an identified core by applying the simple scaling relation presented by Sadavoy et al. (2010a),

$$M_{\rm J,c} = 1.9 \left(\frac{T_d}{10\,{\rm K}} \right) \left(\frac{R_{\rm c}}{0.07\,{\rm pc}} \right) M_{\odot}. \tag{2.2}$$

Here, $T_d = 10$ K is the (assumed) isothermal dust temperature and $\rm R_c$ is the radius of the core.

To determine the stability of each core, we compare the mass attained from inverting Equation 4.1 to the Jeans mass calculated by Equation 2.2. If $M_{\rm c} \geq M_{\rm J,c}$, the object is defined as "super-Jeans" an unstable configuration which should show signs of gravitational collapse if thermal pressure alone were counteracting the force of gravity. $M_{\rm c} < M_{\rm J,c}$ represents a stable, "sub-Jeans" object which would not be expected to collapse since the thermal pressure within the assumed spherical object would be more than enough to balance the gravitational forces.

Once we determined the stability parameter using only the envelope mass, we correlated the positions of protostars (sink particles) with the CLFIND2D objects. If a protostar lies within 75% of the circular radius (see below) of the centre of a core, we define the core to be protostellar. Therefore, a comparison can be made, for example, between the cores that are observed to be stable (cores without protostars) and the cores with evidence of collapse (due to the fact that they have embedded protostars). We tracked the growth of protostellar and starless core masses through time along with density, stability, and position.

To visually display the cores on the flux maps, the images include circles and squares corresponding to the size of each core at the location of each of the core centroids (see Figure 2.1). Circles represent cores that are Jeans unstable ($M \geq M_{\mathrm{J,c}}$) and squares denote cores with masses less than the calculated Jeans mass. Plus signs symbolise the location of protostars. We constructed movies by stitching together images of sequential outputs (labeled at the top of each frame, see Figure 2.1).

Since protostellar masses cannot be directly measured, adding the protostellar mass to the core mass does not make observational sense but allows us to track the stability of an object. When more than one protostar is associated with a given core, the protostellar masses are simply added. Without sufficient feedback, however, the available material will continue to accrete onto a given protostar. Without outflows, protostellar masses may be overestimated by up to a factor of ~ 3 (Matzner & McKee, 2000; Enoch et al., 2007; Alves et al., 2007).

Once a protostar is formed the inner envelope will be heated. Observationally this makes it harder to convert from observed 850 micron flux to mass and thus makes Jeans stability investigations difficult for protostellar cores. For the simulations investigated here, however, the lack of included heating makes the mass determination and stability analysis straightforward.

Note that the mass, size, and density scales of objects we extract are dependent on the large-scale structure in the image. To investigate, we performed structure identification for maps that had not undergone the $120''$ scale removal. In these cases we find large reservoirs of mass, which are strongly associated with filamentary structure (see Section 2.5.1), surrounding each core. These extended zones are approximately twice the size of cores identified when the large-scale structure is removed. It is useful to consider that it has been previously determined that CLFIND2D works reasonably well when a field is sparsely populated with discrete objects, but struggles to sensibly pick out important structures when the field is "crowded" (see, for example, Pineda

et al. 2009b).

2.4.3 Interferometric Synthetic Observations

The Common Astronomy Software Applications (CASA)[4] package is used to simulate 100 GHz Atacama Large Millimetre Array (ALMA) Cycle 1 interferometric observations of several individual cores in order to compare with the single dish results. We choose a five second "snapshot" integration time to match real observations; 90 seconds in total is required to create a mosaic for each core.

Beginning with the simulated column density maps, we again generate flux maps as described above. For a given core, we use a square 2 arcminutes on a side centred on the object's coordinates as the input sky model (the simulated flux map). Then, we construct the UV visibilities for the most compact arrangement of antennas using the CASA package *simobserve*. We employ *simanalyze* to Fourier transform these visibilities into the image plane.

In this study, the simulation has similar densities and temperatures to the Perseus cloud. Therefore, the declination of the observation is set to a reasonable approximation of the cloud's position: J2000 +30d00m00. We use a hexagonal stitching pattern for each mosaic.

All observations include thermal noise. In CASA, a robust atmospheric profile exists for the ALMA site including the altitude, ground pressure, relative humidity, sky brightness temperature, and receiver temperatures. In *simobserve*, the user need only define the precipitable water vapour (pwv) which had a chosen value of 1.262 mm. With these assumptions, the noise for the ALMA Cycle 1 image is $\sim$ 0.1 mJy/beam. Since these simulated observations are only meant to note whether the source was detected, the maps are not "cleaned"; we simply convolve them with the point spread function of the instrument to produce a "dirty" map for analysis. This will not significantly alter the mass of the objects detected, however, a cleaned map would reveal more structure over a potentially larger area.

Simulated observations using the Submillimetre Array (SMA) and the Combined Array for Research in Millimeter-wave Astronomy (CARMA) were also performed, but we did not detect any cores in the resulting maps.

[4]see http://www.casa.nrao.edu

2.5 Results from Single Dish "Observations"

Over the course of one free-fall time, we traced several core properties both qualitatively and quantitatively. The following sections describe our main results.

2.5.1 Filamentary Structure

The idea that filaments play a role in in the formation of dense cores has been entertained for several decades (see, for example, Schneider & Elmegreen 1979b). The growth of instabilities in filaments and subsequent fragmentation have been numerically analysed in both the linear (e.g. Inutsuka & Miyama 1992) and nonlinear regimes (e.g. Inutsuka & Miyama 1997). Robust simulations of isothermal, self gravitating cylinders have revealed several properties of filaments such as characteristic temperatures, external pressures, densities, and radii which are consistent with Herschel observations (Fischera & Martin, 2012b,a). The Herschel observations show that filaments are present throughout many star forming regions (André et al., 2010b). Additionally, Hacar et al. (2013) performed observations of $C^{18}O$(1-0), N_2H^+(1-0), and SO($J_N = 3_2 - 2_1$) in the Taurus star forming region with the 14 m FCRAO telescope (and supplemented the data with APEX 870 μm and IRAM 30 m 1200 μm) where they found that cores appear to form in a two step process. First, velocity-coherent filaments form. Then, these large structures fragment into cores. Kirk et al. (2013b) and Friesen et al. (2013) have found evidence of filamentary accretion flows in the Serpens star forming region using a variety of spectral lines observed with the ATNF Mopra 22 m telescope and the K-Band Focal Plane Array at the Robert C. Byrd Green Bank Telescope, respectively. Hennemann et al. (2012) suggest that gravitationally unstable filaments are the driving factor for star formation in the Cygnus X region with a specific emphasis on the DR21 ridge. Furthermore, Myers (2009b) shows that young, embedded star clusters are associated with multiple filaments. It has also been shown that filamentary geometry is ideal for the growth of small-scale perturbations that lead to large scale collapse in a preferential dimension (the length of the filament) and that filaments containing only a few Jeans masses can easily fragment (for a thorough description, see Pon et al. 2011).

Of course, some detections of filaments may be attributed to multiple beam diluted objects so careful investigation of properties such as velocity coherence from spectral fitting are necessary to characterise a structure with certainty. As suggested by the authors above and references therein, a typical filament within a molecular cloud has

a width of ∼0.1 pc. We removed scales of 0.15 pc (120″ at the distance of the Perseus star forming region) from the analysis of the simulation presented here, however, to focus on the cores themselves and not their parent structures.

With this in mind, the convolved simulation hosts cores which are forming almost exclusively along what appear to be dense filamentary structures. As the simulation evolves in time, the objects appear to travel along these striations, fragmenting and coalescing into a variety of morphologies (see movies).

Figure 2.1 shows images of four of the sixty-eight snapshots. The top left panel represents an early time in which no protostars have formed; the bottom right panel represents one free-fall time, $t_{\rm ff}$. The filaments stand out clearly and their qualitative association with the identified cores is obvious.

2.5.2 Bulk Properties of the Ensemble

In this section we present the mass and density distribution of the identified cores, where we analyse cores identified from three orthogonal views. Figure 2.2 shows the distributions of core masses and densities at different times throughout the simulation. We calculate the density of each core by assuming the mass is uniformly distributed over the object as if it were a sphere with a radius determined by its projected area.

The top row of Figure 2.2 presents the dataset in which no protostellar masses were included in the mass determination in order to compare directly with observations. We note that the range in core masses and densities found in the simulation are consistent with real observations of Perseus (Sadavoy et al., 2010a; Enoch et al., 2008). The bottom row illustrates the core mass distribution including the protostellar masses in order to analyse the "true" stability of a given core. As time progresses, the core masses increase as gas accretes and collapses to higher densities. This is more evident in the bottom row than the top. New cores are identified throughout the simulation and therefore an approximately constant low mass population of objects is present throughout the later stages of the simulation.

At the end of the simulation when protostars are not taken into account in the mass estimate, the median core mass and the mean core mass are both found to be 0.89 $\rm M_{\odot}$. Including the mass of protostars yields nearly equivalent median and mean masses of approximately 1.9 $M_{\odot}$. The median and mean number densities of the dataset without protostellar masses are both $n_{\rm H} = 1.3 \,{\rm x}\, 10^5$ cm^{-3}. The dataset including protostellar masses has a median number density of $n_{\rm H} = 1.8 \,{\rm x}\, 10^5$ cm^{-3}

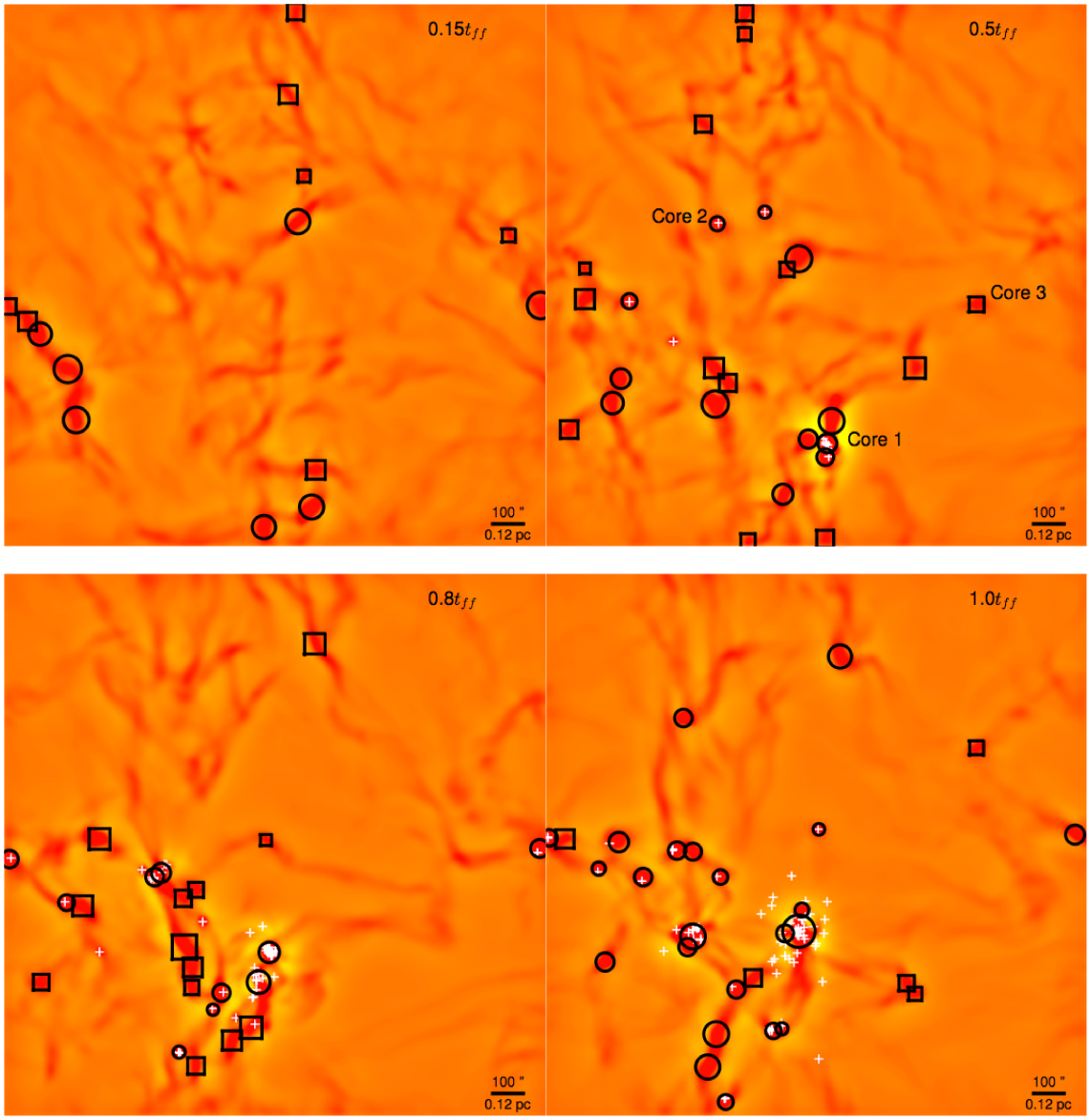

Figure 2.1 Four snapshots ranging from "early" times to "late" times (t = $0.15t_{\rm ff}$ to t = $t_{\rm ff}$, see labels). Protostellar masses have been included in the stability calculations. The Y-dimension integrated images are shown. Circles represent unstable cores, squares show the locations of stable cores, and plus signs display the locations of protostar formation sites. Three cores that we study in greater detail are highlighted in the top right panel.

and a mean number density of $n_{\rm H} = 2.7 \,{\rm x}\, 10^5$ cm^{-3}.

The density of a core can be compared with three reference values: the average density of the box, n_0, the density of a typical shocked region, $n_{\rm s}$, and the "modal density", $n_{\rm c}$.

$n_0 = 1.3 \,{\rm x}\, 10^3$ cm^{-3}. This is an order of magnitude lower than the density of any identified object. To estimate the compressed density, we consider a 1D, isothermal shock at the typical density: $n_{\rm s} = \mathcal{M}_{\rm 1D}^2 n_0 = 1.9 \,{\rm x}\, 10^4$ cm^{-3} (see section 2.7.1 for more details). This value is shown by the vertical line in Figure 2.2, which is close to the lowest densities of the cores.

The "modal density" is an empirically derived density noted by the vertical dashed line in Figure 2.2. Whether or not the masses of the sink particles are taken into account in the analysis, there appears to be a peak in the density distribution at a number density of $n_{\rm H} \sim 1.0 \,{\rm x}\, 10^5$ cm^3. Note that the tail of the distribution in Figure 2.2 is quite different depending upon whether we include the protostellar masses in the estimates, especially at later times.

2.5.3 Core Stability

Over time, cores become visible because gravity produces densities which exceed the threshold of observability. Thus, more cores are identified as the simulation proceeds (see Figure 2.3). At t = $0.5t_{\rm ff}$ there are 78 identified cores over all three projections. 80 cores are identified by t = $0.8t_{\rm ff}$, and the simulation ends with 86 identified cores at t = $t_{\rm ff}$.

As expected, the simulation begins with few identified cores, then mass accumulates and observationally stable starless cores begin to form in what appears to be a bottom-up fashion. As the simulation proceeds, many of these cores become unstable and begin to form protostars (see right hand panel of Figure 2.3).

Figure 2.4 shows the number of cores in different stability states throughout the observed portion of the simulation for cases in which the dust envelope alone is taken into consideration (left panel) and when protostars are added to the flux maps (right panel). Together, the two panels show the evolution of cores defined as sub-Jeans (observationally stable), super-Jeans (observationally unstable to collapse), protostellar (contain a sink particle), and starless (contain no sink particles).

It is important to note that when the protostellar masses are not taken into account, the true masses of the identified objects are underestimated and there is

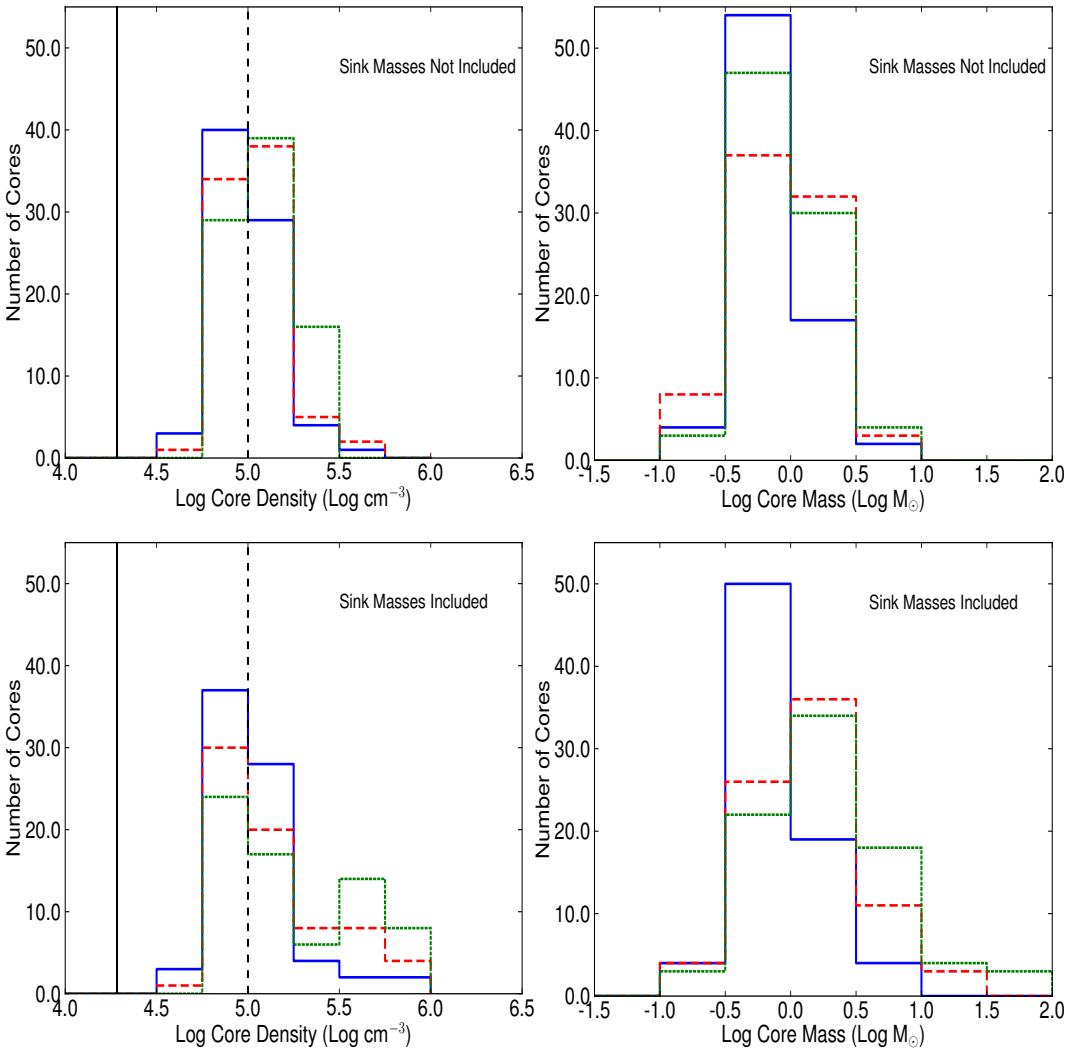

Figure 2.2 The core density (left column) and mass (right column) distributions at three different times: $0.5t_{\rm ff}$ (solid line), $0.8t_{\rm ff}$ (dashed line), and $t_{\rm ff}$ (dotted line) including all three projections. The protostellar masses are not included in the top row (to emulate real observations of cores with hidden protostars); they are included in the bottom row. The solid vertical line in the density plots shows an estimate of the typical density of shocked regions. The dashed vertical line highlights a peak in the density distribution, the "modal density".

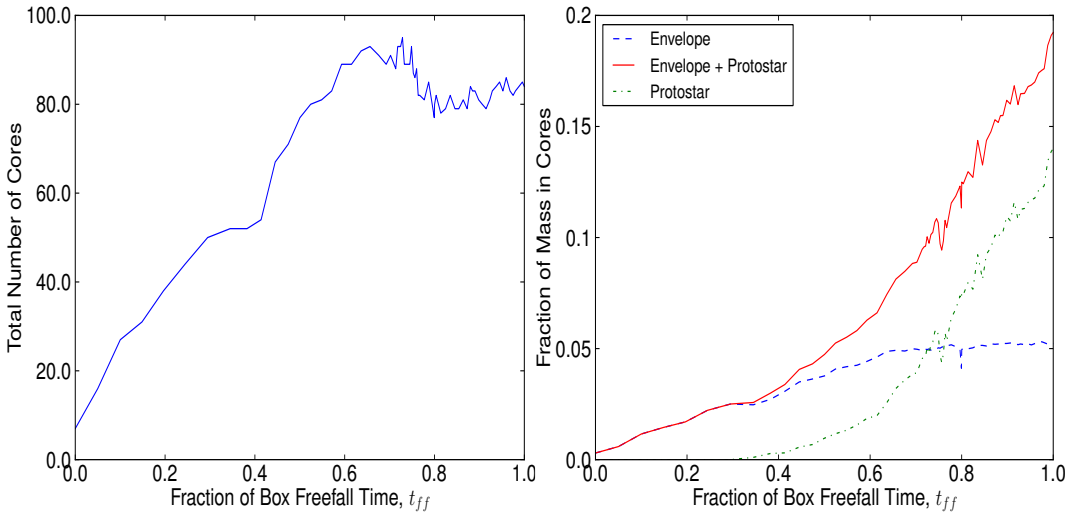

Figure 2.3 *Left:* The total number of cores identified through time during the simulation. *Right:* The fraction of the simulation's total mass contained within identified cores over all three projections. The dashed line represents the dust envelope mass only; the solid line shows the dust envelope mass as well as their contained protostar masses, the dash-dot line shows the protostellar structure mass only. Note that the large majority of the mass contained within cores is locked in protostars where it cannot be directly observed. After one free-fall time, protostellar masses account for 15% of the 600 $M_{\odot}$ box, or, 90 $M_{\odot}$ while core envelopes account for $\sim$5% of the mass of the box, or 30 $M_{\odot}$.

a population of cores that are deemed "stable" even though they are collapsing and forming protostars. This suggests that, when the embedded protostar is unobservable, the Jeans stability argument used by Sadavoy et al. (2010a) may not be sufficient to identify super-Jeans cores.

Although we find super-Jeans cores without any protostars inside, it appears these objects are only marginally unstable. All but one of these cores have masses which are less than a factor of two greater than their respective Jeans masses (see Figure 2.5). As noted by Sadavoy et al. (2010a), starless cores which satisfy $M \geq 4.5 M_{\mathrm{J,c}}$ are those which are deemed "unusual relative to the protostellar cores". We find no such cores throughout this simulation.

When protostellar masses are included, the observed core stability changes significantly. We see that practically all of the previously sub-Jeans cores which had protostars are now classified as super-Jeans as expected.

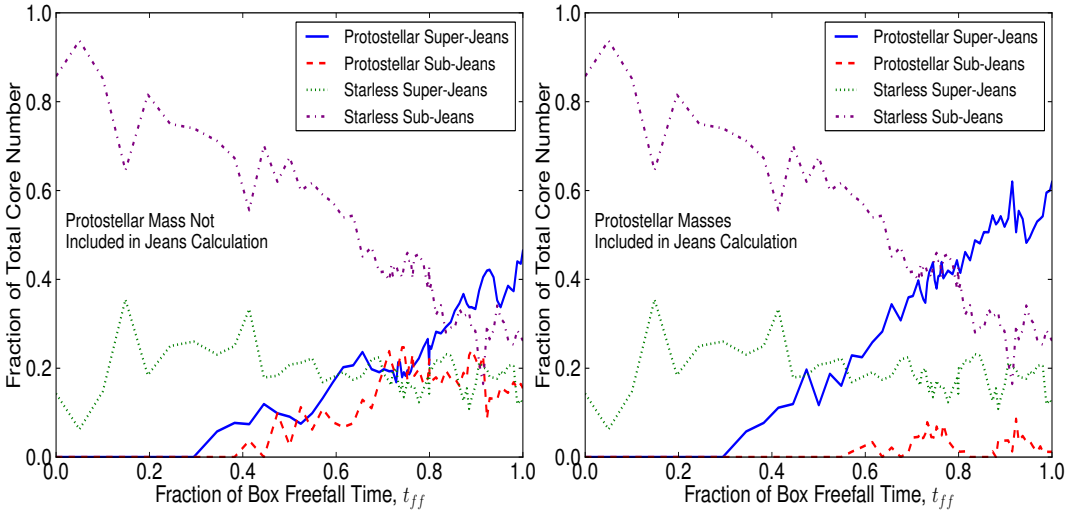

Figure 2.4 Different core stability states. *Left:* Protostellar masses are not included in the analysis, *Right:* Protostellar masses are included. M_p is the protostellar mass.

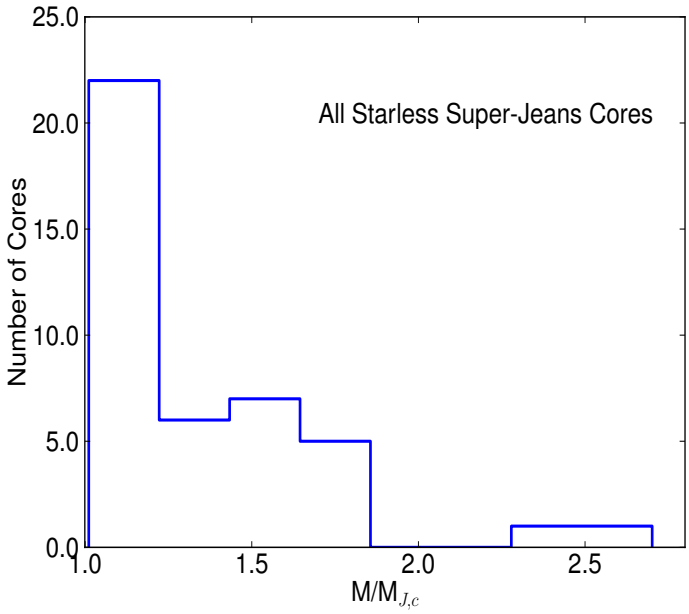

Figure 2.5 The masses of the starless super-Jeans core population (the unstable prestellar cores) over all timesteps and projections in the simulation given in terms of their individual Jeans masses.

2.5.4 Evolution

We selected several cores to study in greater detail. These cores are taken from isolated positions in the flux maps so other objects and protostars will not significantly affect the measurements (three are highlighted in Figure 2.1). We track one of these cores through the entire simulation and choose specific timesteps for the others based on the protostar formation time. Figure 2.6 shows the mass and density of three example cores tracked over a number of times.

In Figure 2.6, the solid horizontal line shows the density associated with the shocked material (see Section 2.7.1). The dashed horizontal line highlights the "modal density" as defined in Section 2.5.2. The diagonal line indicates the minimum density for a core to be considered observationally unstable (Equation 2).

It is evident that there are a few discontinuous jumps (annotated by "D's") in Figure 2.6. These are due to CLFIND2D itself and how it defines multiple objects.

Although a core is initially isolated, it fragments and coalesces with its pieces as it evolves. When an extended object becomes large enough to exceed the flux threshold between two regions, CLFIND2D draws a boundary between the regions and labels each as a separate object. Sometimes, this bifurcation lasts only for a brief period of time and the object reassembles into its previous configuration in the next timestep. Of course, a sudden decrease in radius becomes a sudden increase in density and vice versa. Both in the synthetic observation and in actual observations, there are occasionally multiple objects and filaments that have been "smeared" into one identified core due to the $20''$ smoothing.

Both panels in Figure 2.6 highlight specific regions of interest. In the left panel, which is directly comparable with real observations, stage 1 shows the beginning of the core evolution when a protostar has not yet formed.

There is a short period (stage 2) in which the mass increases but the density remains constant. A brief subdivision and merging takes place before the core splits into two distinct objects, losing mass and becoming far more dense as it enters stage 3. Another CLFIND2D identified bifurcation and amalgamation takes place when the defined flux threshold is briefly achieved before the object settles into its final evolutionary state (stage 4). From this point until the end of the simulation, the mass and the density both increase as in stage 1, but to a much larger degree. When considering the envelope mass alone, the evolution is less monotonic but still exhibits periods of collapse.

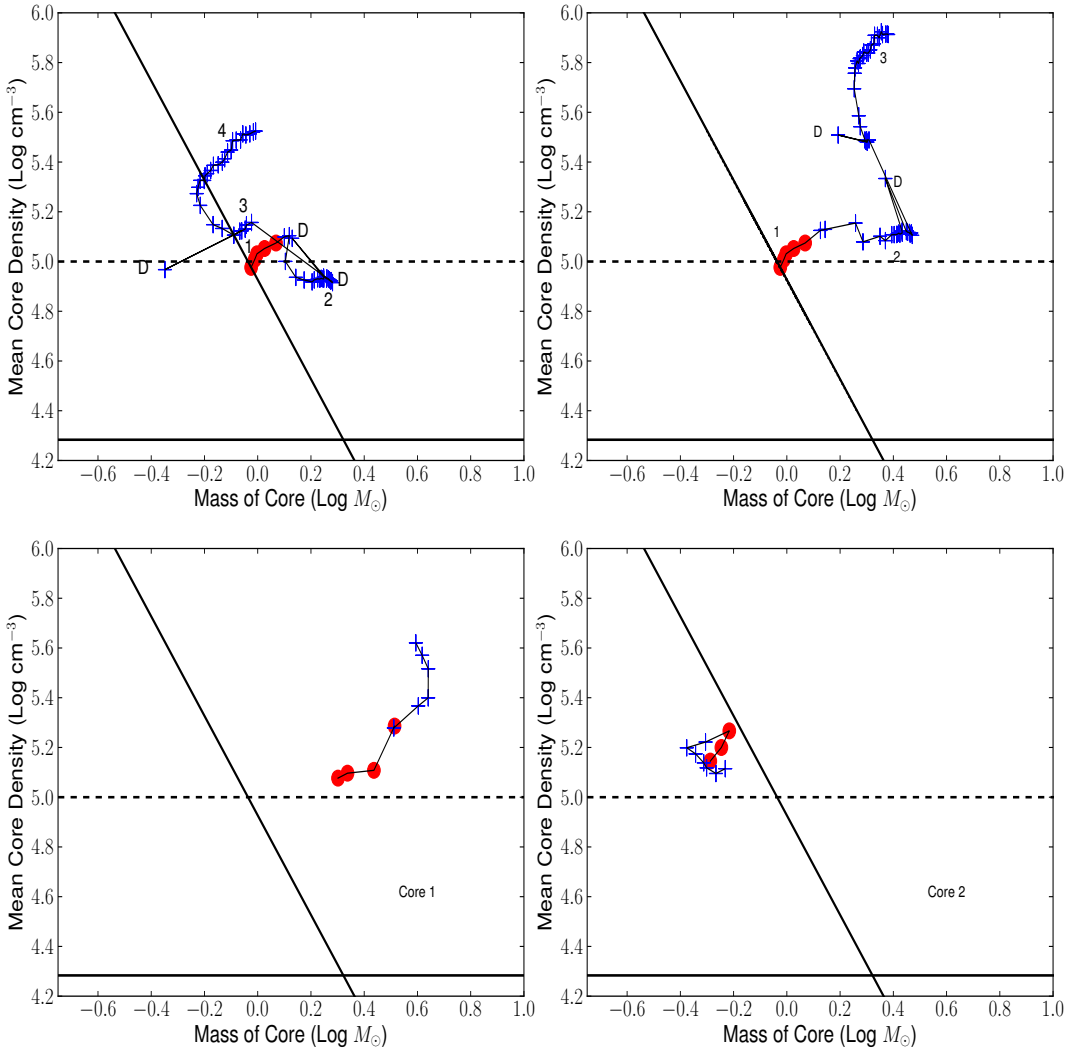

Figure 2.6 Top panels: One core tracked over all the outputs of the simulation. *Left:* Dataset in which protostellar masses are not included. *Right:* Dataset in which protostellar masses are included. Bottom Panels: Densities of two individual cores which form protostars tracked over a subset of the outputs of the simulation. The left panel shows the object labeled "Core 1" in Figure 2.1 and the right panel shows "Core 2". Protostellar masses have not been taken into account for either of these latter cores. Circles indicate when the core does not contain a protostar within its boundaries. Plus signs indicate at least one protostar exists within the core boundaries. Points lying above the solid diagonal line are defined to be observationally unstable using Equations 4.1 and 2.2; points lying below are classified as observationally stable. The solid horizontal line shows the fiducial shock density (see Section 2.7.1). The dashed horizontal line shows the empirically derived "modal density". "D" represents a discontinuous feature introduced by CLFIND2D.

The right panel of Figure 5 shows density versus mass including the protostellar mass. There are two obvious regions marked with "D's" in which CLFIND2D subdivided, then merged this object. Beginning in stage 1, there is a very steady mass and density increase as this object forms a protostar and becomes observationally Jeans unstable shortly thereafter. After the early collapse, the density begins to level off for a short period of time. Meanwhile, the mass continues to increase, indicating that the radius must also be increasing before a large upward jump in density. Here again, the core bifurcates causing an abrupt density spike. During this period, the mass is essentially constant for the rest of the simulation, which suggests the core is simultaneously decreasing in size.

The bottom left panel of Figure 2.6 shows the evolution of a core which is recognisably Jeans unstable before a protostar forms. The right panel shows an isolated core that we select at random in the simulation to highlight the diversity in the core population. When only the envelope masses are taken into account, each core resembles the left panel of Figure 2.6. When protostellar masses are included as shown there is a rapid evolution in the core properties. Both the mass and the density increase substantially over time, such that the cores appear observationally unstable.

2.5.5 Protostar and Envelope Relationship

In this section, we explore the relationship between the mass of a protostar and its parent core. Figure 2.7 shows the fraction of core mass in sink particles. The points which lie at exactly 1.0 on the ordinate axis are protostars which did not have an associated envelope. These protostars lie outside 75% of their nearest core's radius (measured from the core centre). Thus, with no apparent envelope, the sink mass is one hundred percent of the object's mass. Note that because of the background subtraction, some of the core mass may be lost in this analysis.

As expected, many young objects have not formed protostars and lie along the bottom of the plot. As time progresses, the sink particles begin to dominate the core masses quickly. The bottom right quadrant of Figure 2.7 is empty. This means that the more massive cores observed in the simulation are dominated by the protostars present. Stepping through time, it is clear that this is a rapid process. Once sink particles form, they quickly accrete a large amount of mass. Therefore, observations ignoring the embedded protostars could miss a significant portion of mass. This will lead to errors in stability classification using non-interferometric observational

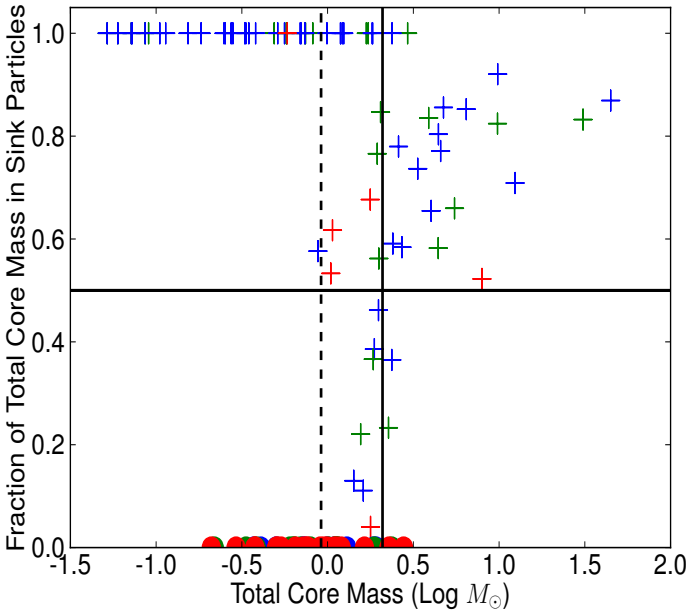

Figure 2.7 The fraction of a total core's mass (protostar and envelope) found in the protostars contained within the object's boundaries plotted against total core mass for all objects in all three projections observed at three timesteps. The Y dimension integrated images only are shown here for clarity. Red represents 50% of the box free-fall time, green represents 80% of the box free-fall time, and blue represents one free-fall time. The solid vertical line is drawn at the Jeans mass corresponding to the shocked density (see section 2.7.1). The dashed vertical line highlights the Jeans mass associated with the empirically derived "modal density". The solid horizontal line simply shows the 50% mark (i.e. where the collapsing regions dominate the core mass).

Table 2.1 ALMA Cycle 1 observations performed on three cores.

ID	Radius (AU)	Env. Mass ($M_\odot$)	Sink Mass ($M_\odot$)	$\frac{\text{Env. Mass}}{M_\text{J}}$	Density (cm^{-3})
1	829.30	0.27	0.619	2.44	1.70 x 10^7
2	579.48	0.09	0.090	1.17	1.66 x 10^7
3	645.38	0.13	0.078	1.57	1.81 x 10^7

techniques.

When each of the timesteps are analysed in a sequential fashion, the points travel from the bottom left through an "S" shape to the top right of the plot. Since the total mass of a given object substantially increases throughout the formation and growth of a protostar, it is clear that the protostar mass cannot come from the initial material detected in the envelope alone. One possibility is that cores extend below our flux limit and are collapsing to higher densities such that they enter the observable regime. Another likely possibility is the accretion of mass due to bulk flows in the simulation in conjunction with gravity. The obvious filamentary structures in the map are the most likely sources of mass. In fact, mass flow along filaments associated with protostars have been observed in many star forming regions (e.g. Kirk et al. 2013b; Friesen et al. 2013; Hacar & Tafalla 2011; Schneider et al. 2010).

Since the final mass of the protostars is sometimes larger than the initial observed core mass, this suggests either observed cores are initially more massive than observed or that they continue to accrete. In either case, this undermines the comparison of a single time snapshot of the core mass distribution with the IMF.

2.6 Interferometric Analysis

In this section, we assess the conditions for which the detection of an embedded protostar is possible. Employing the high resolution and sensitivity offered by interferometers is the logical next step in characterising the dynamic nature of cores.

As described in section 2.4.3, we performed synthetic ALMA Cycle 1, SMA, and CARMA simulated interferometric observations. It was found, however, that a ninety second observation performed at 100 GHz with ALMA Cycle 1 is comparable to an eight hour observation taken by SMA at 230 GHz and achieves a far better signal to noise ratio than an eight hour observation taken with CARMA at 100 GHz. Offner et al. (2012) found a similar result. The SMA and CARMA observations produced

only non detections; evidently, to identify any substructure present in faint cores or to even detect the objects with 3σ confidence, a greater sensitivity is required. This null result is compatible with recent interferometric observations (see Schnee et al. 2012b).

Thus, we focus primarily on ALMA. We analyse each interferometric image down to the same flux threshold (6σ = 0.6 mJy/beam, defined by-eye) for a consistent analysis. Purely investigating the results of CLFIND2D, we see that in most cases there is no significant buildup of mass before a protostar forms. In two of the cases the core is identified very briefly after the formation of the protostar. In one case, the core is identified concurrently with the formation of a sink particle and continues to grow in time. In the last case, CLFIND2D does not identify a core at any time output.

Figure 2.8 shows the observations of the object in the bottom left panel of Figure 2.6 (labeled "Core 1" in Figure 2.1) at three different timesteps; two approaching the formation of the first protostar and one at the time the first protostar appears. The core begins in an undetected state. By the time a protostar forms, a clear detection is possible.

Table 2.1 shows the properties of the three identified objects at the point of their first detection. In all three cases, the objects already contained sink particles. Cores 1 and 2 are the same as in Figure 2.6 (left and right panels, respectively); note the increase in density in the centre of the core compared to the core average (compare with Section 2.5.4).

CASA simulations such as these provide a strong prediction for real interferometric observations. Currently, ALMA Cycle 1 telescope time has been awarded with highest priority to observe the 3mm continuum emission from all 60 starless cores and 13 protostellar cores in the Chamaeleon I molecular cloud, as identified in Belloche et al. (2011). These observations will be sensitive to point sources with masses $\gtrsim 0.01\ M_{\odot}$, with less than 2 minutes of on-source integration time per object (see Table 2.1). Once these data are collected, we will be able to perform robust comparisons between simulated core properties and their observed counterparts.

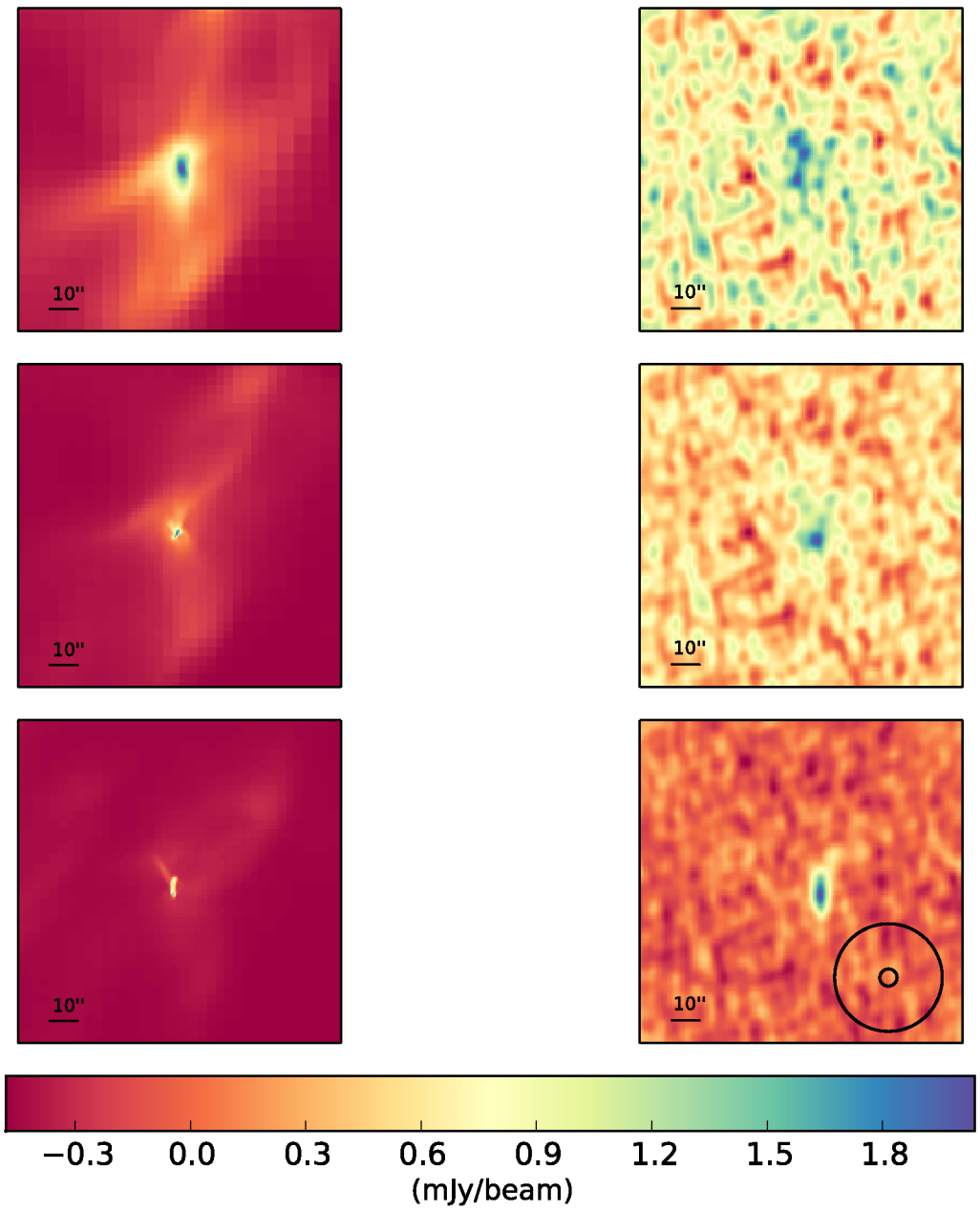

Figure 2.8 ALMA Cycle 1 simulated observations of Core 1. The left column shows three original, simulated, images at different timesteps. The right column shows the interferometric observations of these same three timesteps. The top and middle rows show times $0.20t_{\rm ff}$ and $0.24t_{\rm ff}$. The third time shows the object at 0.29 $t_{\rm ff}$, just after a protostar has formed. The large circle on the bottom right hand panel represents the effective $20''$ smoothed beam in the single dish analysis. The smaller circle shows the $3.2''$ 100 GHz synthesised ALMA beam.

2.7 Discussion

2.7.1 Shocked Densities and Structure

In this section we consider some simple estimates of the role of turbulence and gravity to place our results in context.

The characteristic size scale at which gravity dominates over thermal pressure is given by:

$$L_{\rm J} = \sqrt{\frac{\pi c_{\rm s}^2}{G\rho_0}}. \tag{2.3}$$

where $c_s = (k_{\rm B}T/\mu m_{\rm H})^{\frac{1}{2}}$ is the sound speed, $\mu = 2.33$ is the mean molecular weight, $k_{\rm B} = 1.38$ x 10^{-16} ergK^{-1}, G is the gravitational constant, $m_{\rm H}$ is the mass of hydrogen, T is the isothermal gas temperature, and ρ_0 is the average mass density in the simulation.

In a typical shocked region in the simulation, the density and hence the Jeans length will be higher. The shocked density of a 1D isothermal shock is given by $\rho_{\rm s} = \mathcal{M}_{\rm 1D}^2\rho_0$, where $\mathcal{M}_{\rm 1D} = \mathcal{M}_{\rm 3D}/\sqrt{3} = 3.8$ is the 1D simulation Mach number. Plugging this into Equation 3, we can expresses the compressed Jeans length as:

$$L_{\rm Jm} = \sqrt{\frac{\pi c_{\rm s}^2}{G\mathcal{M}_{\rm 1D}^2\rho_0}} \tag{2.4}$$

or,

$$L_{\rm Jm} = \mathcal{M}_{\rm 1D}^{-1}L_{\rm J}. \tag{2.5}$$

Values of $T = 10$ K and $\rho_0 = 5.1$ x 10^{-21} g cm^{-3} give a compressed Jeans length of $L_{\rm Jm} = 4.7$ x 10^{17} cm or $126.42''$, assuming a distance of 250 pc. For the 2 pc box, the low resolution (512 x 512) grid used in this analysis had 3.2 x 3.2 arcsecond pixels. So, a typical shock forces material together on scales of $\sim$40 pixels in the low resolution grid.

The Jeans mass, $M_{\rm J}$, associated with the Jeans length is given by Equation 2.2 replacing $R_{\rm c}$ with the Jeans radius, $R_{\rm J} = L_{\rm J}/2$. Thus, the Jeans mass corresponding to the average density in the simulation is $M_{\rm J,0} = 7.92\,M_\odot$ and the Jeans mass corresponding to shocked densities is $M_{\rm J,m} = 2.08\,M_\odot$. The average CLFIND2D core mass is much closer to the shocked Jeans mass than the Jeans mass corresponding to

the average density of the box.

This is, of course, a very simple estimate. The actual processes at play are more complicated and can involve a number of oblique shocks and shears. Note that the "modal density" is approximately a factor of 5 greater than the shocked density calculated here; this corresponds to a higher characteristic velocity than that associated with $\mathcal{M}_{1D}$.

To gain a better understanding of the true densities attained in the centre of an individual object, we analysed one of the cores tracked in Sections 4.3 and 4.4 in more depth at a higher resolution (level 2 in the AMR simulation). The core we selected was the first object to achieve a super-Jeans state in the Y-dimension flux maps.

Figure 2.9 shows number density maps for Core 1 at four different timesteps centred on the formation of the first sink. The outer contours show the expected number density achieved using the $\mathcal{M}_{1D}^2$ coefficient ($n_H = 1.9 \times 10^4$ cm^{-3}). The inner contours show the "modal density" ($n_H = 1.0 \times 10^5$ cm^{-3}); approximately a factor of 5 larger. Clearly, both these values are significant in tracing the structure present in the map.

Evidently, much higher densities are achieved than those expected by the simple argument presented above. Throughout the observed frames, both before and after the protostar has formed within the core, gravity quickly creates regions of high density on scales much smaller than the beam. Thus, important structure will remain unobserved without deep interferometric maps.

Analysing the simulation itself, a typical number density value within Figure 2.9's inner contour was found to be $n_H = 5 \times 10^5$ cm^{-3} by averaging over the projection. The highest inferred average density of a region exceeds $n_H = 10^6$ cm^{-3} (see Table 2.1). This typical density corresponds to a dynamical collapse time of approximately 5% of the total box free-fall time. Near the beginning of the simulation, this is close to the time resolution in which observations were performed. Therefore, for densities significantly greater than 5 x 10^5 cm^{-3}, the collapse will not be resolved temporally with the chosen, observed simulation snapshots in the earlier stages of core evolution.

2.7.2 Single Dish Results

The CLFIND2D objects span a range of masses and morphologies. The objects are initially detected when they are starless; quickly, a subset undergoes mass accretion, gravitational collapse, and protostar formation. In fact, the majority of the cores

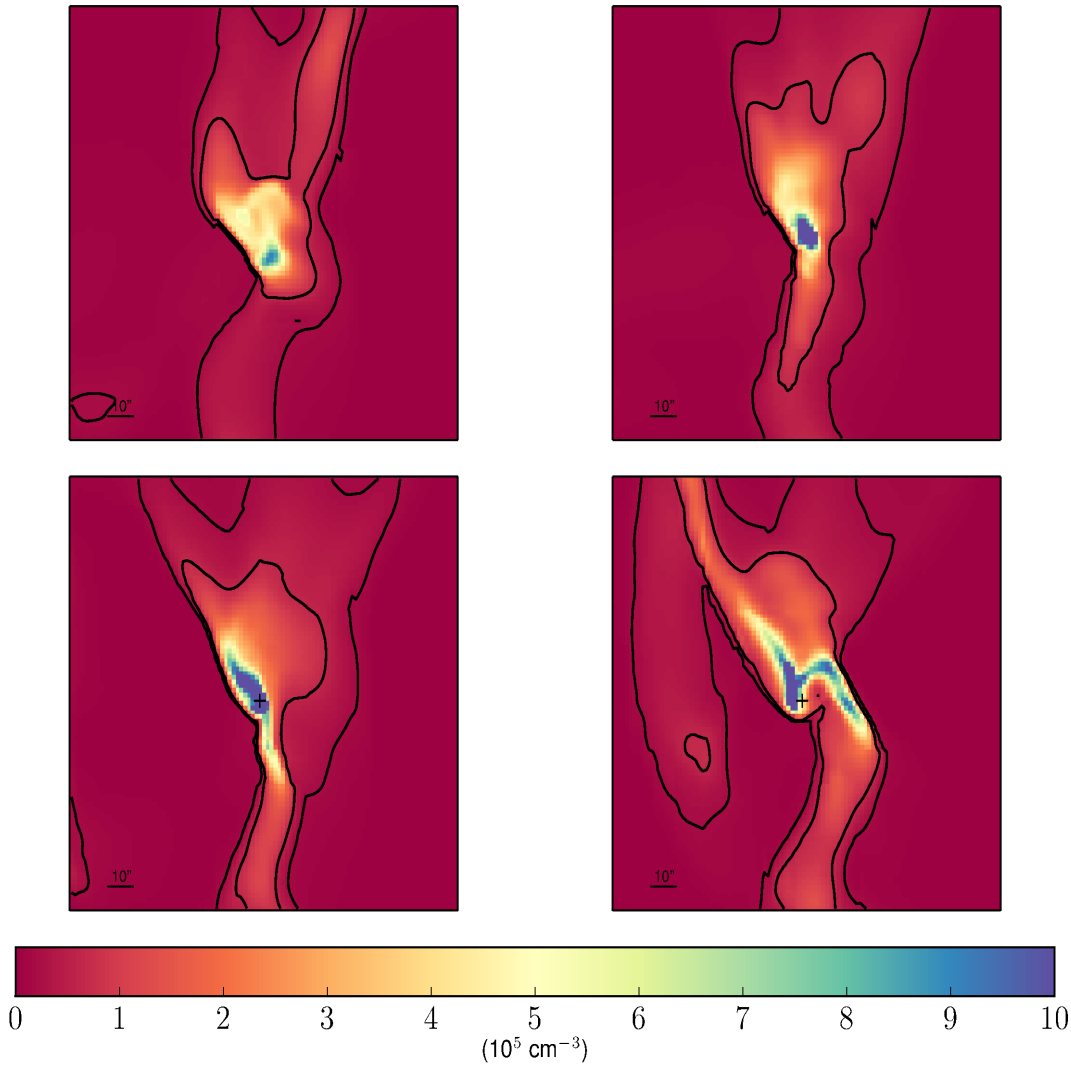

Figure 2.9 Density map for one individual core observed at a resolution of 1.6″/pixel. The top row shows the core before it forms a protostar (Left to right: $0.15t_{\rm ff}$ and $0.24t_{\rm ff}$); the bottom row shows two timesteps shortly after a protostar forms (Left to right: $0.34t_{\rm ff}$ and $0.41t_{\rm ff}$). The plus signs indicate the locations of the protostar. The outer contour indicates a density of $1.9\,{\rm x}\,10^4$ cm^{-3}; the inner: $1.0\,{\rm x}\,10^5$ cm^{-3} (see text).

detected go on to form protostars. This indicates that the objects observed are not transient, but "real" star formation sites. In the earliest timesteps, before gravity has had a chance to significantly affect localised regions, there are very few cores identified. As time progresses, the number of observationally defined super-Jeans cores as well as the number of protostars increases.

It is interesting to note that the majority of the mass in cores accretes onto the protostars and the protostar mass rapidly dominates the mass budget. In fact, in this simulation the most massive envelope including at least one protostar was approximately 10 $M_{\odot}$. The cumulative mass of the protostars present within the largest core, however, totalled more than 60 $M_{\odot}$. Recall, however, that without removing the 120″ scale structure from the flux maps, we find these cores reside within much larger mass envelopes (Section 2.4.2). These extended regions predominately trace the filamentary structure in the simulation and act as reservoirs for the smaller scale cores.

When the mass of the protostars is not included (to resemble observations of cores wherein the dense central object is unobservable) there exists a small population of cores forming stars which are deemed stable from an observational perspective. When the protostellar mass is added, however, these cores are found to be unstable to collapse as expected.

Observationally detecting collapse proves to be quite difficult. For example, if the protostar is deeply embedded and undetectable, its mass cannot be accounted for in the gravitational analysis. The problem of detecting embedded protostars is generally expected to be more severe when the protostars are small and dim. Consequently, the results presented here are most applicable to the transition between the starless and protostellar stage. In many cases, the core, the protostar, or both may be too faint to detect in the first place; and detection is especially difficult at early times (Schnee et al., 2012b; Pineda et al., 2011; Dunham et al., 2008; Bourke et al., 2006; Young et al., 2004).

Smith et al. (2012) show that the problem of detecting protostars extends to observations of molecular lines. They performed radiative transfer calculations for cores embedded in filaments in a turbulent hydrodynamic simulation. They find that in over 50% of viewing angles, there is no "blue asymmetry": a classic sign of material infall in an isolated spherical core. In a continuation of this work, Smith et al. (2013) highlight the need for high resolution observations with ALMA in order to test how line profiles and results change with beam size.

Note that a few significantly super-Jeans starless objects (core mass $> 4.5M_{J,c}$) were identified by Sadavoy et al. (2010a), little evidence of objects fitting this classification is found in this simulation.

Of course, the detection and analysis of cores relies on many assumptions. We adopted typical values for the dust properties (Johnstone et al., 2000c; Kirk et al., 2006a; Schnee et al., 2012a; Sadavoy et al., 2010a). We neglected internal heating due to protostars. In actual observations, the warmed dust grains cause an increase in flux which can easily be misconstrued as a core with a larger mass.

One can clearly see a low mass core population which is maintained throughout the simulation in Figure 2.2. It appears that once a core is identified, it continues to collapse and gain mass. Most of this mass is accreted onto embedded protostars. A sufficient amount of the mass flow, however, replenishes the dust envelope, leaving it detectable.

This distribution of mass within an evolving protostellar core can be best illustrated by Figures 2.2 and 2.7. The top right hand panel of Figure 2.2, which takes into account only what is observable in the submillimetre regime, shows the total remains approximately constant over time. If the mass of protostar is included, the total mass within the core increases over time. Even when the embedded protostars become quite massive, the core masses remain comparatively low. When only considering the material in the envelope, the density increases only slightly over time. In general, when the protostellar masses are added, the peak of the mass and density distributions stay approximately constant while more higher mass objects are observed. This is also shown in Figure 2.7 where the protostars dominate the mass by a significant factor.

These distributions were also analysed assuming each protostar was a factor of 3 less massive in order to compensate for the overestimate inherent in the simulation (see Section 2.3). We found a less accentuated but still significant increase in higher mass objects as expected. A modified version of Figure 2.7 did not undergo any substantial changes. The protostar masses still greatly dominate the envelope masses.

2.7.3 Interferometric Results

To truly determine the nature of a given core, one needs to look more closely at the internal structure. The large JCMT beamsize "washes out" the more compact

structure, causing the object to appear less dense. In order to investigate the details of protostar formation at the scales, sensitivity, image fidelity, and resolution necessary, an interferometer such as ALMA is required.

The bottom right panel of Figure 2.8 shows the difference between the JCMT and the ALMA beams for a simulated ALMA Cycle 1 observation (100 GHz). It is clear that the JCMT beam blends much smaller structures that *can* be detected with an interferometer.

Comparing the Table 2.1 values with the same cores as in the single dish data, we highlight several interesting points. Beginning with Core 1, the mass inferred using interferometry is an order of magnitude less than found by the JCMT. This is to be expected as the envelope observed by ALMA is much smaller than that observed by the JCMT. The reduction in mass indicates that there is structure present that is on larger angular scales that cannot be recovered by ALMA's 12m array in its most compact configuration at 100 GHz. The object was detected concurrently with the snapshot in which the protostar formed.

Core 2 appears more unstable when synthetically observed by ALMA. Removing the noise from the observations and redefining the clump boundaries at a lower flux threshold which is discernible by-eye, the object is found to be up to 1.5 times more massive. This indicates that the signal to noise ratio significantly influences the core classification and stability calculation. The object was detected shortly after the sink particle first appeared. The third isolated core in which a detection was made with ALMA is similar to the second. The core mass to Jeans mass ratio indicates more instability in the case of ALMA. Probing the central densities of these cores is important for understanding the single dish data.

Our interferometric analysis of core stability also assumes isothermal dust and spherical cores. It is clear, however, that the morphologies of these objects could indicate collapse along preferred axes (see Pon et al. 2011 for a thorough description of collapse modes). This type of analysis is vital to perform at small scales near the centre of identified objects in order to truly observe how stars are forming.

2.8 Conclusion

In this study, we performed synthetic single dish and interferometric observations of a simulated star forming region. Assuming the gas and dust were optically thin, we inferred masses and densities by assuming the objects were spheres. We calculated

the gravitational stability using the density of each core and correlated protostars with the objects. The single dish analysis was performed with and without including protostellar masses; the former was to emulate real observations while the latter was to compute the core's "true" stability. We investigated the relationship between the protostar and its parent envelope in terms of their mass and we considered the significance of the core densities with respect to turbulence and gravity.

There are several key results:

A. Our analysis is consistent with various observations. Namely, the masses and densities of the simulated cores we detect are very similar to "real" cores in Perseus (see Section 2.5.2). We find many more sub-Jeans cores than super-Jeans, in terms of their mass and size, which is consistent with Sadavoy et al. (2010a). The fact that we do not detect substructure with simulated CARMA observations is consistent with Schnee et al. (2012b).

B. Nearly all cores that we detect eventually form protostars. This suggests that observed cores detected in this manner (assuming the physical conditions and distance of Perseus) are probably "real"; that is, they will likely go on to form protostars in the future (see Section 2.7.2). The mass of the observed envelope, however, does not appear to be a good tracer of the eventual protostellar mass. This has implications for comparing the core mass function with the stellar initial mass function (see section 2.5.5). Note, however, that the simulation does not include magnetic fields, which could provide additional support that may inhibit a core from collapsing.

C. Nearly all cores we identify are associated with filaments. This is consistent with the ubiquity of filaments recently observed by Herschel and suggests that if observations had better resolution and sensitivity they would also see a similar correspondence between cores and filaments (see Section 2.5.1).

D. Single dish observations such as those with the JCMT as well as previous-generation interferometers appear to miss significant core structure on small scales due to flux averaging. Interferometric observations with ALMA are necessary to recover this information (see Sections 2.6 and 2.7.3).

Chapter 3

Investigating Data Reduction Methods for Robust Submillimetre Observations

"If you can hold the stars in place,
You can hold my heart the same..."
-Skillet, Stars

3.1 Foreword

In the previous chapter, I addressed the evolution of starless and prestellar cores and the connection between large-scale mass reservoirs and smaller scale structures by synthetically observing numerical simulations. To further my understanding of ground-based submillimetre observations and the prominent challenges involved with interpreting this data, I joined the JCMT Gould Belt Survey (GBS; Ward-Thompson et al. 2007c). This allowed me to continue investigating star formation from a more purely observational perspective as part of a large team dedicated to mapping several nearby star-forming regions in a consistent manner. The GBS focuses on 450 and 850 μm continuum data taken using SCUBA-2 and spectroscopic data of three CO isotopologues (^{12}CO, ^{13}CO, and C^{18}O, J = 3-2 transitions) observed using the

The material presented in this chapter (excluding the foreword) has been published in Monthly Notices of the Royal Astronomical Society: Mairs et al. 454, 2557, 2015. DOI: 10.1093/mnras/stv2192.

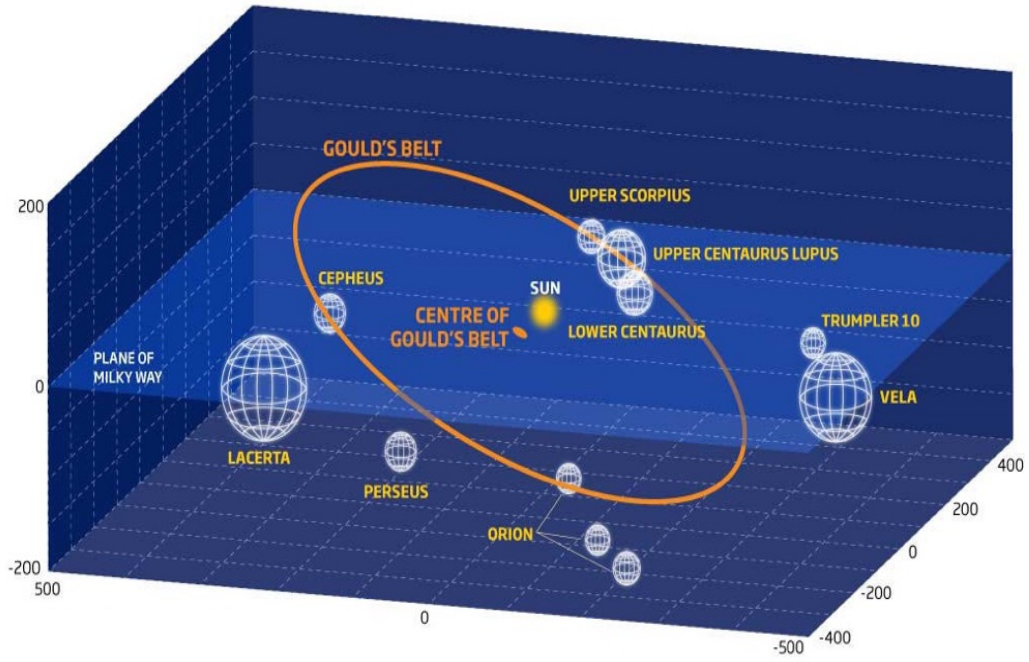

Figure 3.1 The Gould Belt. This Figure, produced by Dr. Isabelle Grenier at the University of Paris, shows the orientation of the Gould Belt with respect to the Sun along with the locations of many star-forming molecular clouds.

Heterodyne Array Receiver (HARP; Buckle et al. 2009) instrument.

All of the GBS targets reside within the **Gould Belt**, a ring of bright, young stars 700 pc in diameter. Its centre is approximately 200 pc from the Sun and the ring is inclined to the Galactic plane by approximately 20° (Herschel 1847, Gould 1879; see Figure 3.1). This belt is home to many well known star-forming molecular clouds within 500 pc of the Sun such as Orion, Perseus, Serpens, Lupus, Ophiuchus, Taurus, and Serpens. Its proximity to the Sun and wealth of objects undergoing each stage of star formation makes it a prime choice to observe. The target molecular clouds were selected from extinction maps (Dobashi et al., 2005) in order to avoid blank areas of the sky and increase observing efficiency. SCUBA-2's ability to map regions spanning several degrees relatively quickly allows for a statistically significant sample of objects to be catalogued and analysed. This has been a prominent goal of the GBS since investigating the earliest stages of star formation at submillimetre wavelengths is a burgeoning field that has suffered from a lack of thorough, consistent observations over multiple clouds. In total, 412 hours were spent continuum mapping ∼100 square degrees to a depth of 4 mJy/beam at 850 μm. In the era of SCUBA-2's predecessor,

SCUBA, instrument limitations only allowed for a mapping of 50 square degrees of the sky to a depth of 70 mJy/beam (The SCUBA Legacy Catalogues; Di Francesco et al., 2008b).

As I described in Section 1.4, SCUBA-2 is not a straight-forward camera and the data reduction efforts necessary to recover robust astronomical signal are rather involved. At the time I joined the GBS team, there was an initial version of the data released to team members and efforts underway to understand the limitations of the reduction methods in place while momentum was building for a second, more robust, internal data release. By attending the data reduction team discussions and offering my own insights, I became fascinated by the instrumentation and the best practices for atmospheric signal removal. To this end, I volunteered to lead the official investigation into the differences between the GBS data reduction pipeline which was tailored to the specific science goals of the consortium and the more basic, default data reduction procedures employed automatically at the JCMT. In doing so, I would end up deriving further improvements to the GBS procedures while quantifying the limitations of the astronomical signal recovery with SCUBA-2 for the first time in a practical way using case studies.

Thus, every further project performed by GBS members using the second internal data release (later renamed the *GBS Legacy Release 1*) utilises the work presented in the following paper (Mairs et al., 2015) in order to understand their own data reduction limitations and, therefore, to determine which claims they can make with certainty. My work on the data reduction team, and especially the project presented in this chapter resulted in a series of papers on which I was able to contribute as a co-author, offering my insights and practical data reduction skills for the benefit of several different region and science analyses (see Rumble et al. 2015; Salji et al. 2015a,b; Buckle et al. 2015; Pattle et al. 2015; Kirk et al. 2016a; Chen et al. 2016; Lane et al. 2016; Rumble et al. 2016; Mowat et al. 2017; Johnstone et al. 2017).

Further, I was able to build on these data reduction skills by designing procedures to reduce and analyse data for other JCMT projects. For example, I modified my methods to effectively reduce observations taken using different JCMT scan methods as part of the effort to characterise an explosive transient event for the All-Sky Automated Survey for Supernovae (ASAS-SN; Herczeg et al. 2016) and I performed the initial data reduction tests for the JCMT SCUBA-2 Continuum Observations of Pre-protostellar Evolution (SCOPE) survey (Liu et al. in preparation).

Abstract

Performing ground-based submillimetre observations is a difficult task as the measurements are subject to absorption and emission from water vapour in the Earth's atmosphere and time variation in weather and instrument stability. Removing these features and other artifacts from the data is a vital process which affects the characteristics of the recovered astronomical structure we seek to study. In this paper, we explore two data reduction methods for data taken with the Submillimetre Common-User Bolometer Array-2 (SCUBA-2) at the James Clerk Maxwell Telescope (JCMT). The JCMT Legacy Reduction 1 (JCMT LR1) and The Gould Belt Legacy Survey Legacy Release 1 (GBS LR1) reduction both use the same software (*Starlink*) but differ in their choice of data reduction parameters. We find that the JCMT LR1 reduction is suitable for determining whether or not compact emission is present in a given region and the GBS LR1 reduction is tuned in a robust way to uncover more extended emission, which better serves more in-depth physical analyses of star-forming regions. Using the GBS LR1 method, we find that compact sources are recovered well, even at a peak brightness of only 3 times the noise, whereas the reconstruction of larger objects requires much care when drawing boundaries around the expected astronomical signal in the data reduction process. Incorrect boundaries can lead to false structure identification or it can cause structure to be missed. In the JCMT LR1 reduction, the extent of the true structure of objects larger than a point source is never fully recovered.

3.2 Introduction

In an effort to probe the cold dust in several well-known nearby star-forming regions with the James Clerk Maxwell Telescope (JCMT), the Gould Belt Survey (GBS, Ward-Thompson et al. 2007c) has been performing submillimetre continuum observations using the Submillimetre Common-User Bolometer Array 2 (SCUBA-2). The SCUBA-2 instrument (Holland et al., 2013) is a wide field submillimetre bolometer camera with an unprecedented 10,000 pixels. The device maps regions at 450 μm and 850 μm simultaneously with effective resolutions of 9.6″ and 14.1″ (Dempsey et al., 2013), respectively. Mapping the sky over 100 times faster than its predecessor, SCUBA (Holland et al., 1999), this next generation detector has offered star formation researchers the chance to analyse nascent stellar systems at submillimetre wavelengths with a higher efficiency and a broader context than ever before with a

single dish, ground-based telescope (see, for example, Sadavoy et al. 2013, Salji et al. 2015a, and Pattle et al. 2015).

Reducing SCUBA-2 data is a complex process with a variety of solutions, each designed to best uncover particular features (e.g. bright, compact emission versus faint, diffuse emission). This variety is, in part, due to the nature of the observations. While performing observations using the PONG scanning mode (the method employed in this study; see Kackley et al. 2010 and Holland et al. 2013), the JCMT continuously scans back and forth across the sky at differing angles to fill in a circular pattern. By visiting the same locations from different angles and at different times, sources of low frequency drift are manifested as a length-scale feature which can be separated from the sources of interest so that spatially invariant structures can be identified. These sources of drift include instrument-based noise (see Holland et al. 2013) but are dominated by atmospheric noise, which varies temporally. In this way, many individual bolometers will observe each sky location. Constructing a final image requires identifying significant structure and removing those large-scale features created by the noise. Quantifying how the observing process affects the observed signal is therefore of utmost importance as it characterises how confident we can be that we are detecting true astronomical emission and not artificial constructs at each scale of interest.

Determining the optimal image reconstruction of submillimetre bolometer data has been an area of acute interest for researchers using JCMT data since before the operation of the original SCUBA instrument. For example, Richer (1992) presented the "maximum entropy" reconstruction method, which is based on the assumption that the most likely reconstruction is the one which has maximum entropy (see Narayan & Nityananda 1986, for a review). Wilson et al. (1999) and Pierce-Price (2002) went on to develop maximum entropy reconstruction methods for data taken by SCUBA. Several other methods were also employed. For instance, Borys (2002) wrote a SCUBA map-making algorithm based on a least squares approach while Johnstone et al. (2000a) developed a "matrix inversion" reconstruction which accounted for the varying uncertainty in a given map's background noise. The latter was based on a technique for the Wilkinson Microwave Anisotropy Probe (WMAP) described by Wright et al. (1996). At approximately the same time, Jenness et al. (2000) implemented a Fourier deconvolution method developed by Emerson (1995) (Emerson 2) as the reduction method for the standard SCUBA data analysis software at the JCMT.

The issue of effective and accurate submillimetre data reduction is not unique to the JCMT. For example, the Bolocam Galactic Plane Survey (BGPS; see Aguirre et al. 2011 for the 1.1mm survey and Merello et al. 2015 for the 350 μm images) uses an algorithm called *CRUSH* (The Comprehensive Reduction Utility for SHARC-II; Kovács 2006) to reduce the 350 μm continuum images taken using the Submillimetre High Angular Resolution Camera II (SHARC-II; Dowell et al. 2003) at the Caltech Submillimetre Observatory (CSO). Like SCUBA-2, SHARC-II is a ground-based bolometer array which must contend with instrumental imperfections, atmospheric interference, and electronic noise. The CRUSH algorithm is an iterative process which determines a series of gain and weight estimations for each array component one-by-one while filtering noise spikes and other bad data (such as cosmic rays and electronic discharges; see Kovács 2006 for more information). Other examples include *SANEPIC*, the maximum-likelihood map-making algorithm used for the Balloon-borne Large Aperture Submillimeter Telescope (BLAST; Patanchon et al. 2008) experiment which uses a series of approximations to reduce the required computational power necessary for image production, and the AzTEC (Aztronomical Thermal Emission Camera, located at the Large Millimetre Telescope) Data Reduction Pipeline, which uses Principal Component Analysis (PCA) to model and remove correlated components of the bolometer signals. The latter method, however, is only ideal for the recovery of compact structures as extended emission will have correlated components that will be flagged as noise (Scott et al., 2008).

In this paper, we explore the data reduction method used by the JCMT GBS team for their first Legacy Release (GBS LR1; Kirk et al., in prep.) of SCUBA-2 data by first comparing and contrasting with another method employed by the JCMT science and computing group (JCMT LR1, Graves et al., in prep.) then analysing how well each method preserves structures with known properties. We focus here only on the 850 μm maps. The same arguments can be extended to 450 μm maps but there is less high signal-to-noise data available for comparison and the absolute calibration uncertainties are higher.

To construct an image from the raw SCUBA-2 data, the GBS LR1 and the JCMT LR1 reduction teams both use the *makemap* algorithm found in Starlink's[1] *smurf* package (Chapin et al. 2013; also see the SCUBA-2 data reduction cookbook Thomas & Currie 2014). The *makemap* algorithm employs an iterative technique which applies flat field corrections, performs an extinction correction, models and removes

[1] `http://www.starlink.ac.uk`

noise correlated between detectors, estimates and masks the astronomical signal, and measures the noise of each bolometer contributing to each pixel in the reduced image. In total, for all the different observational strategies available, *makemap* has over one hundred configurable parameters which are supplied in a text file called the "Dynamic Iterative Map Maker configuration file", or, "*dimmconfig* file". With these parameters, the user has significant control over the entire reduction algorithm from the preprocessing stages to what is included in each model (astronomical, noise, etc.). Varying the parameters supplied in *makemap*'s *dimmconfig* file, therefore, will give rise to different final images. Many of these differences will be subtle but any differences between reductions should be well understood.

The *dimmconfig* file employed is dependent on the scientific goals desired. For example, since the beginning of the SCUBA-2 mapping initiative, the JCMT Science Archive's (Economou et al., 2015) Legacy Release project has been focused on producing public images and subsequent catalogues which could answer the simple question: "Is there compact emission in an observed region?". In this way, the archive can provide a useful set of information to a wide variety of user projects without doing more complex analyses that require careful human oversight.

To this end, the JCMT LR1 data reduction was tuned to downgrade extended structure while effectively identifying compact emission. The GBS SCUBA-2 team, however, has a wide range of specific scientific interests including but not limited to an investigation of the emissivity spectral index of the thermal dust emission (Hatchell et al. 2013, Coudé et al., in prep.) and its relationship to temperature and column density (in conjunction with Herschel Space Telescope data; Sadavoy et al. 2013; Chen et al. 2016), structure mapping (Salji et al. 2015a, Salji et al. 2015b), investigations into protoplanetary disks (Dodds et al. 2015, Buckle et al. 2015, Broekhoven-Fiene et al., submitted.), fragmentation analyses (Mairs et al., 2016), virial studies (Pattle et al., 2015), clustering (Lane et al., 2016; Kirk et al., 2016c), and radiative feedback processes around young stars (Rumble et al., 2015). The GBS LR1 is the most current data reduction product available from the GBS team to suit these individual goals while remaining consistent across all the star-forming regions observed by the GBS. This broad mandate means that the data reduction strategy requires both compact and extended emission recovery. The latter is a more difficult process as the separation of large, faint structures from time-varying noise is non-trivial. To this end, the GBS LR1 reduction employs a two-step process in which significant recovered emission is first identified automatically based on the signal-to-noise ratio (SNR) then, based on

those resulting maps, a rigorous analysis is performed wherein the observer uses the structure detected and in some cases knowledge from other data sets (for example, from the Herschel Space Observatory) to define a boundary around any emission that is likely real. After the significant structure is more rigorously identified by the observer, the map undergoes a second round of data reduction.

The format of this paper is as follows: In Section 3.3, we outline in more detail the specific differences between the JCMT LR1 reduction and GBS LR1 reduction methods. In Section 3.4, we compare the final maps produced using each method in three regions of interest within the Orion A South star-forming complex. In Section 3.5, we explore the scales and flux levels at which the reductions preserve structure by constructing artificial Gaussian sources and recovering them after they have been processed by *makemap* in a pure noise field. In Section 3.6, we investigate the effect of changing the flux density threshold at which SCUBA-2 data are considered to be significant astronomical signal. We then carry on this investigation by determining the effects of changing the size of a user-defined boundary around emission that has been labelled as significant. In Section 3.7, we give a brief overview of how data reduction can affect the results of common observational metrics used when studying star forming regions. Finally, in Section 3.8, we summarise the main results and present our conclusions.

3.3 Data Reduction Parameters

The SCUBA-2 data reduction process, *makemap*, is explained in detail by Chapin et al. (2013) (see their Figure 6). To summarise here, the raw data from each scan is first assembled into a continuous time series and a flat field correction is applied. Then, the data is downsampled and discontinuities such as steps, spikes, and gaps are repaired. Following that, the mean of each bolometer time series is removed from the map and the iterative portion of the mapmaking procedure begins.

There are six models iteratively constructed and improved upon in five steps before the final map is created:

1. The COM and GAI models first estimate and remove the common mode signal across the bolometers at each time step, respectively. The common mode removal can be performed over the full SCUBA-2 focal plane array ($\sim$400″ scale) or over each sub-array individually ($\sim$200″ scale; see the `com.perarray` parameter in Sections

3.3.1 and 3.3.2, below).

2. The EXT model then corrects for extinction.

3. Next, the FLT model (based on a high-pass filtering algorithm) removes independent low-frequency noise associated with each individual bolometer directly from the time series. The physical scale to which we filter is initially input as a length (see the `flt.filt_edge_largescale` parameter in Sections 3.3.1 and 3.3.2, below) since the scanning speed of the telescope is known and thus a length scale can be converted to a time scale.

4. The AST model then identifies significant astronomical signal in the estimated map and removes its projection from the time series so that the noise can be measured accurately.

5. Finally, the NOI model measures the noise in the residual time series after the removal of the AST signal.

If the solution converges, the algorithm produces the final map. Otherwise, the process repeats itself by inverting the previous solution and re-estimating each model until convergence is achieved.

All continuum observations presented in this paper are taken from the GBS survey (Ward-Thompson et al., 2007c) and were made with the PONG1800 mapping mode (Bintley et al., 2014) which produces individual circular regions called "pongs" with a usable diameter of $\sim$0.5°. To map large regions, as in the case of Orion A South (see Section 3.4), circular pongs are placed so their edges overlap to allow for a more uniform noise level in the final mosaic. This final mosaicked dataset includes four to six repeats of every $\sim$0.5° observing field, with a higher number of repeats for data taken in worse weather conditions. The maps are created with 3″ pixels and the final images, originally in units of picowatts (pW), are converted to Jy Beam^{-1} using the peak intensity conversion factor 537 Jy pW^{-1} Beam^{-1} (Dempsey et al., 2013) for the GBS LR1 reduction and 567 Jy pW^{-1} Beam^{-1} (Graves et al. in prep) for the JCMT LR1 reduction. For the GBS LR1 reduction, the iterative process was terminated when the average pixel value changed by less than 0.1% of the estimated map rms. In contrast, the JCMT LR1 reduction uses a termination value of 1%. The

difference in the stopping criteria (and other paramaters) was based on the specific goals of each data reduction. A more stringent threshold was used for the GBS LR1 because this allows more diffuse, extended structure to be recovered. In contrast, the less stringent threshold was sufficient for the JCMT LR1 reduction as it was only important to reach convergence after recovering bright, compact structure which takes less computing time (see Sections 3.3.1 and 3.3.2, below). Note that the three regions presented here have a noise level of $\sigma_{rms} \approx 0.0038$ Jy Beam^{-1} (for a description and analysis of the entire Orion A South region, see Mairs et al. 2016). In the following two subsections, we discuss individual choices for a subset of *makemap*'s configurable parameters for each of the JCMT LR1 reduction and GBS LR1 reduction methods.

3.3.1 JCMT LR1 Data Reduction

The JCMT science and computing group is currently producing for release to the wider astronomy community a uniform reduction and co-addition of its publicly available SCUBA-2 850 μm data (for more information, see Bell et al. (2014) and Graves et al. in prep.). This legacy release will consist of a) individual Hierarchical Equal Area isoLatitude Pixelization (HEALPix) tiles with equal area but some non-square pixels (see Górski et al. 2005) reduced using a map-maker configuration chosen to work for a diversity of regions and observational types; b) these individual observations coadded together to produce HEALPix tiles covering all the regions observed; and c) catalogues of the emission detected in each map.

The *makemap* parameters chosen are available with the Starlink *smurf* map-maker software in a text file named *dimmconfig_jsa_generic.lis*. The parameters were developed with a focus on minimising the possibility of artificial emission being created during the reduction process while still producing high quality results across a diversity of observation types towards a range of astronomical regions. To accomplish this task, it was decided that no attempt to recover large-scale structure would be made. In addition, given the automated nature of these reductions, external masks rigorously defined by an observer (like in the case of the GBS LR1, below) were not a viable option, and so, a more restrictive automasking configuration was used. The following are the most important of the *makemap* parameters:

`com.perarray = 1` This parameter creates a separate common mode for each sub-array of SCUBA-2, which means that sources larger than the sub-array size ($\sim$200″) will not be recovered. As stated previously, accurately recovering com-

pact structure is one of the main goals of the JCMT LR1 reduction; this reduction is not suitable for an analysis of extended structure.

`flt.filt_edge_largescale = 200` This parameter filters all emission on scales above 200″ and is consistent with `com.perarray=1`; it operates in the time stream and uses the scanning speed to convert the length scale to a time scale.

`numiter = -25` & `ast.skip = 5` The first 5 iterations are done without an AST model and then up to a further 20 iterations are performed. The reduction will exit at that point even if it hasn't converged. Processing of all the Orion observations, however, converged. This choice of 25 iterations helps keep the reduction of a very large number of observations to a reasonable time scale.

`ast.zero_snr = 5` Pixels which have a value of at least 5 σ_{rms} will be identified as astronomical signal.

`ast.zero_snrlo = 3` This parameter allows identified sources with pixel values of at least 5 σ_{rms} to expand in area until the flux density values are 3 σ_{rms}.

`maptol = 0.01` This parameter specifies when to terminate the mapmaking procedure. Using this reduction method, the process will terminate when the average pixel value in the map changes by less than 1% of the estimated map RMS.

3.3.2 The Gould Belt Legacy Survey Legacy Release 1

The GBS LR1 reduction is a two-part process. In part one, a reduction similar in approach to the JCMT LR1 reduction is run, i.e., flux is assigned to the AST model based on pixels with high signal-to-noise-ratios. This is referred to as the "automask" reduction.

Part two is an additional step which is employed in the GBS LR1, but not the JCMT LR1 reduction. After the automask reduction is performed, the individual maps are coadded for a higher SNR and the resulting image is used to define regions of likely emission. The boundaries drawn around the significant signal become the user-defined "external mask" and this mask is used to perform a second round of data reduction to better recover faint and extended structure. In this re-reduction, instead of basing the AST model on pixels which achieve a specific SNR value, the

pixels within the external mask boundaries are defined as containing astronomical signal. This allows for a more well-defined masked area around structure which we are confident is real to be included in the AST model when compared using a single observation.

Major differences from the GBS Internal Release 1 reduction method (IR1; see Hatchell et al. 2013, Buckle et al. 2015, Rumble et al. 2015, and Pattle et al. 2015) include smaller pixel sizes (GBS LR1 pixels are half as wide as GBS IR1 pixels, allowing for better characterization of small-scale emission as well as more accurate peaks and positions of compact sources), and additional filtering of the raw data which better prevents the appearance of large-scale noise features in the reduced maps. Note that despite the attempts to minimize noise and reconstruct the diffuse emission, there are still challenges in retrieving all the signal for large sources (see Section 3.5). The following are the most important parameters to be compared with the JCMT LR1 reduction, above. Unless otherwise stated, these parameters are the same for both the automask reduction and the external mask reduction:

`com.perarray = 0` No separate common mode for each sub-array of SCUBA-2 is created. Thus, sources with sizes up to the full array size ($\sim$400″) can be confidently recovered. Sources with sizes approaching and exceeding this value will have large-scale features subtracted by the common mode model.

`flt.filt_edge_largescale = 600` This parameter, operating on the time stream, filters all emission on scales above 600″. This value is three times the size of the JCMT LR1 reduction emission scale.

`flt.filt edge_largescale_last = 200` Only on the last iteration, the emission outside the AST mask is filtered at 200″ instead of 600″. This parameter was defined to help suppress uncertain emission structure outside the masked regions. The detection of extended emission and the accuracy of our calibration are trusted within the masked regions but outside the mask boundaries we cannot be confident that the extended structure is real. By filtering the unmasked data harshly on the final iteration, we remove the large-scale features and uncover any underlying, robust, small-scale sources.

`numiter = -300` & `ast.skip = 5` The first five iterations are done without an AST model, and up to a further 295 iterations are performed. The reduction will

exit at that point even if it hasn't converged. All processing of the Orion observations, however, converged.

`ast.zero_snr = 5` Pixels which have a value of at least 5 σ_{rms} will be identified as astronomical signal. This only applies to the automask reduction as the external mask reduction defines what will be considered as astronomical signal using clear physical boundaries.

`ast.zero_snrlo = 0` This parameter does not allow sources identified as astronomical signal to extend to lower flux densities. Instead, a pixel must have a value of at least 5 σ_{rms} to be included in the AST mask in the automask reduction. While the final reduction employs a user-defined external mask, the boundaries of that external mask will be based on the sources identified by the automask.

`maptol = 0.001` This parameter specifies when to terminate the mapmaking procedure. Using this reduction method, the process will terminate when the average pixel value in the map changes by less than 0.1% of the estimated map RMS.

3.4 Data Reduction Comparison in Orion A South

In Figures 3.2 to 3.4, we compare two reductions using representative areas of the GBS-defined "Orion A South" region by resampling the JCMT LR1 HEALPix images to match the GBS LR1 pixel size and projection. Orion A South is a 2.2° × 3.1° subsection of the Orion cloud complex, an active star-formation site approximately 450 pc from the Sun (see Johnstone & Bally 2006, Allen & Davis 2008, and Davis et al. 2009 for more information). The entire Orion cloud complex has a mass in excess of $2 \times 10^5 M_\odot$ (Wilson et al., 2005) and is comprised of two individual molecular clouds: Orion A and Orion B (Reipurth 2008; page 459: Overview of the Orion Complex; Megeath et al. 2012, and references therein). The northern section of the Orion A Cloud (Orion A North) is home to the Orion Nebula and the well-known integral shaped filament (Johnstone & Bally, 1999). The Orion A South region is also a target of interest and, although less complex and dense, it exhibits several different stages of star formation (see Mairs et al. 2016 for more information on Orion A South).

From Figures 3.2 to 3.4, we see that the qualitative difference between the JCMT LR1 and the GBS LR1 reductions rests in the extended emission. As expected,

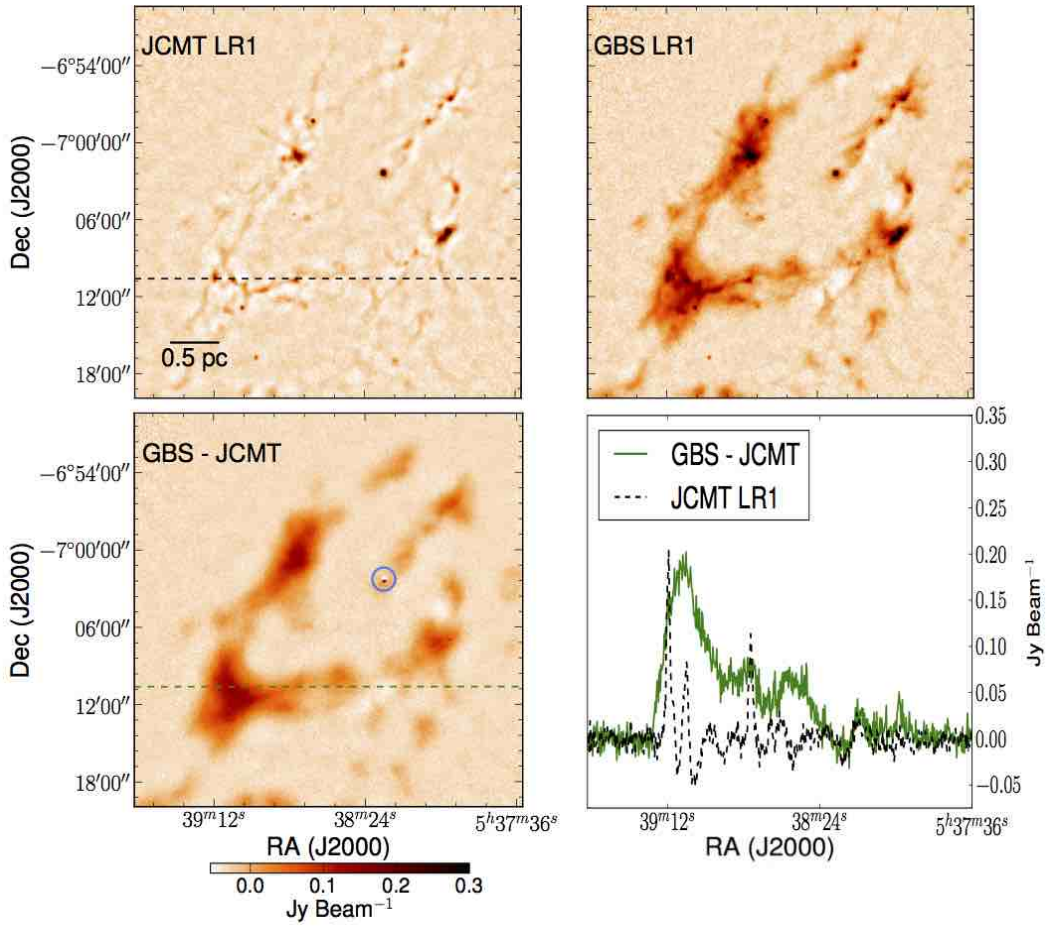

Figure 3.2 Region 1: The first of three representative regions of Orion A South. *Top left:* 850 μm SCUBA-2 image reduced with the JCMT LR1 reduction parameters. *Top right:* 850 μm SCUBA-2 image reduced with the GBS LR1 reduction parameters including the external mask. *Bottom left:* The GBS LR1 map subtracted by the JCMT LR1 map. The blue circle indicates a peculiarity in the map due to realigning the HEALPix projection of the JCMT LR1 reduction to the tangent plane projection of the GBS LR1 reduction. *Bottom right:* The intensities of the JCMT LR1 map subtracted from those of the GBS LR1 map across the positions corresponding to the dotted line shown in the bottom left (green) and the intensities of the JCMT LR1 map across the same coordinates (black).

compact structures present in the data are well accentuated in the former. Indeed, if one's goal is simply to determine where compact emission exists in the map, this style of data reduction is entirely reasonable. One must, however, be cautious when analysing the JCMT LR1 maps any further as the total flux density present in a given region will likely be underestimated even in tight boundaries around the brightest sources (see Section 3.4.1 below).

The GBS reconstruction gives a more accurate picture of the large-scale structure, as required for the science goals of the consortium. Beyond simply identifying where emission exists, the intent here is to recover the full emission structure. The less drastic filtering parameter and the manual external masking process allow, for example, much more extended emission associated with a given object to be included in stability calculations, providing the opportunity to characterise the wide varieties of dense gas/dust morphologies seen in all regions of the survey. In comparison, the JCMT LR1 reduction's recovery of fractional extended emission inhibits these goals.

In the bottom left panels of Figures 3.2 to 3.4, we present maps depicting the JCMT LR1 reduction subtracted from the GBS LR1 legacy reduction for each representative region of Orion A South. With only a few exceptions (blue circles have been drawn around prominent examples in Figures 3.2 and 3.4), we see that the compact structure has been almost completely canceled out and only the extended emission remains. This situation is not unexpected since both reduction techniques process compact objects in the same manner. Instead, the significant differences are found in the large-scale emission.

To see the similarity of the compact structure between the two reduction techniques more easily, the bottom right panel of each Figure shows the flux density through a slice of each region. The solid green line shows the GBS LR1 intensities with the JCMT LR1 intensities subtracted while the dashed black line shows only the JCMT LR1 intensities across the same cut. The physical positions of each slice is represented in the top left and bottom left panels of each figure by the dashed lines. Indeed, the features seen are easily recognisable by comparing the image to the intensity plots. We see in many cases that the peaks in the JCMT LR1 image are fainter than the peaks in the GBS LR1 image. This is because the GBS LR1 data reduction recovers more of the underlying flux density when using an external mask covering a larger area than the automatically detected emission in the JCMT LR1 map. Evidently, the better recovery of this extended structure occasionally increases the flux density of small scale features associated with the parent source, resulting in

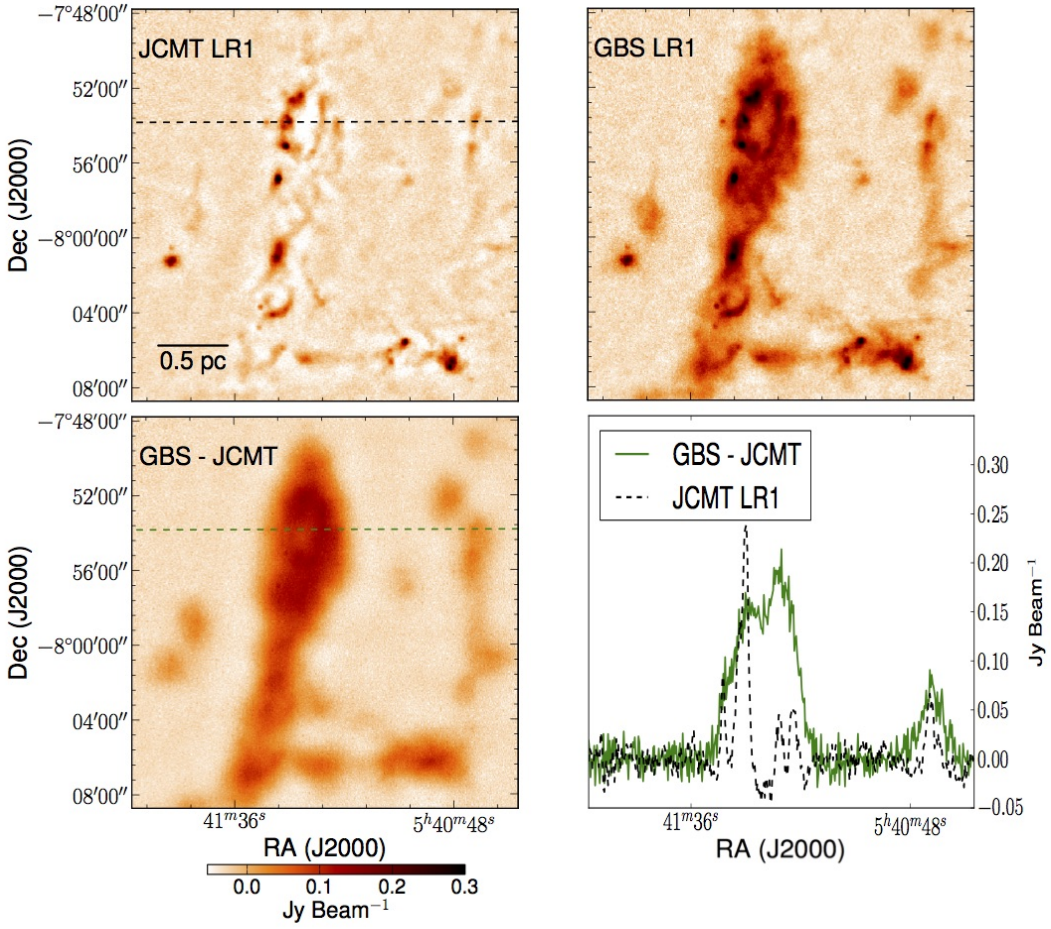

Figure 3.3 Region 2: The second of three representative regions of Orion A South. Each panel is presented in the same manner as in Figure 3.2.

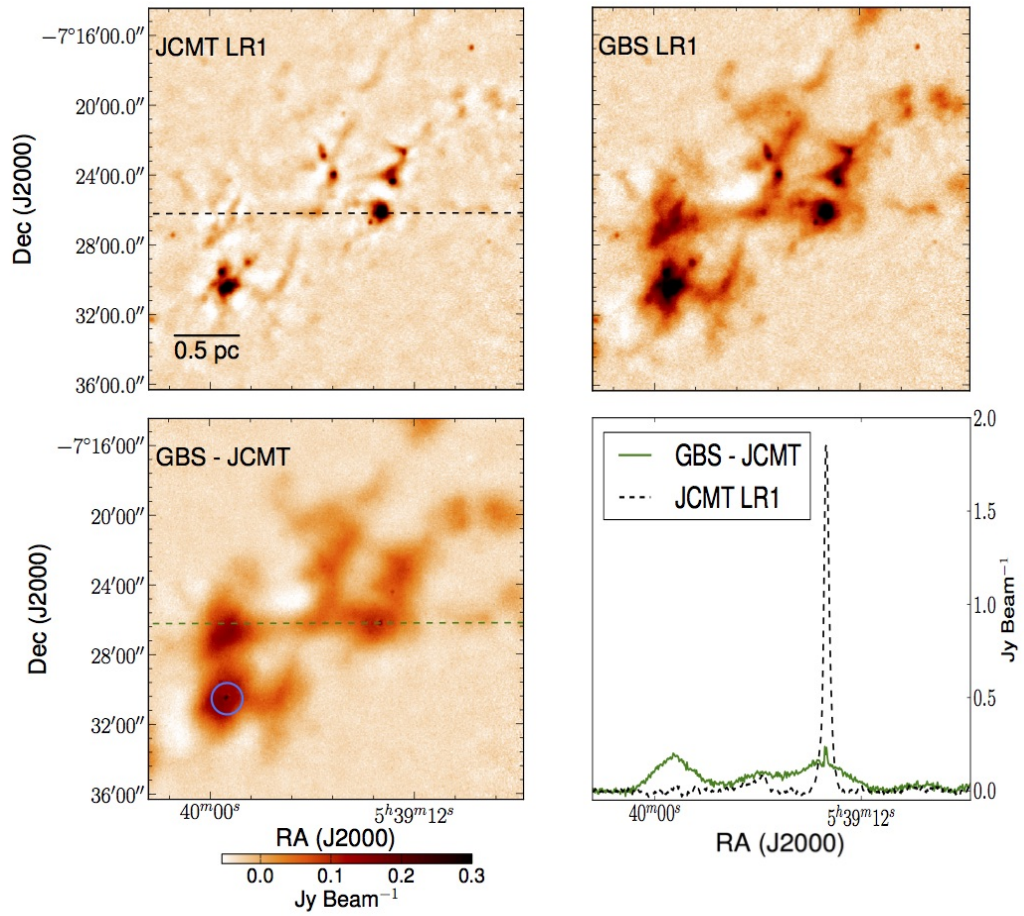

Figure 3.4 Region 3: The final representative region of Orion A South discussed. Each panel is presented in the same manner as in Figure 3.2. The blue circle indicates an example of a residual peak left over after the subtraction.

features like that which is indicated by the blue circle in Figure 3.4. The residual peak intensity left over in this example is 12% of the peak intensity measured in the GBS LR1 image. The amount in which the flux density increases depends on the properties of the larger-scale parent source. This difference can cause discrepancies where the JCMT LR1 peak intensities are as low as 40% of the GBS LR1 peak intensities in the observed regions of Orion A South. In most cases, however, the JCMT LR1 peak intensities are ∼60% of the GBS LR1 peak intensities (see Figure 3.6). The brightest peaks have the smallest differences. Note that fainter, compact, isolated peaks also appear to have a bias to slightly lower intensities in the JCMT LR1 map due to the harsh filtering parameter and less thorough masking procedure. This effect, however, is not as strong as the pedestal caused by the recovery of extended structure.

Compact objects near the boundaries of HEALPix tiles can deform and elongate. The blue circle in the bottom left panel of Figure 3.2 highlights a peculiarity resulting from converting the HEALPix projection employed by the JCMT LR1 reduction to the tangent plane projection used by the GBS LR1. The oblong shape of the circled source could potentially alter the position of a detected peak in this region. We note, however, that this event is uncommon and we only see this one example in the entire Orion A South map.

3.4.1 Quantitative Differences between the GBS LR1 and JCMT LR1 reductions

Structure Identification Algorithm

To compare the two reductions fairly, we need to identify structure in a consistent manner across each of the two maps. This situation is where the GBS LR1's diffuse, extended emission presents us with a challenge. There are many structure identification algorithms freely available to apply to data such as Orion A South and each program will break up large-scale structures or amalgamate smaller ones in different ways (see Stutzki & Guesten 1990; Williams et al. 1994; Rosolowsky et al. 2008; Men'shchikov et al. 2012; and Berry 2015 for algorithm examples). We note that several individual JCMT LR1 "sources" can reside within a single GBS LR1 reduction "source" no matter which algorithm is used to identify structure, due to the lack of extended emission in the former defining smaller areas of significant signal.

Since we are specifically interested in the differences between compact structure and extended structure separately, for this analysis we employ the JCMT Science Archive algorithm *jsa_catalogue* found in *Starlink's PICARD* package (Gibb et al., 2013). The catalogues generated with this algorithm are based around the concept of *islands* (or extents) and *peaks* (blue contours and magenta Xs, respectively in Figure 3.5). The routine was designed to do a good job of cataloging all regions where emission was strongly detected (the islands), and then to provide a list of local peak positions within each island to categorise the nature of the emission. Source catalogues based on this approach will be released along with the JCMT LR1 maps (Graves et al., in prep.).

The *jsa_catalogue* routine was used to identify regions of contiguous emission above a minimum number of pixels (9 pixels), using an SNR cut of 5 (the noise level in these maps is ~ 0.0038 Jy Beam^{-1}). These regions are found using the *FellWalker*

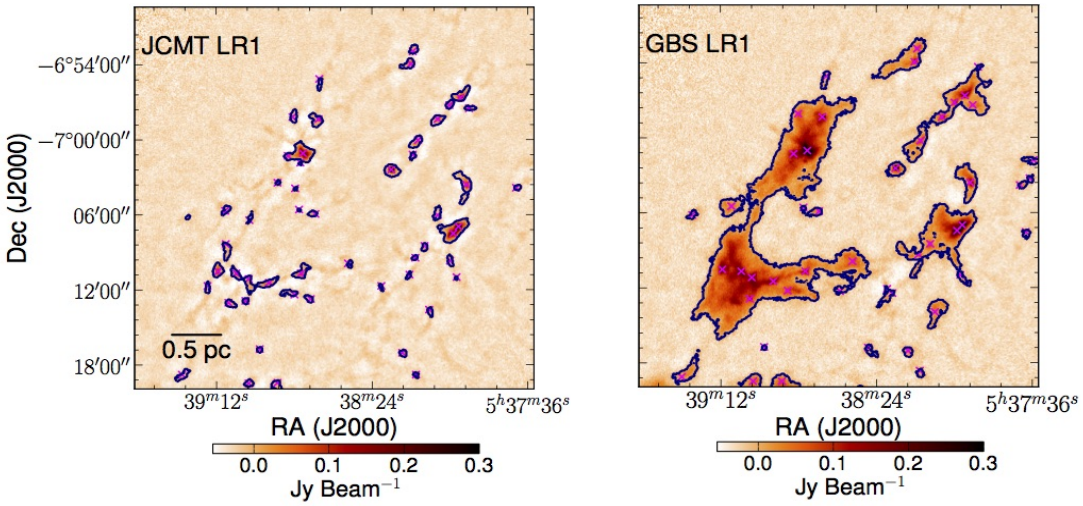

Figure 3.5 Islands (blue contours) and peaks (magenta Xs) identified by the *FellWalker* algorithm for both reductions tested using Region 1 as an example. See text for information on the basic algorithm parameters used to identify structure.

Table 3.1 Summary of the three regions analysed and the number of sources found within each. The RA and DEC represent the centre coordinates of each region.

Region	RA, DEC	Size	# Peaks		# Islands	
			GBS	JCMT	GBS	JCMT
1	5h38m35.632s, -7:04:39.80	0.51° × 0.51°	47	51	25	48
2	5h41m16.139s, -7:58:16.84	0.35° × 0.35°	35	35	13	32
3	5h39m30.365s, -7:25:23.70	0.37° × 0.37°	29	44	12	35

algorithm (Berry, 2015) as implemented in the *cupid* package (Berry et al., 2007) on the SNR map, and then their shapes are extracted from the data map so that the total flux density, average noise across the region, and the flux density at the peak can be calculated. These regions are identified as the islands or extents of emission.

Within each of these detected regions, the routine then searches for peaks, again using the *FellWalker* algorithm. The routine is configured to identify a pixel as a peak if it has a) a peak value of magnitude 5 times higher than the average noise in the island; b) a minimum dip of magnitude 5 times grater than the average noise towards the nearest larger peak; and c) more pixels than the minimum of 9 assigned towards this peak (to avoid noise clumps). The peaks are identified only by their position and brightness. No attempt is performed to assign a shape to them. Selecting this set of parameters was a result of extensive testing of the *FellWalker* algorithm on many different SCUBA-2 maps as well as maps which only included artificial structure. There is no standard set of parameters as the algorithm can be tuned differently depending on the specific scientific question of interest. More generally, the debate about which boundaries to draw around different structures, especially in regions with complex emission, has been present in the literature for many years (see, for example, Pineda et al. 2009a) and it should be performed carefully and with an approach that addresses specific goals.

Properties of the Structure in Each Reduced Map

For both reductions, Table 3.1 shows the number of peaks and the number of islands detected in each region shown in Figures 3.2 to 3.4 along with the centre coordinates and sizes of each region. Table 3.2 provides the total, maximum, and median effective radius and total flux density found in each population of island sources as well as the peak intensity found in each population of sources identified by *jsa_ catalogue* in each

Table 3.2 Comparison of the identified structure in the GBS LR1 and JCMT LR1 reductions. Three metrics are used to compare the GBS LR1 and JCMT LR1 methods in the three regions. The areas are calculated by summing the number of pixels within a given source identified by *jsa_catalogue's* island catalogue, the total flux densities are the summation of the pixel values in each source's footprint, and the peak intensities refer to the sources identified by *jsa_catalogue's* peak catalogue.

Region: Metric	Total		Maximum		Median	
	GBS	JCMT	GBS	JCMT	GBS	JCMT
1: Area (arcsec^2)	3.8×10^6	6.1×10^5	2.5×10^6	7.4×10^4	1.4×10^4	7.2×10^3
1: Total Flux (Jy)	142.4	17.5	101.8	4.0	0.3	0.1
1: Peak (Jy beam^{-1})	–	–	1.3	1.0	0.1	0.1
2: Area (arcsec^2)	3.3×10^6	5.2×10^5	2.4×10^6	1.1×10^5	5.5×10^4	6.2×10^3
2: Total Flux (Jy)	149.0	18.4	118.4	4.4	2.2	0.1
2: Peak (Jy beam^{-1})	–	–	0.8	0.6	0.2	0.1
3: Area (arcsec^2)	3.1×10^6	6.3×10^5	2.7×10^6	1.4×10^5	3.3×10^4	6.4×10^3
3: Total Flux (Jy)	127.7	26.9	119.2	10.0	0.8	0.1
3: Peak (Jy beam^{-1})	–	–	2.6	2.4	0.2	0.1

reduced dataset. The effective radius given is the radius of a circle with the same area as the object of interest.

Figure 3.6 shows a comparison of the source radii, total flux densities, and peak intensities identified in all three regions. Since the islands we identify in the JCMT LR1 reduction are smaller and more fragmented than the sources we identify in the GBS LR1 reduction, we match our JCMT LR1 reduction sources with the associated GBS LR1 reduction "parent source" so that we can compare specific structures in the same location of each map. We assign JCMT LR1 sources to a GBS LR1 parent based on the position of the geometric centre of a given source. If a JCMT LR1 source centre falls within the boundaries of a GBS LR1 island, we consider those emission structures to be associated. There are only a few cases where a JCMT LR1 source is not associated with a GBS LR1 source or *vice versa* but these are small, faint objects which have little bearing on our final results. Thus, for the radii and total flux densities, we only include objects in the Figure if they have a counterpart in each image. When comparing the peak locations between the GBS LR1 and JCMT LR1 images, the overwhelming majority of detected peaks lie within one pixel of their counterpart. Notably, there are relatively small numbers of isolated GBS LR1

peaks and JCMT LR1 peaks across the entire Orion A South region, this is simply due to the degree of smoothness of the diffuse emission recovered by each respective reduction (see Section 3.4.1). As Table 3.1 shows, region 3 has the largest disparity in peak number due to the manner in which the bright, diffuse emission is broken up by the JCMT LR1 reduction. Many borderline peaks are identified that would not have been if the underlying continuous structure was more visible. The results presented here only include peaks which are associated with the same emission in each map.

In Figure 3.6, the JCMT LR1 reduction source property is on the ordinate and the GBS LR1 reduction source property is on the abscissa. For the radii and total flux densities, we plot each of the JCMT LR1 reduction sources associated with a given GBS LR1 source in black and we sum all of the associated JCMT LR1 sources and plot that as a red plus sign. With this approach we can compare how much emission is being found in each region in a fair way. For the peak intensity, we directly compare *jsa_ catalogue's* catalogue detections found in each map produced by the two data reduction methods. The blue lines in Figure 3.6 all show a one to one relationship and the green lines have a slope of unity at the shown percentage of the GBS LR1 values. The latter is meant to give an indication of the representative difference between the two reductions based on each measurement.

Since the *jsa_ catalogue* algorithm gives us information on both the peaks as well as the extended structures within a given map, we discuss each of these aspects individually.

Peaks

The GBS LR1 and JCMT LR1 reductions have similar compact structure in regions without extended flux (see, for example, the isolated source to the left of the main structure in the top two panels of Figure 3.3). This similarity is because the main differences in the data reduction parameters deal with structure that is much greater than one 14″ beam. For example, the `flt.filt_edge_largescale` parameter (see Section 3.3) chosen by each reduction impacts recovered emission on the scale of $>$ 200″. As well, the larger number of iterations employed in producing the GBS LR1 maps will not have a large effect on the bright, compact structure, but that parameter is set for the recovery of faint emission seen at larger scales.

Since more extended emission is recovered in the GBS LR1 reduction than in the JCMT LR1 reduction, more faint locations are detected as individual sources.

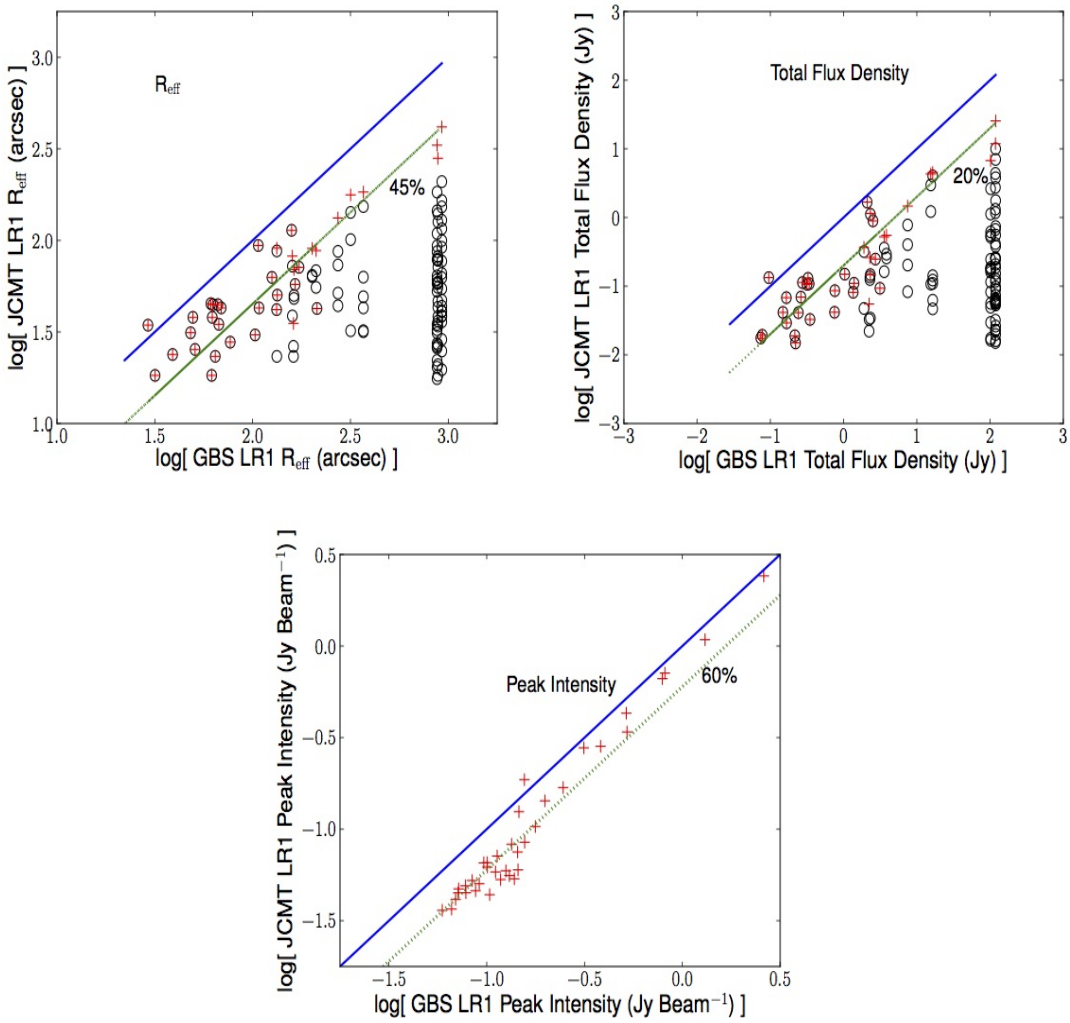

Figure 3.6 Comparing R_{eff} (the radius of a circle with the same area as a given source identified by *jsa_catalogue's* island catalogue), total flux density, and peak intensity between the two data reductions in the three representative regions of Orion A South. In the former two, all the JCMT LR1 reduction islands associated with a given GBS LR1 island are plotted in black. We sum the effective radius and the total flux density of all of the associated JCMT LR1 islands, respectively, and plot the total as a red plus sign. For the peak intensities, we plot the peak sources with the maximum flux density identified by *jsa_catalogue's* peak catalogue within a given associated island. The blue (solid) lines show a one to one relationship and the green (dotted) lines have a slope of unity at the shown percentage of the GBS LR1 values.

The JCMT LR1 reduction, however, produces maps which divide up large structures into individual, compact components. The overall effect is that the number of peaks detected in the GBS LR1 and the JCMT LR1 maps are very similar. In two of the regions, there are more JCMT LR1 map peaks since locations that contain diffuse emission in the GBS LR1 maps will not meet the peak detection criteria (but do meet, in some cases, the island detection criteria) whereas the more fragmented JCMT LR1 maps will contain borderline detections in these regions (see Table 3.1). It is clear from the statistics presented in Table 3.2 that, in general, the peak intensities are consistently higher in the GBS LR1 map in every region. As seen previously (recall the bottom right panel of Figure 3.4), the externally masked GBS reduction changes the amount of flux occasionally on the small-scale as well as the large-scale in regions with extended emission (see Figure 3.6). Evidently, going deeper into the GBS LR1 image with an external mask and allowing that structure to grow raises the peaks by a pedestal. The pedestal is not constant, however, because it depends on the larger-scale, fainter emission structure. This behaviour is made clear once more in Figure 3.6 which shows a positive correlation between the brightest JCMT LR1 peak intensities and their associated GBS LR1 peak intensities in log-log space. Indeed, most of the brightest JCMT LR1 peak intensities below 1 Jy Beam^{-1} are only $\sim$60% as bright as their GBS LR1 counterparts because the diffuse background is not included in the former. As the peaks become brighter in each map, they also become more similar to one another. No aperture fitting is performed in this study, however. We perform no background subtraction for the flux extraction to account for large-scale structure.

Extended Structure

We see many similarities between the three regions shown in Figures 3.2 to 3.4. In fact, when using *jsa_ catalogue* to investigate the significant structure in the maps, it was clear that the identified sources in each JCMT LR1 image largely trace the same structure as the corresponding GBS LR1 image. The lack of diffuse emission connecting the bright, compact peaks in the JCMT LR1 map, however, causes *jsa_ catalogue* to divide up the larger structures seen in each GBS LR1 map into many smaller ones. Therefore, between the two reduction methods, the number of "extended" sources identified in each region is always higher for the JCMT LR1 map (see Table 3.1). The lack of extended emission in the JCMT LR1 map is shown clearly in the relative area occupied by identified sources in Orion A South. The total flux density of all

the identified sources is closely related to the area since the structure identification algorithm identifies roughly the same peaks in both maps.

In general, we see that the JCMT LR1 image sources are smaller, as expected, except for the smallest (sometimes faint and spurious) sources present in both reduced images. A positive correlation is followed in radii in log-log space but it is not one to one. We find that the summed radii of all JCMT LR1 islands detected within one GBS LR1 island are typically ∼45% those of the GBS LR1 island radius (as seen in Figure 3.6). This corresponds to a total JCMT LR1 island area of only ∼20% of the GBS LR1 island area which is exactly what we see in the total flux density relationship of Figure 3.6.

3.5 Completeness Testing

To test how well each data reduction method preserves structure, we study the effect of *makemap* on artificial Gaussians with known properties. We construct and "observe" a broad range of Gaussians by varying the sources' full widths at half maximum (FWHM) and peak intensity values. In this section, we approximate 1 beam to be 15″. For each FWHM and peak value, we insert a grid of Gaussian sources into a pure noise field via *makemap*'s *fakemap* parameter (see Figure 3.7). In this manner, the Gaussian grids are added to the raw time stream of the data and are subjected to the usual data reduction steps. We inserted 32 sets of Gaussians in total with FWHMs of 1 beam (15″), 3 beams (45″), 5 beams (75″), and 7 beams (105″). For each of these FWHM values, we use a series of peak intensity values between 3 σ_{rms} and 25 σ_{rms}.

The field in which we insert these regular grids of Gaussian sources is an 850 μm field nearly devoid of structure obtained by the Cosmology Legacy Survey (CLS; Geach et al. 2013) in the PONG1800 mapping mode (see Figure 3.7). This field is a 42 minute integration of a circular region with a diameter of ∼0.8 degrees observed on September 30^{th}, 2013; it is a small subset of the CLS data in this region and, thus, it provides a representative sample of the noise in typical SCUBA-2 images in this configuration. We identify structure in the reduced dataset by employing a Gaussian curve fitter[2] at the known position of the sources located away from the noisy edges of the map. By a simple visual analysis, it appears that artificial structure outside the inserted Gaussians is effectively non-existent. To use the most robust method of

[2]See *SciPy*'s generalised *curve_fit* function: `docs.scipy.org/doc/scipy-0.14.0/reference/generated/scipy.optimize.curve_fit.html`

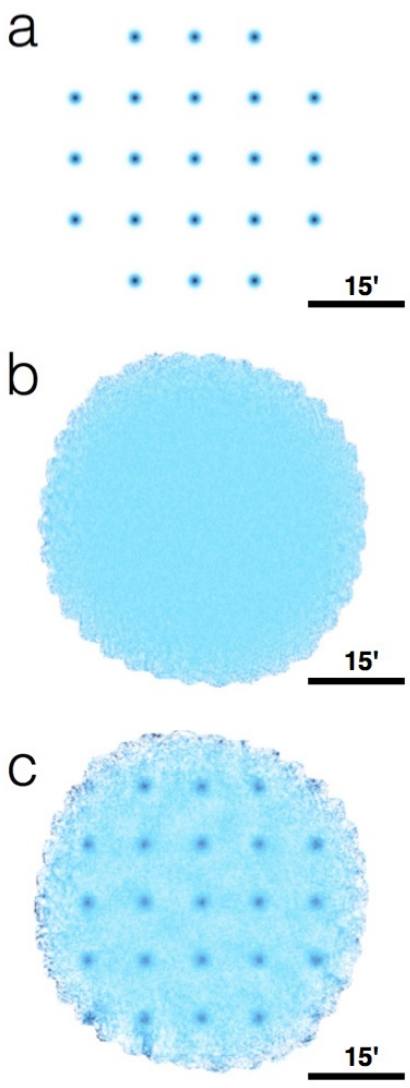

Figure 3.7 *Top, a*: An example Gaussian grid. Here, each Gaussian has a FWHM of 7 beams and a peak of 9 σ_{rms}. The constructed grids are spaced accordingly for the given Gaussian FWHM. When the Gaussians are smaller, more sources are added to the noise field. *Middle, b*: The field nearly devoid of structure in which the Gaussians were inserted. *Bottom, c*: The final map depicting the 7 beam FWHM, 9 σ_{rms} peak Gaussians combined with the noise field using the GBS LR1 reduction method.

returning the true structure, we provide the fiducial Gaussian location, peak intensity, and FWHM values as initial "guesses" for the peak coordinates, peak intensity, and the size of the expected structure to the fitting algorithm. We then compare the obtained output properties of each fitted Gaussian to the nominal input properties.

We run each Gaussian grid run through *makemap* three times. In the first case, we use the standard GBS LR1 automasking procedure (see Section 3.6.1 for tests of different automask parameters). Recall, however, that the GBS LR1 reduction employs a user-defined external mask based on this type of automask for the final product. The second time, we apply an external mask which covers only half of the Gaussians in the image. The external mask we use is not generated using the normal GBS LR1 external masking procedure. Instead, we use a simple checkerboard pattern of square masks, where each mask is 20 beams ($5'$) on a side and centred upon every second Gaussian source (see Figure 3.8 for an example and Section 3.6.2 for the effect of changing the size of the masks). For the final execution of *makemap*, we reduce the data using the JCMT LR1 reduction parameters.

With these three sets of maps, we are able to compare the output properties of the GBS LR1 automasked Gaussians, the Gaussians lying inside and outside an external mask, and the JCMT LR1 reduction Gaussians. In addition, we construct a fourth set of maps wherein the artificial Gaussians are spatially added directly to the reduced noise field. We call this latter set the "non-DR" case, as *makemap* was not used for Gaussian reconstruction.

It is pertinent to note that these tests are all based on Gaussian structures. There is, however, a wide variety of clump morphologies, from nearly spherical dense cores to long, thin filaments. Consideration of the effects of data reduction on Gaussians should inform even those more complex sources.

3.5.1 Results from the Gaussian Recovery

The results of the Gaussian curve fitter are compared to the nominal Gaussian input values in Figures 3.9 to 3.17. In the following sections, we will address each of the measures used to compare between the output structure and the input objects: peak intensity, size, and total flux density.

In each of the images, only the central nine Gaussians are included in the analysis to avoid the high noise locations on the edge of the image. This was done to mimic the approach to the GBS LR1 data itself as the trusted sources in each map lie far

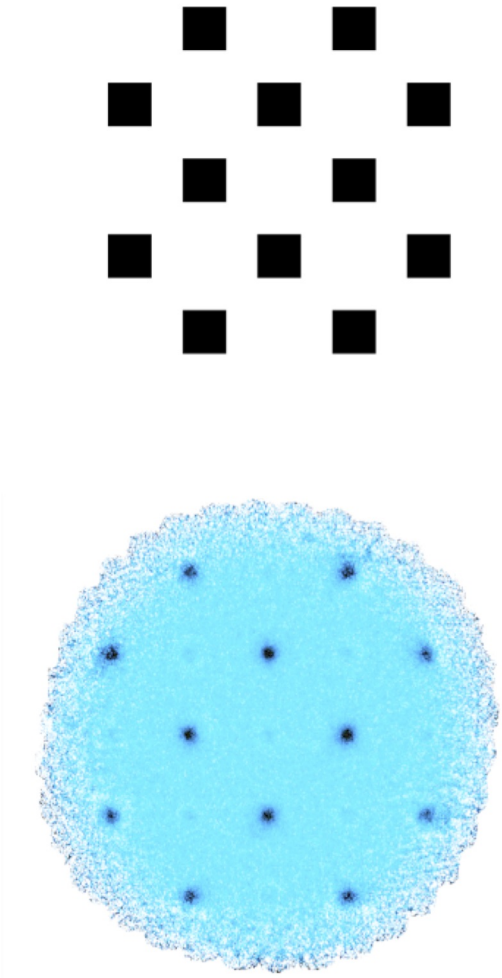

Figure 3.8 *Top*: The checkerboard pattern of the external mask for the 7 beam FWHM Gaussians. Black indicates the positive mask. *Bottom*: The final map after the GBS LR1 reduction using the checkerboard mask on the 7 beam FWHM, $9\sigma_{rms}$ peak Gaussians in the noise field.

from the noisy edges.

In Figures 3.9 to 3.17, the ordinate represents the measured Gaussian properties divided by the nominal input properties at each peak intensity for each of the four FWHM values used. There are seven plot symbols used:

1. The spatial addition of Gaussians onto the noise field (non-DR) are represented by black Xs.

2. Gaussians included in the GBS LR1 external mask (in the images which are produced including an external mask) are represented by dark blue circles.

3. Gaussians which lie outside the GBS LR1 external mask (in the images which are produced including an external mask) are represented by light blue circles.

4. Gaussians included in the GBS LR1 automask (in the images which are produced *without* including an external mask) are represented by dark red squares. We define an object to be included in the automask if at least half of the total number of pixels within the respective Gaussian's FWHM are found in the AST automask.

5. Gaussians which have at least half of the total number of pixels within one FWHM lying outside the GBS LR1 automask (in the images which are produced *without* including an external mask) are represented by light red squares.

6. Gaussians included in the JCMT LR1 reduction automask are represented by dark green triangles. Again, we define an object to be included in the automask if at least half of the total number of pixels within the respective Gaussian's FWHM (in all directions) are found in the AST automask.

7. The Gaussians which lie outside the JCMT LR1 reduction automask are represented by light green triangles.

We performed all reduction tests using the same input Gaussian peak brightness values. In each Figure, however, the symbols have been slightly separated along the abscissa for clarity as they often overlap.

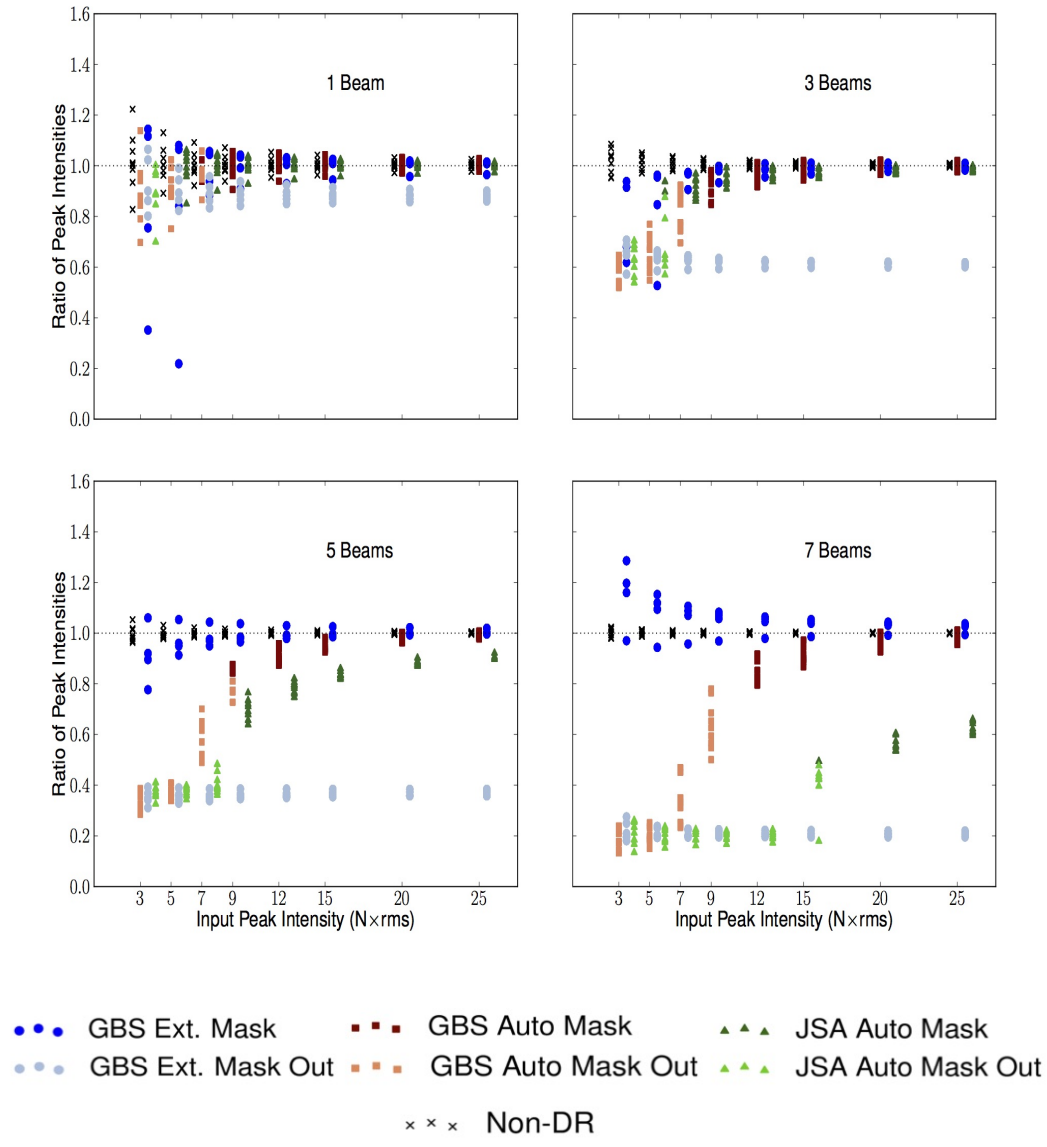

Figure 3.9 Artificial source recovery comparison for different data reduction methods: peak intensities. The plot symbols have been separated along the abscissa for better legibility. The ordinate represents the measured output peak intensity divided by the nominal input peak intensity. *Top left*: Gaussians with a 1 beam FWHM. *Top right*: Gaussians with a 3 beam FWHM. *Bottom left*: Gaussians with a 5 beam FWHM. *Bottom right*: Gaussians with a 7 beam FWHM.

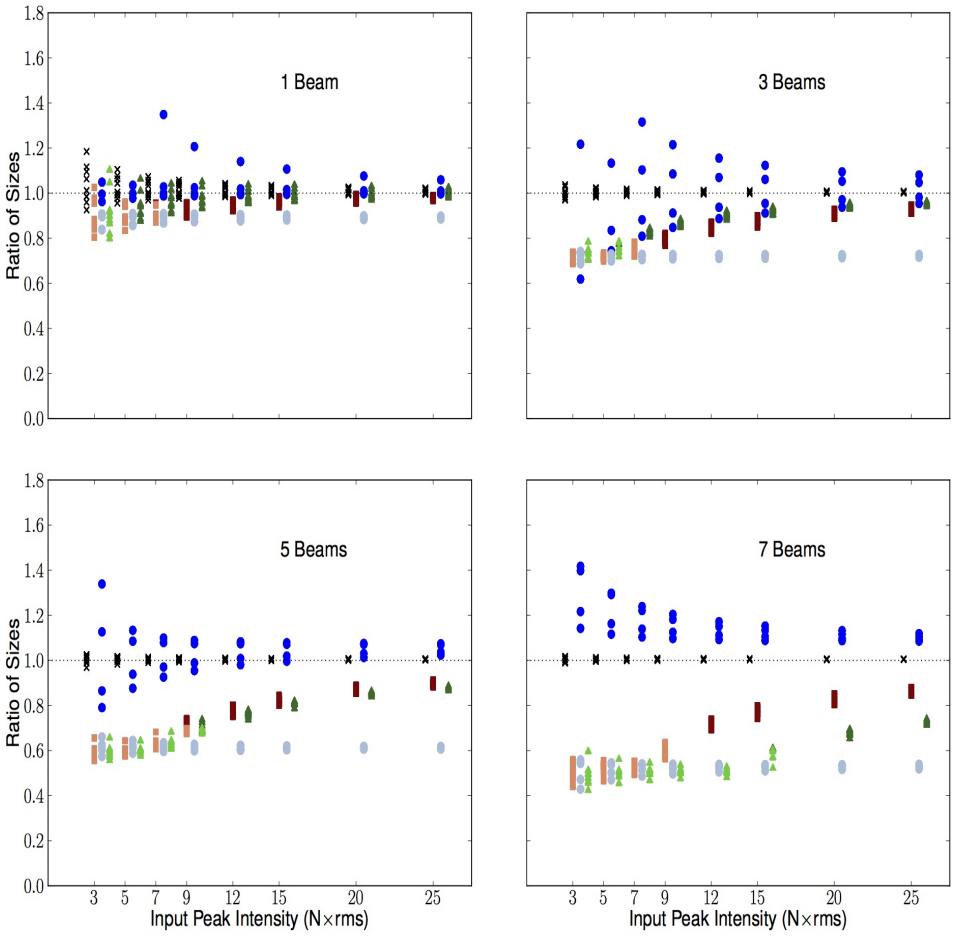

Figure 3.10 Artificial source recovery comparison for different data reduction methods: sizes. The ordinate represents the measured output Gaussian size divided by the nominal input size. The plotting style follows Figure 3.9.

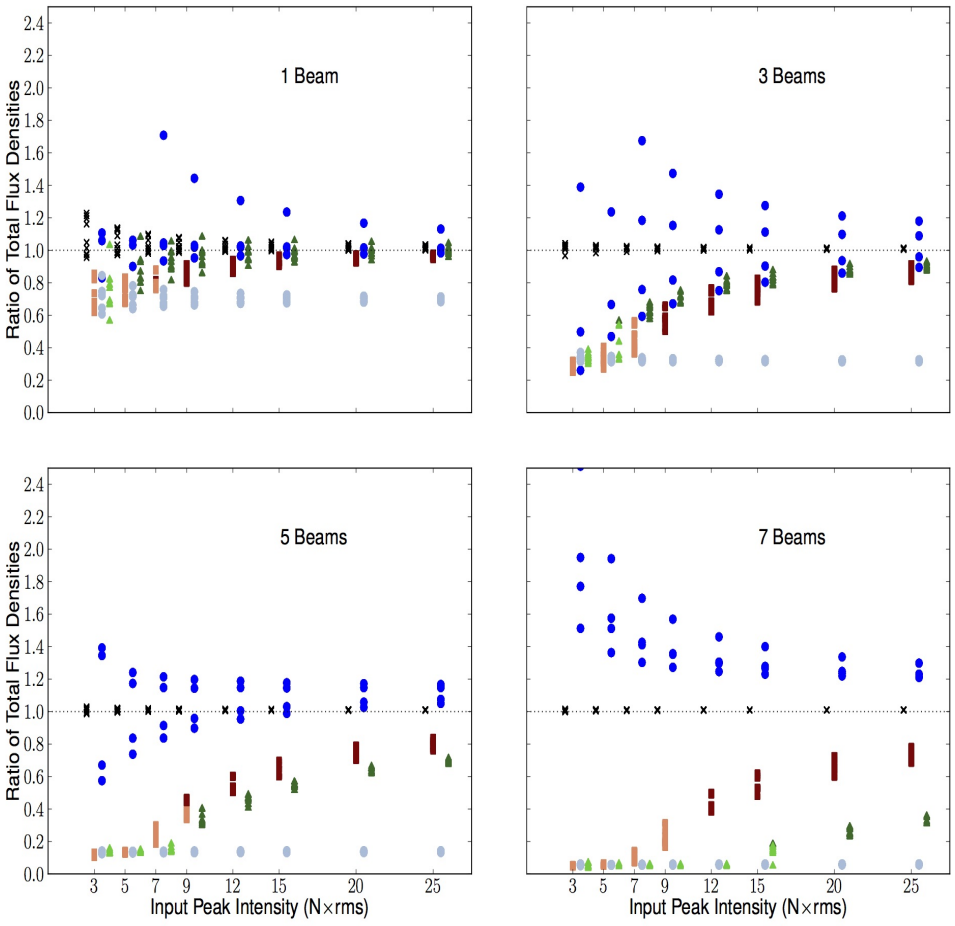

Figure 3.11 Artificial source recovery comparison for different data reduction methods: total flux densities. The ordinate represents the measured output Gaussian total flux density (peak $\times$ size^2) divided by the nominal input total flux density. The plotting style follows Figure 3.9.

Peak Intensity

In Figure 3.9, we see that small objects are well recovered even when they are relatively faint. As the Gaussian FWHMs are increased (top left to bottom right), the masked results converge only for brighter Gaussian peaks. For faint objects larger than a point source, however, the unmasked (light red squares and light blue circles for the GBS LR1, light green triangles for the JCMT LR1 reduction) and automasked (dark red squares for the GBS LR1 reduction, dark green triangles for the JCMT LR1 reduction) cases display significant deviations from the original Gaussian peak values in both reductions. As the Gaussian sizes are increased, the unmasked, reconstructed source properties become lower than those of the source inserted into the map. We also find that as a Gaussian becomes brighter, the given source is recovered more reliably. This behaviour is expected since the pixel-to-pixel variation is steeper for a cut across a Gaussian of a given size with a brighter peak. In contrast, shallow variations tend to get filtered out. Thus, we note that larger Gaussians require brighter peaks for significant pixels to be identified and placed in the automask.

The GBS LR1 Gaussians within an external mask (dark blue circles) and the non-DR Gaussians (black Xs) display the most consistent results with the input peaks and the GBS LR1 automask reduction (dark red squares) recovering the objects well, even for a 7 beam FWHM source (with a peak of at least 9 σ_{rms}. Larger objects will need to be even brighter to be detected). There are obvious sources within an external mask that are lying in a negative bowl in the more compact Gaussian grids (see the external masked Gaussians lying significantly below their nominal size in the top right and bottom left panels of Figure 3.10). This negative bowl is part of the artificial structure introduced by an external mask that is too large for the astronomical signal present (see Section 3.6.2). As the sources begin to resemble the mask size, the negative bowl is no longer apparent. For these and smaller sources which are sufficiently bright, the peak intensities are generally accurate to within 10% of the nominal value, which is similar to the expected calibration uncertainty, while larger and fainter sources are accurate to within 20% (with some exceptions). The variation seen in the small, faint non-DR Gaussians is simply due to the Gaussian curve fitter algorithm looking for the optimal solution. When it is faint, recovery of a Gaussian source will noticeably suffer more from noise variations, causing the algorithm to find the "best" peak. When the structure is small, any deviation from the true location will have greater impact on the peak intensity value and size of the Gaussian fit than the same deviation would

have for a larger, smoother source with more pixels near the correct peak value in the same, central vicinity.

We see also in Figure 3.9 that the JCMT LR1 reduction (triangles) reliably recovers compact structure The peaks found for large objects, however, are significantly underestimated. In both the GBS LR1 and JCMT LR1 reductions, we see that the automasked sources resemble the nominal peak brightness more accurately as the peak brightness is increased before the object is defined to lie within an automask. This behaviour occurs simply because the compact central region of the Gaussian has been identified as it is the brightest location of the source. Less than 50% of the pixels within one FWHM of the Gaussian centre, however, have been included in the astronomical signal (AST) mask at this point.

Size and Total Flux Density

In Figure 3.10, we see results similar to those of the peak intensity for the fitting algorithm's calculated object sizes. It is obvious that the GBS LR1 and JCMT LR1 automask reductions (squares and triangles) miss large structure, as expected. In both cases, however, they identify that at least some structure exists at locations of extended emission, assuming the peak brightness is high enough. The GBS LR1 automask recovers nearly 50% of the pixels within one FWHM of a 7 beam FWHM Gaussian with a peak of 9 σ_{rms}, as evidenced by the increase in peak intensities in Figure 3.9. The JCMT LR1 reduction requires a 15 σ_{rms} peak for the same size, however. Once the external mask is applied to this structure in the second step of the GBS LR1 reduction, the values which are measured resemble the original Gaussian properties. Nevertheless, occasional pedestals and bowls are found which can increase or decrease the size of a given source by up to 40% (see Section 3.6.2 for more information). As discussed above, the GBS LR1 reduction is tuned to recover extended structure whereas the JCMT LR1 reduction is tuned specifically to find compact emission. This means that the JCMT LR1 reduction will always underestimate the large-scale structure present in an observed region.

There are Gaussians that clearly lie on deviations in the noise background induced by the external masking procedure (see Section 3.6.2 below for a discussion on external mask size). The noise field used is very uniform (see Figure 3.7b), however, in Figures 3.9, 3.10, and 3.11 we see the recovered compact Gaussians' properties are overestimated and underestimated while the largest Gaussians' properties only

exhibit the former simply due to their placement in the map. The masks used here are too large, causing a pedestal effect on some sources and a negative bowl on others. This result reinforces the idea that large-scale noise features present in the map and the size of the external mask around a given source can play an important role in source recovery. Again, just as in the case of the recovered peak intensities, bright sources are found to be within 20% of their nominal value and many are within 10%. Looking to the non-DR data (black Xs), we see that there is a fundamental difference in the large-scale structure when we compare with the external masked case (circles). Evidently, in some cases, *makemap* introduces additional structure in the image reconstruction when large external masks are employed and, to conserve flux, it compensates by reducing the real structure present. This behaviour can potentially create bowls around the borders of brighter sources. As the sources increase in size, the external mask's pedestal effect becomes more apparent (see Figures 3.10 and 3.11). For an example of a bowl, see the 3 beam FWHM and 5 beam FWHM cases in Figure 3.10. The fractional importance of the pedestal or bowl, however, declines with input Gaussian peak strength. Separating the background sky signal from the astronomical signal using a tight boundary around significant structure is, therefore, very important so that *makemap* does not allow features in the noise to grow during subsequent iterations. As we explore below in Section 3.6.2, an external mask should not be larger than twice the size of an emission region if the errors in the measured properties of the source are to remain within 10-20% of their nominal value (up to the size of the array footprint and/or characteristic high-pass filter scale). This gives the researcher an opportunity to safely mask a whole region with a generous boundary in case there is indeed faint extended structure that is not apparent from a simple automask reduction.

It is important to reiterate that in the GBS LR1 reduction, the external mask size which is used is based on the previously performed automask reduction (see Section 3.3.2). In this automask reduction, the common mode subtraction over the spatial scale of the bolometer array at each time step and the filter size acting on the time stream are the most important considerations when determining the scales we can trust in the final images (see parameters `com.perarray` and `flt.filt_edge_largescale` in Section 3.3; also see Chapin et al. 2013). The full SCUBA-2 focal plane, including all four subarrays, is $400'' \times 400''$. This nominally means that objects with sizes up to $\sim 400''$ can be confidently recovered during the common mode subtraction at each time step. Large objects approaching this scale, however, can create a similar signal

in a high percentage of bolometers causing them to be targeted as common mode, low frequency noise. Thus, large-scale modes can be subtracted from these structures, diminishing their sizes and leading to uncertainties in drawing the external mask boundaries.

In addition to this common mode subtraction, the filter operating on the time stream was chosen to be 600″, approximately the diagonal size of the full 400″×400″ focal plane array. As noted in Section 3.3, this filter uses the scanning speed of the JCMT combined with the provided spatial scale to subtract large-scale modes from each individual bolometer time series. Thus, on scales of ∼400″ to 600″ and larger (depending on the external mask boundaries), significant structures are recovered but with diminished sizes and total fluxes due to the subtraction of large-scale modes (see Section 2 of Pattle et al. 2015). The degeneracy between significant large-scale sources and the common mode, however, can cause artificial structure to arise in various parts of the map (see Chapin et al. 2013, section 4). Therefore, drawing external masks which are larger than necessary can fuel these degeneracies and create obvious pedestals and bowls. Note that in the case of the JCMT LR1 reduction, we cannot reliably identify structures larger than 200″ as this is the time stream filter scale as well as the subarray footprint (the common mode is calculated over each individual subarray in this reduction) and no external mask reduction is subsequently performed.

An interesting question for non-artificial sources is how much real structure we are missing at large-scales. An automask will certainly pick up the brightest inner locations of the larger Gaussians, but, the correct size of the external mask to use surrounding this area is clearly debatable. An external mask which is too small will miss valuable structure but one that is too large will result in artificial structure, as mentioned above (also see Section 3.6.2 for a more quantitative analysis). Large Gaussians which are not included in the external mask will evidently be missed, especially faint objects, and there is already an appreciable amount of unrecovered emission (∼30%) missing from the unmasked and automasked Gaussians with FWHMs of only 3 beams (see the squares, triangles, and light blue circles).

Table 3.3 Summary of the *ast.zero_snr* and *ast.zero_snrlo* parameters tested. The *ast.zero_snr* parameter represents flux threshold for identifying astronomical signal. The *ast.zero_snrlo* parameter allows (or disallows if it is set to 0) identified sources with pixel values of at least the flux threshold defined by *ast.zero_snr* to expand in area until a second flux threshold is met. Bold font indicates the current GBS LR1 automasking parameters investigated in Section 3.5.

ast.zero_snr	*ast.zero_snrlo*	Gaussian FWHM
5	**0**	**7 beams**
5	3	7 beams
5	2	7 beams
3	2	7 beams

3.6 Other Reduction Considerations

3.6.1 Changing the Automask Parameters

To explore how an automasked reduction would differ using different thresholds for the AST model, we change the parameters *ast.zero_snr* (the threshold at which significant structure is identified) and the *ast.zero_snrlo* (the flux level of the surrounding pixels to which the identified significant peaks will be extended) using the GBS LR1 automask reduction method (see Table 3.3). Since the automask reduction accurately recovers compact structures over a broad range of these two parameters and borderline island detections are found within the extended emission, we only perform this analysis for 7 beam (105″) FWHM Gaussians. Note that setting the *ast.zero_snrlo* parameter to 0 does not allow any extension to flux levels lower than the threshold defined by *ast.zero_snr*.

Peak Intensity

In Figure 3.12, we compare four different automask reductions. The reduction using the original GBS LR1 automask parameters are shown in the top left and the other three reductions were performed with the *ast.zero_snr* and *ast.zero_snrlo* parameters in the *dimmconfig* file changed to the values shown. Clearly, when the *ast.zero_snrlo* parameter is not used, significant structure in faint sources is missed in the AST automask. When one allows identified structures with masked pixels (brightnesses above 5 σ_{rms}) to grow down to a level of 2 σ_{rms} or 3 σ_{rms}, however, much more of the expected Gaussian brightness is recovered, especially for the fainter input peaks. This

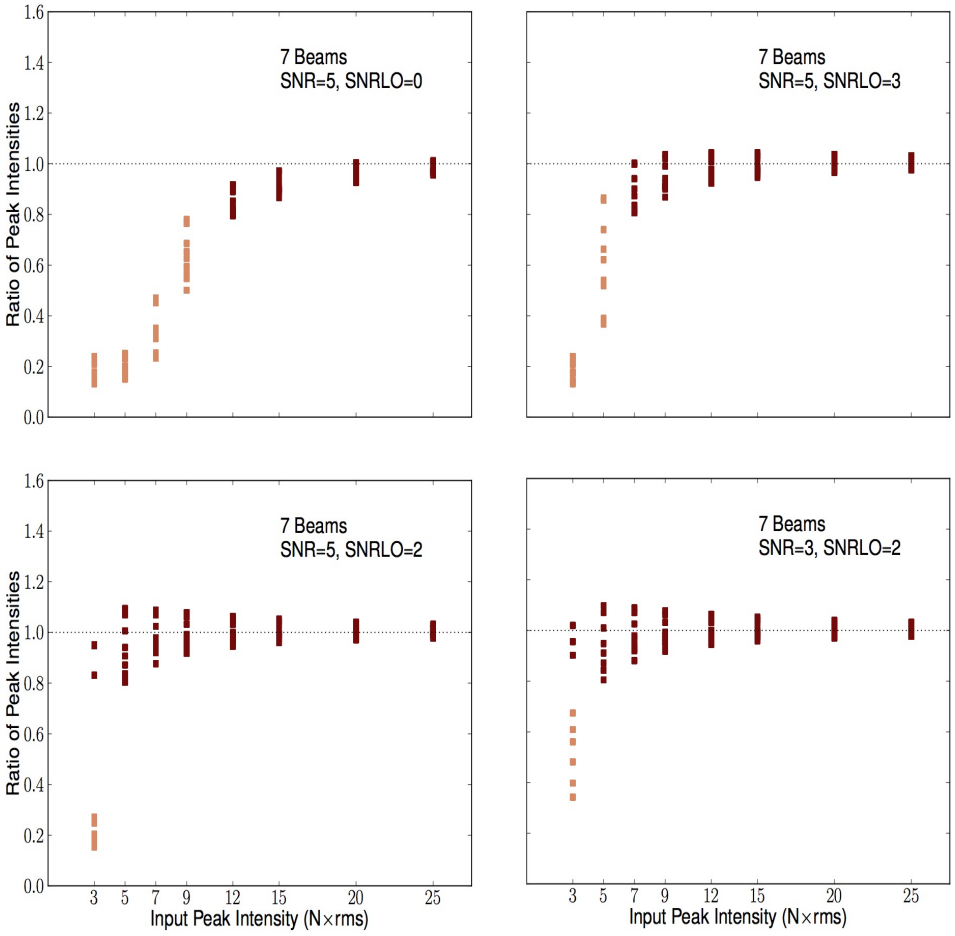

Figure 3.12 Artificial source recovery comparison for different GBS LR1 automask parameters: peak intensities. The ordinate represents the measured output peak intensity divided by the nominal input peak intensity. Light red indicates that the object had less than 50% of the pixels within one FWHM of the peak location detected in the AST mask, dark red indicates it had at least 50%. *Top left*: *ast.zero_snr* = 5, *ast.zero_snrlo* = 0, the original GBS LR1 automask parameters. *Top right*: *ast.zero_snr* = 5, *ast.zero_snrlo* = 3. *Bottom left*: *ast.zero_snr* = 5, *ast.zero_snrlo* = 2. *Bottom right*: *ast.zero_snr* = 3, *ast.zero_snrlo* = 2.

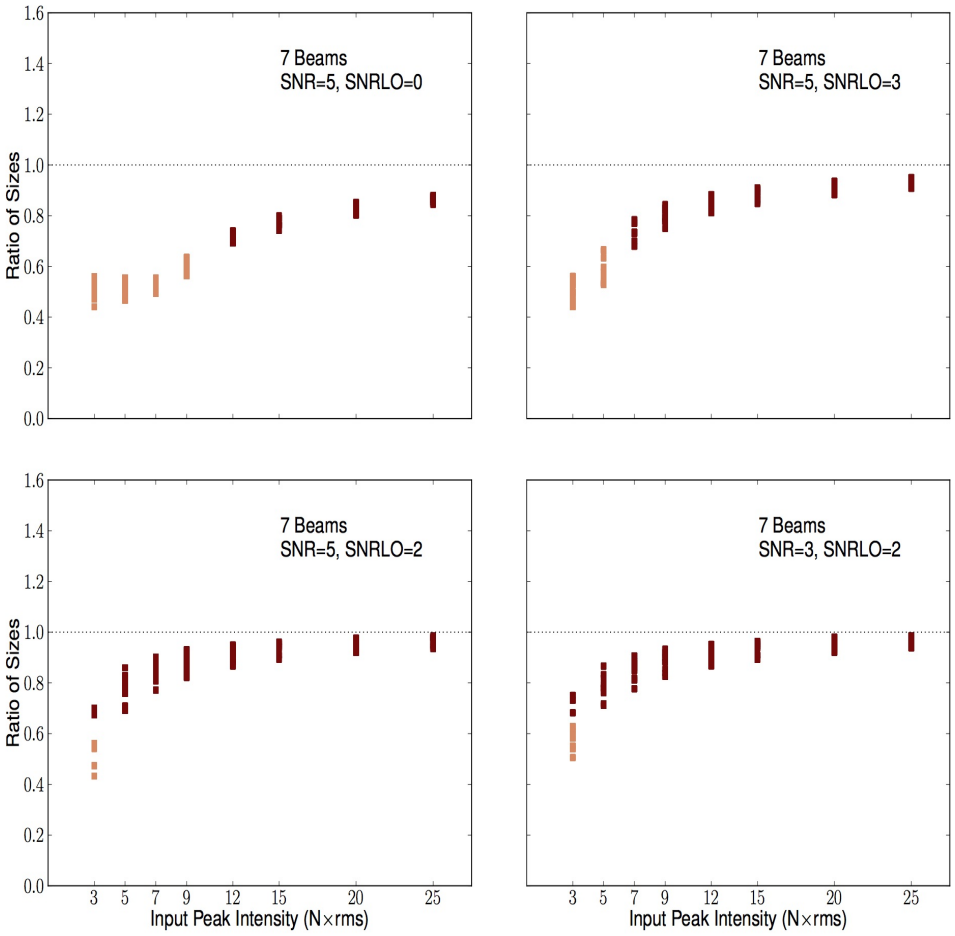

Figure 3.13 Artificial source recovery comparison for different GBS LR1 automask parameters: sizes. The ordinate represents the measured output size divided by the nominal input size. The plotting style follows Figure 3.12.

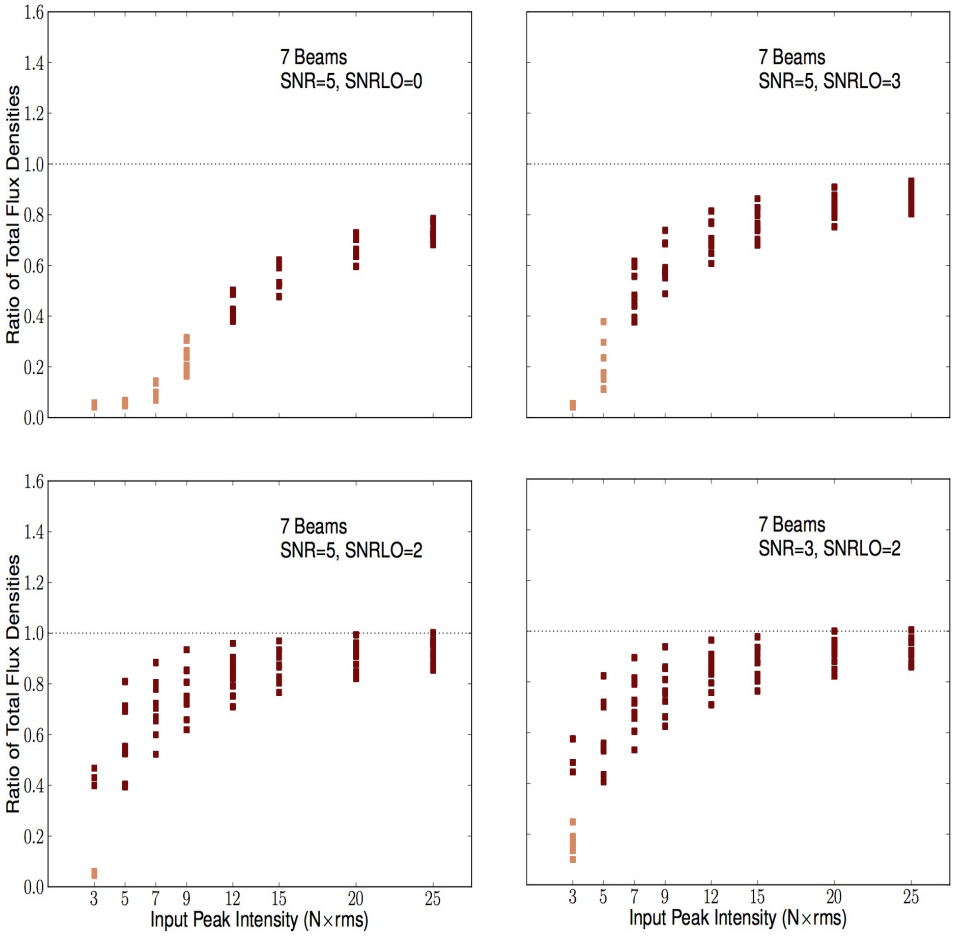

Figure 3.14 Artificial source recovery comparison for different GBS LR1 automask parameters: total flux densities. The ordinate represents the measured output total flux density divided by the nominal input total flux density. The plotting style follows Figure 3.12.

Table 3.4 Summary of the sizes of the square masks in the checkerboard style external mask tests. The "size" indicated here is the length of the sides of the square external masks placed over every second Gaussian. Bold font indicates the original external mask size investigated in Section 3.5.

Size of Square Patch in Checkerboard	Gaussian FWHM
4 beams	7 beams
12 beams	7 beams
20 beams	**7 beams**
36 beams	7 beams

improvement happens because when the constraint on the minimum flux included in the AST model is relaxed, more of the full Gaussian extent is identified as astronomical signal earlier in the iterative map making process, allowing more of the significant emission to be extracted from the noise.

Size and Total Flux Density

A similar trend is seen in the recovered sizes and total flux densities (Figures 3.13 and 3.14) as in the recovered peak brightnesses, above. When the *ast.zero_snrlo* parameter is set to zero, much of the expected emission lies outside the AST mask for fainter objects. When the automask is extended from the identified 5 σ_{rms} peaks down to a level of 2 σ_{rms} or 3 σ_{rms}, we see that more significant emission is recovered in the AST mask. As expected, the measured total flux density shows very similar results to the size of the Gaussian structures recovered by the automask.

3.6.2 External Mask Size

Due to the observed pedestals and bowls induced by the size of a masked region around a source, we perform a further test of the external mask reductions where we change the size of each mask in the checkerboard (see Figure 3.8). Table 3.4 outlines the different mask sizes explored, with bold font indicating the original external mask size used in the analysis presented in Section 3.5. Again, tests are performed only for the 7 beam FWHM Gaussians using the GBS LR1 external mask data reduction and in this case we only observed a pedestal effect (the bowls arose from different Gaussian grid configurations).

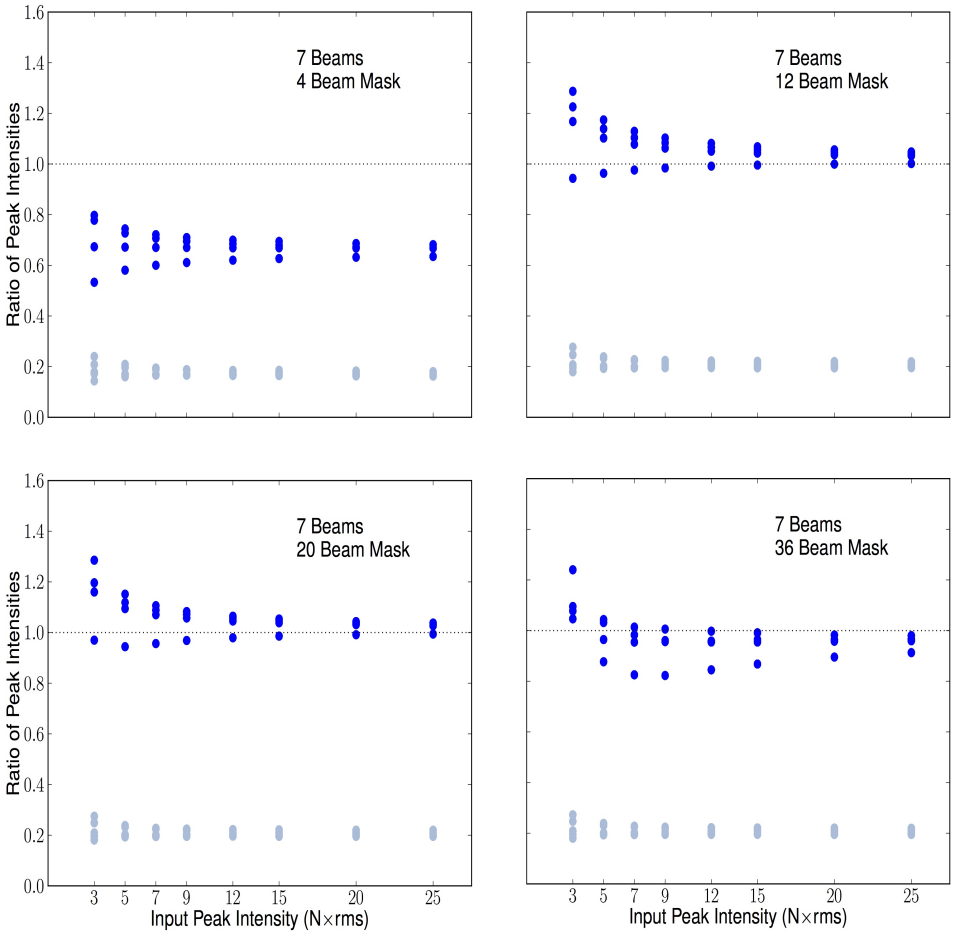

Figure 3.15 Artificial source recovery comparison for different external mask sizes: peak intensities. The ordinate represents the measured output peak intensity divided by the nominal input peak intensity. Light blue indicates that the object was outside the mask, dark blue indicates it was inside the mask. *Top left*: 4 beam masks. *Top right*: 12 beam masks. *Bottom left*: 20 beam masks (original). *Bottom right*: 36 beam masks.

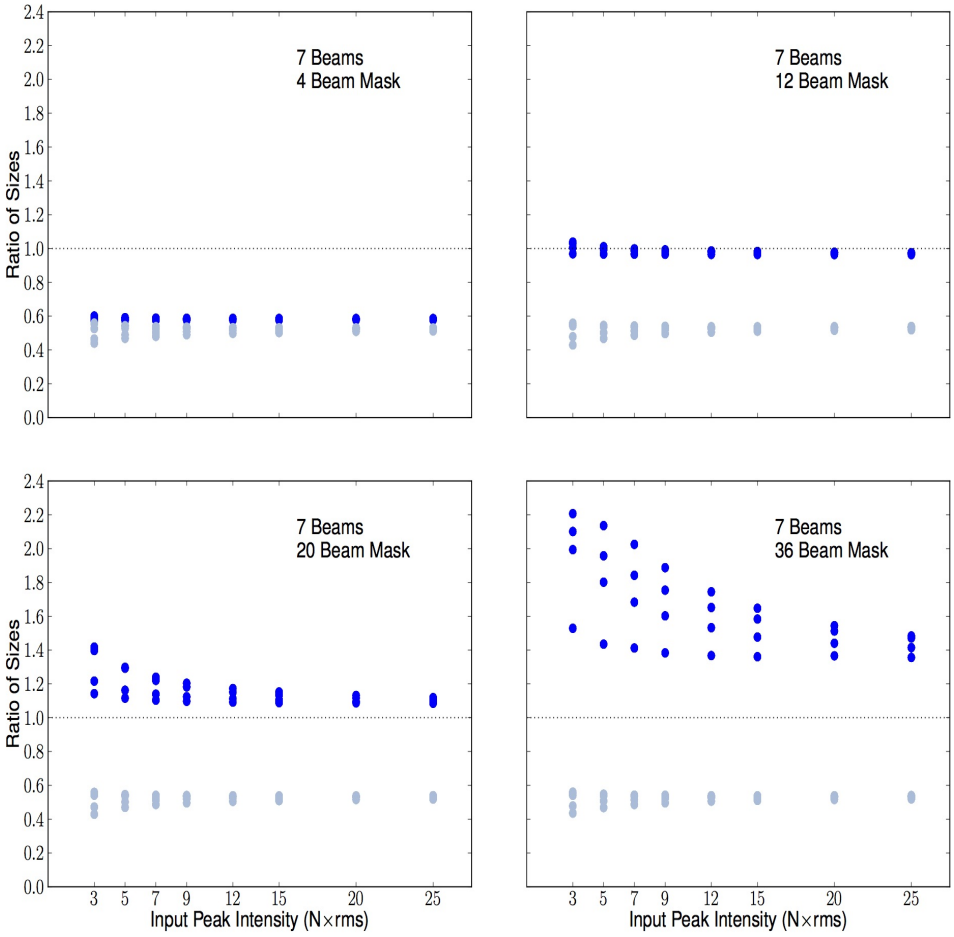

Figure 3.16 Artificial source recovery comparison for different external mask sizes: sizes. The ordinate represents the measured output size divided by the nominal input size; note the change in the ordinate's range from the figures above so the data points would be visible on all panels. The plotting style follows Figure 3.15.

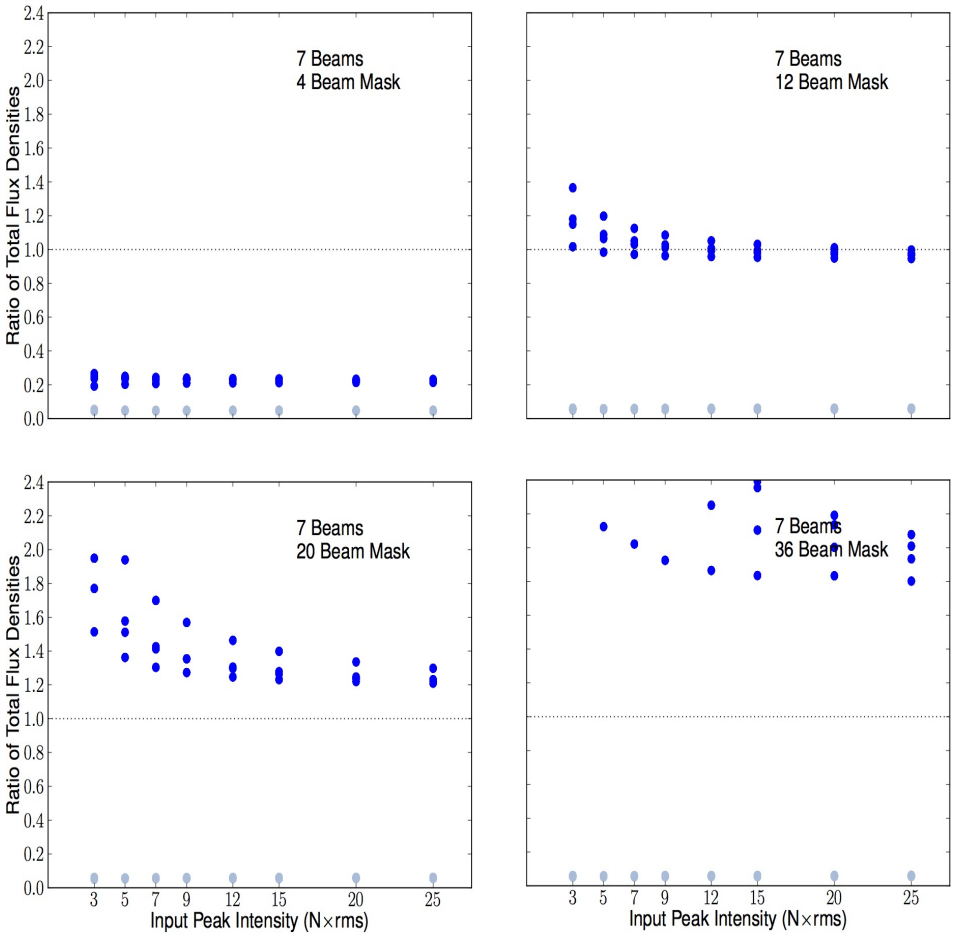

Figure 3.17 Artificial source recovery comparison for different external mask sizes: total flux densities. The ordinate represents the measured output total flux density divided by the nominal input total flux density; note the change in the ordinate's range from the figures above so the data points would be visible on all panels. The plotting style follows Figure 3.15.

Peak Intensity

In Figure 3.15, we see that the application of different sizes of external masks can play a key role in the extracted data. For the small, 4 beam mask cases, much of the flux is suppressed since the Gaussian FWHM itself is almost double the mask size. Once the mask is larger than the Gaussian, however, we see that the expected peak intensity of the object is returned reasonably well, even in the faintest cases. For masks larger than 4 beams, we see the introduction of artificial structure (up to $\sim$30%) and a higher uncertainty for the fainter sources as the pedestal effect increases for larger masks. Brighter peaks in general result in more accurate measurements, as expected, since more of the Gaussian emission will be more significant relative to the noise.

Size and Total Flux Density

Again, in the size and total flux density plots (Figures 3.16 and 3.17) we see similar results to the peak intensities discussed above. In the smallest 4 beam mask case, we see tightly constrained recoveries that miss the outer emission. This result is expected because we are focusing on the brightest region of each Gaussian. A tighter mask that is large enough to cover the whole source (e.g., 12 beams in our case) produces the best results. It is clear that uncertainties grow rapidly for the faint sources. Also, in the 36 beam mask case, the brighter objects are also affected by artificial large-scale structure introduced by *makemap*. Ideally, the mask should just encompass the source with little background flux at the edges to ensure none of the fainter extended emission is missed and that no substantial noise is included in the external mask. By using an external masking procedure based on a rigorous analysis for each individual region observed by the GBS, it is unlikely that the 850 μm maps produced for the GBS LR1 reduction will suffer from mask areas overestimated by much greater than twice the size of the source. Thus, the reduction performed with the 12 beam external mask masks in this section shows the closest example to the real GBS LR1 data. The measured total flux density shows very similar behaviour to the size plots, as expected.

3.7 Data Reduction and Common Physical Measurements

Evidently, the JCMT LR1 and GBS LR1 data reduction methods recover different amounts of extended structure. In this section, we qualitatively discuss the impact of using these different data reduction techniques on two common physical measurements in star-forming regions: 1. the core mass function (CMF) and 2. the derivation of the temperature. Note that in any project, the reduction method should be chosen based upon the specific scientific goals one is researching with an understanding of the benefits as well as the drawbacks offered by that method.

3.7.1 The Core Mass Function

There have been many studies on the mass distribution of core populations derived from the flux due to dust in nearby star forming regions (for examples, see Johnstone et al. 2000b, Ward-Thompson et al. 2007a, Enoch et al. 2008, and Sadavoy et al. 2010a). Although this measurement is intrinsically dependent on the core identification algorithm used, specifically in the ways that boundaries are drawn around cores, the type of data reduction employed can also inform the final results. Along with the definition of the AST mask, the main reduction parameters under consideration when analysing the mass of extended objects are those which govern the time stream filtering and the common mode low-frequency noise removal.

In the optically thin ($\tau << 1$), isothermal limit, the dust emission traces the mass of a given object. A generally accepted result is that the more massive objects are not just brighter but also larger (see, for example, Sadavoy et al. 2010a's Figure 12). With harsh filtering criteria like those employed in the JCMT LR1 reduction, the most extended structure is not recovered and the AST mask consists of fairly tight boundaries around the most concentrated, compact regions of the map. The common mode noise is also estimated over each individual subarray, limiting the size of confidently detected structure to $200''$. This may not result in an accurate assessment of the population of core masses as any larger objects will be "missing" flux. Thus, since larger objects correlate with larger intrinsic masses, the core mass function may be steepened.

The GBS LR1 is a much more robust reduction technique to use for determining core mass functions when compared to the JCMT LR1 assuming the same core iden-

tification algorithm. The larger size over which the common mode is estimated, the more relaxed filtering parameters, and the greater number of iterations performed work to recover much more significant structure than just the compact sources. The two-stage masking process is also highly beneficial for measurements like the core mass distribution. This ensures that two passes are taken at recovering the maximum amount of structure, including a robust analysis that is not automated. To improve this even further, we have suggested that the next generation of the GBS data reduction be performed with different *ast.zero_snr* and *ast.zero_snrlo* parameters to potentially recover more faint structure (see Sections 3.6.1 and 3.8). Of course, as previously discussed, large-scale modes will still be removed from the final map so it is very important to ensure that this is taken into account. Comparing the SCUBA-2 data with Herschel Space Observatory data is one method that can be used for better understanding the large-scale structure present in a given region.

3.7.2 Derivation of the Temperature with SCUBA-2

Another common measurement performed with SCUBA-2 data involves the temperature maps produced by calculating the 850μm/450μm intensity ratio, or against other data sets (such as the Herschel Space Observatory). In order to perform this measurement, the beams should be matched between the two data sets and the filtering parameters as well as the masks should be identical. The large-scale noise present in each individual map, however, will differ and this uncertainty becomes very important when comparing two maps.Preliminary work performed by GBS team members (Hatchell & Rumble, private communication; also see Hatchell et al. 2013) based on the GBS LR1 reduction suggests that including structures larger than 300$''$ indeed leads to unrealistic ratios between 850μm and 450μm. In order to perform confident measurements, that data must be post-processed with a tighter filter so that only the inner regions of these large objects have accurate associated temperatures.

When determining the extent of the trustworthy temperature calculation, the profile of the structure itself must also be taken into consideration. It will be very difficult to measure accurate ratios on large, faint emission due to the subtraction of large-scale modes. Again, because of the harsh filtering parameter and the common mode removal (see Section 3.7.1, above), the JCMT LR1 reduction method would be appropriate for studying the temperatures of bright, compact objects. Calculating a temperature map for any emission that lies a significant distance from peaked

structure relative to the sub-array footprint ($< 200''$) would be very uncertain. In addition, it is important to consider that the signal to noise ratio is typically lower in the SCUBA-2 450μm data set (compared to the 850μm data) so artificial structure is likely to be more prominent in these observations.

3.8 Conclusions

In this paper, we have presented and compared two methods of data reduction: the JCMT LR1 reduction (Graves et al. in prep.) and the GBS LR1 reduction (Kirk et al. in prep.) which both employ the *makemap* algorithm (Chapin et al., 2013) executed with different configurable parameters. We used data from the Orion A South star forming region (Mairs et al., 2016) to characterise the differences in the scale of the emission and the source morphology recovered by the two methods. We have measured source peak intensities, total flux densities, and radii across three representative regions for each reduction method and compared the results both qualitatively and quantitatively. To further our investigation, we created a series of artificial Gaussians (varied in size and peak brightness) and inserted them into the time domain of a pure noise field using each data reduction method. We then recovered each source using a Gaussian fitting algorithm and compared the measured properties to the nominal input values to observe how much emission was preserved at each scale. Note that although inserting Gaussians into the time stream is an effective way to gain insight into the data reduction process, real structures present in the GBS maps are non-Gaussian and in fact most regions display complex multi-scale structure. To summarise our main conclusions, we find:

1. Both reductions recover the peak intensities of bright compact sources (sources with FWHMs of 3 beams or less and a peak brightness of at least 7 σ_{rms}) to within 10-20% of the true value. The GBS LR1 reduction also accurately recovers the peak intensities of the larger Gaussians whereas the peaks produced by the JCMT LR1 reduction are diminished because of the stringent filtering parameters. As expected, there is more uncertainty in the size and total flux density measurements for both reductions (see below). In general, we see more accurate results for objects which are both brighter and more compact.

2. Although the JCMT LR1 reduction only recovers compact emission present in a

given region and the GBS LR1 reduction recovers the extended structure, the two reduction methods trace the same general areas of significant signal very closely. The JCMT LR1 reduction's diminished extended structure, however, causes island identification algorithms to break up large areas into many smaller objects. Conversely, the GBS LR1 reduction draws out these locations of extended emission and, thus, much more emission can be recovered. These differences are illustrated in Figures 3.2 to 3.4.

3. For faint objects larger than a point source, only a fraction of the true size (and, therefore, total flux density) originally present in an artificial Gaussian is recovered without an external masking procedure. The larger the object, the brighter it must be for an automask detection. In the GBS LR1 automask data reduction, Gaussians with a FWHM of 7 beams must have a peak brightness of 5 σ_{rms} for the peak intensity to be measured to within ∼20%. To measure the total flux density to within 20% of the nominal value, a peak brightness of greater than 25 σ_{rms} is required. For a Gaussian with a FWHM of 7 beams, the JCMT LR1 reduction will never result in *jsa_ catalogue* being able to measure a source's peak intensity or total flux density to within 20% accuracy of the nominal value due to the inherent filtering of large spatial scales. See Section 3.5.1 and Figures 3.9 through 3.17.

4. When identifying objects with the automask employed in the GBS LR1 automask reduction, the most accurate Gaussian parameters are measured when nearby pixels are incorporated by extending to lower flux values. For improved reductions, e.g. GBS Legacy Release 2 (GBS LR2), we recommend setting the *ast.zero_ snrlo* parameter to a value of 2. Similarly, the *ast.zero_ snr* parameter should be set to 3. See Section 3.6.1 for details. One must, however, be cautious when extending the AST mask around significant peaks down to a lower flux threshold as artificial structure could be introduced around noise spikes. Fortunately, in the variety of automask tests performed, there was no significant evidence of any artificial structure outside of the Gaussians being included in the AST model.

5. The external mask used in the GBS LR1 reduction can increase or decrease the brightness of compact peaks depending on the surrounding region. Thus, in some cases where an incorrect external mask size is used, the JCMT LR1 reduction and the GBS LR1 reduction can even differ a little on compact scales (see Figures 3.2

to 3.6). Artificial structure in the data caused by a poorly sized external mask can act as pedestals and bowls, affecting the peak intensity, the size, and the total flux density measured for a given object. A mask that is too small will only highlight compact regions embedded within larger extended emission. A mask that is too large will include noise variations in the AST mask. A reasonable external mask should cover a given source in its entirety and extend a small distance into the noise. It should, however, be less than a factor of 2 larger than a source which was reliably recovered by the automask reduction in order to achieve 20% accuracy in total flux density (see Section 3.5.1 for a discussion on trustworthy scales). In Section 3.6.2, we find that this is possible even for faint, large sources.

Chapter 4

The First Look at Southern Orion A with SCUBA-2

"And I can't look away.
I am captivated.
What else can I say
But sing in adoration..."
-Phil Whickam, Starmaker

4.1 Foreword

After studying and improving the data reduction methods, understanding the successes and limitations of the conversion between raw power received by the SCUBA-2 instrument and the final image produced by the Gould Belt Survey pipeline, I could now begin to robustly analyse the dust emission in the Orion A Molecular Cloud. As part of the policies and procedures put forth by the GBS survey leaders, each observed molecular cloud was given to a consortium member or a small subgroup of members to analyse. Subsequently, the team began releasing a series of "first-look" papers which catalogue the robust objects in a given region while presenting unique analyses of the observed targets based on the primary authors' interests and areas of expertise. The Orion A Molecular Cloud was subdivided into two regions and I led

The material presented in this chapter (excluding the foreword) has been published in Monthly Notices of the Royal Astronomical Society: Mairs et al. 461, 4022, 2016. DOI: 10.1093/mnras/stw1550.

the analysis on the Southern extent.

One of my main goals throughout my graduate work and a theme of this dissertation has been to characterise both the extended and compact structure present in submillimetre continuum maps and highlight the connection between the large-scale and small-scale components. Thus, I approached the Southern extent of the Orion A Molecular Cloud, a region rich with thermal dust emission structures and young stellar objects with this as my motivation. The analysis of localised structure depends on the separation of the large-scale, underlying cloud emission from the dense regions which we study. There are many different algorithms which identify significant, dense structures freely available to apply to submillimetre data (for examples, see GaussClumps Stutzki & Guesten 1990; ClumpFind Williams et al. 1994; Astrodendro Rosolowsky et al. 2008; GETSOURCES Men'shchikov et al. 2012; and FellWalker Berry 2015). Each program, however, will break up large-scale structures or amalgamate smaller ones in different ways. A full summary comparing and contrasting different algorithms could be the topic for a PhD dissertation in itself. Here, I will briefly introduce my main structure identification methodology for this chapter which uses the ClumpFind (Williams et al., 1994) and FellWalker (Berry, 2015) algorithms.

ClumpFind is a useful algorithm that contours the data down to a user-defined sensitivity. In its default mode, ClumpFind identifies regions of significant emission in a top-down manner by starting at the brightest peak and contouring the data using progressively fainter values. Isolated peaks are numbered in order of brightness and when two "clumps" merge at a sufficiently low contour value, the pixels along the clump boundaries are assigned to the nearest peak using a friends-of-friends algorithm. In this chapter, I used ClumpFind only to select the largest significant structures in the map by forcing it to contour the data at a single value (3 times the root mean square noise in the map) while discarding sources smaller than the size of the JCMT beam. I refer to the ClumpFind identified emission as *Islands* (see Figure 4.4).

Next, I identified the smaller-scale, peaked structures using an implementation of the FellWalker algorithm which is tuned to identify compact, localised emission. This algorithm considers each pixel in a given image and identifies the steepest gradient up to an emission peak (see Figure 4.1). After performing tests to ensure that the peak is "real" and not just a noise spike, the local maximum is assigned an identifying integer and all the pixels above a user-defined threshold that were included in the path to the peak are given the same identifier. In this way, all of the robust peaks in the

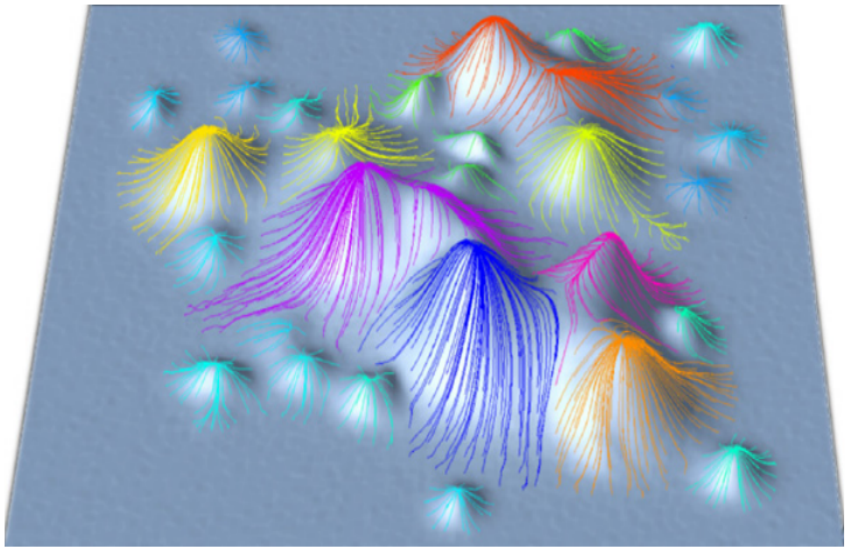

Figure 4.1 A visual representation of the different peaks and associated extended structures identified by the FellWalker algorithm. The "walks" up each slope are colour coded to show which paths are connected to define each individual, isolated structure. This Figure is taken from Berry (2015).

image are catalogued and the structure associated with each peak can be analysed. Very similar structure to the ClumpFind algorithm is extracted, but FellWalker is able to subdivide the larger *Island* structures into smaller-scale components. For this reason, I call the FellWalker identified sources *Fragments*.

In this paper (Mairs et al., 2016), I present catalogues of all of the significant emission structures in the Southern Extent of the Orion A Molecular Cloud, focussing on the fragmentation of *Islands* into more localised *Fragments*. Considering these two populations of objects separately, I perform stability analyses, characterise the morphologies of the objects, identify interesting case studies for possible Super-Jeans starless cores (relating back to Chapter 2), and put this intermediate-scale structure in context by comparing it with larger-scale extinction maps derived from infrared observations and YSO catalogues constructed using *Spitzer Space Telescope* and *Herschel Space Observatory* data (Megeath et al., 2012; Stutz et al., 2013; Dunham et al., 2015). By correlating the previously derived YSO positions with submillimetre dust emission, I comment on the likely misclassification of a significant number of candidate protostars and construct a simple model to recreate the spatial distribution of YSOs with respect to *Fragments*. By combining this latter analysis with information from simulations (Frimann et al., 2016) and observations in different star forming environments (Jørgensen et al., 2007), I provide evidence for a velocity gradient across YSO classes. These are examples of the types of analyses possible when cross-comparing multi-wavelength datasets to reveal larger- and smaller-scale structures. This work is fundamental to understanding the physical connection between protostars and their nascent environments. The analyses I performed here went on to inform the methods employed in the first look investigation of the molecular cloud IC5146 (Johnstone et al., 2017) and prompted a consistent multi-cloud comparison across the Gould Belt SCUBA-2 targets (Lane et al. in preparation).

Abstract

We present the JCMT Gould Belt Survey's first look results of the southern extent of the Orion A Molecular Cloud ($\delta \leq -5$:31:27.5). Employing a two-step structure identification process, we construct individual catalogues for large-scale regions of significant emission labelled as *islands* and smaller-scale subregions called *fragments* using the 850 μm continuum maps obtained using SCUBA-2. We calculate object masses, sizes, column densities, and concentrations. We discuss fragmentation in terms of a Jeans instability analysis and highlight interesting structures as candidates for follow-up studies. Furthermore, we associate the detected emission with young stellar objects (YSOs) identified by *Spitzer* and *Herschel*. We find that although the population of active star-forming regions contains a wide variety of sizes and morphologies, there is a strong positive correlation between the concentration of an emission region and its calculated Jeans instability. There are, however, a number of highly unstable subregions in dense areas of the map that show no evidence of star formation. We find that only $\sim$72% of the YSOs defined as Class 0+I and flat-spectrum protostars coincide with dense 850 μm emission structures (column densities $> 3.7 \times 10^{21}$ cm^{-2}). The remaining 28% of these objects, which are expected to be embedded in dust and gas, may be misclassified. Finally, we suggest that there is an evolution in the velocity dispersion of young stellar objects such that sources which are more evolved are associated with higher velocities.

4.2 Introduction

The James Clerk Maxwell Telescope's (JCMT) Gould Belt Legacy Survey (GBS, Ward-Thompson et al. 2007c) is a large-scale project which has mapped the notable star-forming regions within 500 pc of the Sun such as Orion A (Salji et al., 2015a) and Orion B (Kirk et al., 2016b), Taurus (Buckle et al., 2015), Ophiuchus (Pattle et al., 2015), Serpens (Rumble et al., 2015), Auriga-California (Broekhoven-Fiene et al., submitted), and Perseus (Chen et al., accepted), in 450 μm and 850 μm continuum emission as well as ^{12}CO, ^{13}CO, and C^{18}O spectral lines (see Buckle et al. 2012 and references therein). In this paper, we present the first results from the Southern Orion A region observed at 850 μm with the Submillimetre Common-User Bolometer Array 2 (SCUBA-2) instrument (Holland et al., 2013).

Southern Orion A is a 2.8° x 3.9° region within the Orion cloud complex, predominantly composed of the L1641 cloud, which is an active star-formation site approxi-

mately 450 pc (see Muench et al. 2008 for a detailed review of the distance to Orion) from the Sun. The southern tip of the L1640 cloud to the north, however, is also included (i.e., the region south of $\delta \leq -5{:}31{:}27.5''$). Northern Orion A is arguably the most well-studied nearby star-forming region, as it is home to the Orion Nebula and the integral shaped filament (ISF; Bally et al. 1987, Johnstone & Bally 1999; also see Salji et al. 2015b and Salji et al. 2015a for a GBS analysis of Orion A North). The Southern Orion A region, however, is also an area of interest, showing several different stages of low- and intermediate-mass star and cluster formation (see Chapter 20 of Reipurth 2008).

The most southern declinations observed in this study (-7°:00′ to -9°:25′) have received less focus in previous literature than the northern section of the cloud. There is, however, still a wealth of data available. For example, Bally et al. (1987) analysed extensive ^{13}CO maps observed with the AT&T Bell Laboratories 7 m antenna and noted that the L1641 cloud was concentrated into a filamentary structure down to -9° in declination with a north-south velocity gradient (see Allen & Davis 2008 and references therein for a thorough review of L1641).

The detected emission in Southern Orion A includes OMC-4, OMC-5, and L1641N, several active sites of Galactic star formation close to the Sun. It contains dozens of embedded sources (Johnstone & Bally 2006; Chen et al. 1996; Ali & Noriega-Crespo 2004), the NGC 1999 reflection nebula and its associated A0e star V380 Ori (Stanke et al. 2010; Johnstone & Bally 2006), as well as the famous Herbig-Haro objects (Herbig, 1960) HH 34, HH 1/2, and HH 222 with their sources and their prominent, young outflows (Johnstone & Bally 2006; Stanke et al. 2002; Reipurth et al. 2002; Reipurth et al. 2013). Observations of the cold dust emission from (sub)millimeter detectors, however, are generally limited at the lower declinations in Southern Orion A. Facilities, such as the Caltech Submillimetre Observatory (CSO) or the IRAM 30 m Telescope, have mainly focused on the Orion BN-KL complex or the Orion Bar, and have thus only sparsely sampled these lower declinations (see, for examples, Li et al. 2007, Vaillancourt et al. 2008, Berné et al. 2014, Cuadrado et al. 2015, and references therein). As such, most of the early submillimeter continuum observations of Southern Orion A were made with SCUBA-2's predecessor, SCUBA (Di Francesco et al. 2008b; Nutter & Ward-Thompson 2007; Johnstone & Bally 2006). Indeed, these SCUBA observations revealed many clumps toward Southern Orion A for the first time.

The SCUBA-2 observations presented here, however, have a sensitivity which

is an order of magnitude deeper than the maps presented in Johnstone & Bally 2006 along with a much wider spatial coverage (8100 arcmin^2 compared to 2300 arcmin^2 in the original Southern Orion A SCUBA data). Thus, we have a much better diagnostic to characterize the dense, cold dust in Southern Orion A. To complement these new continuum observations of dense, often gravitationally unstable gas, we use extinction data taken in the J, H and K bands that were determined from the Near-infrared Color Excess (NICE) team (M. Lombardi, private communication, July 18th, 2015), and the young stellar object (YSO) catalogues of Megeath et al. (2012) and Stutz et al. (2013) obtained using the *Spitzer Space Telescope* and the *Herschel Space Observatory*, respectively. The correlation between YSOs of different classes and the observed gas and dust structure is a powerful tool that can be used to help discern the dominant physical processes which influence star formation. Analysing the locations of protostars and their more-evolved counterparts with respect to the gas and dust in a molecular cloud is imperative for studying a variety of topics including cluster formation and the effect of feedback on the star-formation process.

In Section 4.3, we summarise the observations and data reduction methods employed in this study. In Section 4.4, we display the 450 μm and 850 μm SCUBA-2 maps of Southern Orion A, present our structure identification procedure, and discuss the population of objects in terms of larger-scale extinction, Jeans stability, and concentration. In Section 4.5, we examine the associations between YSOs and dense continuum structure. We also investigate fragmentation as observed in the continuum data in terms of its effect on star formation and note interesting candidates for follow-up studies. We conclude this section with a discussion on the spatial distribution of young stellar objects, and we construct a simple model to understand the widespread locations of young stars across Southern Orion A. Finally, in Section 4.6, we summarise our main results.

4.3 Observations and Data Reduction

The observations presented throughout this paper were performed using the SCUBA-2 instrument (Holland et al., 2013) as part of the JCMT Gould Belt Survey (Ward-Thompson et al., 2007c). This instrument has provided continuum coverage at both 850 μm and 450 μm simultaneously at effective beam sizes of 14.1$''$ and 9.6$''$, respectively (Dempsey et al., 2013). In this work, we present Southern Orion A in both wavelengths, but focus mainly on the 850 μm data for analysis. All of the observa-

tions were taken in the PONG1800 mapping mode (Kackley et al., 2010), yielding circular maps ("PONGs") of $\sim$0.5° in diameter. There are seventeen 0.5° subregions across the Orion A Molecular Cloud, thirteen of which cover Southern Orion A. These locations were individually observed four to six times throughout February 2012 to January 2015, and were then co-added (once co-added, these structures are referred to as "tiles") and mosaicked to form the final map. The tiles slightly overlap to provide a more uniform noise level throughout the whole of the Orion A Molecular Cloud. For a summary of the typical noise present in each tile after contamination from CO(J=3-2) has been removed (see the discussion below and the Section 4.7), see Table 4.1. All observations were taken in dry weather ($\tau_{225\,\mathrm{GHz}} < 0.08$) and two PONGs were taken in very dry weather ($\tau_{225\,\mathrm{GHz}} < 0.05$). To define the northern boundaries of the Southern Orion A region, a cut-off was then applied at $\delta = -5{:}31{:}27.5$ so that the northern half of integral shaped filament, including the Orion Nebula Cluster (ONC), was not included in this analysis. For analyses performed on Orion A North, which slightly overlaps with this region (OMC-4 is in both the Orion A North map as well as the Southern Orion A map), see Salji et al. (2015b) and Salji et al. (2015a).

The data reduction procedure was performed using the iterative map-making technique MAKEMAP (explained in detail by Chapin et al. 2013) in the SMURF package (Jenness et al. 2013) found within Starlink (Currie et al. 2014). The 850 μm continuum image studied here is part of the GBS LR1 release (see Mairs et al. 2015, for an overview). In this data release, after the iterative map-making procedure was performed for each observation, the individual maps were co-added for a higher signal-to-noise ratio (SNR) and the resulting image was used to define regions of genuine emission. A mask was constructed with boundaries defined by an SNR of at least 2. This mask was used to highlight emission regions and perform a second round of data reduction to recover better any faint and extended structure[1]. The map is gridded to 3″ pixels (as opposed to the GBS Internal Release 1 (IR1) reduction method where the pixels were 6″) and the iterative solution converged when the difference in individual pixels changed on average by $<$0.1% of the rms noise present in the map. The final mosaic was originally in units of picowatts (pW) but was converted to mJy arcsec^{-2} using the 850 μm aperture flux conversion factor 2.34 Jy pW^{-1} arcsec^{-2} and 4.71 Jy pW^{-1} arcsec^{-2} at 450 μm (Dempsey et al., 2013).

[1]Note that the boundaries employed in this paper are more conservative than those used in Mairs et al. (2015). The same SNR was used to identify significant structure, but in this analysis, no smoothing was applied to the boundaries whereas in the analysis of Mairs et al. (2015), the boundaries were smoothed to incorporate more diffuse structure.

Table 4.1 A summary of the typical noise present in each of the seventeen publicly available tiles which comprise the Orion A Molecular Cloud. Contamination from CO has been removed in the 850 μm images.

Tile Name	Central R.A. (J2000)	Central Dec (J2000)	850 μm Noise (mJy beam^{-1})	450μm Noise (mJy beam^{-1})
OMC1_TILE1	5:34:18	-5:09:58	4.0	58
OMC1_TILE2	5:34:57	-5:40:00	3.7	39
OMC1_TILE3	5:36:22	-5:16:56	3.7	34
OMC1_TILE4	5:35:50	-4:46:06	3.6	39
OMC1_TILE56	5:35:44	-6:07:25	3.7	53
OMC1_TILE7	5:36:12	-6:31:30	3.1	34
OMC1_TILE8	5:36:45	-7:02:26	3.5	63
OMC1_TILE9	5:38:16	-6:39:56	3.2	67
OMC1_TILE10	5:38:48	-7:10:27	3.4	63
OMC1_TILE11	5:40:06	-7:33:22	3.0	43
OMC1_TILE12	5:40:58	-8:00:26	3.3	67
OMC1_TILE13	5:42:48	-8:16:14	3.3	63
OMC1_TILE14	5:40:58	-8:32:13	3.4	58
OMC1_TILE15	5:42:49	-8:47:54	3.4	53
OMC1_TILE16	5:40:57	-9:03:53	3.3	53
OMC1_TILE17	5:33:09	-5:37:46	3.3	43

These measurements of the 850 μm and 450 μm noise levels are based a point source detection using pixel sizes of 3″ and 2″, respectively, and beam FWHM values of 14.1″ and 9.6″, respectively.
Note that four of the observations were taken during SCUBA-2 science verification. They can be found in CADC under the project code 'MJLSG22'

The CO(J=3-2) emission line contributes to the flux measured in these 850 μm continuum observations (Johnstone & Bally 1999, Drabek et al. 2012). As Drabek et al. (2012) and Coudé et al. (2016) discuss, however, this line generally contributes low-level emission to continuum observations ($\leq$ 20%) with only a few sources associated with stellar outflows having anomalously high contamination ($\sim$ 80%); see Section 4.7 for our own analysis of the CO(J=3-2) contamination in Southern Orion A. After the 850 μm map was produced, therefore, we subtracted the CO(J=3-2) emission line from the continuum map using ancillary GBS data.

In the following, the 850 μm map refers to the data from which the CO(J=3-2) emission line has been subtracted. The final SCUBA-2 maps are not sensitive to large-scale structures as these are filtered out during the data reduction (Chapin et al., 2013). For an overview of the GBS LR1 filtering parameters as well as results from testing the completeness of this method using artificial sources, see Mairs et al. (2015). Briefly, a spatial filtering scale of 10′ is applied to all the data residing outside the SNR-defined mask. This means that small-scale sources (<5′) are confidently recovered but larger-scale structures between 5′ and 10′ will have missing flux. The severity of this problem depends on the emission structure of the source, the size of the SNR boundary drawn around it during the data reduction, and the inherent background structure of the map. The filter will subtract out of the map any large, faint modes causing the total, observed flux of sizeable objects that have compact, bright components to be underestimated.

4.4 Structure Within Southern Orion A

In Figures 4.2 and 4.3, we present the full 850 μm and 450 μm maps of Southern Orion A, respectively. Note that the northern boundary we have chosen (δ = −5:31:27.5) includes the "V-shaped" OMC-4. This southern extension of the Orion A Giant Molecular Cloud (GMC) is less confused than its northern locations (e.g. the ISF) but it still shows a diverse set of objects defined by localised emission. It is, therefore, an intriguing location to study the initial stages of star formation at submillimetre wavelengths.

There are many locations of interest across these maps, several of which are displayed as insets in Figure 4.2. Even a cursory glance across the structure reveals a wealth of shapes and sizes of significant emission. Broadly speaking, there are no notable differences in the locations of emission structure between the 850 μm and

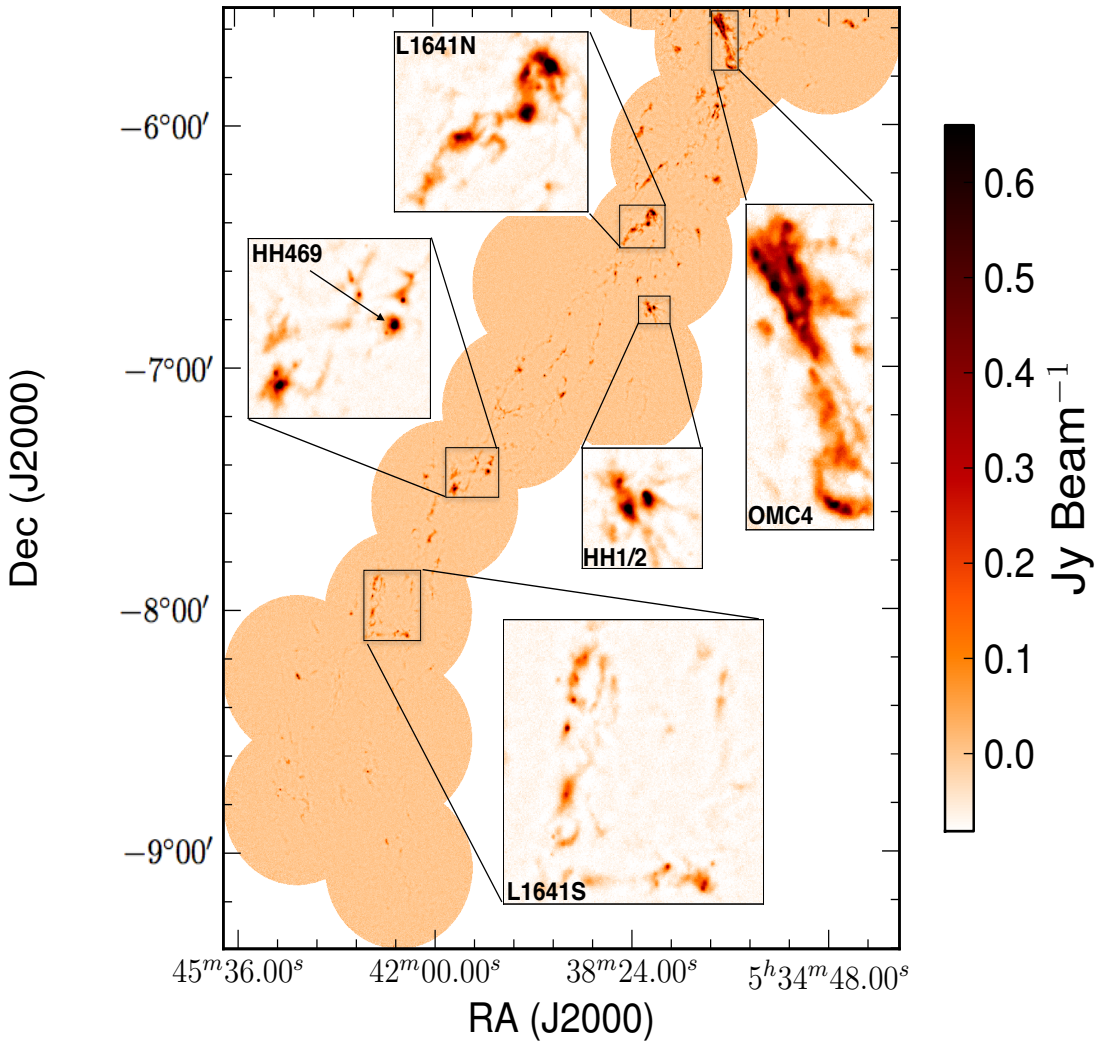

Figure 4.2 The 850 μm SCUBA-2 map of the GBS-defined Southern Orion A region. Several areas of significant emission are highlighted as insets in the main image. These include the "V-shaped" OMC-4 structure at the northern tip of the map (Johnstone & Bally, 1999), HH 1/2 (Johnstone & Bally 2006; also see Herbig 1951, Haro 1952, and Haro 1953), HH469 (Aspin & Reipurth, 2000), L1641-N, and L1641-S (Fukui et al., 1986).

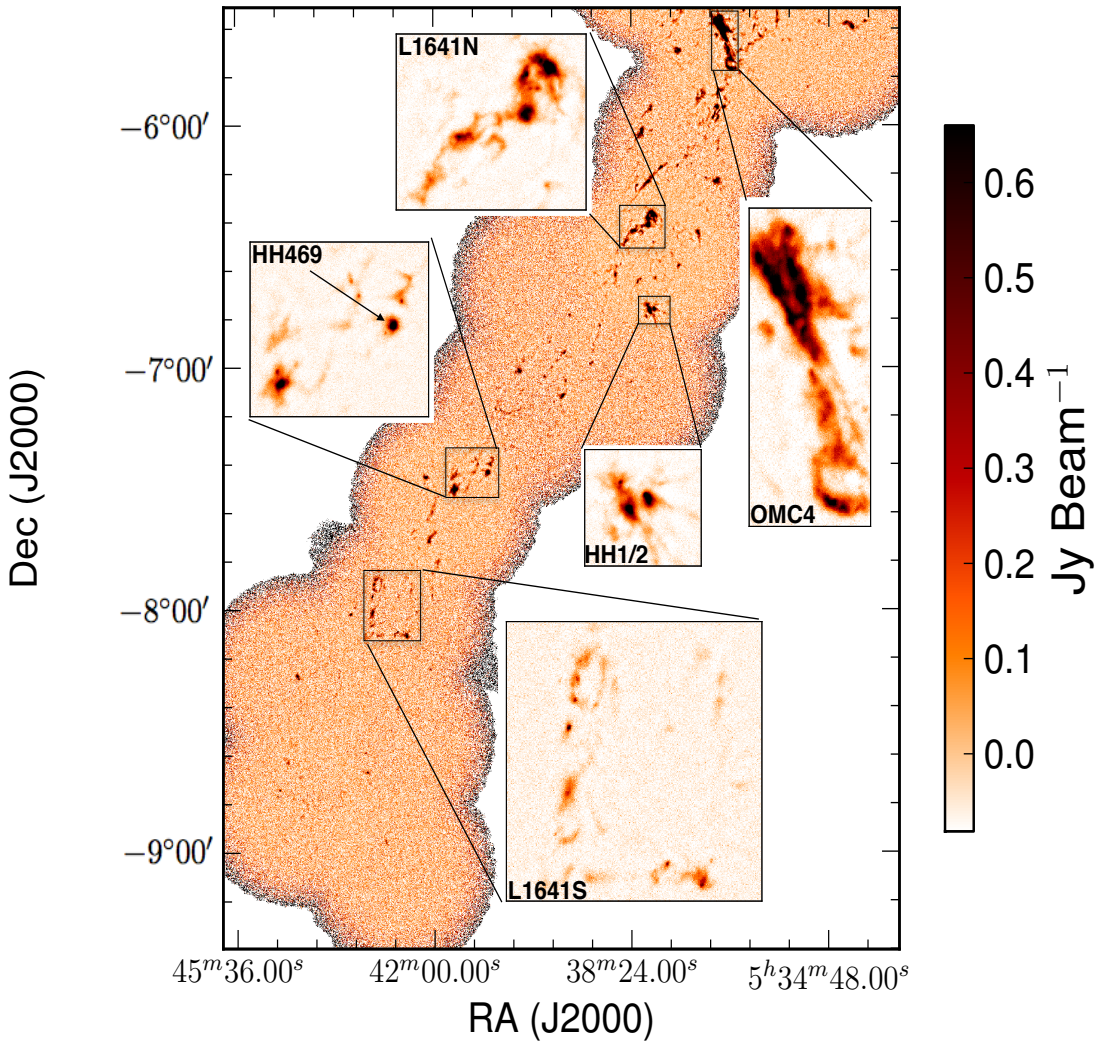

Figure 4.3 The 450 μm SCUBA-2 map of the GBS-defined Southern Orion A region.

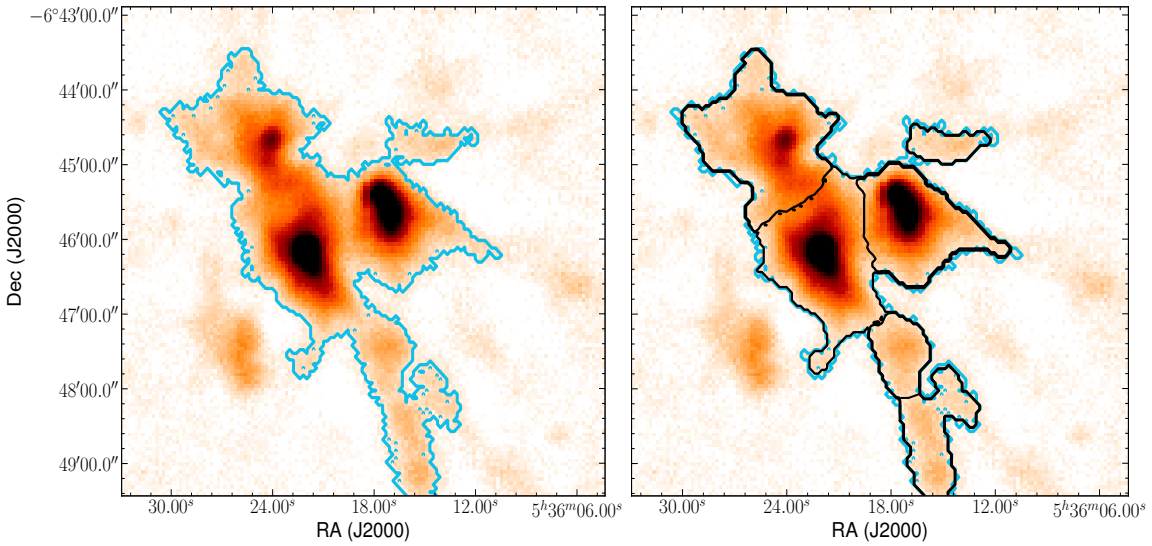

Figure 4.4 *Left*: An example of an identified island. This blue $3\sigma_{rms,pix}$ contour contains the Herbig-Haro objects HH 1/2 (Johnstone & Bally, 2006). *Right*: The blue contour again shows the boundaries of the island while the black contours show six individual compact fragments identified by the JSA_CATALOGUE algorithm.

450 μm maps. To quantify this structure, several algorithms designed to extract, in an automated manner, structure from a given region are available (for example, see GAUSSCLUMPS Stutzki & Guesten 1990, CLUMPFIND Williams et al. 1994, ASTRODENDRO Rosolowsky et al. 2008; GETSOURCES Men'shchikov et al. 2012,and FELLWALKER Berry 2015). Each method amalgamates locations of significant emission differently based on user supplied criteria. Nevertheless, in maps such as the 850 μm one presented here, structure should always be identified with a goal of answering specific scientific questions. Currently, there is no single technique that is commonly agreed to work well for the broad array of physical analyses possible for these data so different algorithms are used even within the GBS papers (see, for examples, Salji et al. 2015b, Salji et al. 2015a, Pattle et al. 2015, Kirk et al. 2016b, Broekhoven-Fiene et al., submitted, and Lane et al. 2016.).

Our goal here is to characterise both the extended and compact structure present and highlight the connection between the large-scale (up to $\sim 7.5'$ to $10'$) and small-scale components ($< 2'$). We define a pixel to be "significant" if it has a value of at least $3\sigma_{rms,pix}$ ($\sigma_{rms,pix} = 9.4\,\mathrm{mJy\,beam^{-1}}$ [2]) in the CO-subtracted 850 μm map.

[2]This value is higher than what is shown in Table 4.1 as the flux in a pixel only measures a fraction of the flux in the beam.

Thus, we first extract the largest objects studied in this work by simply drawing a contour at $3\sigma_{rms,pix}$ and retaining all enclosed structures larger than approximately one beam (15″ in circularly projected diameter). We accomplish this identification using Starlink's version of the algorithm ClumpFind (Williams et al., 1994) as implemented in the Cupid package (Berry et al. 2007) by defining only one flux level over which significant structure is identified. Each non-spurious object detected is referred to as an "*island*"; any flux present in the map outside of an island is considered to be dominated by noise. The simplicity of this initial step prevents the otherwise sophisticated structure identification algorithms from separating adjoining structures based on more complex criteria. Figure 4.4 (left panel) shows an example island which corresponds to HH 1/2.

In the second step, we employ the JCMT Science Archive algorithm jsa_catalogue found in Starlink's PICARD package (Gibb et al., 2013). This algorithm uses the FellWalker routine (Berry, 2015). Briefly, FellWalker marches through a given image pixel by pixel and identifies the steepest gradient up to an emission peak. After performing tests to ensure that the peak is "real" and not just a noise spike, the local maximum is assigned an identifying integer and all the pixels above a user-defined threshold that were included in the path to the peak are given the same identifier. In this way, all of the robust peaks in the image are catalogued and the structure associated with each peak can be analysed. The user-defined parameter, *MinDip*, governs the separation of distinct, significant structure. FellWalker separates structure based on the relative brightness of the region between two areas of peaked emission. If two adjacent structures have peak emission values of $P1$ and $P2$ with $P1 < P2$, and the pixels connecting these two peaks have brightnesses larger than $P1 - MinDip$, the two emission structures are merged together. For this work, the catalogue produced is focussed on smoothly varying, peaked structure and the *MinDip* parameter was set to $5 \times$ local noise.

For simplicity in the definition of the largest structures identified, we rely on the *islands* described above and we use the "compact catalogue" produced by the FellWalker algorithm to describe the localised, peaked structure visible in the map. These localised peaks are often akin to the individual mountains on an island. jsa_catalogue is run independently of the initial contouring, separating emission contained within the larger islands into multiple components. In this way, the compact catalogue generated reveals the substructure present within the context of coincident large-scale emission. For this reason, we refer to the compact components

as "*fragments*". Fragments are allowed to be somewhat smaller than one beam, their circular projected radius must be at least 5″ (compare this to the JCMT's half width at half maximum of 7.5″). Therefore, they can also exist outside of islands as isolated objects. Note that in many cases, however, the smoothly varying emission structure causes several fragments to be of comparable size to islands, so they should not be directly compared to individual, star-forming cores in all cases. Throughout the rest of this paper, an island which contains at least two fragments will be referred to as a "complex island" and an island that contains only one fragment will be referred to as a "monolithic island". Note that in the case of the monolithic islands, their corresponding fragments often trace almost the exact same structure. Generally, the total area of a fragment associated with a monolithic island is 80-100% of the total area of the island. The right panel of Figure 4.4 shows how the HH 1/2 island (blue contours) is separated into six fragments by this technique (black contours). The detected fragments typically trace the islands quite well (to within $\leq$10-20% in area). Accuracy depends, however, on the morphology of the emission structure.

4.4.1 Calculation of Physical Properties

For each island or fragment, we use the associated identification algorithm and the 850 μm SCUBA-2 data to measure the number of pixels associated, the brightest pixel and its location, as well as the total flux density. Table 4.2 summarises the main observational parameters for each 850 μm-identified island. Note that we align the 850 μm - identified island boundaries with the 450 μm map and we extract the total flux and the peak flux from the latter to include it in Table 4.2. We limit the analysis of the 450 μm data to finding the total and peak fluxes of 850 μm-identified island locations as a full comparison between these two datasets goes beyond the scope of this work. Assuming a constant dust emissivity and temperature, we then calculate the mass (M), the peak column density (N_{peak}), the radius (R; calculated from the circular projection of the given object), the Jeans mass (M_J, the maximum mass that can be thermally supported in a spherical configuration), and the "concentration" (or "peakiness"). We present this derived information organised in order of the peak brightness of the sources for 850 μm islands and 850 μm fragments in Tables 4.3, and 4.4, respectively. The 450 μm Orion A data convolved to match the 850 μm data along with temperature maps of all the GBS regions are currently under production and will be released by Rumble et al. (in prep). For a discussion of the determination

of source temperatures using 450 μm and 850 μm data in the Ophiuchus Molecular Cloud, see Pattle et al. (2015).

Assuming the optical depth, τ, is much less than 1, the dust emission observed at 850 μm can be used to derive the mass of a given island or fragment using the following equation

$$M_{850} = 2.63 \left(\frac{S_{850}}{\mathrm{Jy}}\right) \left(\frac{d}{450\,\mathrm{pc}}\right)^2 \left(\frac{\kappa_{850}}{0.012\,\mathrm{cm^2 g^{-1}}}\right)^{-1} \times \left[\frac{\exp\left(\frac{17\,\mathrm{K}}{T_d}\right) - 1}{\exp\left(\frac{17\,\mathrm{K}}{15\,\mathrm{K}}\right) - 1}\right] M_\odot, \tag{4.1}$$

where S_{850} is the total flux density of the observed emission structure at 850 μm, d is the distance to Southern Orion A, κ_{850} is the dust opacity at 850 μm, and T_d is the isothermal temperature of the dust, which we assume to be equivalent to the gas temperature. For this work, we choose $d = 450\,\mathrm{pc}$ (Muench et al., 2008), $\kappa_{850} = 0.012\,\mathrm{cm^2 g^{-1}}$ (following the parametrization of Beckwith et al. 1990, $\kappa_\nu = 0.1[\nu/10^{12}\,\mathrm{Hz}]^\beta\,\mathrm{cm^2\,g^{-1}}$, where $\beta = 2.0$), and $T_d = 15\,\mathrm{K}$. Our chosen dust opacity value is consistent with those in other GBS first-look papers such as Pattle et al. (2015) and Kirk et al. (2016b), though, the uncertainty in κ_{850} is high (see Ossenkopf & Henning 1994). Preliminary results investigating the temperatures of significant emission regions throughout Orion A by Rumble et al. (in prep) show that temperature values range around 15 K for modest flux values in the CO subtracted 850 μm map. This also agrees with the Orion A temperature map derived by Lombardi et al. (2014) using *Herschel Space Observatory* and *Planck Space Observatory* data. Thus, we chose an isothermal dust temperature of 15 K for the sources identified in this analysis. Note that recent data from the *Planck Space Observatory* (Planck Collaboration et al., 2015) suggests that $\beta \sim 1.8$ for the Orion Molecular Cloud. This small difference in β does not affect any of our main conclusions, so we continue to assume a value of $\beta = 2$ which is typically assumed in the ISM (see Chen et al., accepted, for a discussion on β).

The total uncertainty associated with each term involved in calculating a mass is difficult to precisely quantify. There are uncertainties due to the emission properties of dust grains, temperatures and heating due to YSOs, and distance variations from Northern to Southern Orion A combined with the effects of line of sight projections on the total size of a given source. The dominant contributions to the uncertainty are

the temperature and opacity estimates. Temperatures used for similar analyses span 10-20 K (see, for example, Sadavoy et al. 2010a) which introduces a factor of ~ 2 in the mass estimate (see equation 4.1). Preliminary results from Rumble et al. (in prep) also suggest that while most sources we observe appear to have temperatures of ~ 15 K, the distribution has a width of $\sim \pm 5$ K. In addition, different authors use a range of κ_{850} values (such as 0.02 g cm^{-2}, see Kirk et al. 2007) introducing another factor of ~ 2 in uncertainty. Therefore, an estimate of the total uncertainty in mass is a factor of 3 to 4. Note, however, that most of this is in fundamental properties that are expected to be similar across the cloud (for example, dust opacity, mean temperature, and distance).

The column density of H_2 molecular hydrogen at 850 μm is given by

$$N_{peak} = 1.19 \times 10^{23} \left(\frac{f_{850,peak}}{\text{Jy beam}^{-1}} \right) \left(\frac{\kappa_{850}}{0.012\,\text{cm}^2\text{g}^{-1}} \right)^{-1} \times \left[\frac{\exp\left(\frac{17\,\text{K}}{T_d}\right) - 1}{\exp\left(\frac{17\,\text{K}}{15\,\text{K}}\right) - 1} \right] \text{cm}^{-2}, \tag{4.2}$$

assuming a beam width of 14.1″ at 850 μm, where $f_{850,peak}$ is the peak flux density given in Jy beam^{-1}. The Jeans mass can be rewritten in terms of the temperature and the radius of a given island or fragment, R (see Sadavoy et al. 2010b)

$$M_J = 2.9 \left(\frac{T_d}{15\,\text{K}} \right) \left(\frac{R}{0.07\,\text{pc}} \right) M_\odot, \tag{4.3}$$

where R is the given emission structure's projected circular radius, assuming spherical geometry (the value given in the seventh column of Table 4.3). We approximate the aspect ratios of the islands and fragments (tenth column of Table 4.3 and eleventh column of Table 4.4) using flux-weighted horizontal and vertical lengths calculated in the same way by the respective source extraction algorithms, ClumpFind and FellWalker (see Berry et al. 2013 for more detailed information). We note that the distributions of aspect ratios (the length of the horizontal dimension divided by the length of the vertical dimension) for both islands and fragments are peaked near 1.0, implying that our assumption of spherical geometry is reasonable. There are, however, sources which deviate by up to a factor of a few[3]. By calculating the ratio between the island or fragment mass and its associated Jeans mass (assuming only

[3]Only 13% of the islands and 12% of the fragments have aspect ratios greater than 2.

thermal pressure support is acting against gravity), we can identify objects that are unstable to gravitational collapse. A gravitationally unstable object has a ratio of $M/M_J \geq 1$. Nevertheless, due to the inherent uncertainties in the measurements described above, we define a *significantly* gravitationally unstable island or fragment as one which has $M/M_J \geq 4$[4].

The *concentration*, C, is a useful metric to quantify whether or not a structure is peaked. The concentration is calculated by comparing the total flux density measured across a given island or fragment to a uniform structure of the same area wherein each pixel is set to the peak brightness, $f_{850,peak}$ (following Johnstone et al. 2001):

$$C = 1 - \frac{1.13 B^2 S_{850}}{\pi R^2 \times f_{850,peak}}, \tag{4.4}$$

where B is the beam width in arcseconds, R is the radius of the source measured in arcseconds, S_{850} is the total flux of the source measured in Jy, and $f_{850,peak}$ is the peak brightness of the source measured in Jy beam^{-1}. Thus, large islands or fragments which are mostly diffuse will have a low concentration whereas bright, more peaked islands/fragments will have concentration values nearing one. For example, a non self-gravitating, uniform density Bonnor-Ebert sphere has C=0.33 and a critically self-gravitating Bonnor-Ebert sphere has C=0.72 (see Johnstone et al. 2001).

Peaked structure is often indicative of a higher importance of self-gravity in the observed gas and dust (see Johnstone et al. 2001, Kirk et al. 2006b, and Kirk et al. (2016b) or heating due to the reprocessing of emission from the presence of young stellar objects. In general, peaked structure is associated with YSOs (see Jørgensen et al. 2007, Jørgensen et al. 2008, and van Kempen et al. 2009 for examples), though, Kirk et al. (2016b) found many starless cores with high concentrations (>0.72) in the Orion B Molecular Cloud.

4.4.2 Islands

Each identified island is simply defined as a closed, $3\sigma_{rms,pix} = 28$ mJy beam^{-1} contour larger than one beam. In Table 4.3, we present a small sample of individual island properties derived from the 850 μm data (the full catalogue is available on-

[4]Note that the calculated Jeans masses are sensitive to the assumption that the islands and fragments are spheres. If the effective radius of an object is, in reality, smaller than the projected circular radius, the true Jeans mass will be smaller and the object will be more unstable to collapse than our calculation suggests.

Table 4.2 A sample of the observed parameters corresponding to the 850 μm-identified islands (the full catalogue is available online).

Source Name[a] MJLSGJ05...	ID	RA [b] (J2000)	DEC [b] (J2000)	Area [c] (arcsec^2)	S_{850} [d] (Jy)	$f_{850,peak}$ [e] (Jy beam^{-1})	S_{450} [f] (Jy)	$f_{450,peak}$ [g] (Jy beam^{-1})
3619.0-062212I	1	5:36:18.99	-6:22:11.88	81024.57	57.0	1.43	181.79	0.49
3956.2-073027I	2	5:39:56.18	-7:30:27.31	24889.79	18.0	1.04	56.85	0.34
3919.9-072611I	3	5:39:19.88	-7:26:11.05	11887.27	9.0	0.81	31.16	0.3
3623.1-064608I	4	5:36:23.06	-6:46:08.20	33575.05	22.0	0.70	72.66	0.3
3508.8-055551I	5	5:35:08.77	-5:55:51.43	29578.88	18.0	0.52	54.36	0.16
...	...	...	...	...	...	...	...	...
4056.9-081730I	359	5:40:56.87	-8:17:30.23	313.49	0.05	0.02	0.06	0.01

a. The source name is based on the coordinates of the peak emission location of each object in right ascension and declination: Jhhmmss.s±ddmmss. Each source is also designated an "I" to signify it is an island as opposed to a fragment.
b. The 850 μm map location of the brightest pixel in the island.
c. The total area of an island.
d.The total 850 μm flux observed within the island's boundaries.
e. The maximum 850 μm flux value within the island's boundaries.
f.The total 450 μm flux observed within the island's boundaries.
g. The maximum 450 μm flux value within the island's boundaries.

Table 4.3 A sample of 850 μm-identified islands and their properties (the full catalogue is available online). Islands are ordered from highest to lowest N_{peak}.

Island ID	N_{peak} [a] (cm^{-2})	M [b] ($M_\odot$)	R [c] (pc)	$\frac{M}{M_J}$ [d]	C [e]	AR [f]	A_K [g] (mag)	Frags [h]	Protos [i]
1	3.66×10^{23}	148.61	0.35	10.42	0.95	1.14	1.51	13	12
2	2.67×10^{23}	47.8	0.19	6.05	0.93	1.22	2.65	3	6
3	2.08×10^{23}	23.51	0.13	4.3	0.90	1.11	1.82	2	2
4	1.79×10^{23}	58.17	0.23	6.33	0.90	1.0	1.29	6	5
5	1.34×10^{23}	46.19	0.21	5.36	0.88	1.3	0.54	6	4
...	...	...	...	...	...	...	...	...	...
359	4.86×10^{21}	0.13	0.02	0.14	0.17	4.56	1.15	0	0

a. The *peak* column density is calculated by using the flux density of the brightest pixel in the island ($f_{850,peak}$) in Equation 4.2 (using the values shown in the text).
b. The mass is calculated by using the total flux of the island (S_{850}) in Equation 4.1 (using the standard values shown).
c. Effective radius that represents the radius of a circular projection having the same area, A, as the island: $R = (A/\pi)^{0.5}$.
d. The Jeans mass is calculated using the radius of the island in Equation 4.3 (using the standard values shown).
e. The concentration is calculated using Equation 4.4.
f. AR is the aspect ratio of the source. It is defined as the length of the horizontal dimension divided by the length of the vertical dimension.
g. A_K is the average value taken directly from the extinction map provided by M. Lombardi (private communication, July 18^{th}, 2015) of each source footprint. The extinction can be converted to column density using Equation 4.5.
h. The number of fragments associated with the island.
i. The number of protostars identified by Megeath et al. (2012) and Stutz et al. (2013) within the island's boundaries.

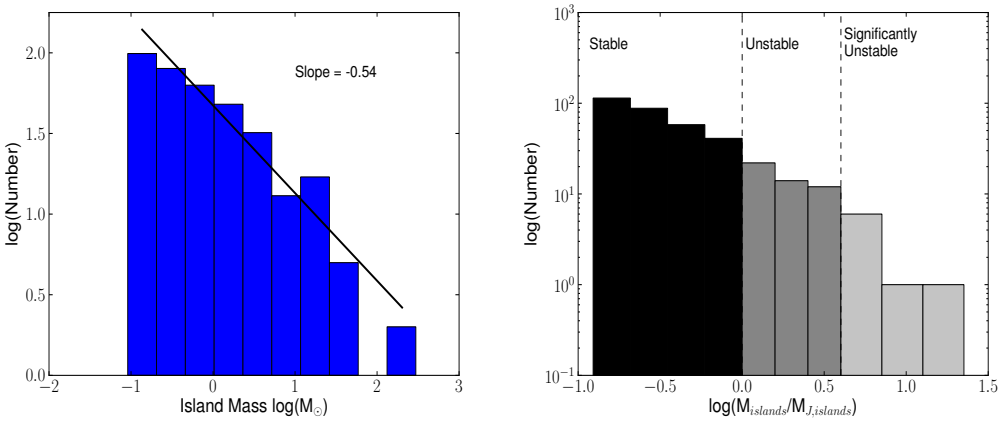

Figure 4.5 *Left*: Histogram of the masses of the island population. The number of islands decreases with mass following a power law with an exponent of -0.54. *Right*: Histogram of the stabilities (M/M_J) of the island population. Islands with a ratio of $M/M_J \geq 1$ may be gravitationally unstable to collapse, whereas islands with $M/M_J \geq 4$ are defined as *significantly* unstable and are expected to show evidence of gravitational collapse.

line). Throughout this section, we give a brief overview of the island population, focussing on the mass and the stability as key observational parameters. In Section 4.5, we elaborate on the connections between these structures and the broader physical perspective involving fragmentation and the population of YSOs. There are 359 identified islands in total which comprise 2.2% of the area of the total map. Out of these, 55 islands were calculated to be Jeans unstable (see Section 4.4.1) and 75 islands were found to harbour protostars within their boundaries.

The left panel of Figure 4.5 shows the mass histogram of the entire island population. The masses were calculated using Equation 4.1, assuming an isothermal temperature of 15 K. As we can clearly see, most island masses are under 10 $M_\odot$ with only a few examples of very large, contiguous structures. This situation is to be expected, as large-scale structure is filtered out in SCUBA-2 data and in many cases we only expect to see the brighter components of this underlying emission.

This histogram does not represent a core mass function as the islands do not uniformly represent pre-stellar objects. Instead, it provides an indication of the largest-scale features to which SCUBA-2 is sensitive. In fact, defining a core mass function from data such as these is inherently difficult due to the broad variety of ways different structure identification algorithms draw borders around adjoining areas of emission

(Pineda et al., 2009a).

For every island, we calculate the Jeans mass using Equation 4.3 and test the stability of the object by comparing it to the observed mass derived from the dust emission. As noted in Section 4.4.1, an object is theoretically unstable if its M/M_J ratio is greater than 1, but we consider a significantly unstable object to have an M/M_J ratio greater than or equal to 4 due to the inherent uncertainties in the mass calculation described above (also see Section 4.5.2). We expect large, unstable islands to collapse and fragment on the Jeans length scale (assuming there is only thermal pressure support counteracting gravity in these objects) and small, unstable islands to show some indication of star formation such as high concentration or association with a YSO. Preliminary results from Rumble et al. (in prep) derived from 450/850 μm flux ratios suggest that a histogram of the median temperature of each island peaks at ~ 15 K within a broad range. The right panel of Figure 4.5 shows the results on the stability of each island across the map. The two dashed lines show which islands are calculated to be unstable ($M/M_J \geq 1$) and which are significantly unstable ($M/M_J \geq 4$). It is important to note that SCUBA-2 is not sensitive to large-scale structure. As we highlight in Section 4.4.4, islands comprise $\sim 1.4\%$ of the cloud's mass. For the purposes of this analysis, we focus on the smaller-scale star forming sources in the regions of highest column density in the SCUBA-2 850 μm map and we assume that the mass on the larger scales can be separated out from the more local analysis. We leave the more thorough stability analysis for the sections below where we combine the island and fragment catalogues, and we can examine individual special cases in the context of fragmentation and YSO association.

4.4.3 Fragments

The JSA_CATALOGUE algorithm which we use to identify fragments employs the structure identification procedure FellWalker (Berry, 2015) to detect objects and separate significant emission into individual sources. In total, 431 fragments are detected by JSA_CATALOGUE, 100 of which are calculated to be Jeans unstable (see Section 4.4.1) and 103 of which contain at least one protostar within their boundaries. The left panel of Figure 4.6 shows the mass distribution of the observed fragments and the right panel shows the Jeans stability associated with the same population. Table 4.4 shows several examples of fragment properties and the full catalogue is available online.

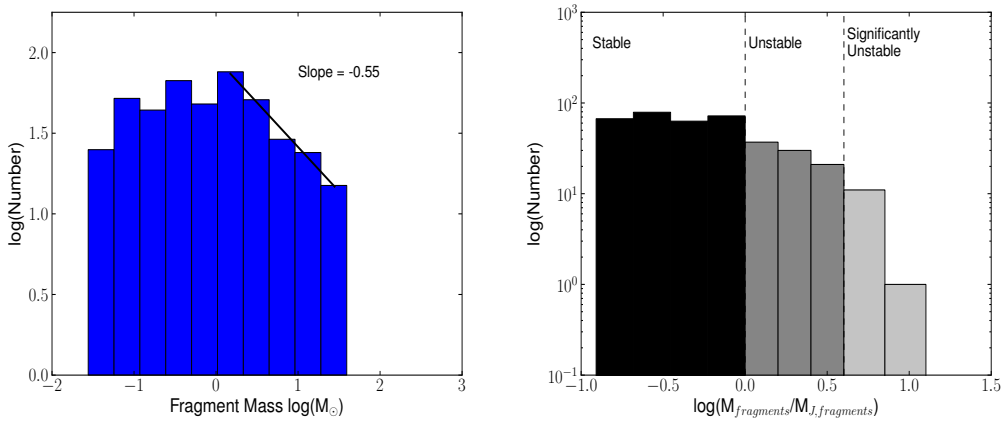

Figure 4.6 *Left*: Histogram of the masses of the fragment population. The high mass slope of the fragment population matches the island high mass slope. *Right*: Histogram of the stabilities (M/M_J) of the fragment population. Fragments with a ratio of $M/M_J \geq 1$ may be gravitationally unstable to collapse, whereas fragments with $M/M_J \geq 4$ are defined as *significantly* unstable and are expected to show evidence of gravitational collapse.

Table 4.4 A sample of 850 μm-identified fragments and their properties (the full catalogue is available online). Fragments are ordered from the highest to lowest N_{peak} within each parent island.

Source Name[a] MJLSGJ05...	Frag ID	Island ID	R.A.[b] (J2000)	Dec[b] (J2000)	N_{peak}[c] (cm^{-2})	M[d] ($M_\odot$)	R[e] (pc)	$\frac{M}{M_J}$[f]	C[g]	AR[h]	A_K[i] (mag)	Protos[j]
3619.0-062212F	1	1	5:36:18.99	-6:22:11.88	3.66×10^{23}	38.88	0.13	7.36	0.9	1.13	1.51	5
3625.4-062500F	2	1	5:36:25.43	-6:24:59.78	9.63×10^{22}	27.31	0.13	4.99	0.76	1.28	1.13	5
3641.7-062618F	3	1	5:36:41.74	-6:26:17.59	7.15×10^{22}	21.1	0.13	3.9	0.74	1.63	0.31	0
3621.0-062151F	4	1	5:36:21.00	-6:21:50.88	6.81×10^{22}	12.71	0.1	3.25	0.69	1.03	1.51	0
3624.8-062239F	5	1	5:36:24.83	-6:22:38.83	6.73×10^{22}	19.02	0.12	3.88	0.7	1.97	1.45	1
...	...	...	...	...	...	...	...	...	...	...	...	...
4250.0-081209F	431	None	5:42:49.95	-8:12:09.16	5.91×10^{21}	0.05	0.01	0.09	0.28	1.8	1.06	0

a. The source name is based on the coordinates of the peak emission location of each object in right ascension and declination: Jhhmmss.s±ddmmss. Each source is also designated an "F" to signify it is an fragment as opposed to an island.
b. The 850 μm map location of the brightest pixel in the fragment.
c. The *peak* column density is calculated by using the flux density of the brightest pixel in the fragment ($f_{850,peak}$) in Equation 4.2 (using the values shown in the text).
d. The mass is calculated by using the total flux of the fragment (S_{850}) in Equation 4.1 (using the standard values shown).
e. Effective radius that represents the radius of a circular projection having the same area, A, as the fragment: $R = (A/\pi)^{0.5}$.
f. The Jeans mass is calculated using the radius of the fragment in Equation 4.3 (using the standard values shown).
g. The concentration is calculated using Equation 4.4.
h. AR is the aspect ratio of the source. It is defined as the length of the horizontal dimension divided by the length of the vertical dimension.
i. A_K is the average value taken directly from the extinction map provided by M. Lombardi (private communication, July 18^{th}, 2015) of each source footprint. The extinction can be converted to column density using Equation 4.5.
j. The number of protostars identified by Megeath et al. (2012) and Stutz et al. (2013) within the fragment's boundaries.

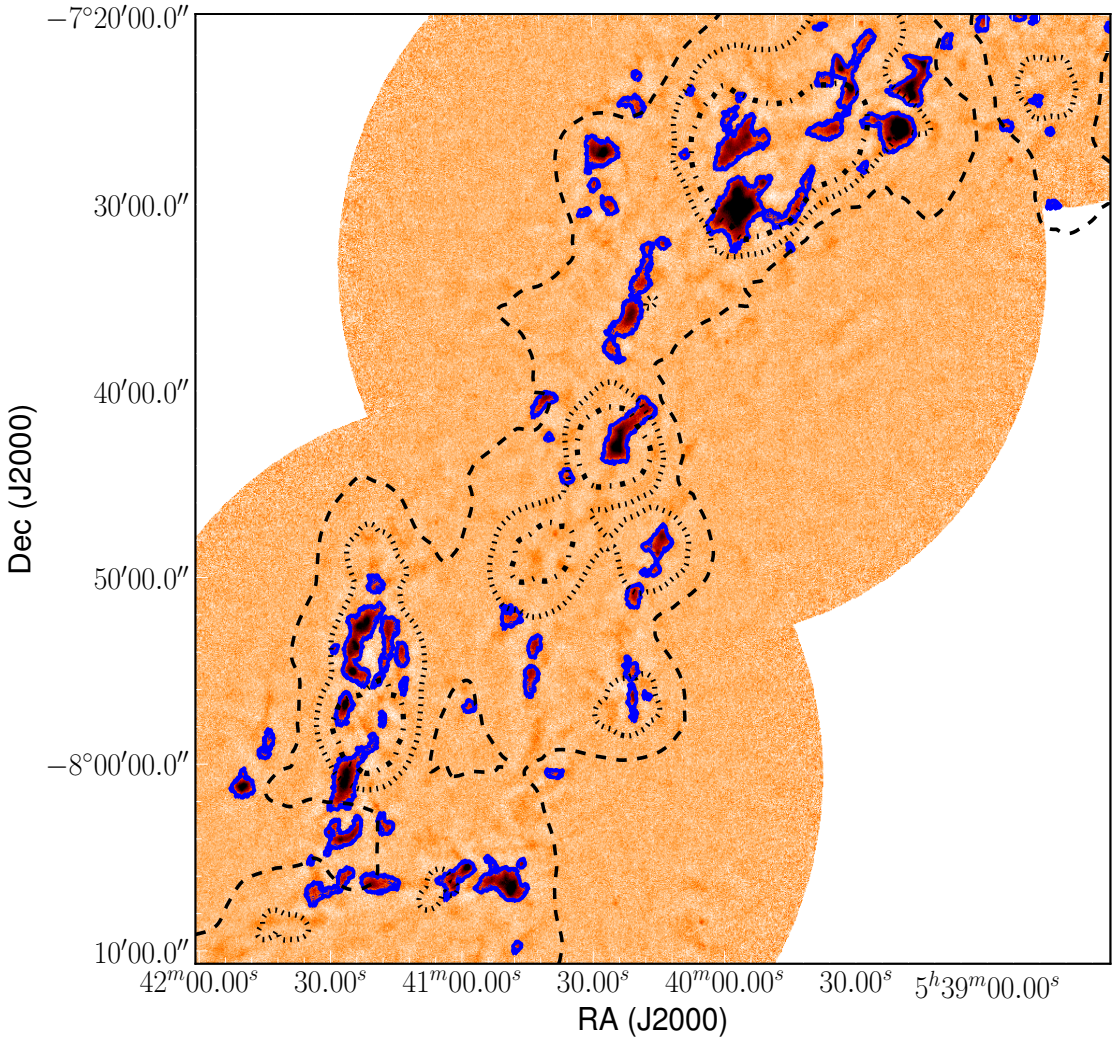

Figure 4.7 A subsection of the 850 μm SCUBA-2 image overlaid with contours from the extinction map obtained from Lombardi (private communication). The solid, blue contours represent islands identified with the SCUBA-2 data while the dashed, dotted, and dash-dot contours represent regions of the extinction map with column densities of 1.67×10^{22} cm^{-2}, 3.32×10^{22} cm^{-2}, and 5.00×10^{22} cm^{-2}, respectively.

Since each fragment is defined to be associated with a local maximum, these objects often subdivide the larger islands into multiple areas of significant emission. While projection effects are difficult to constrain, the fragments highlight the connection between the larger- and smaller-scale structure in star-forming regions and offer a useful reference for more in-depth studies. Since these fragments are often inherently smaller and less diffuse than their island hosts, it is within the context of fragments that we more thoroughly discuss the connection between dust emission and star formation. There is a wide range in observed fragment masses spanning from 0.03 to 39.3 $M_\odot$ with a median mass of $\sim$0.7 $M_\odot$. It is interesting to note, however, that there are no detected fragments with masses above $\sim 39\,M_\odot$ (Figure 4.6). Several sources are detected in this high mass regime, but there is a sudden truncation indicating that objects which achieve higher masses are broken into smaller-scale, localised structures. This is obvious when we compare the high mass end of the fragment distribution with the high mass end of the island distribution in Figure 4.5 (left panel). The highest mass islands each contain at least three fragments within their boundaries. Also, note that the slope of the fragment mass histogram is comparable to the island mass histogram at large masses. This indicates that the large fragments are not completely analogous to cores, but represent more extended regions of smoothly varying significant emission. As in the case of the island mass distribution shown in the left panel of Figure 4.5, this histogram does not represent a core mass function because the fragments do not uniformly represent pre-stellar objects. Note, however, that the FellWalker algorithm separates objects based on the height of a given emission peak relative to its local surroundings. This means that while many fragments may be large, they only contain one prominently peaked region.

4.4.4 Large-scale Structure from Extinction

Here, we analyse the observed islands and associated YSOs from the Megeath et al. (2012) and Stutz et al. (2013) catalogues in the context of large-scale structure. To this end, we use the extinction data from Lombardi et al. (2011) at $1.5'$ resolution (Lombardi, M. priv communication, 2015). Figure 4.7 shows the Lombardi et al. extinction data as contours overlaid on the SCUBA-2 850 μm extinction map. These extinction data were determined using the Near-infrared Color Excess (NICEST) method from Lombardi (2009). In effect, the NICEST method seeks to remove contamination of foreground stars and inhomogeneities introduced by unresolved struc-

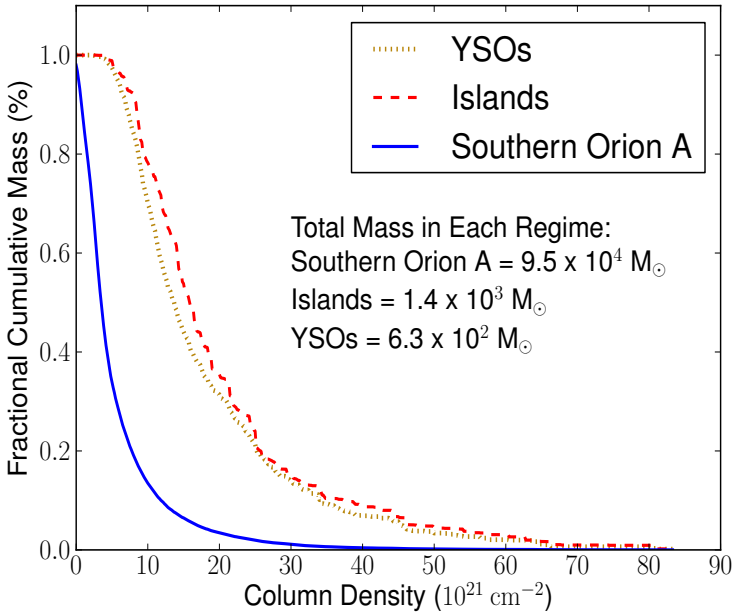

Figure 4.8 Three cumulative mass fractions plotted against the column density: The entire Southern Orion A cloud (NICEST; blue curve), the islands (SCUBA-2; red dashed curve), and the YSOs (*Herschel* and *Spitzer*; dotted curve). The cumulative mass fraction for the whole cloud was derived from the NICEST extinction map. The cumulative mass fraction of the islands was derived from the SCUBA-2 850 μm data of all the pixels contained within the boundaries of each sources. The cumulative mass fraction of the YSOs was derived by counting the number of objects in the Megeath et al. (2012) and Stutz et al. (2013) catalogues and assuming a mass of 0.5 $M_{\odot}$ for each source.

ture. The extinction measurements were calculated using near-infrared observations from the Two Micron All Sky Survey (2MASS; Skrutskie et al. 2006). We note that the difference in the resolution between the SCUBA-2 map and the extinction map results in some small variations in peak emission location as represented in Figure 4.7.

Following calculations presented in Lombardi et al. (2014), we converted the A_K extinction values to column densities using the conversion

$$\frac{\Sigma}{A_K} \simeq 183\,\mathrm{M}_{\odot}\,\mathrm{pc}^{-2}\,\mathrm{mag}^{-1}, \tag{4.5}$$

where Σ is the mass surface density.

Figure 4.8 compares the cumulative mass fraction for all of Southern Orion A,

the islands, and the YSO population plotted against the column density derived from Lombardi et al's extinction map. For the cloud distribution, we derive the mass from the extinction map and consider only those data where SCUBA-2 observed. Similarly, for the islands, we determined the mass associated with the islands from our analysis in Section 4.4.1 (e.g., contiguous regions with 850 μm emission $> 3\sigma_{rms,pix}$). Finally, for the YSOs, we use the number of sources in all classes above each column density level, assuming a standard average YSO mass of 0.5 $M_\odot$ (for example, see Megeath et al. 2012 and Stutz et al. 2013).

Figure 4.8 can be compared with a similar analysis performed in Orion B (Kirk et al., 2016b) with the caveat that the extinction map used in this paper has much coarser resolution and therefore, on average, much smaller column density values. The total mass of the SCUBA-2 observational footprint derived from the extinction map is $9.5 \times 10^4 M_\odot$. The total mass of all identified islands derived from the 850 μm map is $1.3 \times 10^3 M_\odot$ and the total mass of the YSOs is $6.6 \times 10^2 M_\odot$ assuming a typical mass of 0.5 $M_\odot$ for all sources. Clearly, the islands trace the densest material, whereas the broader Southern Orion A cloud includes a significant diffuse component. Also, we see that the YSO population tracks quite well with the islands especially at higher column densities, indicating a connection between the densest gas and the YSO population. The associations between YSOs and observed structure are further explored throughout this paper and especially in Section 4.5.

Note that in Figures 4.7 and 4.8, we can see the effect of the large-scale mode subtraction applied to this dataset. The islands we identify are moderate-scale, heavily extincted regions which comprise a small portion of the map in both mass and area (approximately 1.4% and 2.2%, respectively). These structures we identify undoubtedly lie within larger-scale, less-dense structures; the material which links our islands to the rest of the cloud. The details of how the largest scales in a molecular cloud connect to localised star-forming regions are complex and not yet well understood. As we explore throughout Section 4.5, however, the size scales and mass scales accessible to SCUBA-2 continuum data represent siginificant areas of star forming material. Throughout this analysis, we assume that the larger-scale modes to which our observations are not sensitive only serve to increase the gravitational instability of islands and fragments and therefore fuel the formation of stars.

4.5 Associations with Young Stellar Objects

In this section we analyse the SCUBA-2 emission in conjunction with the YSO catalogues presented by Megeath et al. (2012) and Stutz et al. (2013) in an effort to associate these dense gas structures with evidence of active star formation. Megeath et al. (2012) constructed their catalogue using a large-scale *Spitzer Space Telescope* survey while the catalogue derived by Stutz et al. (2013) targeted more localised regions with the *Herschel Space Observatory* such that their analysis would be sensitive to very deeply embedded protostars. All the figures presented in this section are colour-coded by the given emission structures' individual association with different classes of YSOs. We define an "association" between a YSO and an emission structure as the YSO position falling within the boundaries of the object of interest (island or fragment). A "strong" protostellar association is when a protostar falls within one beam diameter ($\sim 15''$) of the object's peak emission location. In this work, we make no attempt to determine the class of a given YSO independently and rely on the provided designations of these sources in the catalogues of Megeath et al. 2012 and Stutz et al. 2013. There are four YSO designations presented by Megeath et al. 2012 which we combine with a "No YSO" category to separate our detected emission structures into five main groups.

P: Protostars. These objects have characteristics (such as spectral energy distribution and colour) consistent with Class 0, Class I, or Flat Spectrum sources, i.e., young, embedded protostars. We also include five additional confirmed protostars from *Herschel Space Observatory* observations (see objects with a "flag" value of 1, indicating a "confirmed" protostar, in Table 3 in Stutz et al. 2013). We differentiate in the plots here between an island or fragment that simply contains a protostar (denoted by a green outline) and an island or fragment that contains a protostar that lies within one beam of the peak emission position (denoted by a solid green symbol).

FP: Faint Candidate Protostars. These objects have protostar-like colours but *Spitzer* MIPS 24 μm emission that is too faint (> 7 mag) for them to be considered robust protostar detections (see the Kryukova et al. 2012 criteria and Megeath et al. 2012 for more details). We denote associations with faint candidate protostars by blue outlines.

RP: Red Candidate Protostars. These objects have sufficiently bright MIPS 24 μm emission but lack any detection in *Spitzer*'s shorter wavelength bands. Each source

was visually inspected by Megeath et al. (2012) to differentiate it from objects such as asteroids or background galaxies. We denote associations with red candidate protostars by red outlines.

D: Discs. These objects have characteristics consistent with Class II sources, i.e., pre-main sequence stars with discs. We denote associations with discs by brown outlines.

No YSOs: No Associated YSOs. If none of the above objects lie within the boundaries of a given emission structure, we denote it with a black outline.

We also analysed four protostar candidates which were identified in Stutz et al. 2013 (objects with a "flag" value of 2, indicating a "candidate" protostar, in Table 3 in Stutz et al. 2013). Only one of these, however, is contained within the boundaries of an island or a fragment and it lies a significant distance from the nearest 850 μm dust emission peak. We therefore chose not to include it in this analysis. In total, there are 212 protostars, 1081 disc sources (or, discs), 27 faint candidates, and 2 red candidates within the SCUBA-2 mapped area analysed in this paper.

4.5.1 An Overview of the YSO Population in the 850 μm SCUBA-2 map

In the top panel of Figure 4.9, we plot the 850 μm flux measured at each YSO location. The right edge of the first bin represents the threshold flux level for a pixel to be included in an island or a fragment. Each bin has a width of $3\sigma_{rms,pix} = 28$ mJy beam^{-1}. Here, we see that 72% of protostars lie on pixels with 850 μm fluxes above this adopted threshold value. Since young protostars are deeply embedded objects that are still accreting mass from surrounding material, their correspondence with bright 850 μm emission is expected. More-evolved protostars eventually disperse this surrounding material and should have lower associated 850 μm fluxes than their younger counterparts. Due to their still young ages, however, even the more-evolved protostars have not had time to move a significant distance away from their parent emission structure or for this structure to have dispersed and thus still reside within islands (see Section 4.5.5, Stutz & Gould 2015, and Megeath et al. 2016 for further discussion).

The remaining 28% of protostars which do not appear within islands represent an interesting population. In some cases, protostars lie just beyond island boundaries by $\sim 3''$ to $10''$ and these could well be more-evolved objects that formed in the nearest

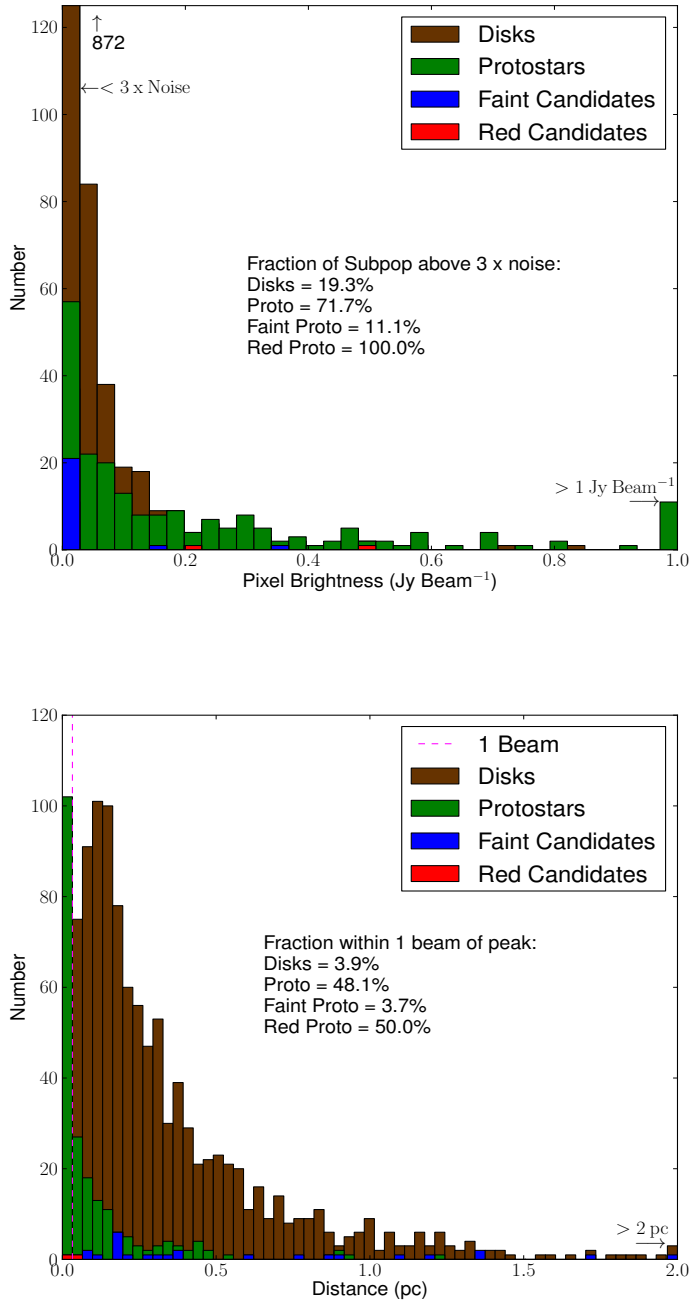

Figure 4.9 Two metrics to analyse the population of YSOs in the context of their association with fragments. *Top:* A measurement of the 850 μm flux at the location of a YSO in units of Jy beam^{-1}. The width of each bin is $3\sigma_{rms,pix} = 0.028$ Jy beam^{-1}. The first bin also includes YSOs which are located on negative 850 μm flux pixels; in this bin, there are 872 disc sources. The final bin shows the number of YSOs coincident with pixels that are brighter than 1.0 Jy beam^{-1}. *Bottom:* The distance between a given YSO and the location of the nearest fragment's localised emission peak. Each bin has a width of $15'' \simeq 1$ beam $= 6750$ AU. The final bin shows the number of YSOs which lay further than 2.0 pc from the nearest emission peak. The magenta line on the right edge of the first bin highlights objects which are within ~ 1 beam of the nearest localised emission peak.

island but shed enough local material or were gravitationally ejected such that they now lie outside its boundaries. In other cases, the protostars may simply be misclassified. Interestingly, Heiderman & Evans (2015) recently found the same percentage of protostars which appear to be misclassified using an independent data set: the Gould Belt "MISFITS" survey. In their survey, Heiderman & Evans (2015) observed HCO^+(J=3-2) toward all the Class 0/I and Flat spectral sources identified by Spitzer (from Megeath et al. 2012) and distinguished protostars from discs following van Kempen et al. (2009). Similar to our results with SCUBA-2 at 850 μm, Heiderman & Evans (2015) found that only 72% of their sample met the line criteria for protostellar classification. Thus, a significant fraction of protostars may be misclassified based on their SEDs. In addition, line-of-sight coincidences between more-evolved Class II/III sources and dense gas could result in additional misclassifications (e.g., from underestimated extinction corrections in the near-infrared bands). Since the Orion cloud has a large and dense YSO population, such coincidences are more likely.

The top panel of Figure 4.9 shows that disc sources, as expected, are found generally at locations of low emission. These more-evolved objects have had time to migrate away from their parent structures and by definition they should not have a dense envelope. Emission we detect around isolated disc sources is presumably due to the remnant of the dispersed natal envelope or excess material finishing its collapse. Of course, we expect some discs to also align with bright emission locations simply because of projection effects. The majority of faint protostar candidates also seem to lie at lower levels of 850 μm flux, indicating that they are likely not young protostellar objects. The two red protostar candidates which fall into our Southern Orion A map, however, do have significant associated flux which strengthens the evidence of their classification.

The bottom panel of Figure 4.9 shows the distribution of distance between a given YSO and its nearest fragment's peak emission location. Fragment peak emission locations were chosen as opposed to islands as it is the former objects that are more likely the formation sites of an individual to a few protostars. We only include YSOs which lie on pixels within the SCUBA-2 footprint of Southern Orion A. Here, we find similar results to the top panel, i.e., disc sources appear to be more scattered about the map than protostars (see Section 4.5.5). In contrast, approximately half of the protostars lie within one beam of the nearest peak flux location and the population as a whole is peaked toward closer distances. Moreover, the red protostar candidates seem to have strong associations with potential star-forming sites whereas the faint

protostars can lie quite separated from these regions, indicating the latter may be misclassified background galaxies.

4.5.2 Star Formation in Fragments

More so than islands, it is the compact, localised fragments for which we expect Jeans unstable cases to be forming (or to eventually go on to form) stars. Thus, in Figure 4.10, we compare fragment concentrations with their Jeans stabilities. Highly concentrated sources are expected to have a higher degree of self-gravity, eventually collapsing and forming one to a few stellar systems. As discussed in Section 4.4.1, the concentration is a measure of the spatial distribution of emission. Using Equation 4.4, we determine which fragments are concentrated (values nearer to 1) or more uniform (values nearer to 0). In Figure 4.10, green dashed lines indicate the nominal gravitational instability line $M/M_J \geq 1$ (horizontal) and $C = 0.5$ (vertical). $C = 0.5$ is chosen because it represents a relatively concentrated core approximately half way between a uniform density (0.33) and self gravitating Bonnor Ebert sphere (0.72) (see Johnstone et al. 2001). Note that the fragments fall broadly into two regimes: 1.) gravitationally stable and with uniform emission and 2.) gravitationally unstable and with peaked emission. We note as well that the diamond symbols in Figure 4.10 represent a fragment which belongs to a complex island (an island containing at least two fragments) and a circle represents a fragment which traces isolated, monolithic structure.

We would expect the gravitationally unstable, peaked fragments to be the population which is associated with protostars. In general, we see this is the case. In Figure 4.10, only 8% of the fragments without discernible signs of YSOs appear unstable and concentrated. Of those, the fragments which were extracted from monolithic islands (or have no island associations) are outnumbered by those which were extracted from complex islands (21% and 79%, respectively). Conversely, we would expect the gravitationally stable, less peaked fragments to be the population which is not actively forming stars. Indeed, only 23% of the stable and uniform fragments appear to have YSOs. Almost all of these fragments are associated with monolithic islands (83%); that is, they do not have "siblings" within the same island.

There are two main possibilities for explaining the fragment population in the bottom left quadrant of Figure 4.10 that are associated with protostars. First, during the formation of the protostar, the mass reservoir around the central, bright object has

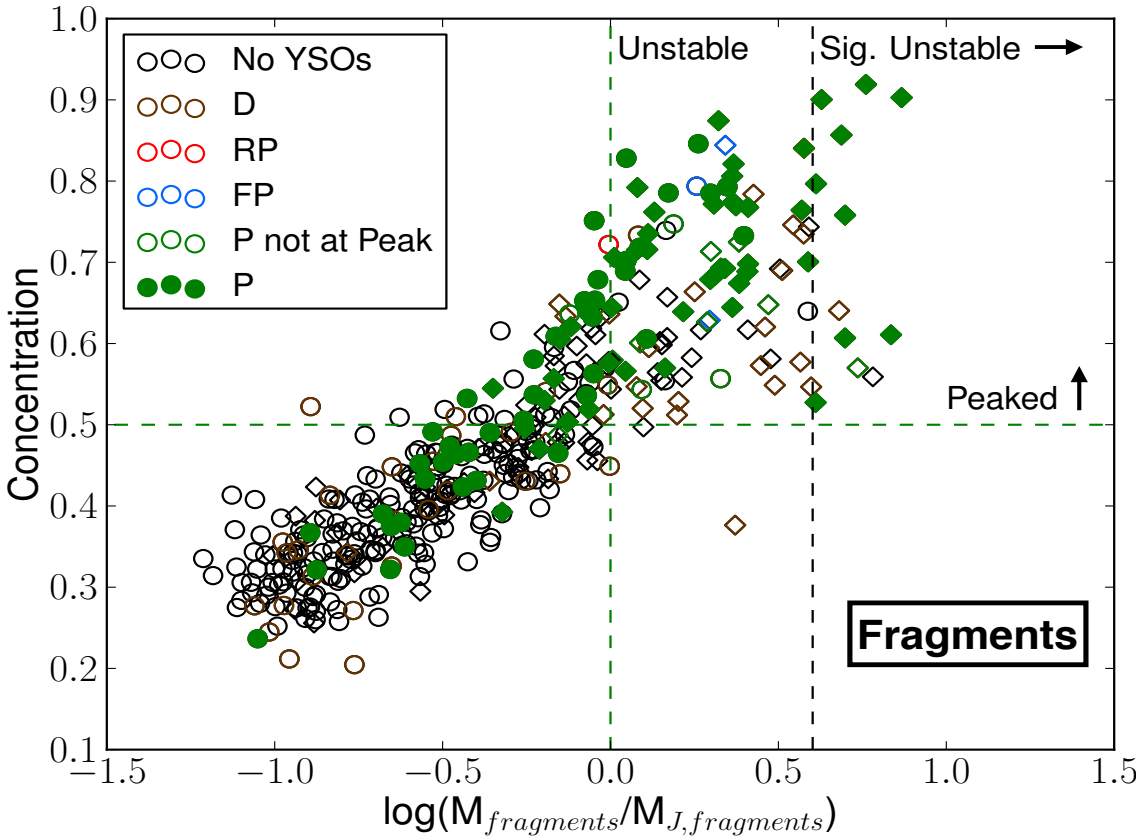

Figure 4.10 Fragment concentration versus fragment stability. The dashed green lines show a concentration of 0.5 on the ordinate and the gravitational instability line on the abscissa. The vertical dashed black line represents an M/M_J ratio of 4 where we define sources to be significantly unstable. Colours represent associations between the identified fragment and several classes of YSOs as denoted in the legend. Diamonds represent a fragment which belongs to a complex island and a circle represents a fragment which traces isolated, monolithic structure.

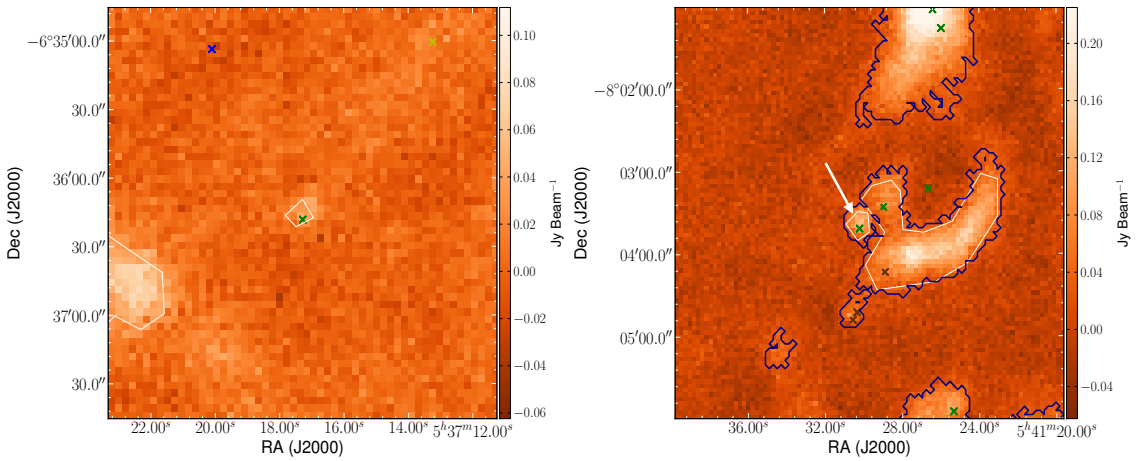

Figure 4.11 Typical examples of fragments calculated to be gravitationally stable to collapse yet having a strong association with a confirmed protostar. In general, it is the lack of large-scale structure in the SCUBA-2 map which leads to these non-intuitive detections. White contours show the boundaries of selected fragments. The crosses show the locations of YSOs following the same colour scheme as outlined in previous figures and the text. *Left*: The isolated monolithic case. This particular fragment of interest (center) has no associated island. *Right*: A case where the fragment is extracted from an island with multiple areas of significant emission. The blue contours show the boundaries of islands in the field of view (part of L1641S). The fragment of interest is highlighted by the white arrow.

been depleted by accretion to the extent that the now diffuse gas and dust falls below our detection limit. Similar situations were noted by Mairs et al. (2014) through the synthetic observations of a numerical simulation. Thus, these objects are more-evolved Class I protostars. Second, our data may be insensitive to some mass due to the large-scale structure subtraction discussed previously (see Chapin et al. 2013 and Mairs et al. 2015). In at least some cases (see below) this can cause structure identification algorithms to detect multiple individual sources instead of one larger source, leading to an underestimate of the true stability. Also note that the dust continuum traces the envelope and disc and not the mass associated with the central protostar itself (which is optically thick but slightly beam diluted at these wavelengths). The actual mass of the system, therefore, is greater than the measured mass (see Mairs et al. 2014 for a discussion on including protostellar masses in stability calculations based on synthetic observations of numerical simulations).

Figure 4.11 shows two examples of the types of fragments we identify with protostellar associations in the purportedly "stable regime" of Figure 4.10. In the left panel, we see bright, dense regions which may sit on top of a more uniform, large-scale background to which the SCUBA-2 instrument is less sensitive. In the data reduction procedure, if we were to filter out less of the large scale structure, the boundaries of isolated sources would broaden further into the diffuse structure and this may result in the blending of multiple islands and fragments. Relaxing the filtering constraints, however, leads to less confidence in the robustness of the detected diffuse structure (see Chapin et al. 2013).

The right panel of Figure 4.11 shows one of the two "stable" fragments associated with protostars extracted from complex (not monolithic) islands. The difference between this structure and the monolithic, stable structure in the left panel which harbours a protostar, however, is that the smaller fragment was close enough to a larger structure to have been included in the boundaries of the same island rather than being identified as an isolated object. Both stability as well as concentration of course will depend on how boundaries are drawn between the significant areas of emission. This example shows why performing source extraction in crowded areas is a difficult process, especially when lacking the entire large-scale component. The unstable, low concentration fragment associated with a disc source in the lower right quadrant of Figure 4.10 is a similar object to the small fragment with the protostar near its peak presented in the right panel of Figure 4.11. As described in Section 4.4, the FellWalker algorithm has chosen the boundaries of these individual fragments

based on the minimum value between localised peaks, i.e., the valleys between the mountains. If a sufficiently low value is achieved, the algorithm will separate structure accordingly (see Berry 2015). Again, a robust recovery of the large-scale background structure may prove useful in identifying how each fragmented area is related, depending on the morphology of that structure. Any algorithm designed to extract structure will have uncertainties in object boundaries based on the user's specific input parameters, culling processes, and end goals. Similarly, without spectroscopic information, any algorithm will also be subject to projection effects, i.e., the possibility of more than one source in the same line of sight. In terms of associations with YSOs, however, we expect projection effects to be a larger factor when associating dust-emission regions with disc sources as opposed to protostars as the latter tend to be embedded in their parent material. A further discussion of the distribution of disc sources and protostars is provided in Section 4.5.5.

While there is an intrinsic uncertainty in the opacity (by assuming a fixed dust grain size) and the distance of each object, we assume these two values are fairly consistent across the entire Southern Orion A map. What may change in different areas, however, is the temperature. We have calculated each fragment's M/M_J stability ratio based on the assumption of an isothermal temperature of 15 K. If this temperature was higher by 5 K, the stability ratio would decrease by approximately a factor of 2 and each object will be found to be "more stable", assuming only thermal support is counteracting the force of gravity. This difference comes from a combination of the lower fragment mass as well as the higher Jeans mass arising from assuming a hotter temperature. Potential sources of heating include nearby high-mass stars, the embedded YSOs themselves, and cosmic rays. If the temperature was 5 K colder, however, the calculated stability ratio would increase by a factor of 3 and objects would be more unstable.

4.5.3 Island Fragmentation

We now turn our discussion to the connection between islands and fragments in the context of fragmentation and star formation. We remind the reader that a "complex island" is defined to contain at least two fragments whereas an island that displays only one area of significant emission is referred to as "monolithic". In Figure 4.12, we compare the mean gas number density with effective radius for islands (top panel) and fragments (bottom panel). The colour scheme of symbols remains the

same for the YSO associations but there is a subtle difference in the symbols themselves. For the islands, a diamond represents a complex island and a circle represents a monolithic island whereas for the fragments, a diamond represents an object extracted from a complex island and a circle represents an object extracted from a monolithic island. The number densities were calculated assuming spherical symmetry using the effective radii (see Table 4.3). Two lines of instability are shown representing one Jeans radius (beyond which we expect an object to be unstable to collapse) and two Jeans radii (beyond which we observe all objects to be fragmented). A third, dashed green, line represents the detection lower limit for an island ($3\sigma_{rms,pix} = 28$ mJy beam$^{-1} = 3.73 \times 10^{21}$ cm^{-2}). The reason there is a gap between larger structures and this detection limit is because the data reduction process filters out uniform, extended emission. An area of the sky with significant emission will only be recovered if it has some slope, otherwise it will be filtered out with the signal attributed to the sky. Thus, a uniform $3\sigma_{rms,pix}$ flux across an island's area is a conservative, rather than realistic, lower limit. The Jeans radius is calculated by inverting Equation 4.3, assuming the observed mass is the Jeans mass.

In Figure 4.12, larger objects are generally less dense, but more unstable, as expected. The majority of the 43 complex islands (79%) lie beyond the Jeans instability line (R_J) and all the islands beyond the second instability line ($2R_J$) are complex (19% of the complex sample). An object can be unstable to collapse and not fragment when it is only slightly too large (between R_J and $2R_J$), but for an island to remain monolithic above two Jeans radii, a non-thermal pressure support would be needed in addition to thermal energy to counteract gravity[5].

The bottom panel of Figure 4.12 shows the break-up of the larger islands into significant, individual fragments. We see several cases where the individual fragments drawn from complex islands are larger than two Jeans radii. The small-scale monolithic objects in both panels are fairly consistent with one another, indicating isolated regions have similar properties whether we lay a simple contour around the emission region (as we did for islands) or we employ the FellWalker algorithm (as we did for fragments). Between the two instability lines we see several cases of fragments that

[5]Note that if the molecular gas is indeed cooler than 15 K, each object will be shifted upward to higher densities (recall that assuming a temperature of 10 K results in masses which are a factor of three larger) and more of the complex islands would lie beyond the lines of instability. The lines of instability will also vertically shift as they vary linearly with temperature (e.g., a factor of 1.5 downward assuming 10 K as opposed to 15 K), but to a lesser degree than the density. We note that the majority of the large islands show signs of star formation via associations with YSOs. There are, however, a few special cases which will be explored in more detail in Section 4.5.4, below.

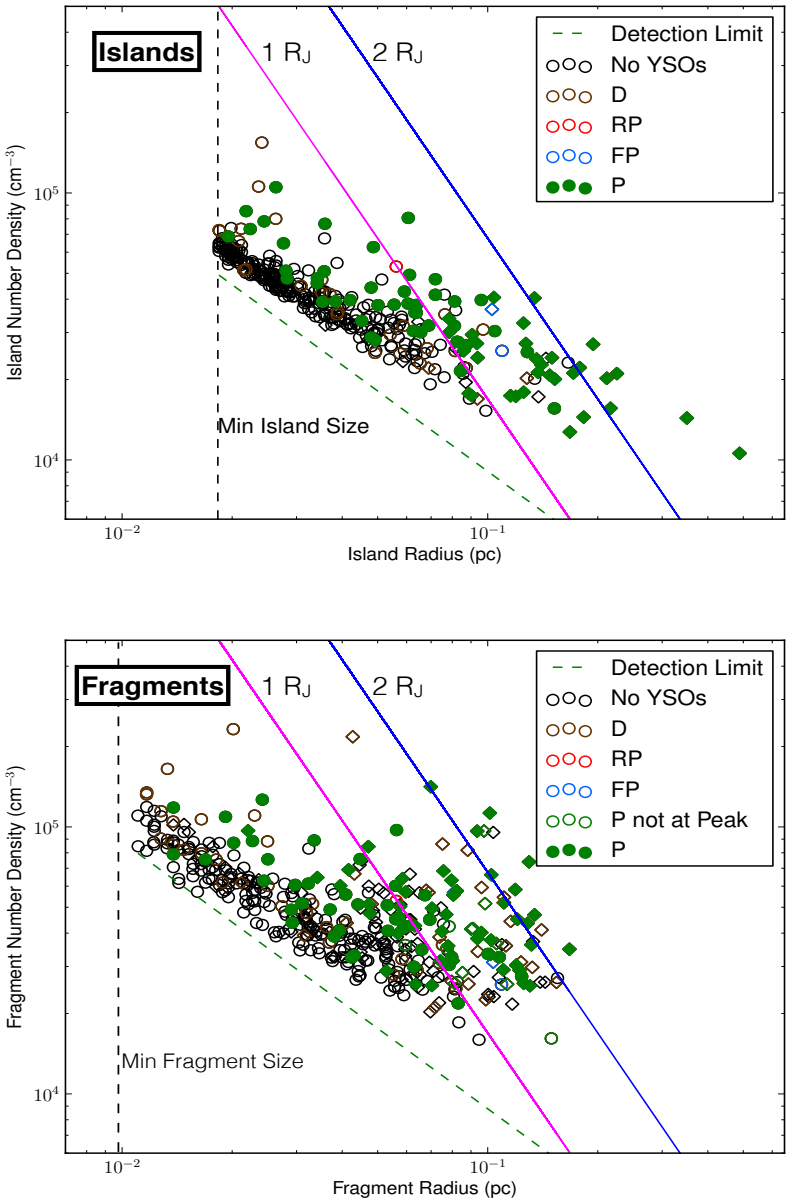

Figure 4.12 The number density of a given object assuming a spherical configuration versus the radius of the object's circular projection. The colour scheme follows Figure 4.10. *Top:* Islands; diamonds represent complex islands and circles represent monolithic islands. The green dashed line shows the detection limit. We chose the minimum island size such that every object had at least some measurable structure. *Bottom:* Fragments; diamonds represent fragments extracted from complex islands and circles represent fragments extracted from monolithic islands. Note that the smallest fragments were allowed to be smaller than the minimum island size. The magenta and blue lines show 1 Jeans radius and 2 Jeans radii, respectively.

do not have associated YSOs but which can be found in complex islands. There are also many interesting areas of seemingly unstable, starless dust emission (see Section 4.5.4), though new, deeper surveys such as VISION[6], however, may uncover previously undetected embedded protostars.

To investigate further the connection between fragmentation and star formation, Figure 4.13 shows histograms of Jeans radii for the fragments in monolithic islands (top) and complex islands (bottom), with separate distributions for all sources and for those sources with protostars residing less than 15" from the fragment peak flux position. In both panels, the percentages above each bar show the fraction of fragments within a particular bin that have a strong association with a known protostar. The top panel percentages reveal that more unstable ($R > R_J$) monolithic structures indeed show increasingly more evidence of star formation (except in the final bin which represents one curious object discussed further in Section 4.5.4). The bottom panel percentages, however, reveal the same cannot be said for fragments in more complicated, clustered environments. Here, it appears that more unstable structures within complex islands do not necessarily show more evidence of star formation. Although their parent islands may have protostars within their boundaries, there are still some significantly dense, unstable emission peaks which have no associations with YSOs. Such examples could indicate on-going collapse across a time longer than the collapse of a single core (i.e. clustered star formation may be more drawn out). Similar objects were noted in models by Mairs et al. (2014) (also see Offner et al. 2010 for more information on the simulations used in that study and a further analysis on fragmentation).

4.5.4 Starless Super-Jeans Islands

In Table 4.5, we present a list of starless islands in Southern Orion A which are good candidates for follow-up studies. Throughout this section, we highlight two islands which appear to be significantly gravitationally unstable, yet harbour no YSOs of any class (see Figure 4.14). For these two objects, there is no evidence from the existing *Spitzer* and *Herschel* catalogues that star formation is taking place. In the left panel of Figure 4.14, the central island (island index = 29) appears to be entirely monolithic with no sign of fragmentation, e.g., we calculate the M/M_J ratio of this object to be $\sim$4 with a concentration of 0.67. If there are no projection effects making this object

[6] `http://homepage.univie.ac.at/stefan.meingast/vision.html`

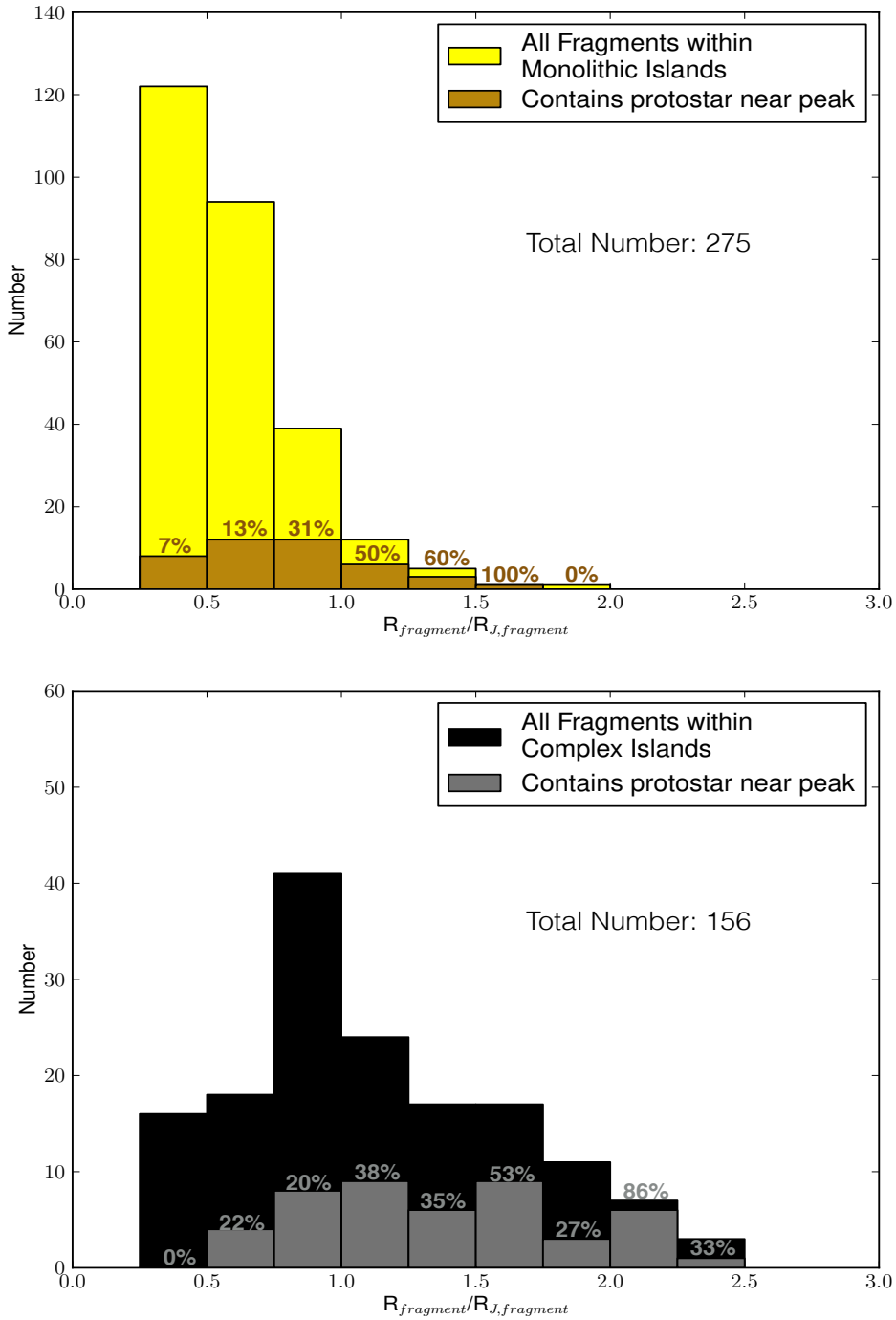

Figure 4.13 Histograms showing the total population of fragments extracted from monolithic islands (275 in total, 23 of which have no island association; *top*) and fragments extracted from complex islands (156 in total; *bottom*) in the context of each object's Jeans radius. The main histograms (light yellow in the top panel and black in the bottom panel) show all fragments within each classification whereas the secondary histograms (dark yellow in the top panel and grey in the bottom panel) show the fraction of fragments which contain a confirmed protostar within one beam width of the peak location. The percentages written are the fraction of the subpopulation which contains a protostar near the peak in each bin.

Table 4.5 A list of gravitationally unstable, starless islands. These objects are good candidates for follow-up studies.

Source (MJLSG)	Island ID	$\frac{\mathrm{M}}{\mathrm{M}_J}$	Conc.	Aspect Ratio	Monolithic/Complex
J053700.5-063711I	20	1.8	0.79	3.14	Monolithic
J053228.4-053420I	25	1.4	0.76	1.36	Monolithic
J053511.0-061400I	29	3.7	0.67	1.25	Monolithic
J053509.8-053754I	45	1.4	0.59	1.10	Monolithic
J053550.8-054142I	33	2.9	0.67	1.15	Complex[a]
J053622.8-055618I	38	1.9	0.73	1.01	Complex[b]
J053403.9-053412I	63	1.9	0.60	5.29	Complex[c]

a. Both fragments are also gravitationally unstable with $\frac{M}{M_J}$ ratios of $\sim$2 and $\sim$3.
b. Both fragments are also gravitationally unstable with $\frac{M}{M_J}$ ratios of $\sim$7 and $\sim$5.
c. Both fragments are nearly gravitationally unstable with $\frac{M}{M_J}$ ratios of $\sim$1.

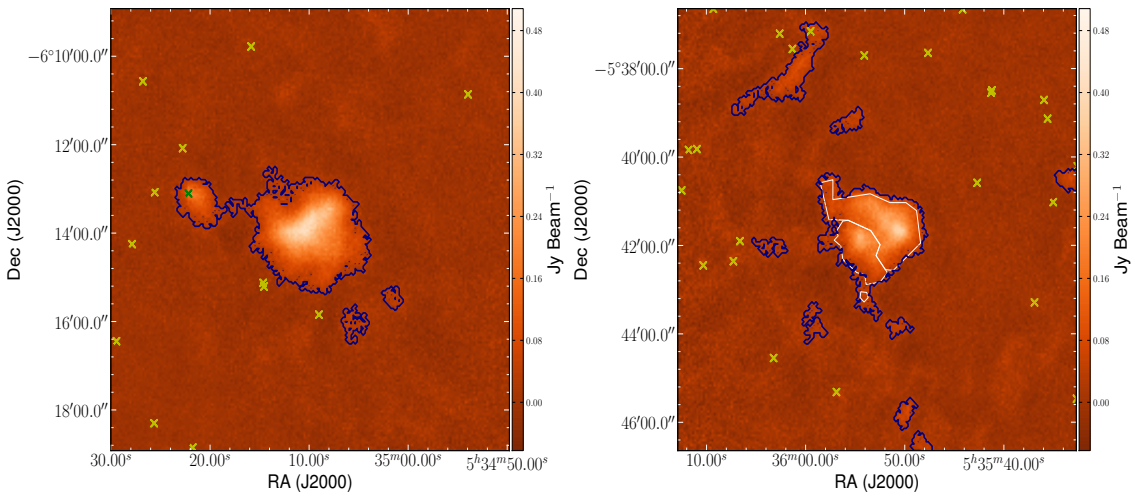

Figure 4.14 Islands which are calculated to be unstable to gravitational collapse yet harbour no evidence of associated YSOs of any class. The blue contours indicate the boundaries of the island and white contours indicate the boundaries of selected fragments. Note that we do not show the singular fragment in the main island in the left panel to emphasise that it is monolithic. Crosses denote YSOs colour coded as in previous figures and outlined in the text (protostars appear in green; disc sources, however, have been shown in yellow so that they are more visible). The colour scale has been chosen to accentuate the main islands of interest. *Left*: A monolithic island with an M/M_J ratio of $\sim$4. The secondary structure to the left of centre is its own island, separate from the main emission region. *Right*: A complex island wherein the two main fragments have M/M_J ratios of $\sim$2 and $\sim$3 from left to right, respectively.

appear larger and brighter than it truly is due to line-of-sight superposition, there are four scenarios which could explain its existence.

1. There are indeed deeply embedded protostars which cannot be detected by *Spitzer* because the optical depth is too high or the protostars are too faint. The Orion A Molecular Cloud has a lot of bright, diffuse infrared emission which can obscure faint protostellar sources (see Sadavoy et al. 2010b for a further discussion). Note that the Stutz et al. (2013) *Herschel* catalogue does not cover this particular island.

2. The M/M_J ratio is slightly overestimated because the gas in this region is hotter than 15 K. Even with a 5 K difference, however, the island would still have an M/M_J ratio of $\sim$2. We also note that preliminary results from temperature maps derived by Rumble et al. (in prep) suggest that the temperature for this specific island is 14 K.

3. The mass in the island has been assembled using a non-thermal support mechanism such as turbulent or magnetic pressure and it is out of thermal equilibrium.

4. The island is still very young and has not had the time to form protostars yet. This island may be a good follow-up location for a first hydrostatic core, an early stage of star formation which has long been theorised in the literature (Larson, 1969).

5. This island is not associated with the Orion Molecular Cloud. If this object lies in the foreground of Orion by a significant distance, the Jeans mass ratio would be overestimated.

In the right panel of Figure 4.14, we see a similar island (island index = 33) but in this case, the object is complex. In total, the island has an M/M_J ratio of $\sim$3 so the observed multiple fragments are consistent with our expectation. Each of the two main fragments, however, are themselves Jeans unstable with M/M_J ratios of 2 and 3, respectively (from left to right), and concentrations of 0.65 and 0.61, respectively. Thus, even if the island is the result of line of sight coincidence, each individual object is both super-Jeans and starless.

4.5.5 A Toy Model for the Spatial Distribution of Young Stellar Objects

In this section, we characterise the observed spatial distribution of disc sources and protostars from the Megeath et al. (2012) *Spitzer* catalogue with a toy model based on the locations of each YSO with respect to the fragments calculated to be Jeans unstable. Figure 4.15 shows the SCUBA-2 850 μm map with the locations of the discs and protostars overplotted. It is clear from the Figure that the surface densities of these sources can be separated into two populations and we label as "clustered" (away from the edges of the map and close to fragments) and "distributed" (the sporadic sources at larger distances from the clustered objects around fragments). Recently, Megeath et al. (2016) studied the spatial distribution of YSOs in Orion A and found that the distributed population has a much lower fraction of protostars than the clustered population, suggesting that this is an older generation of YSOs. Stutz & Gould (2015) found evidence that the Orion A filament may be oscillating, so this distributed population of YSOs may have no association with the dense gas observed as the gas itself has moved away from this generation of forming stars, creating a "slingshot" mechanism.

With a simple model, we attempt to recreate simultaneously both the clustered and distributed populations of YSOs using a few assumptions.

1. The lifetimes of large-scale emission structures are much longer than those of individual discs and protostars such that the currently observed structures are linked to the formation of young stars and their present distribution.

2. All observed YSOs formed in fragments which are calculated to be Jeans unstable and every Jeans unstable fragment has the same probability of producing a YSO.

3. The half-life age of discs is estimated to be $t_{0.5} = 2$ Myr (Mamajek 2009; also see Alexander et al. 2014 for a discussion of disc dispersal) and we detect no discs older than 10 Myr. We choose 10 Myr as a hard limit for two reasons. First, it is unlikely that a YSO older than 10 Myr would have enough surrounding material to achieve a suitable signal to noise ratio to be visible in our 850 μm map (see Dunham et al. 2015 for a review of YSO lifetimes). Second, a YSO moving at a reasonable velocity has a high probability of being ejected from the SCUBA-2 footprint of Southern Orion A within 10 Myr.

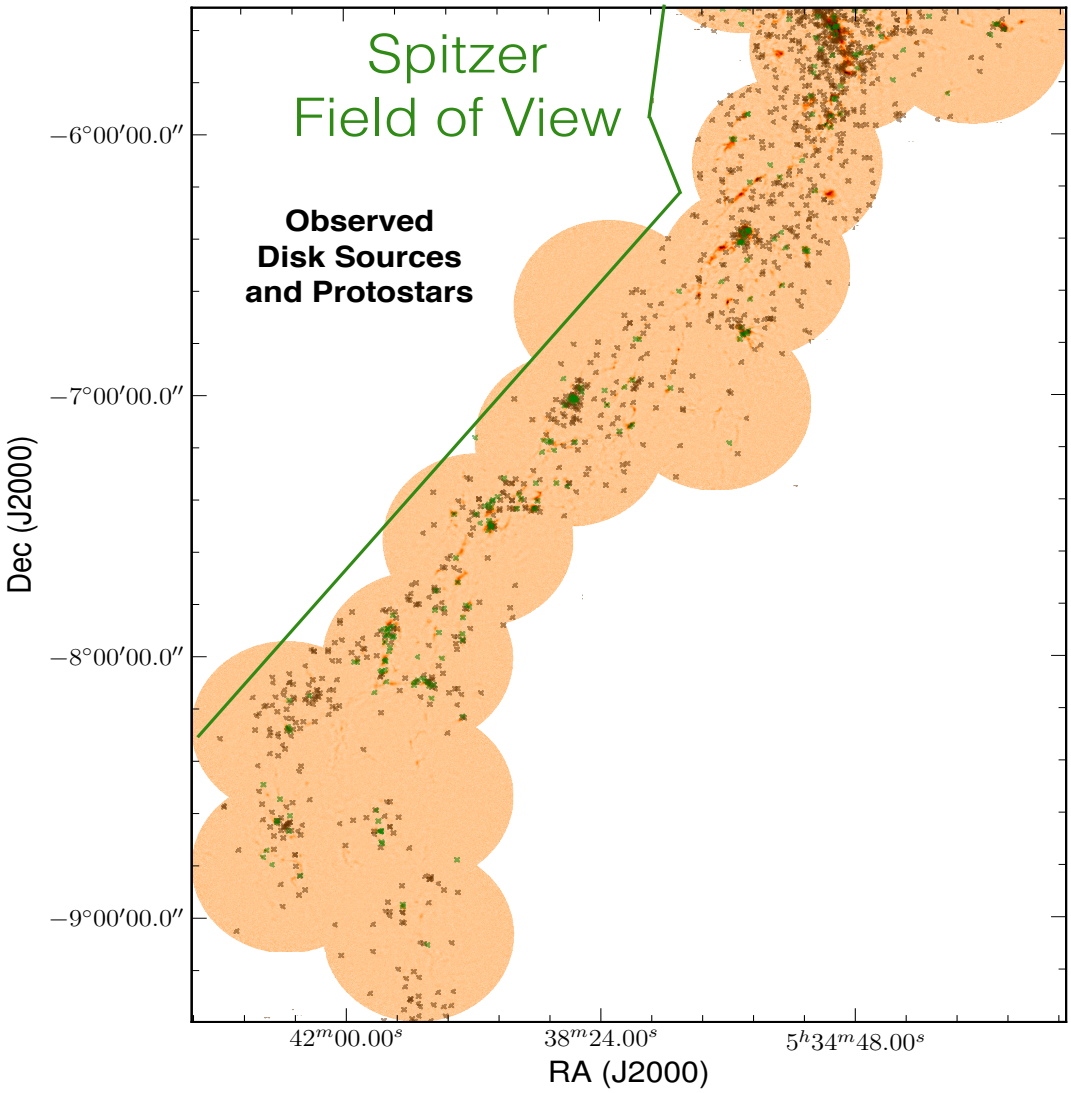

Figure 4.15 The observed spatial distributions of discs (brown) and protostars (green) plotted over the map of Southern Orion A. The positions of these sources have been taken from the Megeath et al. (2012) and Stutz et al. (2013) catalogues.

4. We define protostars to have an age ≤ 0.5 Myr (Dunham et al., 2015).

5. Discs and protostars are ejected in a random (3D) direction from their parent fragment (see Stutz & Gould 2015 for an alternative model).

6. The space velocities of the observed YSOs follow a Maxwell-Boltzmann distribution with a fixed most probable speed, v_p (see below).

For the combined number of discs and protostars present in the map, we first assign for each object a random age between 0 Myr and 10 Myr (assuming a uniform distribution). Then, we determine whether that age corresponds to a protostar or a disc source (see Assumption 4, above) and randomly determine the likelihood, l, that a YSO of that age is detectable based on the half-life age of a disc source ($l = 0.5^{\left[\frac{\text{age}}{t_{0.5}}\right]}$). If the disc source is "not detected", we do not calculate a speed or direction for it, we simply start the code again until we detect the same total number of discs and protostars present in the observed map. The ratio of the numbers of protostars to discs derived through this sampling remains relatively constant and reflects the observed populations to within 7%.

Next, to determine the locations of the protostars and discs which are detected, we select a random speed, v, from a Maxwell-Boltzmann distribution with a specified most probable speed, v_p:

$$\text{PDF}_{Max-Boltz} = \left(\frac{1}{v_p\sqrt{\pi}}\right)^3 4\pi v^2 e^{-\left(\frac{v}{v_p}\right)^2}. \tag{4.6}$$

Ten v_p values were tested from 0.1 km s^{-1} to 1.0 km s^{-1}. Finally, a random 3D direction is selected from an origin representing the location of the peak emission pixel within a selected Jeans unstable fragment, and we calculate the projected distance traveled during the lifetime of the YSO at the constant velocity drawn from Equation 4.6.

The top panels of Figure 4.16 show histograms of the new, "detected" protostar locations based on chosen v_p values of 0.2 km s^{-1} and 0.5 km s^{-1}, respectively, along with the observed distribution. It is important to note that fitting the model protostar projected distances to the observed data in the first few bins is more important than the extended tail. The observed protostars in the extended tail are unlikely to be true Class 0+I or flat-spectrum objects as they would need to have particularly

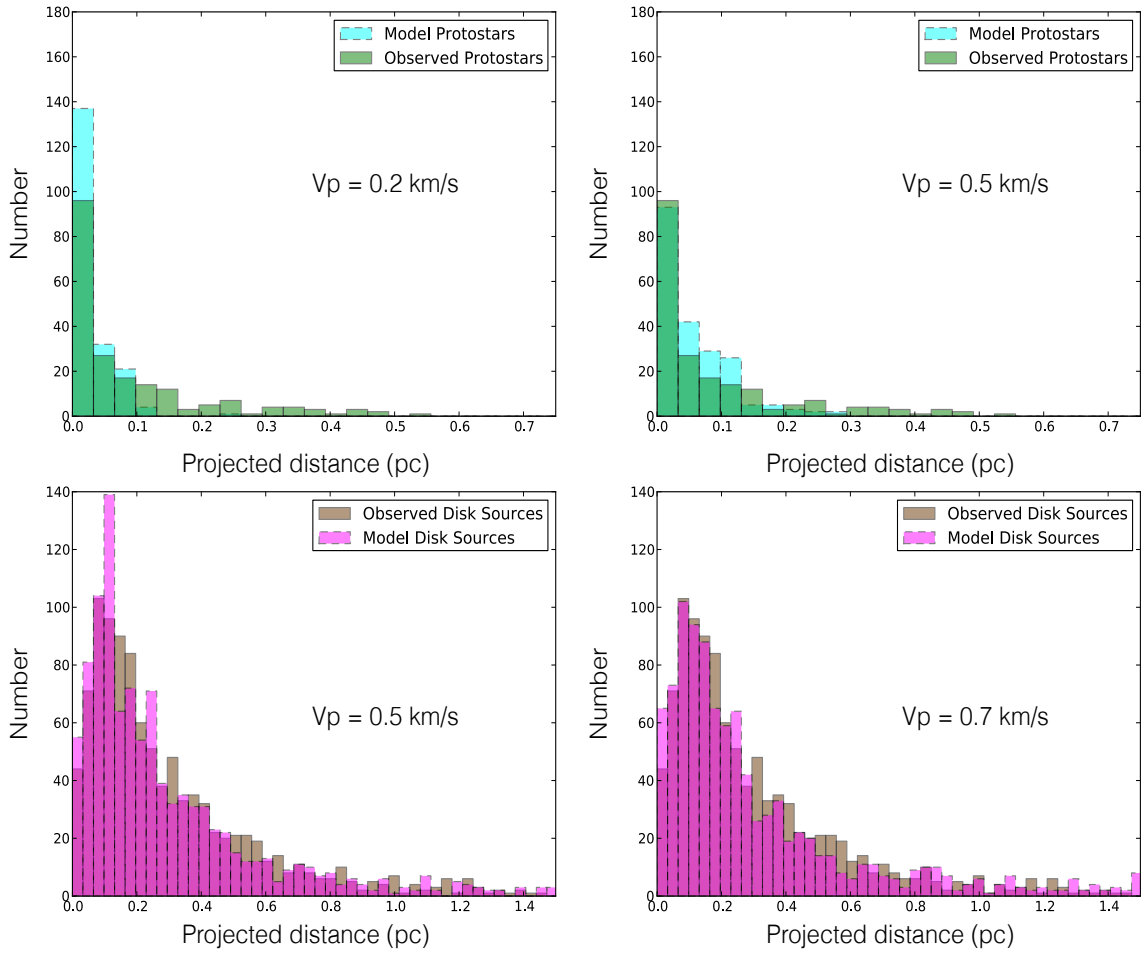

Figure 4.16 *Top Left:* The calculated projected distance between model protostar locations and the nearest fragment peak brightness location assuming $v_p = 0.2$ km s^{-1} in Equation 4.6 (cyan, dashed lines) plotted along with the observed distribution (green, solid lines). We only include YSOs which lie on pixels within the SCUBA-2 footprint of Southern Orion A. *Top Right:* Same as top left, but with a v_p value of 0.5 km s^{-1}. *Bottom Left:* The calculated projected distance between model disc source locations and the nearest fragment peak brightness location assuming $v_p = 0.5$ km s^{-1} in Equation 4.6 (magenta, dashed lines) plotted along with the observed distribution (brown, solid lines). *Bottom Right:* Same as bottom left, but with a v_p value of 0.7 km s^{-1}.

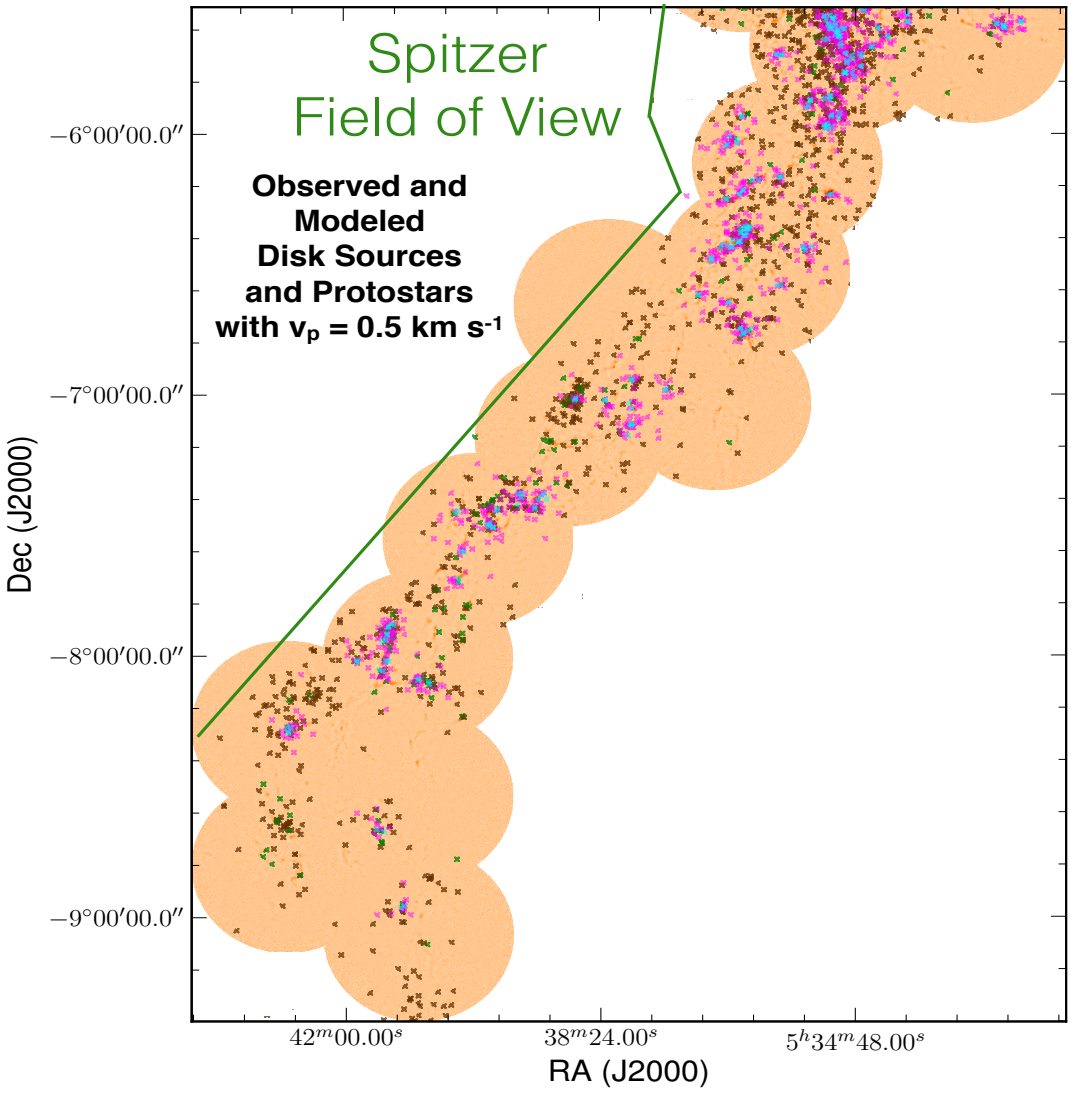

Figure 4.17 The distributions of observed discs (brown), observed protostars (green), model discs (magenta), and model protostars (cyan) plotted over the 850 μm map of Southern Orion A for a v_p value of 0.5 km s^{-1}.

high velocities or advanced ages to have travelled projected distances of more than 0.1 - 0.2 pc. Recall from Section 4.5 that based on the brightness underlying the protostars in the 850 μm continuum map, we expect up to 28% of these objects to be misclassified. We find that 40 to 45 of the 209 total modelled protostars (20 to 22%) lie beyond 0.1 pc in projected distance from their parent fragment (also see the bottom panel of Figure 4.9).

As Figure 4.16 (top left) shows, selecting 0.2 km s^{-1} as the most probable speed somewhat overestimates the number of protostars that are very close to Jeans unstable fragments. Selecting 0.5 km s^{-1} (Figure 4.16, top right), however, overestimates the number of protostars in the second, third, and fourth bins where we expect to find only a few "real" protostars. Thus, the v_p value which best fits the observed projected distances between protostars and fragment peaks is between 0.2 km s^{-1} and 0.5 km s^{-1} assuming the same v_p value applies to the entire Orion A filament. To test the accuracy of this toy model, each set of protostar projected distances produced within this range reasonably fit the data. If the speed is decreased below 0.2 km s^{-1}, the model protostars are too clustered near their parent fragments compared to the observed data while an increased speed above 0.5 km s^{-1} does not recreate this clustered population accurately.

Note that Jørgensen et al. (2007) observe the young, Class 0 protostellar population of the Perseus Molecular Cloud to have a velocity dispersion that is comparable to the sound speed $c_s \simeq 0.2\,\mathrm{km\,s^{-1}}$ in this region. More recently, Frimann et al. (2016) synthetically observed the distribution of Class 0 protostars within the MHD simulation RAMSES and noted that the young, protostellar population has a 2D velocity dispersion of $\sim$0.15 km s^{-1}. In the same analysis, Frimann et al. (2016) also note that the protostellar velocity distribution resembles a log-normal function in the simulations as opposed to our assumed Maxwell-Boltzmann distribution. A log-normal distribution will have a much higher fraction of high velocity sources that would travel further distances from their places of origin in the same amount of time. Frimann et al. (2016) also assumed the age of a Class 0 protostar to be $\leq$0.1 Myr. Note, however, that we follow the protostellar definition from Megeath et al. (2012) that also includes Class I and Flat-spectrum sources in addition to Class 0 objects. Thus, we expect our best fitting v_p values to be somewhat higher in comparison (see below).

In Figure 4.17, we plot the same observed objects as in Figure 4.15 but we now include the model protostars (cyan) and discs (magenta) produced assuming a v_p

value of 0.5 km s^{-1}. In this figure, we see that the overall spatial distribution of model protostars is well matched to that of the observations. Note, however, that Figure 4.17 shows isolated observed protostars (green crosses) that do not lie near the model protostar positions (cyan crosses). This difference results from the fact that we do not consider every fragment to be producing YSOs, only those which we calculate to be Jeans unstable. While this assumption holds true in many cases, clearly there are other fragments which we do not calculate to be Jeans unstable that are also associated with protostars. Our interpretation is that these objects are either more-evolved protostars (e.g. Class I/flat spectrum sources) and thus have had time to blow away much of their outer material (i.e. remnants of what were unstable islands/fragments) or are simply misclassified objects.

The bottom left panel of Figure 4.16 shows the projected distance between the model disc sources and fragment peaks, assuming $v_p = 0.5$ km s^{-1}. This histogram is too peaked relative to the observations. This difference can be seen more clearly in Figure 4.17 where the more distributed population of observed disc sources is not well matched to the positions of the model discs. For the observed discs to have formed in the currently observed emission structure and then migrated to their present locations they either have to live longer (half-life $>$ 2 Myr) or be moving at faster speeds than we are assuming. Possibly, these older objects have undergone a velocity evolution due to a more complicated gravitational interaction history than their younger counterparts. Thus, it is reasonable to assume that they may have a higher v_p than the protostars. We suggest a v_p value of 0.7 km s^{-1} to represent better the observed, distributed disc sources (see the bottom right panel of Figure 4.16).

Note that there appears to be a trend in the velocity with YSO class. Jørgensen et al. (2007), Frimann et al. (2016) and references therein find the velocity dispersion of Class 0 objects to be $\sim$0.1-0.2 km s^{-1}. In this analysis, we find that the population of Class 0, Class I, and flat spectrum sources (the protostars) can be fit reasonably with most probable velocities in the range of $\sim$0.2-0.5 km s^{-1}.We find that the Class II objects (the disc sources) have a most probable velocity of $\sim$0.7 km s^{-1}. These velocities, however, are highly dependent on the lifetimes of each type of object.

Direct measurements of the velocity dispersion of young (1 - 2 Myr; Class II) stars were measured by Foster et al. (2015) in the NGC 1333 star-forming region as part of the INfrared Spectra of Young Nebulous Clusters (IN-SYNC) project (Cottaar et al., 2014). In this region, Foster et al. (2015) find that their sample of young stars have a velocity dispersion of 0.92 ± 0.12 km s^{-1}. This is significantly higher than Offner et al.

2009b's predicted velocity dispersion based on a turbulent star-forming simulation as well as the velocity dispersion of dense cores in the region of $0.51 \pm 0.05\,\mathrm{km\,s^{-1}}$ as measured by Kirk et al. (2007) using N_2H^+(1-0) observations. Evidently, the velocity dispersion of YSOs in NGC 1333 appears to increase quickly after their formation (Foster et al., 2015) which is consistent with our results in Southern Orion A.

4.6 Conclusions

In this paper, we present the first-look analysis for the Southern Orion A (south of $\delta = -5{:}31{:}27.5$) SCUBA-2 continuum maps observed by the JCMT Gould Belt Survey, concentrating on the 850 μm results. At a distance of 450 pc, the Orion A Molecular Cloud is a nearby laboratory for examining active star-formation sites with the relatively less-studied southern extent offering a wealth of objects to aid in a better understanding of the dominant physical processes present in the region. We identify structures in the map using two-step procedure to find islands and fragments, the former based on a simple flux threshold and the latter defined using the algorithm JSA_CATALOGUE (see Section 4.4). We then examine the column-density map derived from 2MASS extinctions (Lombardi, M. private communication) for the whole of Southern Orion A, the islands, and the YSOs to characterise the large-scale context to which our SCUBA-2 map is not sensitive (see Section 4.4.4). We show the mass distributions and comment on the concentration of fragments in terms of their Jeans stability (see Sections 4.4.2 and 4.5.2). We then discuss the number density of the identified emission structures in terms of their Jeans radii and highlight two examples of starless, super-Jeans objects which merit a follow-up study with kinematic information (see Section 4.5.3).

Using the Megeath et al. (2012) and Stutz et al. (2013) *Spitzer* and *Herschel* YSO catalogues, we associate protostars, protostar candidates, and disc sources with the detected islands and fragments. We also discuss the YSO population itself by measuring the 850 μm intensities at the locations of each object (as well as the column densities derived from the extinction map) and the distances between each object and its nearest localised SCUBA-2 emission peak. To extend this analysis further, we examine the spatial distributions of disc sources and protostars in more detail by constructing a toy model of their locations based on simple assumptions and compare them with those of observations (see Section 4.5). The 450 μm and 850 μm maps, their associated variance maps, and the island and fragment catalogues are all publicly

available at: https://doi.org/10.11570/16.0007.

Our main results are enumerated below.

1. There are emission structures with a variety of sizes, flux levels, and morphologies present in Southern Orion A (see Figure 4.2). As expected from local Jeans lengths, many large islands are often subdivided into multiple localised fragments (see Figures 4.5 and 4.12). There are, however, several objects which require further study (see Table 4.5 and Section 4.5.4).

2. Fragments are significant sites of star formation (see Figures 4.10 and 4.12). We find that those fragments that are Jeans unstable tend to have higher concentrations than those fragments that appear stable.

3. The most Jeans unstable, monolithic structures show the most evidence for ongoing star formation due to their associations with protostars near the peak brightness location (see Figure 4.13). This is in contrast to fragments extracted from complex islands (i.e., they have siblings in their parent cloud). Starting at an M/M_J ratio of 1, these latter objects do not necessarily show more evidence of star formation at higher degrees of instability (see Figure 4.13) implying clustered star formation may be more drawn out.

4. Class 0+I and flat-spectrum sources have higher associated 850 μm brightness values and are closer to the nearest fragment's peak emission than their more-evolved disc counterparts. We find a similar result as Heiderman & Evans (2015) in that only $\sim$72% of the objects defined as Class 0+I and flat-spectrum protostars are above a significant flux threshold, suggesting that some of the protostars identified in previous surveys may be misclassified.

5. The observed spatial distribution of disc sources across Southern Orion A has a "clustered" population and a "distributed" population. We can reproduce the projected distances between protostars and their nearest fragment reasonably well by using a simple toy model. Assuming a Maxwell-Boltzmann velocity distribution for these objects, we derive a range of most probable velocity values, $v_p = 0.2-0.5$ km s^{-1}, which reasonably fit the spatial distribution of protostars observed by Megeath et al. (2012) and Stutz et al. (2013). The model disc source locations, however,

do not recreate the distributed population in Southern Orion A using the same v_p values. There appears to be a trend in velocity with respect to YSO classes. We find the Class II objects (the disc sources) require a v_p value of 0.7 km s^{-1} (see Figure 4.16).

4.7 Appendix

In this section, we perform a brief comparison between the Southern Orion A 850 μm map which has had the CO(J=3-2) emission removed and the 850 μm map where it has not been removed. Figure 4.18 shows the relative locations of the fragments detected in each map using the JSA_CATALOGUE algorithm. The magenta squares represent the peak locations of fragments that were found in the map containing no CO(J=3-2) emission and the black crosses denote peak locations of fragments found in the map containing CO(J=3-2) emission. It is clear that the subtraction of this broad emission line has a minimal effect on the detected structure throughout the entire Southern Orion A region. The occasional ($\sim$ 2%) fragments which have no counterpart are small areas of low-level emission that do not have any significant bearing on the final results.

In Figure 4.19, we plot the peak flux values of the fragments which coincide in each of the two maps. If a fragment in one map has a peak pixel location within one beam diameter (15″) of the peak pixel location of a fragment in the other map, it is included in the plot. 408 out of 431 fragments met this condition. The solid black line in the Figure shows a 1:1 ratio. Evidently, even the faintest peak brightness values are not significantly altered when the CO(J=3-2) emission line is subtracted from the 850 μm continuum emission.

To see how structure is affected on larger scales before and after the CO subtraction, we first identify islands in the 850 μm map that includes emission from the CO(J=3-2) line and measure their total fluxes. We then compare these values to the total fluxes measured within the same boundaries using the map which has had the CO subtracted. Figure 4.20 shows the results for all these islands, and in Figure 4.21, we split the results into three sections that highlight low total flux, medium total flux, and high total flux, zooming in for clarity.

In general, we find that the CO-subtracted islands match well the emission from the non-subtracted islands, suggesting that the CO emission is a minor contribution to the total flux. We see in the medium and high total flux regimes, the islands follow a

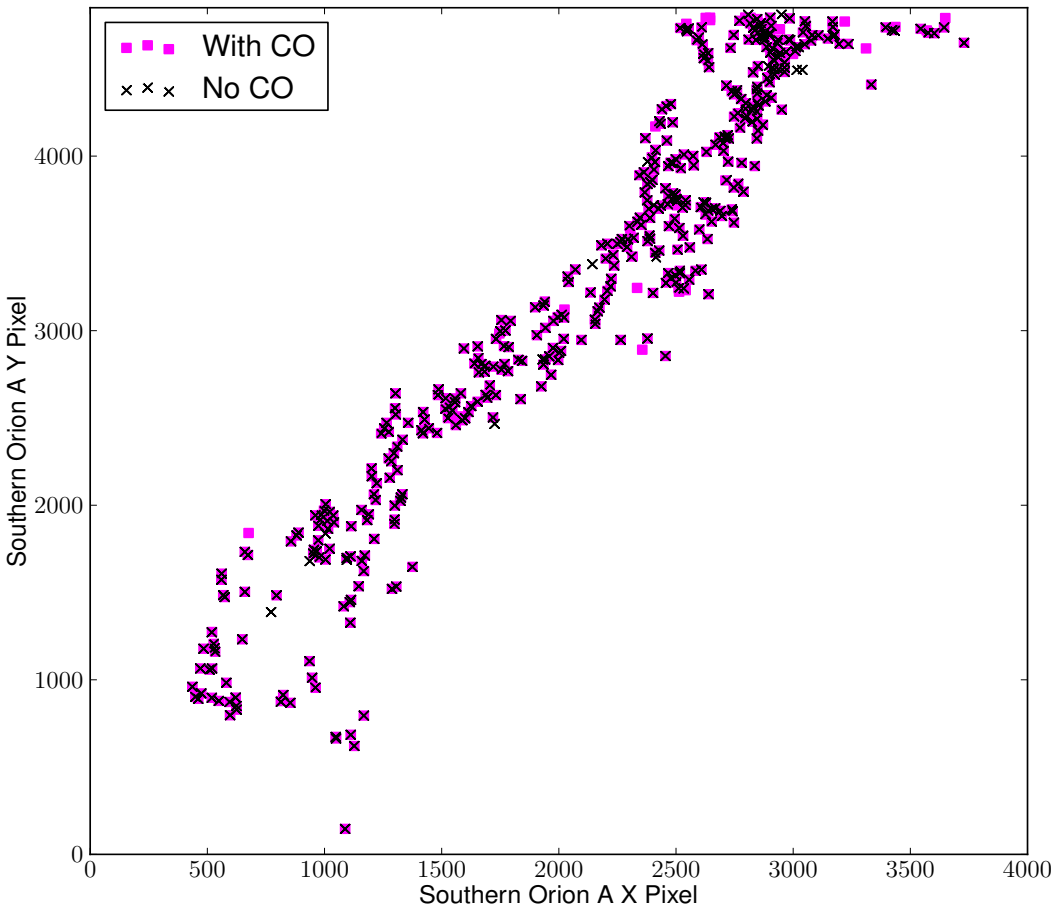

Figure 4.18 The relative locations of detected fragments detected using the JSA_CATALOGUE algorithm in the Southern Orion A map where the CO(J=3-2) emission has been subtracted (magenta squares) and the map which includes the CO(J=3-2) emission (black crosses).

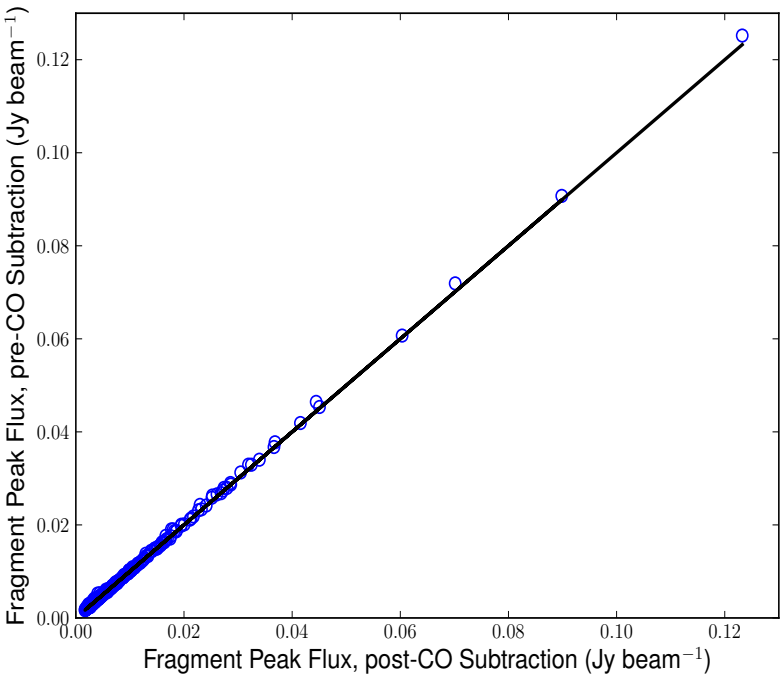

Figure 4.19 The peak flux values of the fragments detected in each map (with and without the CO(J=3-2) emission). The solid, black line is a 1:1 ratio.

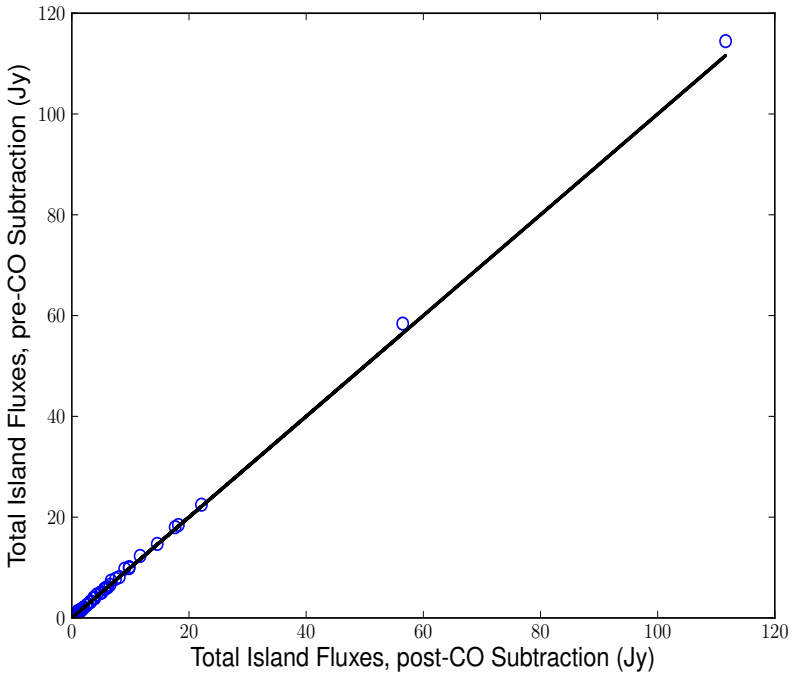

Figure 4.20 The total flux values of the islands detected in each map (with and without the CO(J=3-2) emission). The solid, black line is a 1:1 ratio.

1:1 relationship and they do not vary more than 10%. This is approximately the error associated with flux calibration of the images. In the low total flux regime, however, we see more scatter. The lowest flux objects are not of any particular concern as they will have little bearing on the results and they are clustered quite close to the 1:1 line. We highlight the two sources which are the most affected by the CO subtraction using red circles (although they are both below the 3σ level of the scatter). These two islands are found near the northern border of the map. They are both $\sim$0.2 pc in diameter assuming a circular projection, starless, and faint. Therefore, including or subtracting the CO emission from these small sources will not affect any of the main conclusions in this analysis. In the map that has undergone CO subtraction, one of these islands breaks up into two components (J053318-053421I and J053313-053506I) while the other remains one single structure (J053556-053418I). None of these small features have been analysed in previous literature and they were not included in the SCUBA catalogue constructed by Di Francesco et al. (2008b).

In summary, it does not appear that CO(J=3-2) line contamination has any significant effect on the Southern Orion A 850 μm continuum data. In the analysis performed in this paper, we used the CO subtracted SCUBA-2 maps. Both, however, are available online.

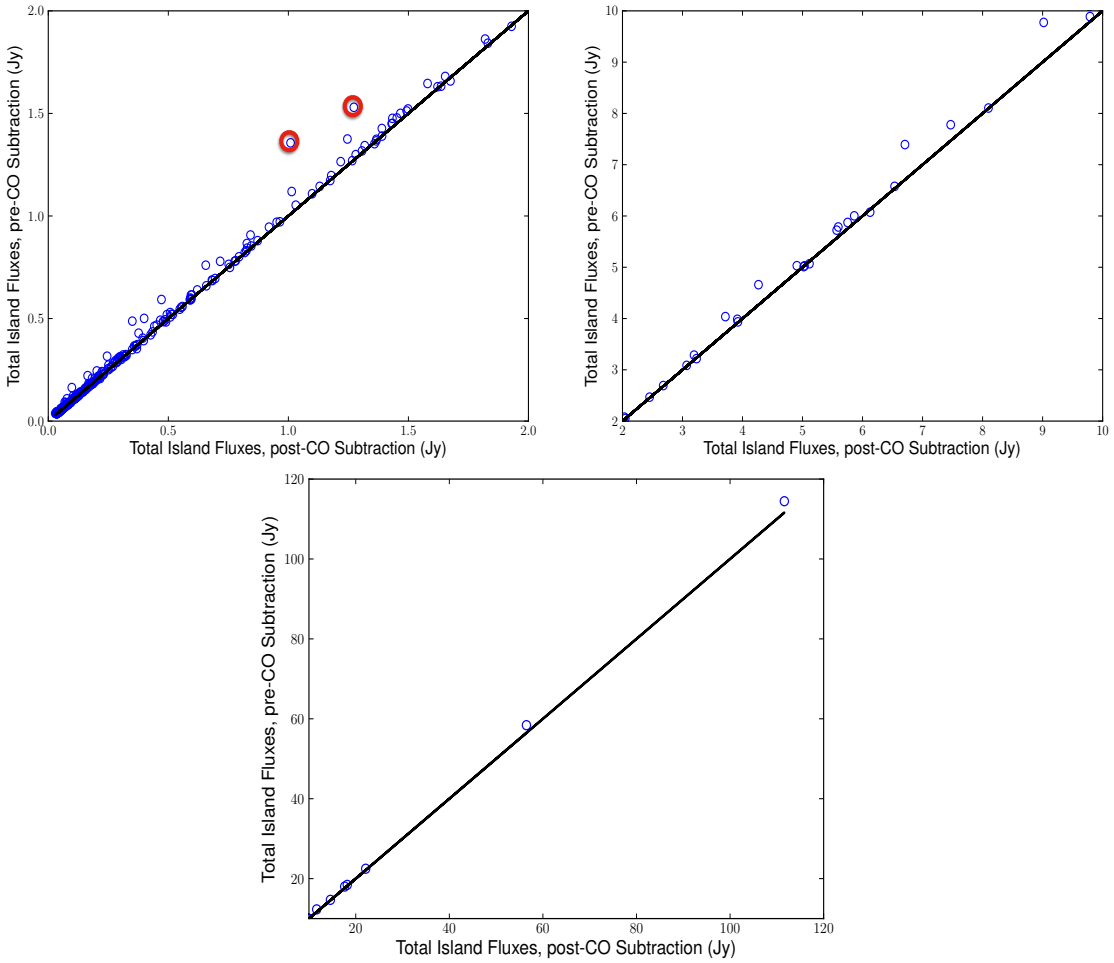

Figure 4.21 Same as Figure 4.20, but zoomed in to three sections for clarity. The solid, black line is a 1:1 ratio. *Top left*: Low total flux. The two red circled islands are the sources which were most affected by the subtraction of the CO line emission. *Top Right*: Medium total flux. *bottom*: High total flux.

Chapter 5

The JCMT Transient Survey: Data Reduction and Calibration Methods

"Take the sun.
Take the moon.
Take the earth and watch it move..."
-Kari Jobe, Stars in the Sky

5.1 Foreword

Throughout the duration of the analysis presented in the previous chapter (connecting larger and smaller scale dust structures in continuum maps and investigating their association with YSOS), I became increasingly interested in how protostars evolve and how submillimetre observations could provide information on deeply embedded YSOs. In Section 1.3, I introduced *The Luminosity Problem* and described the JCMT Transient Survey: the first survey to consistently observe several nearby star-forming regions at submillimetre wavelengths at a regular cadence in order to identify variable sources and constrain theoretical simulations of episodic accretion modes.

The JCMT Transient Survey began in December, 2015 and will continue through at least January, 2019. As part of the initial team which prepared the proposal, I helped select the eight target regions from the Gould Belt Survey coverage (see

The material presented in this chapter (excluding the foreword) has been published in the Astrophysical Journal: Mairs et al. 843, 55, 2017. DOI: 10.3847/1538-4357/aa7844.

Chapter 3 and Ward-Thompson et al. 2007c). Collectively, these regions contain more than 250 protostars (Class 0+I) and 1400 disc sources (Class II YSOs). In order to take full advantage of this unprecedented dataset that will provide the deepest submillimetre maps of these eight regions to date, it was necessary to derive post-reduction image alignment and relative flux calibrations to significantly improve the survey's sensitivity to continuum brightness variations.

Telescopes are not perfectly consistent devices. Nominally, the JCMT has a pointing error of 2-6″ relative to a beam size of ∼15″ at 850 μm. This means that repeated observations of the same region will not place the location of the peak flux of an identified core at the same position and these slight shifts introduce a source of error in measuring the relative peak brightness changes of a population of sources, especially when, for example, differencing images. Similarly, the absolute flux uncertainty for SCUBA-2 observations is $\sim 8-10\%$ in the best conditions (see Dempsey et al. 2013 and Section 5.5). This means that a 3σ detection of a brightness variation would only be possible if a source varied by 30%. While this is certainly possible, current models predict that large outbursts are much more rare than smaller outbursts (see Figure 1.9; Bae et al. 2014; Vorobyov & Basu 2015) so the likelihood of detecting episodic and/or secular accretion dramatically increases with improved sensitivity.

In this paper (Mairs et al., 2017), I develop and present the best practices for reducing SCUBA-2 data with the goal of detecting brightness variations associated with compact emission as well as the full image alignment and relative flux calibration procedures which make detecting variable sources possible. By identifying bright, compact sources and fitting them with Gaussian profiles, I am able to achieve a spatial alignment of 1″ between repeated observations and a relative flux calibration uncertainty of 2.5%, a combination which is unprecedented for large aperture single-dish telescopes operating at these wavelengths. This means that sources which vary in brightness by only 10% would be significant detections, dramatically improving the probability of detecting interesting sources.

In fact, the initial robust detection of the first variable source discovered by Yoo et al. (submitted), using JCMT Transient Survey data was possible due to this improvement in flux calibration. The source, a previously known periodic variable at infrared wavelengths, called EC 53 (Hodapp et al., 2012) was detected to be significant on its initial rise (September 29$^{\text{th}}$, 2016; see Figure 5.1 where EC 53 is compared to a non-varying, calibrator source) which allowed the Transient Survey team to request more frequent observations in and around its peak brightness in order to compare the

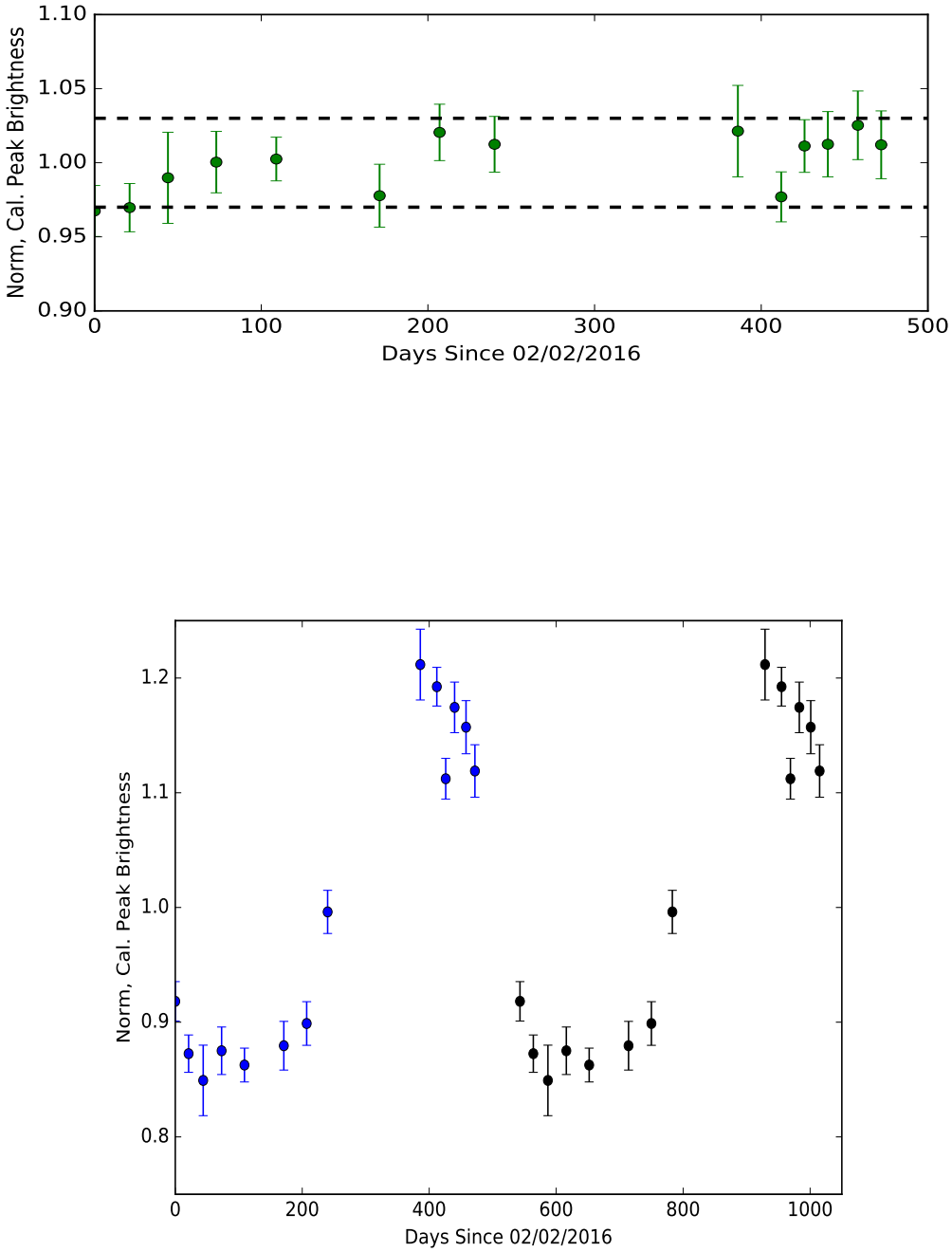

Figure 5.1 *Top:* The measured, normalised brightness of a typical, non-varying source in the same observed field as EC 53 over several observations (Yoo et al., submitted). *Bottom:* The measured, normalised brightness of EC 53 over several JCMT Transient Survey observations and the same observations repeated (black) to show the variable nature of EC 53 discovered by Hodapp et al. (2012) at infrared wavelengths.

submillimetre light curve with the previously measured infrared light curve.

As part of the reduction analysis process, I have designed these post-reduction image calibrations such that they can be applied to any repeated SCUBA-2 observations and can be adjusted for different instruments. Currently, the Gould Belt Survey team is investigating the image alignment methods for future data releases and in Chapter 6, I apply these calibrations to compare source brightnesses over several year timescales using both GBS and Transient Survey data.

In addition to employing these reduction and calibration methods to all JCMT Transient Survey data, I have also maintained leadership of the survey's data management practices. This has included designing infrastructure to obtain results (both automatically and semi-automatically) and produce calibrated images on efficient timescales, managing the data access for the 68 survey members, and addressing individual, region specific issues and requests. This has given me the opportunity to host JCMT data reduction workshops at the Transient Survey team meetings and I have produced many team specific resources including reduction and analysis tutorials for new JCMT users.

Abstract

Though there has been a significant amount of work investigating the early stages of low-mass star formation in recent years, the evolution of the mass assembly rate onto the central protostar remains largely unconstrained. Examining in depth the variation in this rate is critical to understanding the physics of star formation. Instabilities in the outer and inner circumstellar disk can lead to episodic outbursts. Observing these brightness variations at infrared or submillimetre wavelengths sets constraints on the current accretion models. The JCMT Transient Survey is a three-year project dedicated to studying the continuum variability of deeply embedded protostars in eight nearby star-forming regions at a one month cadence. We use the SCUBA-2 instrument to simultaneously observe these regions at wavelengths of 450 μm and 850 μm. In this paper, we present the data reduction techniques, image alignment procedures, and relative flux calibration methods for 850 μm data. We compare the properties and locations of bright, compact emission sources fitted with Gaussians over time. Doing so, we achieve a spatial alignment of better than 1$''$ between the repeated observations and an uncertainty of 2-3% in the relative peak brightness of significant, localised emission. This combination of imaging performance is unprecedented in ground-based, single dish submillimetre observations. Finally, we identify a few sources that show possible and confirmed brightness variations. These sources will be closely monitored and presented in further detail in additional studies throughout the duration of the survey.

5.2 Introduction

Although there have been many advances made in understanding low mass star formation over the past ten years (see, for example, Di Francesco et al. 2007b, Ward-Thompson et al. 2007b, André et al. 2014), the manner in which mass assembles onto a forming star remains a crucial open question. As Kenyon et al. (1990) first demonstrated, assuming the mass accretion process onto a young star occurs at a constant rate (steady inside out collapse; Shu et al. 1987) gives rise to "The Luminosity Problem": the empirical result that the median protostellar luminosity is measured to be approximately an order of magnitude less than the expected value. In recent years, this problem has been confirmed and emphasised by *Spitzer Space Telescope* observations through which even lower luminosities have been discovered (see Dunham et al. 2008, Evans et al. 2009a, Enoch et al. 2009, Dunham et al. 2013, Dunham

et al. 2014). One solution to this problem is that the accretion does not proceed at a constant rate. Rather, it occurs during episodic events which may be accompanied by outbursts that can be detected at infrared, submillimetre, and sometimes optical wavelengths (see McKee & Offner 2011b, Johnstone et al. 2013, and Scholz et al. 2013). There is indirect evidence that episodic accretion occurring while a protostar is still deeply embedded in its nascent gas and dust is an early phase of the more evolved FU Orionis (FUors; Herbig 1977, see also Hartmann & Kenyon 1985) sources (Dunham et al., 2014; Audard et al., 2014).

The physical mechanism responsible for a continuum outburst detected at the submillimetre wavelengths of interest to this survey is re-radiation from heated dust grains in the surrounding protostellar envelope. Outside of the JCMT Transient Survey, there have already been two millimetre sources (both embedded protostars) that have shown direct evidence of an active burst accretion phase accompanied by a dramatic brightening, HOPS 383 in Orion (Safron et al. 2015; using Atacama Pathfinder Experiment and SCUBA archive data), and MM1 in NGC6334I (Hunter et al. 2017; using Atacama Large Millimeter/submillimeter Array and Submillimeter Array data).

The JCMT Transient Survey (Herczeg et al. submitted) is a three year project dedicated to observing continuum variability in deeply embedded protostars at submillimetre wavelengths with the Submillimetre Common User Bolometer Array 2 (SCUBA-2; Holland et al. 2013). To this end, we are monitoring eight regions selected from the JCMT Gould Belt Survey (GBS; Ward-Thompson et al. 2007c) that have a high density of known protostellar and disk sources (Young Stellar Object Classes 0 to II and flat spectrum; see Lada 1987, Andre et al. 1993, and Greene et al. 1994) at an approximate 28 day cadence whenever they are observable in the sky. SCUBA-2 uses approximately 10,000 bolometers subdivided into two arrays to observe at both 450 μm and 850 μm simultaneously. While we expect sources undergoing an accretion burst event to show a stronger signal at 450 μm (Johnstone et al., 2013), in this paper we focus only on the 850 μm data. The noise levels in 450 μm maps are much more dependent on the weather than their 850 μm counterparts, causing the signal-to-noise ratio (SNR) to fall dramatically when there is more water vapour in the atmosphere. In addition, the beam profile is less stable than at 850 μm (as shorter wavelengths are more susceptible to dish deformation, and focus errors. For more information, see Dempsey et al. 2013) requiring careful attention in order to make precise measurements of compact objects. We thus start here by defining the 850 μm calibration and we will use this knowledge to calibrate the 450 μm data at a later

date. As the survey matures and precise 450 μm data calibration is achieved, these simultaneous observations will provide further confirmation of significant variations.

In order to track the peak brightnesses of submillimetre emission sources over each epoch, we test and employ a robust data reduction method and use multiple observations of the same regions to derive post-reduction image alignment and relative flux calibration techniques. Reducing SCUBA-2 data is a complex process with several user-defined parameters that affect the final image produced (for detailed information on SCUBA-2 data reduction procedures, see Chapin et al. 2013). A large amount of work has been invested in understanding the optimal data reduction parameters to use for differing science goals (see, for example, Mairs et al. 2015) depending on the scan pattern of the telescope and the amount of large-scale structure that needs to be robustly recovered. In all cases, the nominal JCMT pointing error is 2-6″ (East Asian Observatory staff, *private communication*) and the flux calibration is uncertain to ∼5-10% (Dempsey et al. 2013; see also, Section 5.5.2). While this is sufficient for most projects which use JCMT data, both of these uncertainties can be improved upon when there are multiple observations of regions with bright sources taken in a consistent manner. In this work, we seek to improve both the spatial alignment and the flux calibration of the JCMT Transient Survey data by approaching the problem from a relative point of view.

Properly matching faint, potential protostellar sources over the observed epochs and co-adding those observations with high precision for the highest SNR requires sub-pixel accuracy («3″ at 850 μm) in the spatial alignment. Similarly, if we were to use the nominal flux calibration, where the uncertainty is taken to be $\sigma \sim 10\%$, the flux would need to vary by 30-50% for a transient event to be deemed significant (3-5σ). Thus, our goal is to reduce this uncertainty by a factor of 3 to 5 (i.e. sigma $\sim 2 - 3\%$) by considering relative brightness changes over time and ignoring the absolute flux calibration. We will then be able to measure flux variations of $\sim 10\%$ to be statistically significant (>3σ). Several models predict smaller flux variations due to episodic accretion over few year timescales to occur much more frequently than large flux variations (see, for examples, Bae et al. 2014, Vorobyov & Basu 2015, and Herczeg et al. submitted). Observations like those performed throughout the JCMT Transient Survey will help constrain the current models. The techniques we have developed here can be applied to any JCMT data obtained in a similar manner, including archival data obtained by the GBS (follow up analysis by Mairs et al., in prep.). Thus, we are able to successfully align and relatively flux calibrate archival

data such as those which were obtained by the GBS and we include these data in a follow-up analysis (Mairs et al. in preparation).

This paper is organised as follows: In Section 5.3 we summarise the details of our SCUBA-2 observations. In Section 5.4 we outline our data reduction methods and showcase four tests we performed which altered the amount of large-scale structure recovered in a given map and the initial priors offered to the map-making pipeline in order to select the most robust techniques for our purpose of detecting transient events in deeply embedded protostars. In Section 5.5 we detail our source extraction, post-reduction spatial alignment, and relative flux calibration methods applied to all current JCMT Transient data. In Section 5.6, we present an analysis on the recovered compact emission sources and highlight objects of interest including the first demonstrably variable source in our survey (Yoo et al. submitted). Finally, we present our conclusions in Section 5.7.

5.3 Observations

The JCMT Transient Survey observations are performed simultaneously at 450 and 850 μm with effective beam sizes of 9.8″and 14.6″(Dempsey et al., 2013), respectively, using the Submillimetre Common User Bolometer Array 2 (SCUBA-2; Holland et al. 2013). We use the *pong 1800″* mapping mode (Kackley et al., 2010) which yields circular maps 0.5° in diameter called "pongs". Each pixel (3″ at 850 μm, 2″ at 450 μm) contains the signal from several bolometers as the telescope scans across the sky, changing direction when it reaches the boundary of the circular field. This scan pattern ensures that each part of the field is observed from multiple position angles, resulting in the recovery of real astronomical structure while short timescale variations due to the atmosphere are attenuated. Eight nearby (<500 pc) regions selected from the Gould Belt Survey (Ward-Thompson et al. 2007c, Herczeg et al. submitted) are each monitored at an approximate 28 day cadence whenever they are observable in the sky. Contained within these regions are a total of 1749 young stellar objects (YSOs) identified by *Spitzer Space Telescope* (Megeath et al. 2012, Dunham et al. 2015) and *Herschel Space Observatory* (Stutz et al., 2013) observations. 344 of these YSOs are identified as Class 0/I or Flat Spectrum protostars while the remaining 1405 are identified as Class II (disk) sources (Herczeg et al. submitted). Table 5.1 shows a list of the regions and their central coordinates along with the average 850 μm rms noise measured in the individual maps (see Section 5.8 for detailed information on each

Table 5.1 A summary of the observed JCMT Transient Survey fields between the first observations on December 22$^{\rm nd}$, 2015 and March 1$^{\rm st}$, 2017.

Region	Central R.A. (J2000)	Central Decl. (J2000)	Number of Epochs[a]	Average 850 μm Noise[b,c] (mJy beam^{-1})	Std. Dev. 850 μm Noise[d] (mJy beam^{-1})	Noise in the Co-add (mJy beam^{-1})
Perseus: NGC1333	03:28:54	+31:16:52	10	12.26	0.40	3.92
Perseus: IC348	03:44:18	+32:04:59	9	12.18	0.43	4.30
Orion: OMC 2/3	05:35:33	-05:00:32	9	11.72	0.54	4.19
Orion: NGC2024	05:41:41	-01:53:51	11	11.29	0.40	4.32
Orion: NGC2068	05:46:13	-00:06:05	10	11.75	0.38	3.85
Ophiuchus: Core	16:27:05	-24:32:37	8	13.35	0.75	5.00
Serpens: Main	18:29:49	+01:15:20	9	12.01	0.27	4.54
Serpens: South	18:30:02	-02:02:48	9	14.56	1.18	4.72

[a] Only observations between December 22$^{\rm nd}$, 2015 and March 1$^{\rm st}$, 2017 are included.
[b]These measurements of the 850 μm noise levels are based on a point source detection in a single observation using 3$''$ pixels and a 14.6$''$ FWHM beam.
[c]The reduction method *R3* was used to derive these noise estimates (see Section 5.4).
[d]The standard deviation of the average 850 μm noise across all epochs.

individual observation). Note that Serpens South has diffuse structure throughout the map even near the edges of the field and, as a result, the measured noise is slightly higher than the other regions. There are five weather grades defined for JCMT observations from Band 1 (very dry: $\tau_{225\,\mathrm{GHz}} < 0.05$, where $\tau_{225\,\mathrm{GHz}}$ is the zenith opacity of the atmosphere at 225 GHz) to Band 5 (very wet: $\tau_{225\,\mathrm{GHz}} > 0.2$). All of the observations performed in this survey were taken in either Band 1, Band 2, or Band 3 weather ($\tau_{225\,\mathrm{GHz}} < 0.12$) as measured by the JCMT Water Vapour Radiometer Dempsey & Friberg (2008). The observing time per observation is set to 20-40 min, depending on the weather band, to maintain a similar noise quality of $\sim 10\,\mathrm{mJy\,beam^{-1}}$ at 850 μm (see Table 5.1).

Due to the higher telluric absorption (see Dempsey et al. 2013) and varying PWV (precipitable water vapour), the 450 μm observations have noise values 10 to 40 times higher than the 850 μm observations and, thus, throughout this paper we focus on the latter. Observations began in December 2015 and are expected to continue until January 2019. Here, we present results between the first observations in December, 2015 and March 1$^{\mathrm{st}}$, 2017.

5.4 Data Reduction Methods

The data reduction procedure was performed using the iterative map-making technique MAKEMAP (explained in detail by Chapin et al. 2013) in the SMURF package (Jenness et al. 2013) found within the STARLINK software (Currie et al., 2014). Briefly, MAKEMAP begins with the raw power detected by the telescope as a function of time throughout the duration of the observation and iteratively works to recover the astronomical signal by modeling and subtracting different sources of noise. First, general fixes (such as removing noise spikes, ensuring continuity, and apodising the edges of the bolometer time series) and a flat field correction are applied. Then, the program removes the *common mode* (COM) noise. This type of noise, the large majority of which is caused by atmospheric emission, dominates the astronomical features we seek to study by causing a significant fraction of SCUBA-2's bolometers to acquire the same signal. As SCUBA-2 scans across a region of the sky at a constant speed, the power received over a given time interval is directly correlated with a spatial scale. Thus, removing the common mode noise results in a loss of extended, faint structure in the final maps produced, while the more compact, bright structure can be more accurately recovered. For an overview of the Gould Belt Survey for their

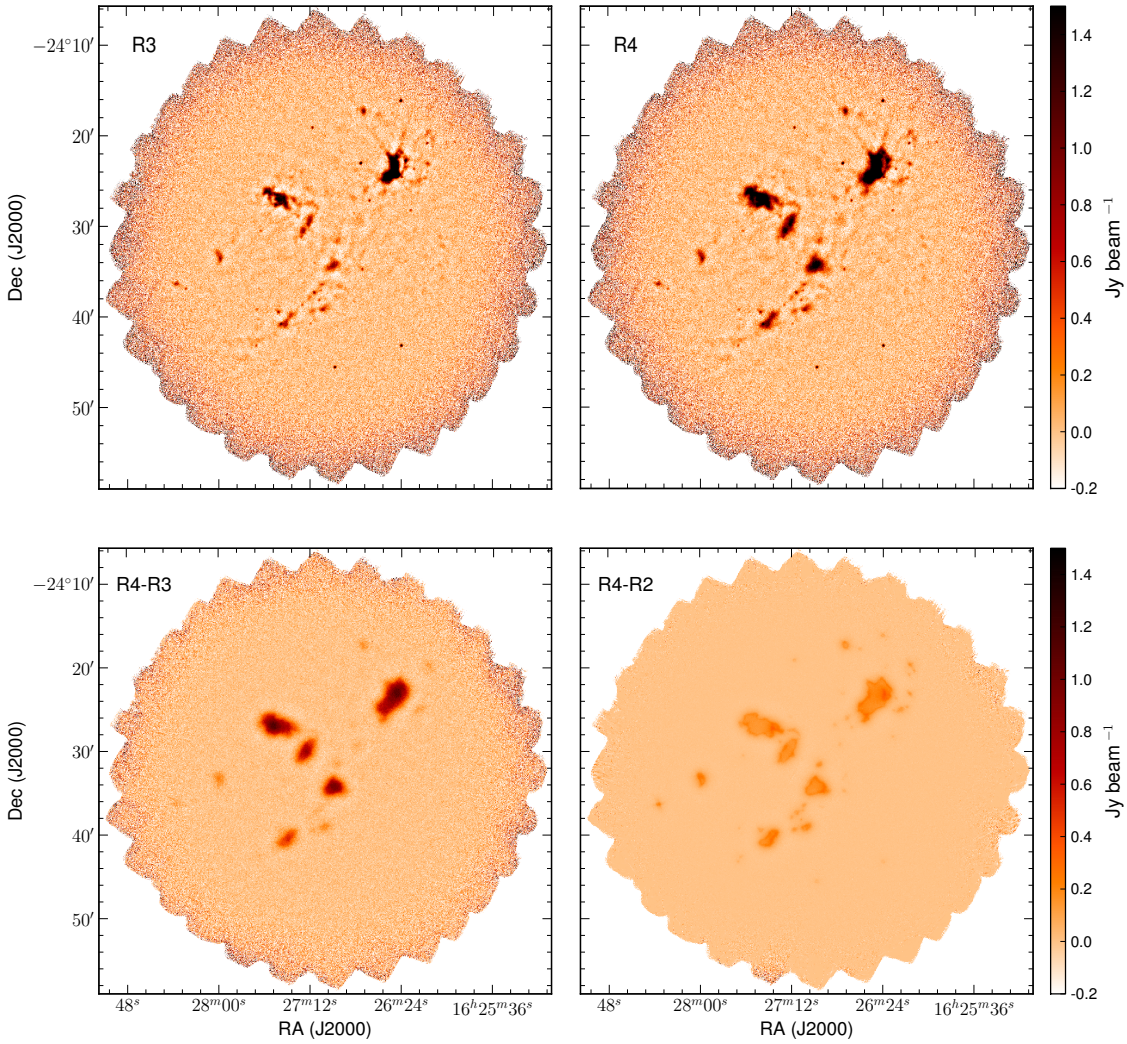

Figure 5.2 *Top*: A single 850 μm observation of the Ophiuchus Core region reduced using reduction methods *R3* (left) and *R4* (right). *Bottom*: Reduction *R4* minus reduction *R3* (left) and reduction *R4* minus reduction *R2* (right). Note that the two small bright sources seen in bottom of the R3 and R4 maps are roughly point-like.

Legacy Release 1 (GBS LR1) filtering parameters as well as results from testing the completeness of this method using artificial sources, see Mairs et al. (2015).

Next, an atmospheric extinction model is applied based on the amount of PWV which was measured during the observation and a second filtering of the data is applied to remove any residual, low frequency $1/f$ noise which was missed by the common mode subtraction. The extent of the final spatial filtering executed in this step is defined by the user. Generally, the largest recoverable scales are $\sim 600''$ before atmospheric signal becomes significant.

Finally, the astronomical signal is estimated and the residual white noise is compared to the previous iteration. The iterative solution converges when the difference in individual pixels changes on average by a user-defined threshold percentage of the rms noise present in the map (we select a value of $< 0.1\%$). The maps produced are originally in units of picowatts (pW) but are converted to mJy arcsec^{-2} using the standard 850 μm aperture flux conversion factor 2340 mJy pW^{-1} arcsec^{-2} and 4710 mJy pW^{-1} arcsec^{-2} at 450 μm (Dempsey et al., 2013). In the case of the JCMT Transient Survey, the final maps are gridded to $3''$ pixels for the 850 μm data and $2''$ pixels for the 450 μm data.

To apply additional constraints to the solution derived by MAKEMAP, the user can also supply an *external mask* which surrounds the astronomical signal deemed to be significant. To construct an external mask, the individual maps produced by the iterative mapmaker are co-added in order to achieve a higher signal-to-noise ratio (SNR). The resulting image is used to define the regions of genuine astronomical emission (pixels with a signal-to-noise ratio of at least 3 are generally deemed significant). This mask is then used in a second round of data reduction in order to recover better any faint and extended structure.

MAKEMAP has over 100 user defined parameters that allow full control over each step of the iterative process. Many parameters will cause negligible changes in the final maps produced, but some will cause significant differences, such as the extent of spatial filtering the user applies. For the JCMT Transient Survey, we begin with the robust data reduction parameters derived by the GBS LR1 dataset as described in Mairs et al. (2015) To ensure, however, that we produced the best calibrated maps which would allow for the detection of the variability of embedded protostars, we tested the effects of altering the size of the spatial filter applied to the data to determine whether or not it was beneficial to apply additional constraints to MAKEMAP by using an external mask.

To this end, we performed four individual data reductions labeled *R1*, *R2*, *R3*, and *R4*, yielding four sets of maps exhibiting different models of the recovered, astronomical structure.

1. *R1*: An effective spatial filter of 200″ was applied and no external mask was used.

2. *R2*: An effective spatial filter of 600″ was applied and no external mask was used.

3. *R3*: An external mask was constructed from a co-add of the *R1* reduction and was used to constrain the solution derived by MAKEMAP. Thus, the structure was filtered to 200″.

4. *R4*: Similarly to *R3*, an external mask was constructed from a co-add of the *R2* reduction and applied to the data. Thus, the structure was filtered to 600″. This reduction is the same as the GBS LR1 data release (Mairs et al., 2015).

Figure 5.2 shows an example of a single observation of the Ophiuchus Core region (see Table 5.1). The top two panels show the resulting maps produced by reductions *R3* (left) and *R4* (right) while the bottom two panels show the subtraction of the *R3* image from the *R4* image (left) to highlight the effect of changing the effective spatial filter and the subtraction of the *R2* image from the *R4* image (right) to highlight the effect of the external mask. Though more extended structure is present in the *R2* and *R4* maps, the compact structure is recovered whether a 200″ or a 600″ filter is used. For the extended emission reconstructions, the mask returns additional flux, some of which appears pedestal-like. As Mairs et al. (2015) discuss, the amount of extended structure which is recovered can produce slightly different results for the compact structure present in the map as the larger-scale background may add a pedestal value to the flux. We minimise the effect of the pedestal by using a localised peak extraction algorithm (described in Section 5.5 and Section 5.9) that filters out the extended background.

The dominant uncertainty between these different reduction methods is how the recovered extended structure and external masks alter the fit to compact emission sources. The measurement of the peak brightness of a source relies on a consistent procedure from observation to observation in conjunction with the optimal data reduction method. By fitting Gaussian profiles to compact emission sources and comparing their centroid positions and peak brightnesses (described in detail in Section

5.5), we determine reduction *R3* to be the most stable for our purposes (although all four reductions work reasonably well). The external mask limits the flux distribution during the map-making procedure while the harsher filter (200″ as opposed to 600″) subdues large-scale structure which is not expected to vary (but is hard to recover due to signal from the atmosphere and the instrumentation).

SCUBA-2's 850 μm filter coincides with the broad ^{12}CO(J=3-2) emission line. No attempt has been made to remove this signal. This excess flux, however, will not affect our ability to measure precisely the variability of deeply embedded protostars. As Drabek et al. (2012) and Coudé et al. (2016) discuss, the CO(J=3-2) line contributes only low-level emission ($\leq 20\%$) except for a few sources of stellar outflow. In addition, as Mairs et al. (2016) show, the peak brightnesses of compact sources are not affected by the removal of the emission line.

5.5 Post Reduction Calibrations

Since the JCMT Transient Survey is interested in measuring the fluxes of individual compact sources over time, it is important to take into consideration both the pointing uncertainty of the telescope (expected to be 2 to 6 arcseconds; East Asian Observatory staff *private communication*) as well as the flux calibration uncertainty (expected to be $\sim 5-10\%$, see Dempsey et al. 2013). To this end, we perform two post-reduction calibrations: 1) We derive and apply a pointing correction to more precisely align the maps with one another and 2) We derive and apply a relative flux calibration factor for each image produced in order to consistently compare a given source from observation to observation. Since both of these calibrations are relative corrections for each region, we can use the most robust, compact emission sources present in each map to calibrate self-consistently. The first step is to identify the appropriate calibrator sources in each of the eight regions.

There are many different, publicly available algorithms designed to extract structure from a given region (for examples, see GAUSSCLUMPS Stutzki & Guesten 1990, CLUMPFIND Williams et al. 1994, ASTRODENDRO Rosolowsky et al. 2008, GETSOURCES Men'shchikov et al. 2012, and FELLWALKER Berry 2015). Each method combines detected emission differently based on user supplied criteria and, thus, the use of such algorithms requires discernment and a goal-based approach. In this work, we are interested in accurately determining the brightness of localised, compact sources in dust emission convolved with the JCMT beam, which we expect to have

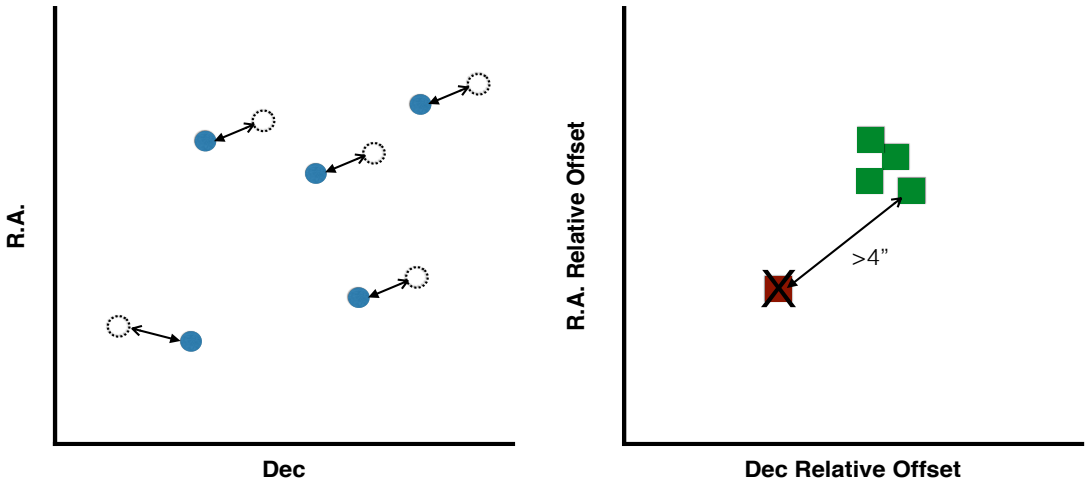

Figure 5.3 Schematic diagram of step 4 in the image alignment process. *Left:* We measure the offsets between bright, compact sources in the reference map (filled circles) and in a subsequent observation (empty circles). *Right:* We compare the relative right ascension and declination offsets of all the sources and remove outliers.

approximately Gaussian features. The most robust (often isolated) Gaussian sources will be used for image calibration. To this end, we have selected the algorithm GAUSSCLUMPS (Stutzki & Guesten, 1990) to identify and extract sources in each observation of a given field as this program is designed to robustly characterise Gaussian structure and subtract background structure, such as pedestals. Specifically, we use the STARLINK software (Currie et al., 2014) implementation of GAUSSCLUMPS found within the CUPID (Berry et al., 2007) package. For more information on GAUSSCLUMPS, refer to Section 5.9.

5.5.1 Image Alignment

To perform the post-reduction relative image alignment, we focus on the 850 μm data. The noise in this dataset is measured to be more than an order of magnitude below its 450 μm counterpart (due to the effect of PWV in the atmosphere) and the beam profile has greater stability, allowing us to more reliably fit the compact emission sources. The 450 μm and 850 μm data are, however, taken simultaneously, so the same alignment correction is applied to both datasets. The alignment procedure we apply to the data consists of five steps:

1. We label the first observation of a given field the "reference observation". Then,

we smooth the map with a 6″ Gaussian kernel to mitigate noise fluctuations. We identify and fit Gaussians to all the sources brighter than 200 mJy beam^{-1} and with radii less than 10″ in the reference observation using the source extraction algorithm GAUSSCLUMPS (Stutzki & Guesten, 1990). The radius of a source, r, is defined as $r = \sqrt{\mathrm{FWHM}_1 \times \mathrm{FWHM}_2}/2$ where the FWHM_N terms are the full widths at half maximum of the fitted two dimensional Gaussian. Fitting Gaussians to bright sources allows us to measure the centroid location of the sources to sub-pixel accuracy. For more information on how GAUSSCLUMPS was executed, see Section 5.9.

2. For later observations, we also smooth the maps and identify and fit Gaussians to all the sources brighter than 200 mJy beam^{-1} and with radii less than 10″ using GAUSSCLUMPS in the same manner as for the reference observation.

3. We next match each source identified in the reference catalogue to the nearest source in the later catalogue (the peak location sources must not differ by more than 10″, given an expectation that the alignment offset is better than this value).

4. We then perform a check to ensure that we have matched the reference sources to the correct corresponding sources in the later catalogue by employing a simple test. Plotting the relative right ascension offset against the relative declination offset for all of the sources, we search for outliers by applying the condition that the resultant offset of every source must be within 4″ of the resultant offset of any other source (see Figure 5.3). 4″ was chosen after extensive testing across all eight regions revealed this threshold to consistently eliminate outliers. If this condition fails, we exclude that source from the final step. In this way, any moving sources or spurious detections will be discounted from our analysis.

5. Finally, we average the right ascension and declination offsets of the matched sources to find the difference between the position of the later observation and the reference observation. We then apply this offset by re-reducing the later observation and correcting the pointing using MAKEMAP's *pointing* parameter. In this way, both the reference and the later observations will be consistently aligned, processed, and gridded to the same world coordinate system grid.

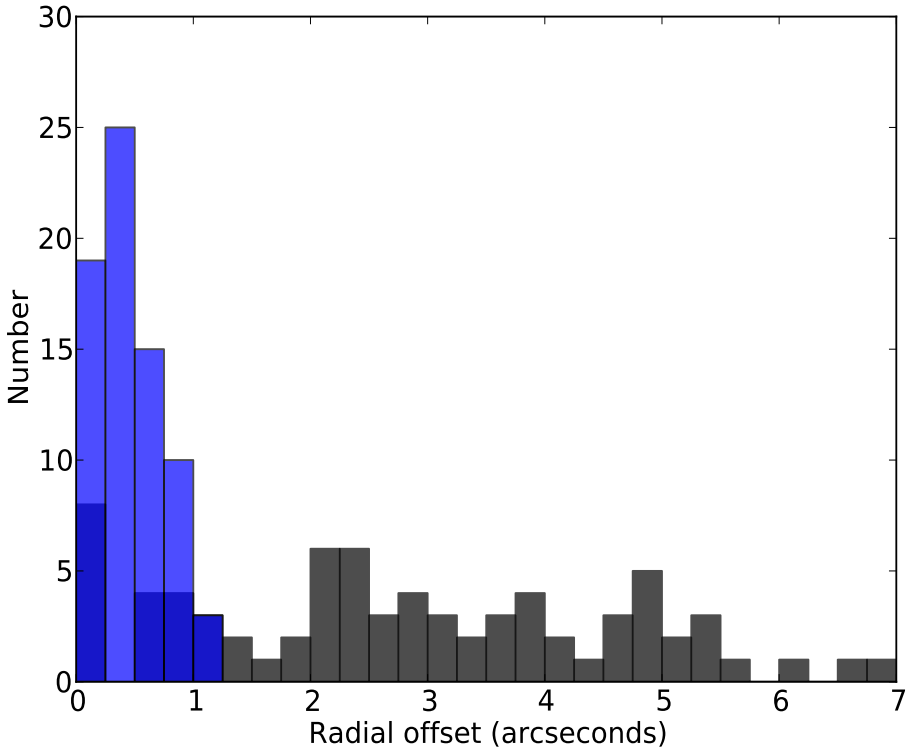

Figure 5.4 Histograms of the measured radial offset between each region's reference field and its subsequent observations. Black represents the original offset without applying any correction; blue represents the corrected offset of the aligned maps.

Figure 5.4 shows the results of applying the post-reduction alignment to the JCMT Transient Survey observations using reduction *R3* (all four reduction methods show consistent results, see Section 5.8). The black histogram shows the original pointing uncertainty while the blue histogram shows the corrected pointing uncertainty. By reliably fitting bright peaks and matching their centroids from observation to observation, we have achieved a mean positional uncertainty of 0.45″ (less than one sixth the width of an 850 μm pixel) with a standard deviation of 0.3″. In nearly all cases, the images are aligned to better than 1″. The few fields that exhibit a slightly higher uncertainty come from the NGC2024 region which contains more clustered sources mixed with larger-scale structure (see Figure 5.5 for an example of the clustered emission in NGC2024 and see Herczeg et al. submitted for co-added images of all eight fields). Isolated, bright emission sources have less fitting uncertainties and therefore produce the best alignments. The alignment of the maps is now part of an automated routine run at the East Asian Observatory (EAO) immediately after the observations are taken at the telescope. The final, aligned images and GAUSSCLUMPS catalogues are deposited in a shared directory which team members can access.

In addition to this image alignment procedure, an independent method based on the cross-correlation of the observations was also tested and found to produce consistent results (see Section 5.10). As the survey matures, we will be exploring this alternate technique and refining our methodology to further improve our alignment calibration.

5.5.2 Relative Flux Calibration

After cataloguing the sources in the reference observation as well as the subsequent, aligned observations, we derive and apply a relative flux calibration factor to each observation in order to plot accurately the brightness variations of a given object over all epochs. The JCMT has an intrinsic absolute flux calibration of ∼5-10% (Dempsey et al., 2013), but we are focused only on the relative brightness changes from epoch to epoch. This allows us to achieve more accurate measurements of the variability in a given field. The procedure to flux calibrate our images consists of six steps:

1. Beginning with the same calibrator sources that we extracted to perform the spatial alignment of the maps (described in Section 5.5.1), we select the subset that have peak brightnesses over 500 mJy beam^{-1} and appear in every single observation of a given region. The choice of 500 mJy beam^{-1} is based on a desire to reach a

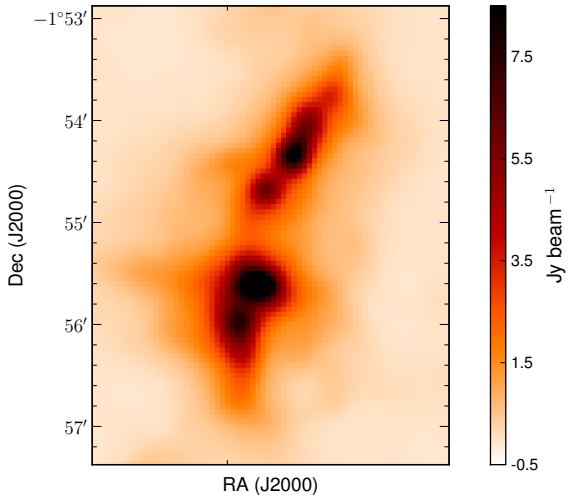

Figure 5.5 The central region of NGC2024 at 850 μm. The tightly clustered sources of emission are blended, causing a higher uncertainty in the Gaussian fits of the individual peaks.

relative brightness calibration of ∼2% and the typical noise is ∼10 mJy beam^{-1} in each image (see Table 5.1), yielding a SNR for the minimum brightness peaks of ∼50:1. We first calculate the average peak brightness over all epochs to remove the uncertainty in flux related to individual measurements and then normalise the observed source peak brightnesses in each observation to their respective averages.

2. We then compare the brightness of each extracted source with respect to each of the others by taking the ratio of their normalised peak brightnesses and plotting the result for each epoch (for example, see Figure 5.6). If a given pair of sources gets brighter or dimmer together from epoch to epoch, due to calibration uncertainties, we would expect the ratio of their normalised peak brightnesses over time to show little scatter.

3. We next measure the amount of scatter in the ratio between two sources by calculating the standard deviation in the ratio of normalised peak brightnesses over time. For every pair of sources, we can plot the measured standard deviation. In Figure 5.7, we show the results of a simple model of the standard deviations measured for pairs of sources by applying a Gaussian error of the value indicated to 1000 sources of peak brightness 1.0 and comparing their expected normalised peak brightness ratios over eight epochs. Overlaid on this figure are the measured standard deviations of the normalised source peak brightness ratios for all nine potential calibrator sources in all eight observations of the Ophiuchus Core region. Note that as more epochs are observed, the central part of the curve (where the majority of the data points lie) regresses to a value of $\sqrt{2} \times$ error.

4. We next identify the largest set of sources wherein every pair has a standard deviation below a threshold set to 0.06. We call this set of stable sources a *Family*. We choose 0.06 through comparison with model curves in Figure 5.7, and as a compromise between decreasing the number of family members versus increasing the reliability of the calibration. Thus, all *Family* members satisfy the threshold when compared against each other. These sources are considered non-varying and appropriate for the relative flux calibration of each epoch. This threshold was chosen after extensive testing for the optimal number of sources contained within the *Family* across all observed regions.

5. For each epoch, the flux calibration factor by which we divide every pixel is the average normalised peak brightness over all the sources within the *Family* during that observation. These factors are plotted in the left panel of Figure 5.8. In the figure, black indicates all observations taken before March 1st, 2017, while grey indicates observations taken after the filters were changed on SCUBA-2 in November, 2016. The standard deviation of a Gaussian fit to all the data is 8%, as expected (Dempsey et al., 2013).

6. The uncertainty in the derived flux calibration factor is taken to be the error in a given measurement of the normalised peak brightness of an individual source which is calculated by finding the standard deviation of the normalised peak brightnesses of all the calibrator sources. This uncertainty is plotted in the right panel of Figure 5.8. Note that the uncertainty peaks at approximately 2%. This is, however, the uncertainty per source while the error in the mean scales with the square root of the number of calibrator sources detected. Again, all four tested reductions show consistent results (e.g. compare the *R3* flux calibration results with *R4* in Section 5.8), though the *R3* reduction is most robust for the JCMT Transient Survey science goals.

The highest flux calibration factor uncertainty is found in the NGC2024 region for the same reasons the residual offset in the aligned maps is larger; the calibrator sources identified in NGC2024 are found within the extended structure where our Gaussian fitting routine encounters more uncertainty. Overall, the flux calibration uncertainties are very low ($\sim 2-3\%$), allowing the JCMT Transient Survey team to robustly detect variations in peak brightness of the most prominent sources to the level of $\sim 10\%$. Previously, Haubois et al. (2012) achieved this relative calibration accuracy over a 5 day monitoring campaign of Sagittarius A* using the Atacama Pathfinder Experiment instrument at the Llano de Chajnantor Observatory. These small uncertantites, however, are unprecedented in ground-based, single dish submillimetre observations for such a wide range of consistent observations. In addition, we fit many sources in each field which allows us to detect sufficiently significant brightness variations on the first epoch they occur. Note that since we determine each epoch's flux calibration factor in a relative sense, the SCUBA-2 filter change in 2016 does not affect our results. The absolute brightness measurements, however, depend on the flux conversion factors (see Section 5.4). The filter change is expected to cause

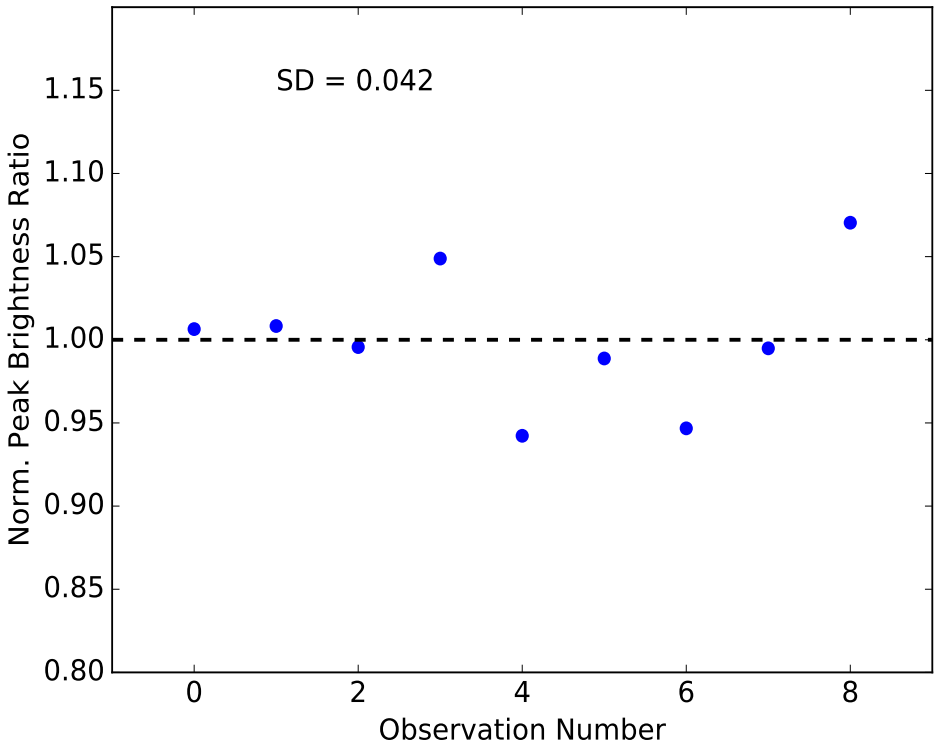

Figure 5.6 An example of the normalised peak brightness of one source divided by the normalised peak brightness of another, plotted from observation to observation. SD is the standard deviation of this set of nine points, highlighting that the uncertainty in the ratio of these two sources (and the underlying uncertainty in the measurement of these individual sources) is about 4%.

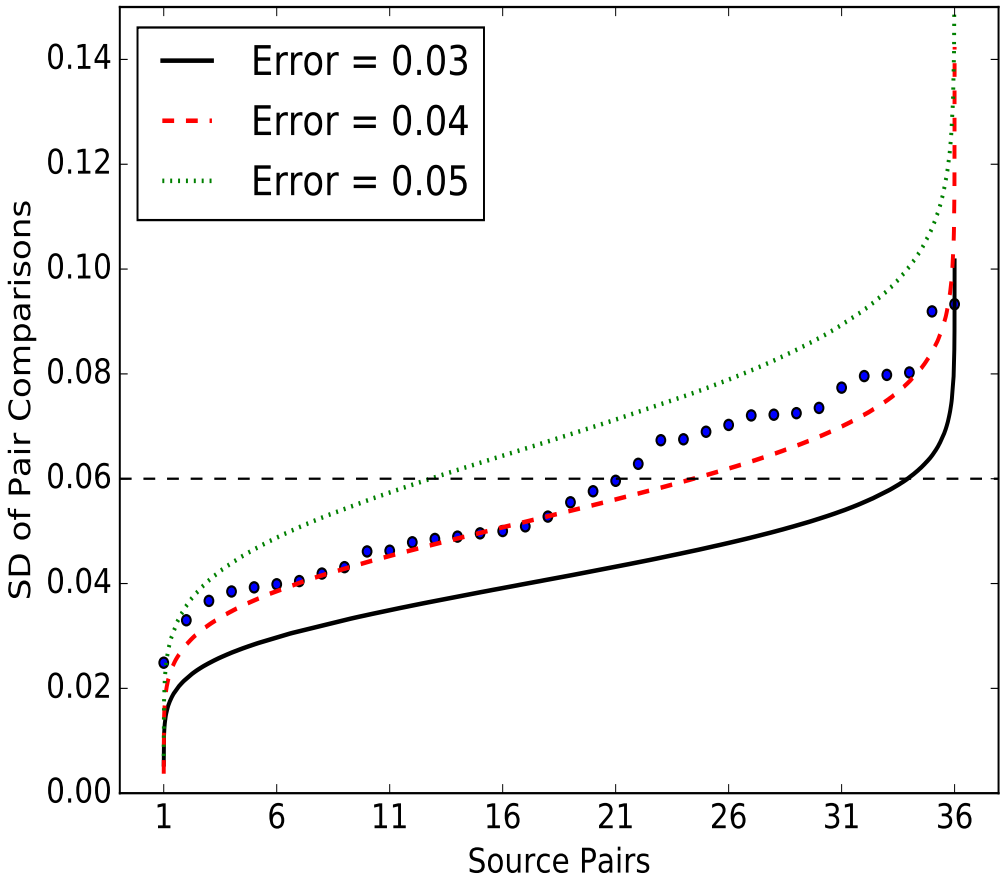

Figure 5.7 The standard deviation of the normalised peak brightness ratios for all pairs of identified sources including all 8 observations of the Ophiuchus Core region observed prior to March 1st, 2017, arranged in ascending order. Each line represents an iteration of a simple model where we applied a Gaussian error of the value indicated to 1000 sources of peak brightness 1.0 and compared their normalised peak brightness ratios over 8 epochs. Note that as more observations are performed, the central part of the curve flattens, approaching a value of $\sqrt{2}\times$ error. Nine potential calibrator sources were found, yielding 36 pairs. The largest *Family* of sources consistent with one another (standard deviations less than 0.06, the threshold indicated by the dashed black line) are the flux calibrator sources we select to perform the correction. In this case, four sources met the criteria to join the flux calibrator *Family*.

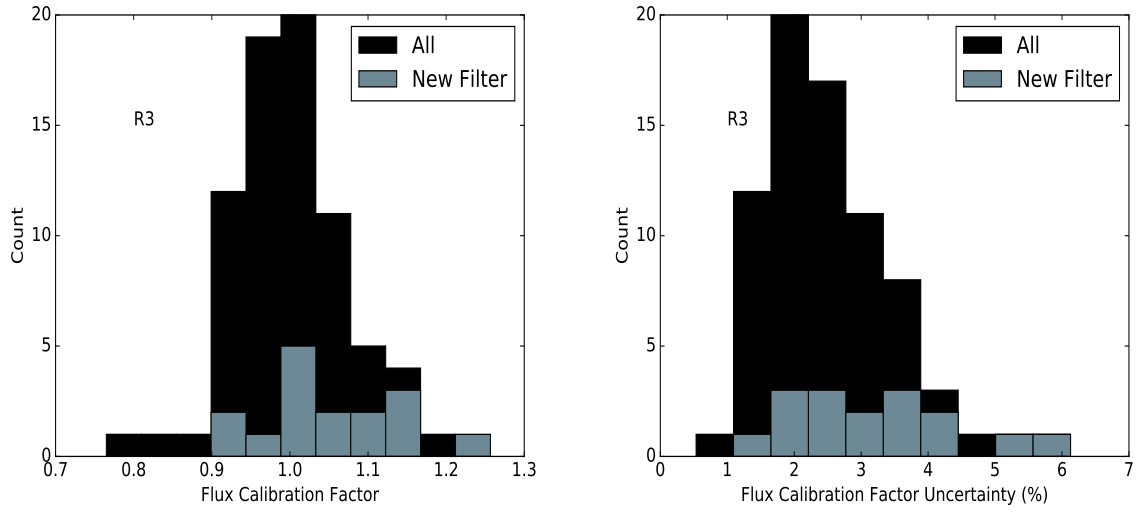

Figure 5.8 *Left:* The derived flux calibration factors for compact emission sources for all observations of the eight regions. *Right:* The relative uncertainty in the flux calibration factors, calculated by finding the standard deviation of the normalised peak brightnesses of the calibrator sources in each respective image. Black indicates all observations taken before March 1st, 2017 while grey indicates observations take after the filter change of November, 2016.

a small but detectable change in these values, but this has not yet been quantified by the observatory.

Our calibration is only expected to improve as we include future epochs and refine our methods throughout the duration of the survey. With additional epochs, we will be able to co-add subsets of our observations to increase our sensitivity at the cost of a lower cadence. Presently, we are working to automate the flux calibration procedure such that it can also be run directly after an observation undergoes the data reduction and alignment procedures at the EAO. For a given observation, the aligned and flux calibrated data are presently available to team members within 24-48 hours.

5.6 Discussion

The goal of this calibration work is to extract robust, non-varying sources from SCUBA-2 maps and apply the spatial alignment and flux calibration methods. The majority of this process involves excluding sources from flux calibrator *Families* which do not meet our set of criteria. These excluded sources, however, are of particular interest to the JCMT Transient Survey as they may be transient.

Figures 5.9 and 5.10 show the measured fractional variation in the fluxes (standard deviation) of each observed source across all epochs that it was observed, ordered by source brightness. For a source to be included on these plots, it must be detected in every epoch of the given region. Thus, there are many additional, potentially interesting, submillimetre sources which are not included in these figures as our focus is on potential calibrators. A source may not be detected in a given epoch for two reasons: 1) It has properties near enough to the detection threshold that it is too faint or too extended on some observation dates but not on others (a source in a clustered environment is difficult to fit which may cause the shape to change). 2) The peak brightness of the source may vary such that it was too faint to be detected at the time of the reference observation but it was bright enough at a later date (or vice versa). The sources in both scenarios are of little importance to the flux calibration since we only want to use the most robust sources available. Detecting the sources in the second scenario is one of the goals of the JCMT Transient Survey and follow-up studies are currently underway to quantify their number and amplitude (for example, Mairs et al. in preparation). Including all observations of all eight regions, using our source extraction methods based on detecting compact structure and fitting Gaussian profiles with GAUSSCLUMPS as detailed in Section 5.9, we see a total of 265 unique

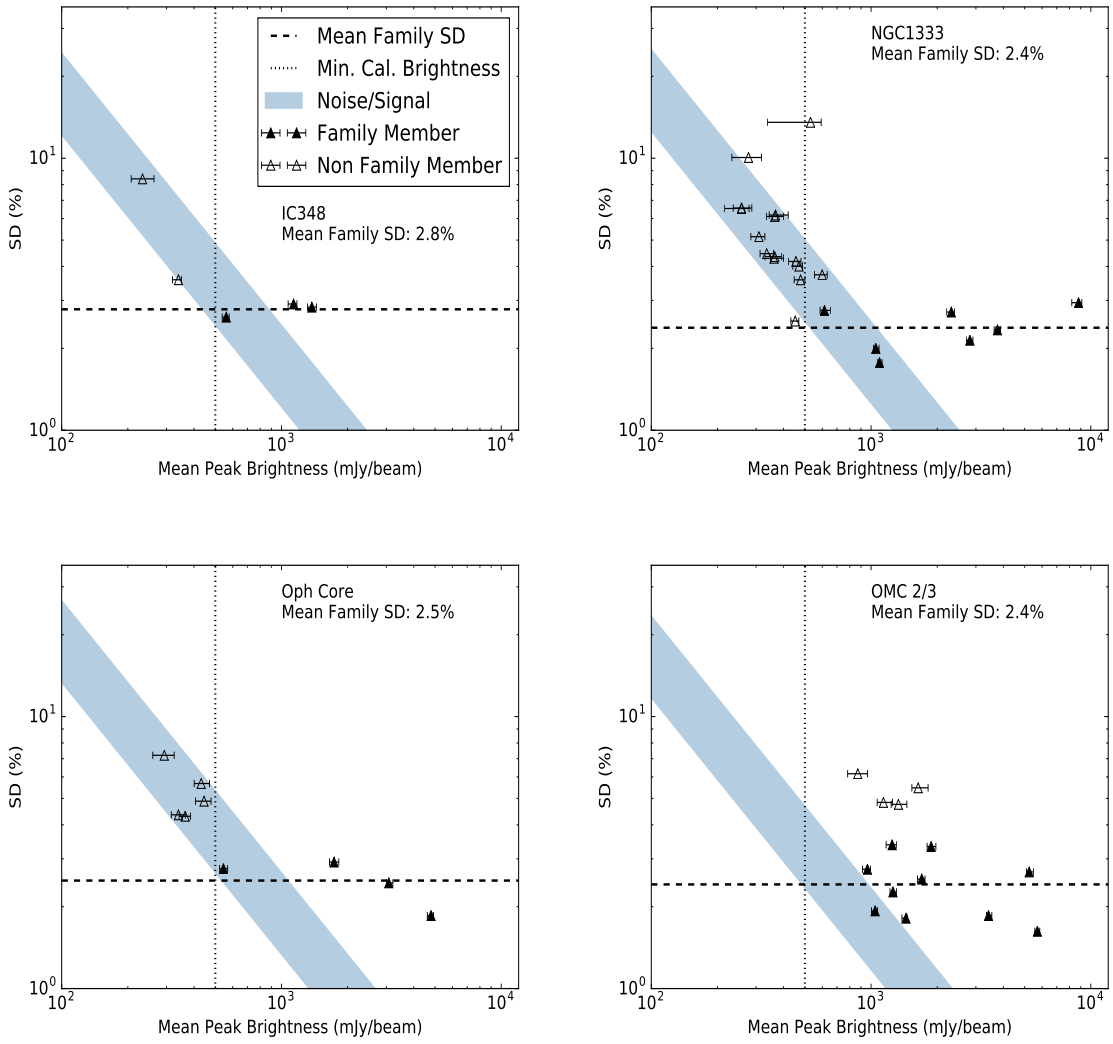

Figure 5.9 The standard deviation in the peak brightness versus the mean peak brightness of a source for four of the Transient fields. The horizontal errorbars indicate the range of peak brightnesses observed across all dates. Filled triangles represent *Family* members while empty triangles represent other sources not included in the flux calibration. The vertical dotted line indicates the minimum brightness threshold to be considered a member of a *Family*. The horizontal dashed line shows the average standard deviation in the mean peak brightness of all the *Family* sources. The lower bound of the shaded region shows the average noise as a percentage of source peak brightness and the upper bound of the shaded region assumes the noise is higher by a factor of two.

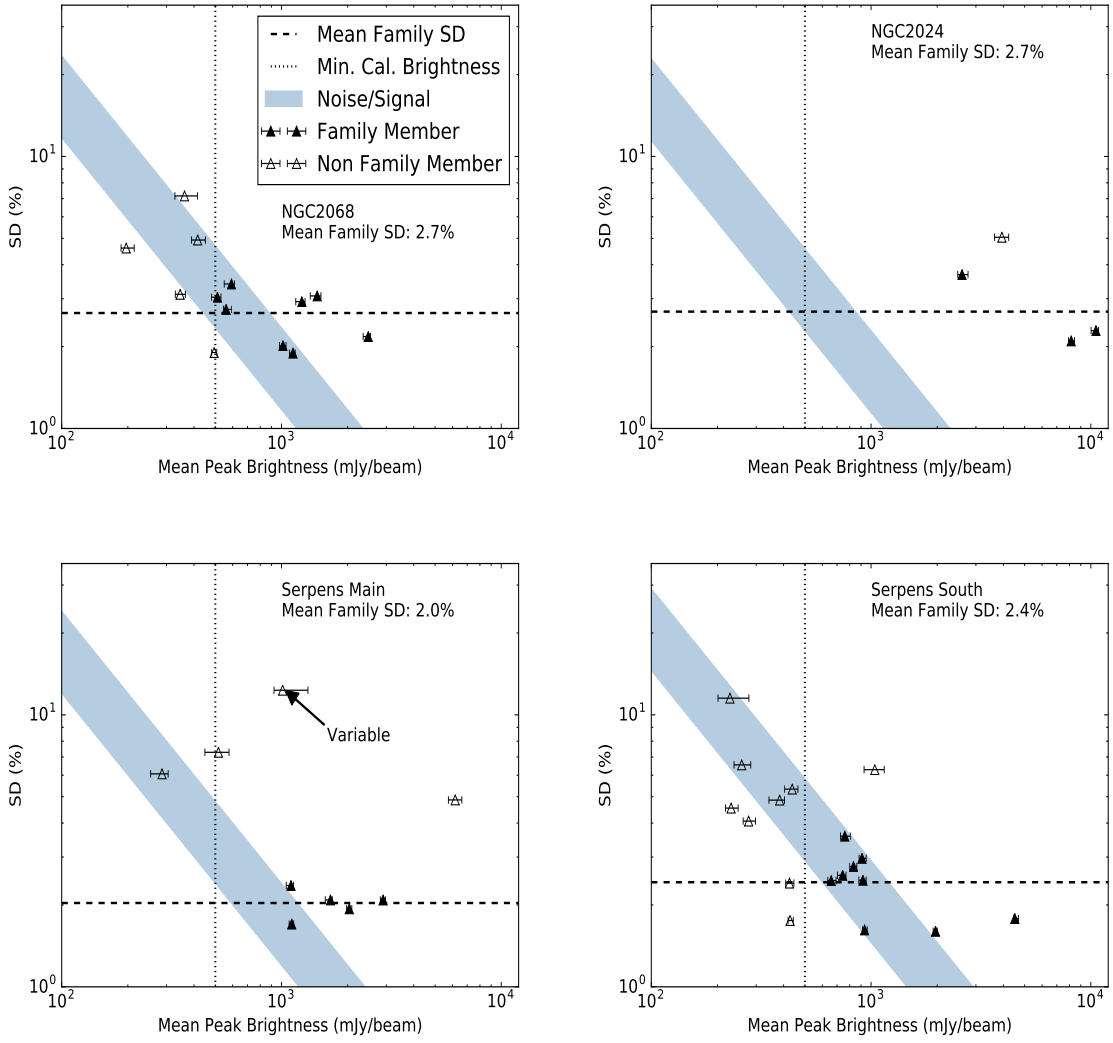

Figure 5.10 Same as Figure 5.9, showing the other four Transient fields.

areas of significant, localised emission (see Table 5.2). This number is expected to vary depending on the source identification procedure used and the amount of data received.

The lower bound of the shaded regions in Figures 5.9 and 5.10 show the average noise in each region (see Table 5.1) as a percentage of the mean peak brightness while the upper bound represents the noise multiplied by a factor of two to take into consideration additional uncertainties due to, for example, the source fitting procedure. In general, we expect fainter sources to approximately follow the shaded region whereas we expect *Family* members to lie further to the right and display low standard deviations dominated by the Gaussian fitting uncertainties. The vertical dotted line shows the minimum peak brightness threshold for a source to be considered a *Family* member (500 mJy beam^{-1}) and the horizontal dashed line shows the mean standard deviation of the *Family* members in that specific region.

Most of the sources behave as expected for objects which do not vary with time. There are, however, a few notable exceptions. The OMC 2/3 and NGC2024 fields are where localised Gaussian profiles are extracted from particularly clustered and confused emission (see, for example, Figure 5.5). These two regions have the highest number of relatively bright sources not included in their *Families*, most likely due to the source extraction procedure but also possibly due to intrinsic variability. GAUSSCLUMPS is able to extract and fit well isolated, compact emission sources while sources extracted from clustered regions have more uncertainty. Depending on the morphology of the surrounding background structure, emission from multiple sources can be blended which causes some sources to deviate from Gaussian profiles, fluctuating in elongation from epoch to epoch as the algorithm attempts to separate the significant structure from the background. Examples of these sources include the two which meet the minimum brightness threshold but fail to be included in a *Family* in NGC1333 (Figure 5.9, top right), the brightest source in the Serpens Main region (Figure 5.10, bottom left), and the source on the *Family* brightness threshold in the Serpens Main region (Figure 5.10, bottom left). Since this paper is concerned with calibration, we simply ignore these more complicated sources. In future papers, however, we will adapt techniques to better identify variability in the most crowded regions in our fields. In general, sources which fail the flux calibrator criteria are lower peak brightness, as expected (see Figure 5.11).

Another reason a source may significantly deviate from what we expect and fail to be included in a *Family* is that it is undergoing an observable, physical variation.

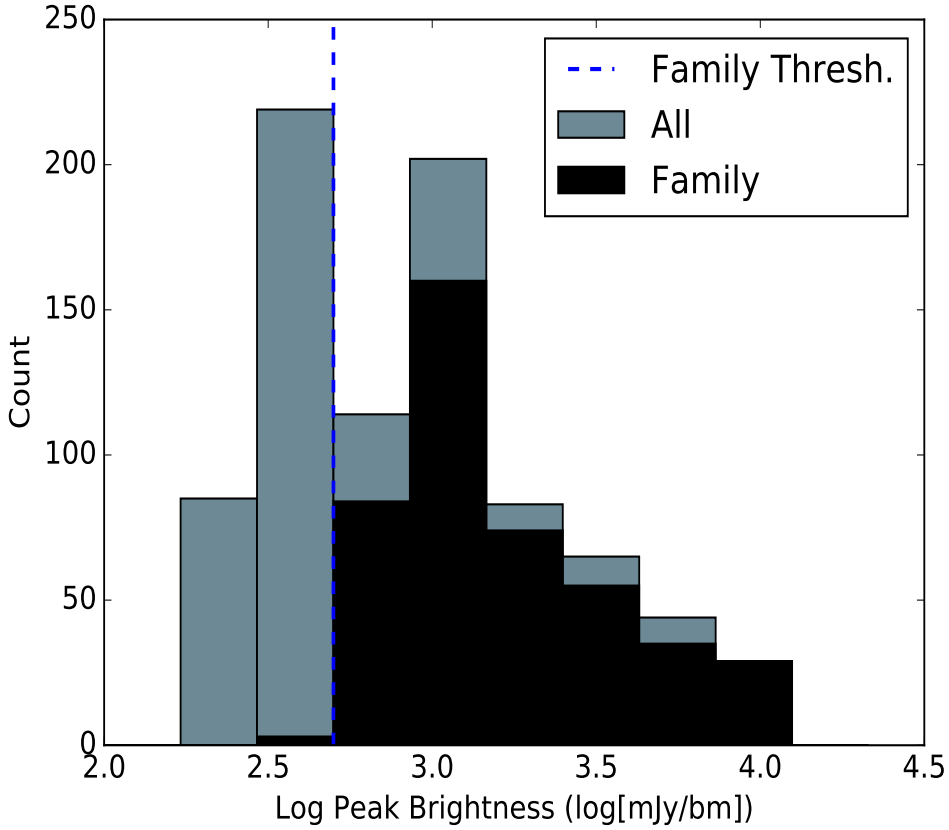

Figure 5.11 Peak Brightnesses of all sources detected in every observation (grey) and only those included in the flux calibrator *Families* (black). The dashed line indicates the minimum average brightness threshold required to be considered a *Family* member. In some individual observations, *Family* members have peak brightnesses which are slightly less than the threshold. Sources from every epoch of all eight fields prior to March 1st, 2017 are included.

Our relative flux calibration algorithm has been designed to exclude sources which are varying so that their contribution would not suppress the signal we seek to study. One variable source, has been identified (see Figure 5.10, bottom left) and verified over multiple observations in our dataset (for more detail on this source, refer to Yoo et al. submitted). A careful but cursory analysis of each source that was detected in every observation and was excluded from a *Family* has been carried out and no other clear and robust detections of significant variability have so far been identified. Investigations will continue, however, to uncover any long term trends. In addition, there are many sources present in each map which are not presented in this paper. Analyses employing different source extraction methods as well as procedures which consider the variability of faint sources are currently underway (for example, Yoo et al. submitted, Mairs et al. in preparation).

5.7 Conclusion

The primary goal of the JCMT Transient Survey is to detect variability in the brightness of deeply embedded protostars. The pointing accuracy of the JCMT is nominally 2 to 6 arcseconds while the nominal flux calibration uncertainty of 850 μm SCUBA-2 data is 8% (see Figures 5.4 and 5.8). In order to dramatically increase our sensitivity to variable signals, we have developed a calibration pipeline which further spatially aligns multiple observations of a given field and provides a relative flux calibration correction for bright, compact sources. We use the algorithm GAUSSCLUMPS (see Section 5.5 and Section 5.9) to extract locations and peak brightnesses of emission objects in the 850 μm SCUBA-2 maps and we apply minimum brightness (200 mJy beam^{-1} for the spatial alignment and 500 mJy beam^{-1} for the relative flux calibration) and maximum radius (10″) thresholds to ensure we have the best fit objects in our sample. These methods could be applied to any submillimetre data with multiple observations of bright, compact objects. Our main results can be summarised as follows:

1. We thoroughly tested four different data reduction methods and found the most robust parameters for our scientific goals (Reduction *R3*, see Section 5.4).

2. We achieve a sub-pixel alignment uncertainty of $\sim 1''$ (see Figure 5.4 and Section 5.5.1), improving on the pointing error of the telescope by a factor of ~ 4.

3. We achieve a relative flux calibration factor uncertainty of $2-3\%$ for bright sources (see Figure 5.4 and Section 5.5.1), improving on the native, absolute flux calibration uncertainty by a factor of ~ 3. This is unprecedented in ground-based, single dish submillimetre observations.

4. By analysing the bright sources that are not included in flux calibrator *Families*, we have noted a variable source at 850 μm (Yoo et al. in preparation) and identified good source extraction practices for further analysis to improve the calibration procedure.

The JCMT Transient Survey is expected to continue through at least January, 2019, increasing the number of observed epochs for each region by a factor of three to about thirty. Throughout this time, we will be working to improve the data reduction and calibration procedures (see Section 5.10) in order to detect fainter signals and working to achieve similar results for the relative flux calibration uncertainty at 450 μm. By the end of the survey, we will have the deepest submillimetre maps of these eight regions which will create many opportunities for additional science, including co-adding across several epochs to uncover variability in fainter sources, but with a lower cadence.

5.8 Appendix 1: Observational Data

Table 5.2 presents detailed information about all of the JCMT Transient Survey observations taken between December 22$^{\text{nd}}$, 2015 (the beginning of the survey) and March 1$^{\text{st}}$, 2017. Reduction *R3* is used in each case. Figure 5.12 highlights that the four tested data reduction methods produce consistent spatial alignment results overall while Figure 5.13 shows that the *R3* and *R4* (and, by extension, *R1* and *R2*) relative flux calibration results are also consistent.

Table 5.2: A summary of all JCMT Transient Survey observations obtained between December 22$^{\rm nd}$, 2015 (the beginning of the survey) and March 1$^{\rm st}$, 2017.

Region	Date	Scan	τ^a	850 μm Noise^{b,c} (mJy beam^{-1})	Number of Sources Above $10\sigma_{rms}$	Number of Alignment Sources	Number of Family Members
IC348	20151222	19	0.06	12.54	9	6	3
IC348	20160115	22	0.07	9.99	12	6	3
IC348	20160205	18	0.04	12.79	12	6	3
IC348	20160226	20	0.05	12.39	13	5	3
IC348	20160318	27	0.05	11.1	12	5	3
IC348	20160417	09	0.04	11.0	13	5	3
IC348	20160826	40	0.08	14.33	12	6	3
IC348	20161126	22	0.05	12.29	14	6	3
IC348	20170209	28	0.09	13.17	12	5	3
NGC1333	20151222	18	0.06	12.22	39	36	7
NGC1333	20160115	10	0.08	11.76	40	29	7
NGC1333	20160205	17	0.04	12.99	39	29	7
NGC1333	20160229	17	0.04	11.46	42	26	7
NGC1333	20160325	11	0.06	11.58	33	25	7
NGC1333	20160802	31	0.09	12.31	43	28	7
NGC1333	20160830	48	0.09	14.05	39	33	7
NGC1333	20161119	88	0.07	9.65	38	28	7
NGC1333	20161126	21	0.05	12.78	36	27	7
NGC1333	20170206	29	0.12	13.85	42	26	7
NGC2024	20151226	49	0.12	12.58	12	10	3
NGC2024	20160116	22	0.06	9.8	15	7	3
NGC2024	20160206	13	0.04	11.88	21	7	3

Continued on next page

Table 5.2 – continued from previous page

Region	Date	Scan	τ^a	850 μm Noise^{b,c} (mJy beam^{-1})	Number of Sources Above $10\sigma_{rms}$	Number of Alignment Sources	Number of Family Members
NGC2024	20160229	22	0.04	13.01	17	7	3
NGC2024	20160325	21	0.06	11.35	19	8	3
NGC2024	20160329	10	0.05	9.1	19	7	3
NGC2024	20160427	12	0.05	11.91	9	6	3
NGC2024	20160826	29	0.09	12.84	23	8	3
NGC2024	20161119	99	0.07	9.13	16	9	3
NGC2024	20161126	53	0.06	10.29	18	8	3
NGC2024	20170206	25	0.11	11.68	15	8	3
NGC2068	20151226	52	0.12	13.4	32	23	8
NGC2068	20160116	27	0.06	9.65	33	21	8
NGC2068	20160206	15	0.05	12.08	31	21	8
NGC2068	20160229	13	0.04	12.21	29	18	8
NGC2068	20160329	11	0.06	10.82	33	22	8
NGC2068	20160427	13	0.05	12.68	28	16	8
NGC2068	20160827	53	0.08	11.8	31	21	8
NGC2068	20161120	88	0.09	11.98	30	20	8
NGC2068	20161126	56	0.06	10.16	30	21	8
NGC2068	20170206	17	0.11	12.76	32	20	8
OMC 2/3	20151226	36	0.11	12.48	55	51	10
OMC 2/3	20160116	19	0.06	9.94	30	22	10
OMC 2/3	20160206	12	0.04	12.03	26	21	10
OMC 2/3	20160229	11	0.04	11.8	45	30	10
OMC 2/3	20160325	15	0.06	10.74	29	20	10

Continued on next page

Table 5.2 – continued from previous page

Region	Date	Scan	τ^a	850 μm Noise^{b,c} (mJy beam^{-1})	Number of Sources Above $10\sigma_{rms}$	Number of Alignment Sources	Number of Family Members
OMC 2/3	20160422	11	0.05	11.4	28	23	10
OMC 2/3	20160826	20	0.11	15.21	25	17	10
OMC 2/3	20161126	52	0.06	9.74	56	40	10
OMC 2/3	20170206	21	0.12	12.13	43	32	10
Oph Core	20160115	84	0.07	11.9	26	23	4
Oph Core	20160205	63	0.04	12.47	22	13	4
Oph Core	20160226	51	0.05	11.08	27	17	4
Oph Core	20160319	65	0.04	12.56	27	16	4
Oph Core	20160417	43	0.04	12.03	24	16	4
Oph Core	20160521	34	0.08	15.03	27	15	4
Oph Core	20160826	11	0.11	17.56	24	14	4
Oph Core	20170206	83	0.11	14.2	22	16	4
Serpens Main	20160202	54	0.09	12.11	23	21	5
Serpens Main	20160223	50	0.05	11.68	22	18	5
Serpens Main	20160317	51	0.04	12.2	21	14	5
Serpens Main	20160415	46	0.04	11.82	22	16	5
Serpens Main	20160521	39	0.08	14.01	22	15	5
Serpens Main	20160722	23	0.1	11.49	23	14	5
Serpens Main	20160827	12	0.09	11.32	24	15	5
Serpens Main	20160929	12	0.09	11.95	18	13	5
Serpens Main	20170222	70	0.1	11.47	26	12	5
Serpens South	20160202	58	0.09	11.27	39	35	9
Serpens South	20160223	65	0.05	18.66	39	32	9

Continued on next page

Table 5.2 – continued from previous page

Region	Date	Scan	τ^a	850 μm Noise^{b,c} (mJy beam^{-1})	Number of Sources Above $10\sigma_{rms}$	Number of Alignment Sources	Number of Family Members
Serpens South	20160317	52	0.04	11.41	34	25	9
Serpens South	20160415	48	0.04	11.57	38	29	9
Serpens South	20160521	44	0.07	12.61	38	27	9
Serpens South	20160721	11	0.08	19.42	41	31	9
Serpens South	20160827	17	0.09	17.05	43	32	9
Serpens South	20160929	18	0.08	11.34	39	30	9
Serpens South	20170222	81	0.1	17.68	36	28	9

[a]The average 225 GHz zenith opacity measured throughout the duration of the observation.
[b]These measurements of the 850 μm noise (σ_{rms}) levels are based on a point source detection in a single observation using 3″ pixels and a 14.6″ FWHM beam.
[c]The reduction method R3 was used to derive these noise estimates (see Section 5.4).

5.9 Appendix 2: Gaussclumps

GAUSSCLUMPS (Stutzki & Guesten, 1990) identifies first the brightest peak in a user-supplied map and fits a 2D Gaussian profile to the surrounding structure with a least-squares method. If the structure is deemed to be real (i.e., not a spurious detection of a noise spike, a test which is based on a series of user-defined parameters), the fit is subtracted from the data and the algorithm iteratively identifies and fits a Gaussian to the next brightest peak until all of the significant structure is identified. The algorithm is designed to weight the Gaussian fits to smaller-scale structures (at least the size of the instrument beam) such that locally peaked objects are preferred over underlying, larger-scale features. Identified sources are allowed to overlap.

There are many user defined parameters that control how GAUSSCLUMPS identifies structure as well as when it terminates after successfully extracting all of the emission

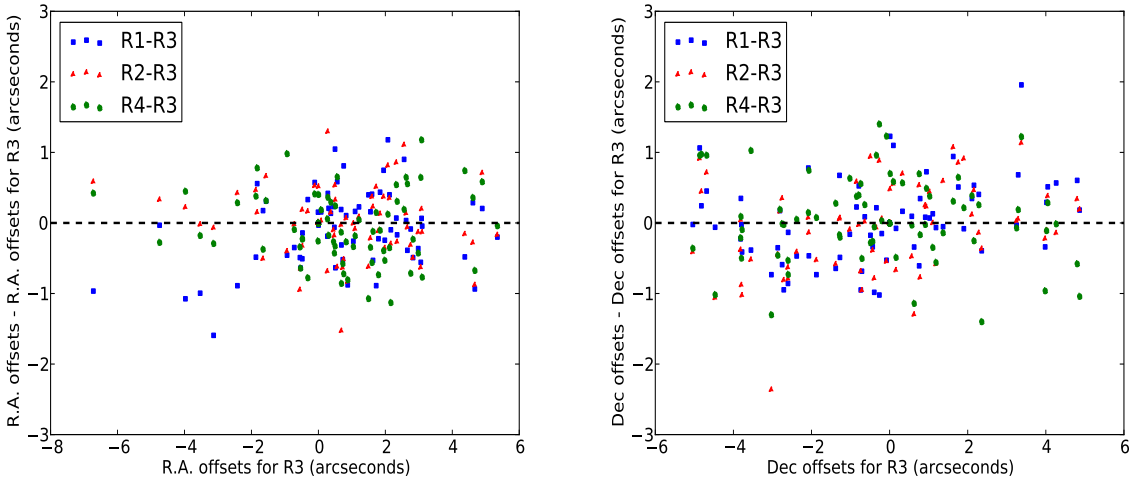

Figure 5.12 *Left:* The derived right ascension offsets measured in each of the four reductions compared to reduction *R3*. *Right:* Same as left, but showing the declination offsets. In both panels the x-axis is used to discriminate between observations and to show that our ability to align is independent of the original pointing error at the telescope.

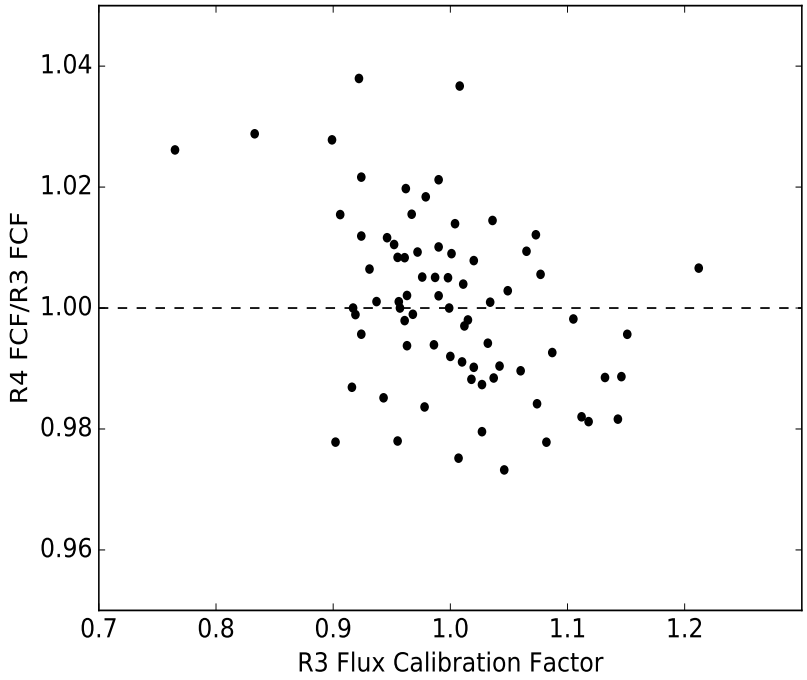

Figure 5.13 The derived flux calibration factors for compact emission sources for all observations of the eight regions using the *R4* reduction normalised by the flux calibration factors derived using the *R3* reduction. As in Figure 5.12, the x-axis is used to discriminate between observations.

found to be significant. Here, we summarise the main parameters we have used. For the parameters not listed, we simply use the default values:

1. *BACKOFF* = True. This parameter subtracts the background level from each identified emission source before calculating the sizes and centroid positions.

2. *FwhmBeam* = 5. This parameter defines the full width at half maximum (FWHM) size of the JCMT beam in pixels. No Gaussians which are smaller than this will be considered robust. For the 850 μm data, we use a pixel size of 3″ while the data smoothed with a 6″ Gaussian kernel has a FWHM beam size of 15.8″.

3. *MaxBad* = 0. This parameter determines the maximum fraction of bad pixels which can be included in an identified source.

4. *MaxNF* = 150. This parameter determines the maximum number of times the chi-squared between the Gaussian model and the data will be iteratively evaluated and adjusted.

5. *MaxSkip* = 20. This parameter sets the maximum number of consecutive failures to fit Gaussians. If GAUSSCLUMPS fails to fit a Gaussian to the data more than 20 consecutive times, the algorithm terminates.

6. *Thresh* = 10.0. This parameter defines the minimum peak brightness of a fitted Gaussian in units of the measured root mean square (RMS) noise. Note that we also measure the RMS noise for each map individually and supply that value to GAUSSCLUMPS' *RMS* parameter.

The typical RMS noise in a given 850 μm observation is $\sim$ 10 mJy beam^{-1} (see Tables 5.1 and 5.2), so we catalogue sources with peak brightnesses above $\sim$ 100 mJy beam^{-1}. Once we obtain the results from GAUSSCLUMPS, we apply an additional cull to the catalogue to select the brightest, locally peaked objects to select the image alignment and flux calibrator sources. Based on a series of tests varying the minimum brightness threshold and maximum source radius of identified objects, we select sources with peak brightnesses greater than 200 mJy beam^{-1} and radii less than 10″. We define the radius of a source to be $r = \sqrt{\mathrm{FWHM}_1 \times \mathrm{FWHM}_2}/2$ where the FWHM_N terms are the full widths at half maximum of the two dimensional Gaussian. For

the flux calibrator sources, we select sources with peak brightnesses greater than 500 mJy beam^{-1}.

5.10 Appendix 3: Alternative Alignment Method

As an alternative approach to calibrating the image alignment we present a method currently under investigation based on cross correlation between epochs. In this section we present results from the *R1* 850 μm reductions, however, this Cross Correlation method has proven to be successful for all four of the 850 μm reductions.

The Cross Correlation method computes the cross correlation between a reference epoch to each succeeding science epoch:

$$cor(\text{R.A.}, \text{Decl.}) = \sum_{\text{pixels}_x} \sum_{\text{pixels}_y} \mathcal{R}(x, y) \times \mathcal{S}(x - \text{R.A.}, y - \text{Decl.}) \tag{5.1}$$

where $\mathcal{R}$ is a reference epoch map, which we choose to be the first epoch from each region, $\mathcal{S}$ is a succeeding science epoch map to be aligned, and both maps have identical dimensions. The cross correlation of a reference epoch to a science epoch is the measure of how similar the two maps are as a function of the displacement of the science map relative to the reference map. If the two maps were identical and there were zero offset, then the measure of the cross correlation would be an auto correlation, where the peak $max\,(cor(\text{R.A.}, \text{Decl.}))$ resides at $(\text{R.A.}, \text{Decl.}) = (0, 0)$. The measured radial offset between the reference map and the science map is:

$$\text{Radial offset} = \sqrt{(\Delta\text{R.A.})^2 + (\Delta\text{Decl.})^2} \tag{5.2}$$

where ΔR.A. and ΔDecl. are the angular offsets between $max\,(cor(\text{R.A.}, \text{Decl.}))$ and $(\text{R.A.}, \text{Decl.}) = (0, 0)$ in the right ascension and declination.

To determine the position of $max\,(cor(\text{R.A.}, \text{Decl.}))$ a non-linear least squares regression is used to fit a 2D Gaussian to the inner 5×5 px^2 area, equivalent to a 15″ beam at 850 μm (Dempsey et al., 2013) surrounding the most correlated pixel (e.g. Figure 5.14). The uncertainty in the measured radial offset is estimated as the uncertainty of the 2D Gaussian fit.

The Cross Correlation method is advantageous to the GAUSSCLUMPS method as the GAUSSCLUMPS method considers a flux-limited sample, where it uses a list of bright compact small-scale structures, for which there could only be a few in

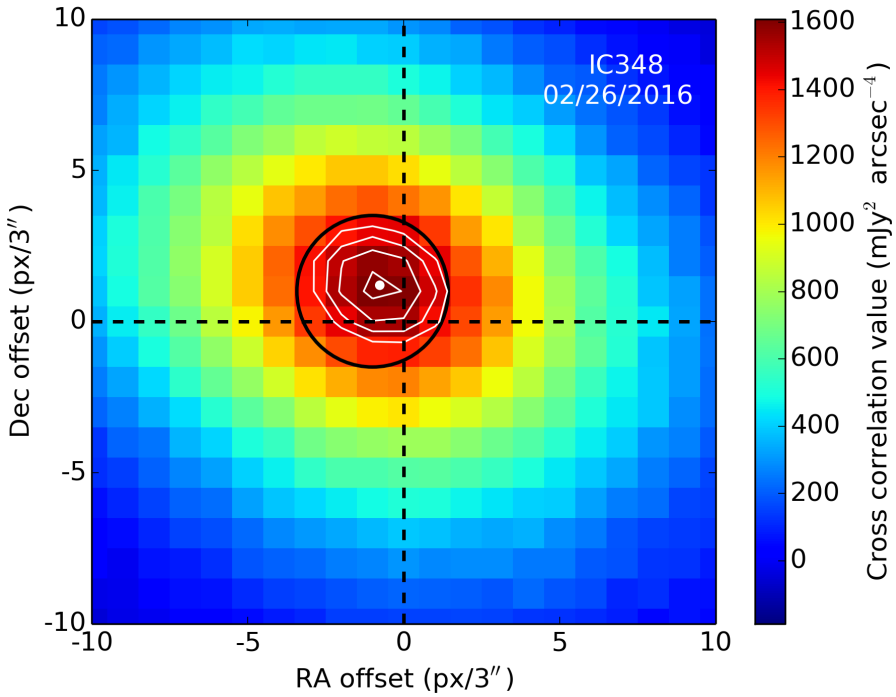

Figure 5.14 An example cross correlation of the IC348 region on 02/26/2016 compared to the reference image on 22/12/2015 for an *R1* reduction at 850 μm. The black circle represents an effective 15″ beam, the white contours represent the 2D Gaussian fit to the data, the white filled circle represents the position of the maximum of the fit, and the dashed black lines represent the zero offset position.

some cases (e.g. IC348). Comparatively, the Cross Correlation method takes in consideration the entire map, including fainter and complex structures possibly missed by GAUSSCLUMPS.

Positional offsets are measured for a total of 51 science epochs over all eight regions, and the median offset is $3.41 \pm 1.74''$, consistent with the initial position offsets measured from GAUSSCLUMPS (see Figure 5.15). Subsequently, each science epoch is re-reduced with *makemap* taking into account the derived offset relative to its reference map. Then, the same correlation and fitting method as described above is applied to the original data to the aligned maps in order to deduce any residual pointing uncertainty.

Using the GAUSSCLUMPS method, we find comparable offset distributions for the unaligned maps. In Figure 5.15, we compare the right ascension and declination offsets derived using the Cross Correlation method (C.C.) with those derived using GAUSSCLUMPS (G.C.) in a similar manner to Figure 5.12 and find them to be consis-

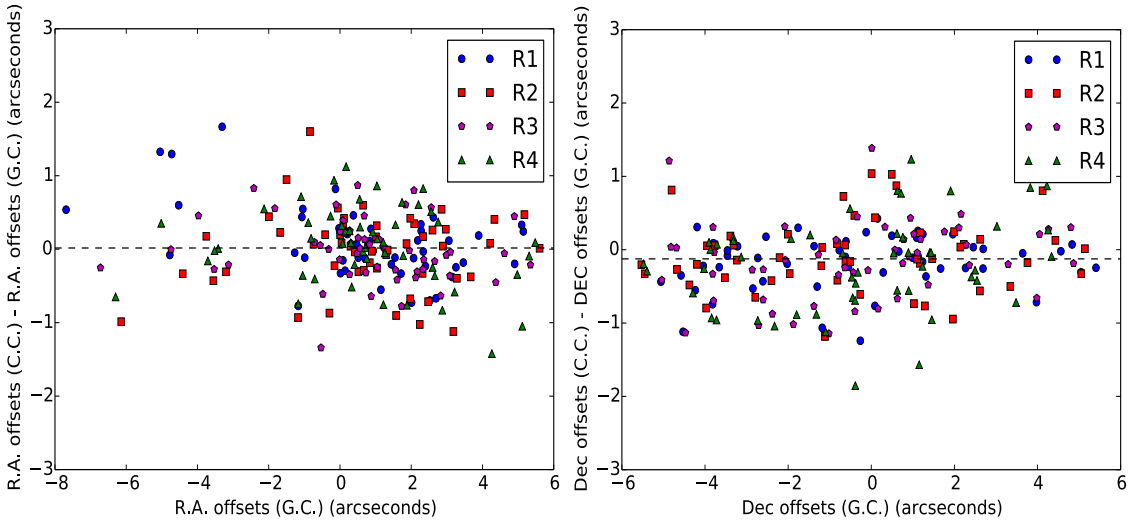

Figure 5.15 The right ascension (left) and declination (right) offsets derived using the Cross Correlation method compared with the offsets derived using the method described in the main paper. Compare with Figure 5.12.

tent. The median residual offsets after alignment using the GAUSSCLUMPS method is $\sim 0.6''$. Comparatively, the Cross Correlation method is able to self-consistently align maps to a scale $\sim 20\times$ finer than the GAUSSCLUMPS method with median residual offsets after alignment of $\sim 0.03''$. This alignment is $100\times$ smaller than a the pixel size at 850 μm, and a factor of $\sim 100\times$ better aligned than the telescope's pointing error.

Although the median residual offset is $0.03''$, the accuracy of the alignment is limited by the uncertainty in the residual offset, which is typically larger than $\sim 0.04''$ (see Figure 5.16). The uncertainty in the residual offset is limited by the uncertainty in the 2D Gaussian fit to the cross correlation, which is a result of the large spread of the cross correlation product (see Figure 5.14). Therefore, this image alignment method is limited to a single iteration of the Cross Correlation method, as it will not improve on itself with succeeding iterations.

There do not seem to be any strong correlations between the measured residual offset and the maximum cross correlation value, nor any biases due to the fitting algorithm (see Figure 5.16). We find that the more bright compact small scale structure which resides within a region, the larger the peak cross correlation value. While using GAUSSCLUMPS, data in the NGC2024 region exhibits a higher uncertainty due to clustered sources mixing with larger-scale structure. Isolated, bright emission sources

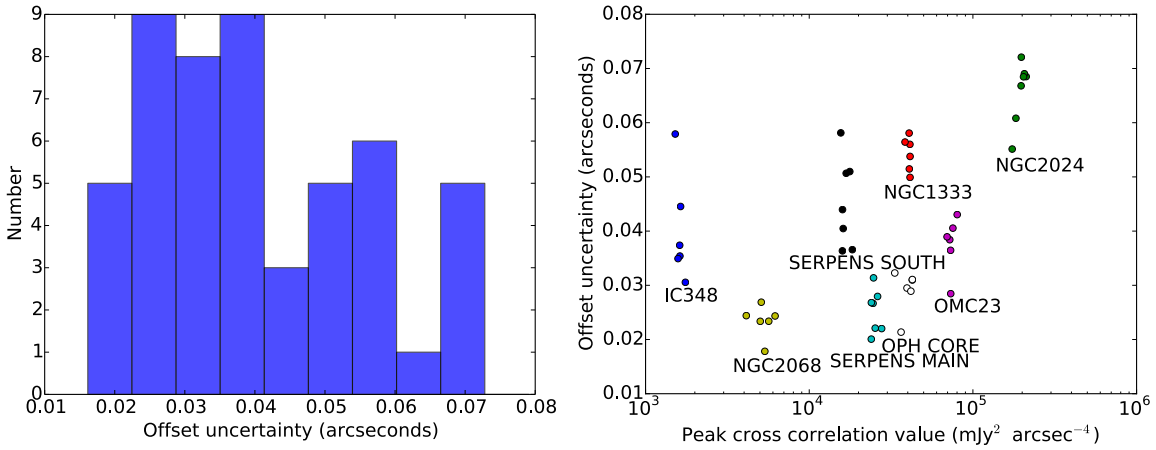

Figure 5.16 *Left:* Residual offset uncertainty distribution for aligned maps. *Right:* Residual offset uncertainty as a function of maximum cross correlation value for aligned maps.

have less fitting uncertainties in GAUSSCLUMPS (Stutzki & Guesten 1990) and therefore produce the best alignments for the Transient Survey's current data. Thus, the GAUSSCLUMPS method is biased towards having more accurate alignments for fields with compact bright sources embedded within small-scale structure, whereas the Cross Correlation method doesn't show strong correlation towards fields with either small-scale or irregular structures. As the survey matures, we will be exploring this alternate technique and refining our methodology to further improve our alignment calibration.

Chapter 6

The JCMT Transient Survey: Hunting for Variability Over Several Year Timescales

"Indescribable,
Uncontainable,
You placed the stars in the sky and
You know them by name..."
-Chris Tomlin, Indescribable

6.1 Foreword

For the final project in this dissertation, I use the data reduction and calibration procedures described in the previous chapter and apply them in a consistent manner to both JCMT Gould Belt and JCMT Transient Survey data to find and characterise variable sources over 2-4 year timescales. Each GBS field consists of 4 to 6 observations in order to reach the desired sensitivity of the survey and several GBS fields may overlap a single Transient Survey field since the Transient Survey fields have been shifted to optimise the number of YSOs observed. The GBS data were not observed with the goal of detecting variability. Therefore, the images were often taken over

The material presented in this chapter (excluding the foreword) has been published in the Astrophysical Journal: Mairs et al. 849, 107, 2017. DOI: 10.3847/1538-4357/aa9225.

the span of only a few nights, though submillimetre brightness variations linked to accretion bursts are expected over ∼month long timescales (Johnstone et al., 2013). One of the goals of the Transient Survey, however, is to determine constraints on the magnitude and the frequency of variable sources and the GBS data, which were acquired between 2012 and 2014, provides an excellent reference point to compare to current Transient survey observations.

Systematically addressing variability over several year timescales is unprecedented at submillimetre wavelengths. In this project, I led the first targeted, consistent comparison of 850 μm source brightnesses over such a wide range of observed fields. By first aligning and flux calibrating the GBS images self consistently (see Chapter 5), I compare the overlapping sources which were detected in both surveys and determine the relative flux calibration factor between the average GBS images and their corresponding average Transient Survey images. Out of the 175 850 μm emission sources I identify, I determine 7 to be robust variable candidates that display significant differences in peak brightness during the GBS and Transient survey observations. Out of these 7, two sources have shown signatures of variability in the literature such as spectroscopic classification as an "FU Orionis-like" object (Greene & Lada, 1996; Connelley & Greene, 2010) and outflowing jets with "bullet-like" substructure, a phenomenon that has been characterised around protostellar and Herbig-Haro objects for many years (see, for examples, Reipurth, 1989; Cernicharo & Reipurth, 1996; Reipurth et al., 2004, and references therein).

Throughout this work, I develop a system for determining variable candidate quality, highlight sources that are likely to have deeply embedded protostars that are not included in any catalogues so far, constrain the fractional brightness change per year for this large sample of submillimetre sources, and follow-up the observation of the submillimetre variable source EC 53 introduced in Chapter 5 (see, also, Yoo et al., submitted). I have also provided the JCMT Transient Survey sub-teams in charge of independent analyses of each of the 8 fields a list of variable candidates such that they can perform follow up studies using different analysis techniques at higher temporal resolutions (see, for example, Johnstone et al., in preparation). This project required a careful analysis of the uncertainties in both datasets to determine the variable candidates I am confident are robust.

Abstract

Investigating variability at the earliest stages of low-mass star formation is fundamental in understanding how a protostar assembles mass. While many simulations of protostellar disks predict non-steady accretion onto protostars, deeper investigation requires robust observational constraints on the frequency and amplitude of variability events characterised across the observable SED. In this study, we develop methods to robustly analyse repeated observations of an area of the sky for submillimetre variability in order to determine constraints on the magnitude and frequencyof deeply embedded protostars. We compare 850 μm JCMT Transient Survey data with archival JCMT Gould Belt Survey data to investigate variability over 2-4 year timescales. Out of 175 bright, independent emission sources identified in the overlapping fields, we find 7 variable candidates, 5 of which we classify as *Strong* and the remaining 2 as *Extended* to indicate the latter are associated with larger-scale structure. For the *Strong* variable candidates, we find an average fractional peak brightness change per year of $|4.0|\%\,\mathrm{yr}^{-1}$ with a standard deviation of $2.7\%\,\mathrm{yr}^{-1}$. In total, 7% of the protostars associated with 850 μm emission in our sample show signs of variability. Four of the five *Strong* sources are associated with a known protostar. The remaining source is a good follow-up target for an object that is anticipated to contain an enshrouded, deeply embedded protostar. In addition, we estimate the 850 μm periodicity of the submillimetre variable source, EC 53, to be 567 $\pm$ 32 days based on the archival Gould Belt Survey data.

6.2 Introduction

The accretion history of low-mass stars has been under investigation for many years (see, for examples, Kenyon et al., 1990; Bell & Lin, 1994). Despite recent advances (Vorobyov & Basu, 2005; Rice et al., 2010; McKee & Offner, 2011a; Dunham & Vorobyov, 2012; Bae et al., 2014; Vorobyov & Basu, 2015), few observational constraints exist regarding the dominant mass transfer processes occurring during the earliest phases of star formation. The presence of a disk around a protostar complicates how matter is moved from the nascent envelope to the central source. Through a combination of rotation and magnetic fields, anisotropies develop in the otherwise symmetric infalling material predicted in the seminal model of Shu (1977), causing this material to first accrete onto the disk before being transported to the protostar (for a review on pre-main sequence accretion, see Hartmann et al., 2016). The rate

of this mass transport likely varies on both long and short timescales due to gravitational (Vorobyov & Basu, 2005, 2006), magnetorotational (Armitage et al., 2001; Zhu et al., 2009), and spiral wave (Bae et al., 2016) instabilities. Material that builds up in the disk can compress the magnetosphere of a forming star, leading gas to rapidly flow onto the star through directed funnels (Romanova et al. 2003; see also Cody et al. 2017). In addition, the formation of giant planets (Nayakshin & Lodato, 2012) and stellar encounters in binary systems (Forgan & Rice, 2010; Hodapp et al., 2012) can also affect the rate at which a protostar gains mass.

Episodic accretion (short bursts of mass accretion separated by long, quiescent periods) caused by these instabilities in the disk has been gaining considerable attention in the literature (see Audard et al., 2014, and references therein). These events may be related to known outbursts observed in FU Orionis (Herbig, 1977; Hartmann & Kenyon, 1985; Reipurth, 1990) and EX Lupi (Herbig, 1989) objects. In addition to these large outbursts, Classical T Tauri Stars (CTTS) have been known to exhibit lower levels of variability (e.g. Johns & Basri, 1995; Alencar et al., 2001; Bouvier et al., 2007; Donati et al., 2013; Blinova et al., 2016). Accretion variability events with analogous intensities and timescales may occur during the youngest stages of a forming star's evolution. A non-steady accretion rate is also one solution to "the luminosity problem": the order of magnitude discrepancy between the fainter, observed median protostellar luminosity and the predicted protostellar luminosity assuming constant, steady state accretion (Kenyon et al., 1990). Other solutions to this problem, such as longer timescales over which low-mass stars form, have also been posed (e.g. McKee & Offner, 2011a). A recent study of 3000 Young Stellar Objects (YSOs) present within 18 different molecular clouds conducted by Dunham et al. (2015) using data obtained by the *Spitzer Space Telescope*, however, has provided evidence that Class 0+I protostellar lifetimes are relatively short (0.46-0.72 Myr; see also, Evans et al. 2009a; Heiderman & Evans 2015; Ribas et al. 2015; Fischer et al. 2017).

Observing the changes in accretion rate around a forming star is fundamental to understanding the earliest stages of star formation. This is possible by measuring significant changes in the protostar's peak brightness over time since the protostar's luminosity is generated primarily by the accreting material. Johnstone et al. (2013) modelled the spectral energy distribution (SED) of a deeply embedded protostar undergoing an outburst due to an increased mass accretion rate and concluded that while a stronger signal will be detected at the peak of the SED (mid- and far-infrared wavelengths), the outburst also would be observable in the submillimetre regime. The

submillimetre luminosity arises from cascade reprocessing of the stellar radiation by the surrounding dust. The negligible heat capacity for interstellar dust causes the time lag between the burst and the observation at submillimetre wavelengths to be dominated by the light crossing time of the protostellar envelope, which Johnstone et al. (2013) calculated to be several weeks to months long.

The benefit of observing variability at submillimetre wavelengths is that ground-based instruments such as the James Clerk Maxwell Telescope (JCMT) are available to monitor large areas of the sky at a regular cadence. The JCMT Transient Survey (Herczeg et al., 2017) is obtaining simultaneous continuum data at 450 μm and 850 μm on 8 nearby ($<$500 pc) star-forming molecular clouds at approximately 28 day intervals, when the targets are observable using the Submillimetre Common-User Bolometre Array 2 (SCUBA-2). These eight, 30′ in diameter, regions were originally selected from the JCMT Gould Belt Survey (GBS; Ward-Thompson et al. 2007c) and shifted on sky to optimise the number of Class 0+I and Class II YSOs present in each field. The GBS data that overlap with the Transient Survey data were collected between 2012 and 2014 while the Transient Survey data collection began in December, 2015. Therefore, these two surveys can be compared to identify and investigate variable signals over 2-4 year timescales. Here, we consider Transient Survey data obtained prior to March 1$^{\rm st}$, 2017. In the present work, we only use 850 μm data, which has higher signal to noise ratio than the 450 μm data (see Section 6.3).

The GBS data were not obtained with the goal of detecting protostellar variability, so the observations are not regularly spaced in time and they often occur over only one or two nights for a given field. Therefore, in this study, we measure the flux-calibrated peak brightnesses of extracted sources in the co-added GBS images and compare them to the same sources in the co-added Transient Survey images. In this way, we robustly characterise the properties of all identified sources and become more sensitive to long-term changes. Furthering our investigation, we also correlate the identified 850 μm emission sources with the positions of known YSOs (Megeath et al., 2012; Stutz et al., 2013; Dunham et al., 2015). This is the first study that systematically analyses two consistent submillimetre datasets separated in time in order to determine constraints on the magnitude and the frequency of deeply embedded, variable protostars.

This paper is organised as follows: in Section 6.3, we summarise the Transient Survey, GBS, and YSO catalogue observations we use throughout this work. In Section 6.4, we give an overview of our data reduction, image alignment, and relative flux calibration procedures. In Section 6.5, we present the results of the comparison between

the GBS and Transient Survey. This includes the identification of variable candidates, a description of the quality of those candidates, and the calculated fractional peak brightness changes per year. In Section 6.6, we discuss the results, highlight previously known variable sources in our sample, and construct a light curve for the variable source EC 53 (Hodapp et al. 2012; Yoo et al. 2017). Finally, in Section 6.7, we summarise our main results and provide concluding remarks.

6.3 Observations

In this analysis, we combine JCMT Transient Survey (Herczeg et al., 2017) observations with archival data of the same regions observed by the JCMT Gould Belt Survey (hereafter, GBS; Ward-Thompson et al. 2007c). All observations in both surveys are performed using the Submillimetre Common-User Bolometer Array 2 (SCUBA-2) instrument (Holland et al., 2013) at the James Clerk Maxwell Telescope (JCMT). SCUBA-2 provides continuum coverage at both 450 μm and 850 μm simultaneously with half-power bandwidths of 32 μm and 85 μm (Holland et al., 2013) and effective beam sizes of 9.8$''$ and 14.6$''$, respectively (Dempsey et al., 2013). While we expect a stronger variability signal toward the peak of the spectral energy distribution, typically the mid to far-IR (Johnstone et al., 2013), the practical data reduction and analysis of SCUBA-2 450 μm images is complicated by a strong atmospheric water vapour dependency in addition to a less stable beam profile due to dish deformation and focus errors (Dempsey et al., 2013). These effects dramatically influence the signal to noise ratio (SNR) and require further investigation before careful corrections are possible.In this paper we focus only on the 850 μm data. All of the observations were taken in the PONG1800 mapping mode (Kackley et al., 2010), yielding circular maps ("PONGs") $\sim$0.5° in diameter.

In total, there are eight Transient Survey fields (Herczeg et al., 2017): three in the Orion A and B Molecular Clouds (OMC 2-3, NGC 2068, and NGC 2024), two in the Perseus Molecular Cloud (IC348 and NGC 1333), two in the Serpens Molecular Cloud (Serpens Main and Serpens South), and one in the Ophiuchus Molecular Cloud (Oph Core). Eleven Gould Belt Survey fields include bright, compact sources within areas of significant overlap of submillimetre emission with the Transient Survey data (central locations, observation dates, 850 μm noise, and programme identification numbers for all observations are summarised in Table 6.1). Figures 6.10 through 6.17 in Appendix 6.8 show the archival GBS data mosaicked with the JCMT Transient

Table 6.1 A summary of the observed fields and their co-added noise at 850 μm. JCMT Transient Survey Fields are in bold and associated JCMT Gould Belt Survey fields are listed below each Transient Survey field.

Tile Name[a]	Central R.A. (J2000)	Central Dec (J2000)	Start Date[b]	End Date[b]	Δt[c]	850 μm Noise[d] (Jy beam^{-1})	# Obs.[e]	SCUBA-2 Programme Identification
IC348	03:44:18.3	32:05:16.0	20151222	20170209	–	0.0043	9	M16AL001
IC348-E	03:44:24.4	32:02:08.6	20120816	20130205	3.5	0.0055	4	MJLSG38
NGC 1333	03:28:54.5	31:17:09.0	20151222	20170206	–	0.0039	10	M16AL001
NGC1333-N	03:29:06.3	31:22:26.7	20120702	20120703	4.0	0.0052	4	MJLSG38
OMC 2-3	5:35:33.2	-5:00:32	20151226	20170206	–	0.0042	9	M16AL001
OMC1 tile4	5:35:49.4	-4:46:23	20120817	20130826	3.2	0.0045	4	MJLSG31
NGC 2068	5:46:13.0	-0:06:05	20151226	20170206	–	0.0039	10	M16AL001
OrionBN_450_S	5:46:13.0	-0:06:05	20141116	20141122	1.6	0.0046	6	MJLSG41
NGC 2024	5:41:41.0	-1:53:51	20151226	20170206	–	0.0043	11	M16AL001
OrionBS_450_E	5:42:48.0	-1:54:36	20141027	20141109	1.6	0.0045	6	MJLSG41
OrionBS_450_W	5:40:32.2	-1:48:00	20130212	20130303	3.3	0.0045	4	MJLSG41
Oph Core	16:27:03.2	-24:32:46.5	20160115	20170206	–	0.0050	8	M16AL001
L1688-1	16:27:02.9	-24:41:44.5	20120506	20120508	4.0	0.0053	4	MJLSG32
L1688-2	16:27:15.1	-24:10:09.7	20120518	20120520	4.0	0.0051	4	MJLSG32
Serpens Main	18:29:48.7	01:15:39.5	20160202	20170222	–	0.0045	9	M16AL001
SerpensMain1	18:29:59.8	01:14:46.9	20120518	20120519	4.1	0.0058	4	MJLSG33
Serpens South	18:30:02.2	-02:02:23.0	20160202	20170222	–	0.0047	9	M16AL001
SerpensS-NE	18:31:35.4	-01:53:50.3	20120421	20120503	4.2	0.0049	4	MJLSG33
SerpensS-NW	18:29:30.8	-01:47:07.3	20120503	20120505	4.2	0.0048	5	MJLSG33

[a] The Tile Name corresponds to the target identifier in the JCMT archive.
[b] The start and end dates refer to the date of the first observation taken by each survey and the last observation taken before March 1st, 2017 (yyyymmdd).
[c] The time between the average GBS date and the average Transient Survey date (years).
[d] These measurements of the 850 μm noise levels are based on a point source detection in each field's co-added image after smoothing with a 6″ FWHM Gaussian kernel. The effective beam size after smoothing is 15.8″.
[e] The number of observations included in the co-add.

Survey data.

6.3.1 The JCMT Transient Survey

JCMT Transient Survey (Herczeg et al., 2017) observations began on December 26^{th}, 2015 and have continued at an approximate cadence of 28 days whenever a given field is observable at the JCMT. In this paper, we address all observations obtained prior to March 1^{st}, 2017. All of the observations performed in this survey were taken in either band 1, 2, or 3 weather, where the zenith opacity at 225 GHz, $\tau_{225\,\mathrm{GHz}}$ is less than 0.12 (corresponding to a precipitable water vapour of less than 2.58 mm). For more details on the individual observations included in this work, see Mairs et al. (2017).

6.3.2 The JCMT Gould Belt Survey

GBS data were obtained from 2012 to 2014 and are publicly available on the JCMT archive. The observed fields, however, are not necessarily centred on the same locations as the JCMT Transient Survey fields. Thus, multiple fields may overlap to cover the same area of the sky (see Table 6.1 and Figures 6.10 through 6.17). All GBS observations were designed to reach a uniform depth across a wide area of each star-forming cloud. The data were collected in weather bands 1, 2, or 3 with 4 to 6 repeats such that a consistent sensitivity was achieved across the different atmospheric conditions. The GBS observations were not originally intended for studying protostellar variability, so they were not taken at a regular cadence. Often, all integrations of a given field were obtained within 1-2 nights. These data, however, are useful to compare with our recent observations as they provide brightness measurements of our identified sources across longer time separations (see Δt in Table 6.1).

Additional GBS fields that overlap with the Transient Survey fields are not included in this study. Fields are excluded if a self-consistent relative flux calibration could not be performed for the data (see Section 6.4) or if there are no significantly bright or compact sources in the region of overlap between the two survey coverages. Often, these cases occur if a GBS field has a significant amount of extended structure (complicating the disentangling of compact structures from background emission as in the case of OMC 2-3) or compact structure that is very near the edge of the map where the noise is higher. In total, 24 GBS fields have some overlapping area with

the Transient fields, of which 11 produced self-consistent flux calibration using bright, compact peaks that are also observed in the Transient fields (see Appendix 6.8).

6.3.3 *Spitzer Space Telescope* and *Herschel Space Observatory* YSO Catalogues

In order to associate 850 μm emission sources with known Young Stellar Objects, we cross-match the *Spitzer Space Telescope* catalogues of Megeath et al. (2012) and Dunham et al. (2015), and the *Herschel Space Observatory* YSO catalogue presented by Stutz et al. (2013). Megeath et al. (2012) and Stutz et al. (2013) focus on the Orion A and B Molecular Clouds while the Dunham et al. (2015) catalogue provides information for the remaining regions addressed in this paper. We adopt the YSO classifications of Megeath et al. (2012) throughout the area of their survey. In the catalogue, the authors denote Class 0+I and Flat spectrum YSOs as "P", for protostars, and Class II YSOs as "D", for disks. They also include protostellar candidate designations "FP", for faint protostar candidate, and "RP", for red protostar candidate. We make no attempt to further differentiate these four classes. In the case of YSOs discovered by Stutz et al. (2013), we only include the objects labelled by the authors as reliable protostars (Flag 1) in our analysis and generically refer to them as "'protostars" throughout this work. Finally, Dunham et al. (2015) provides the extinction-corrected infrared spectral index, α', for each YSO and the standard classification scheme to differentiate them (Greene et al., 1994; Dunham et al., 2015):

Class 0+I: $\alpha' \geq 0.3$

Flat Spectrum: $-0.3 \leq \alpha' < 0.3$

Class II: $-1.6 \leq \alpha' < -0.3$

Where possible (all regions except those in the Orion A and B Molecular Clouds), we differentiate Flat Spectrum sources from protostars and refer to Class II sources as "disks" throughout the rest of this paper.

6.4 Data Reduction and Image Calibration

We largely follow the three step data reduction and calibration methodology adopted by the JCMT Transient Survey, which is described in detail by Mairs et al. (2017). We develop further methods, however, described in Section 6.4.2 to perform a relative flux calibration between the two independent datasets (the GBS and the Transient Survey). We first construct robust images from the raw SCUBA-2 data for all observations. Then, we perform a spatial alignment for each image using a reference field. Finally, we perform a relative flux calibration to bring all observations into agreement with the mean, co-added image (for the GBS and Transient surveys separately).

6.4.1 Data Reduction

Following Mairs et al. (2017), we first perform the data reduction using the iterative map-making software MAKEMAP (described in detail by Chapin et al. 2013) in the SMURF package (Jenness et al. 2013) found within the STARLINK software (Currie et al., 2014). We grid each map to 3″ pixels and define convergence of the iterative solution when the difference in individual pixels changed on average by $<0.1\%$ of the rms noise present in the map. For both the GBS and Transient data independently, we first run an "auto-mask" reduction where the map-making software identifies regions of significant emission and separates this signal from the atmospheric noise that is eventually subtracted from the final output image. We co-add the first 4 observations for each survey individually in order to create corresponding "external masks" with boundaries defined by a signal to noise ratio of at least 3. The external masks applied to the GBS and Transient surveys have negligible differences. Then, we perform a second round of data reduction using these masks to define areas of robust astronomical emission as an additional constraint in MAKEMAP's solution. In this way, we are able to simultaneously recover faint, extended structures as well as isolated and embedded compact sources. The final mosaic produced is in units of picowatts (pW), which we initially convert to Jy beam^{-1} using the 850 μm JCMT default aperture flux conversion factor 565 Jy pW^{-1} beam^{-1}, based on a beam FWHM of 14.6″ (Dempsey et al., 2013).

The constructed SCUBA-2 maps are not sensitive to large-scale structures because these are filtered out during the data reduction process (Chapin et al., 2013). For detecting submillimetre variability of compact sources, Mairs et al. (2017) determined that the most robust results can be obtained by filtering out information on scales

$> 200''$ (reduction *R3* in Mairs et al. 2017). In this way, the peak fluxes of compact objects are well recovered and bright, compact source extraction is less confused by extended emission[1]. The CO(J=3-2) emission line contributes to the flux measured in these 850 μm continuum observations (Johnstone & Bally 1999, Drabek et al. 2012, Coudé et al. 2016). Mairs et al. (2016) show, however, that the peak brightnesses of compact sources are not significantly affected by the removal of this line.

6.4.2 Post-Reduction Alignment and Flux Calibration

Nominally, the JCMT has a pointing error of $2''$-$6''$ and a flux calibration uncertainty of $\sim 5\% - 10\%$ (Dempsey et al., 2013; Mairs et al., 2017). Using the methods developed by Mairs et al. (2017), we achieve an alignment of $< 1''$ and a flux calibration uncertainty (in a typical measurement) of 2%-3%. Since each image has a similar flux calibration uncertainty, co-adding the data further reduces the uncertainty in a given measurement by the square root of the number of observations included in the co-add. Therefore, a source's peak brightness may have an uncertainty as low as 1% or less (see Tables 6.1 and 6.2). Briefly, the image alignment and flux calibration procedures rely on comparing the properties of bright, compact sources detected across multiple observations of the same area of the sky. To identify these sources, subtract larger-scale background flux, and extract properties such as the central position, size, and peak brightness, we employ the algorithm GAUSSCLUMPS (Stutzki & Guesten, 1990), which models each compact object with a Gaussian profile. Specifically, we use the STARLINK software (Currie et al., 2014) implementation of GAUSSCLUMPS found within the CUPID (Berry et al., 2007) package. We expect the bright, point-like sources in an image to resemble Gaussian structures based on the shape of the JCMT beam. In order to mitigate spurious noise features, before running the source extraction algorithm we first smooth the maps with a $6''$ (FWHM) Gaussian kernel (see Appendix B of Mairs et al., 2017).

As described by Mairs et al. (2017), the image alignment is performed by selecting the robust, Gaussian sources that have a peak brightness of at least 200 mJy beam^{-1} (SNR ~ 10 for an individual Transient Survey observation) and a maximum effective radius of $10''$ (the effective radius is $r = \sqrt{\mathrm{FWHM}_1 \times \mathrm{FWHM}_2}/2$ where the FWHM_N terms are the full widths at half maximum of the major and minor axes of the fitted two dimensional Gaussian), comparing their central locations in each observation to

[1]For an overview of the effect of spatial filtering on SCUBA-2 data see Mairs et al. (2015, 2017).

a reference image, and then correcting for that offset. For both the Gould Belt and Transient Surveys, the chosen reference field for each region is the first Transient Survey observation of that region. The absolute position of each source is of little importance for our goals, as the most critical measurement for understanding the variability of a given point source is the relative peak brightness and the alignment uncertainty is small enough that we are able to confidently associate known protostars with the emission peaks.

Mairs et al. (2017) describe the procedure to identify and use robust calibrator sources in each field to self-consistently perform a relative flux calibration. The chosen calibrator sources are referred to as *Family members*. A given *Family Member* in the Transient Survey is selected by measuring the peak brightness of all sources that are brighter than 500 mJy beam^{-1} with effective radii $< 10''$ normalised to their average peak brightness and comparing that value to all of the other sources in a given image with these properties. The largest set of sources that display a low amount of scatter from observation to observation with respect to one another (defined by a threshold of 6% in the standard deviation) is selected to be a *Family*. The fact that these sources agree well with one another over time suggests that none of them are intrinsically varying to the level we can detect and that they are tracking the flux uncertainty of the telescope. In this manner, we determine if each observation, as a whole, is slightly brighter or fainter than the mean image allowing each epoch (image) to be corrected by a constant multiplicative factor.

We perform the relative flux calibration individually for the GBS data and the Transient data. As described in Section 6.3, the GBS data were often taken over a short time frame (one or two days) while the Transient data were taken over more than one year. Therefore, sources that do not appear to vary across the GBS observations could show signs of variability in the Transient data. In addition, a slowly varying source may look constant in both datasets individually, but given the long separation in time between the two surveys (see Table 6.1), the peak brightness could be dramatically different when cross-compared (see Section 6.5).

In order to bring the GBS data and the Transient Survey data into relative flux calibration with one another, we first identify sources common to both surveys. The sources we select have peak brightnesses larger than 200 mJy beam^{-1} and effective radii less than $10''$. For each source, we measure the average peak brightness ($f_{\rm GBS}$ and $f_{\rm trans}$) and derive the associated uncertainties ($\sigma_{f_{\rm GBS}}$ and $\sigma_{f_{\rm trans}}$) by calculating the measured standard deviation across all observations within each survey individually

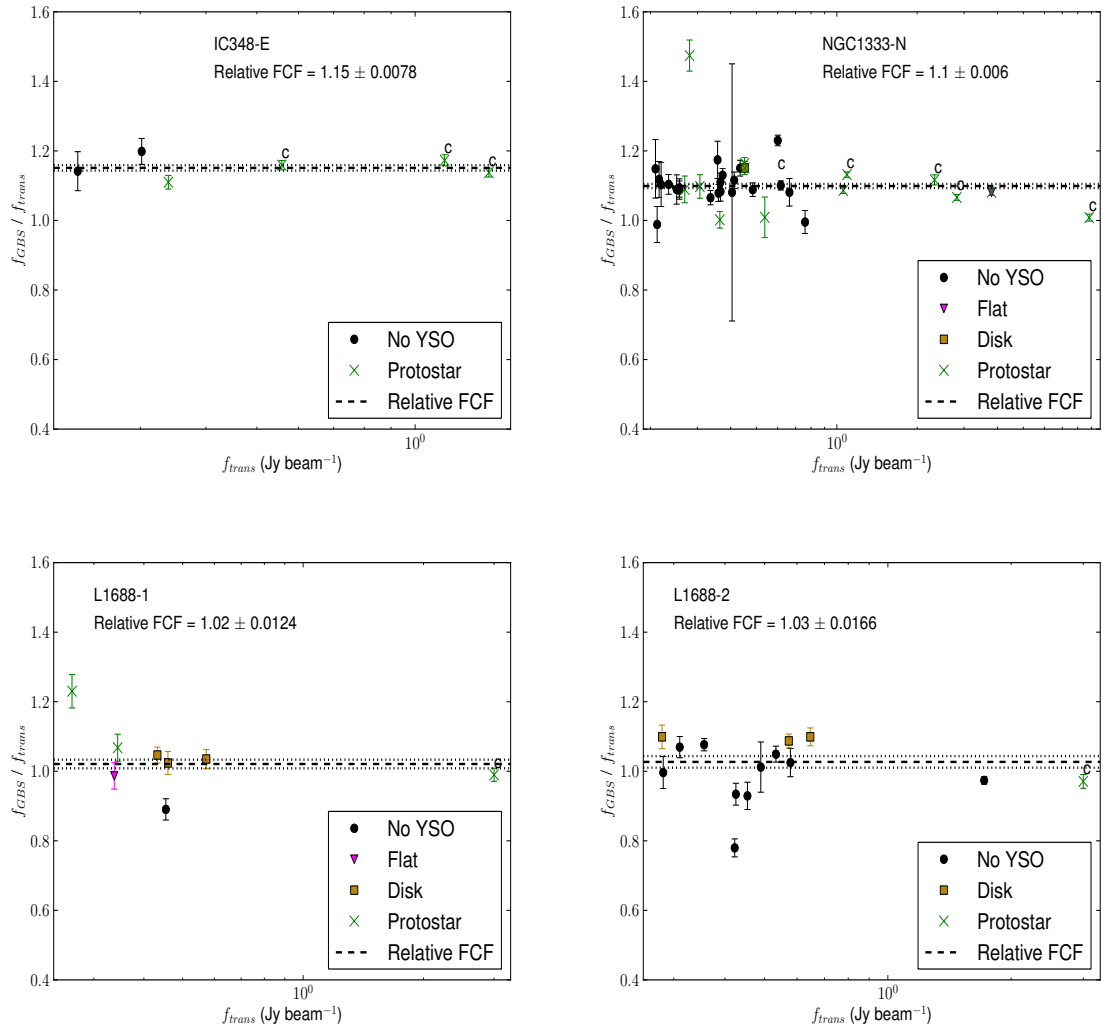

Figure 6.1 The mean GBS peak brightness divided by the mean Transient Survey peak brightness for all sources brighter than 200 mJy beam^{-1} with radii less than 10″ in the Perseus (top) and Ophiuchus (bottom) Molecular Cloud fields. The ratios are plotted against their mean peak brightnesses as measured across the Transient Survey. Points labeled with a "c" are chosen to be calibrators (*Family members*) in both the GBS and Transient Survey data independently. Each point is coloured according to its association with YSOs (see text and legend). The error bars represent the combination of the uncertainty in the rescaled GBS peak brightness measurements and the uncertainty in the Transient Survey peak brightness measurements. The dashed line represents the derived relative flux calibration factor between the GBS data and the Transient Survey data (the number by which to divide to bring the GBS data into relative calibration with the Transient Survey data). The dotted lines represent the FCF uncertainty.

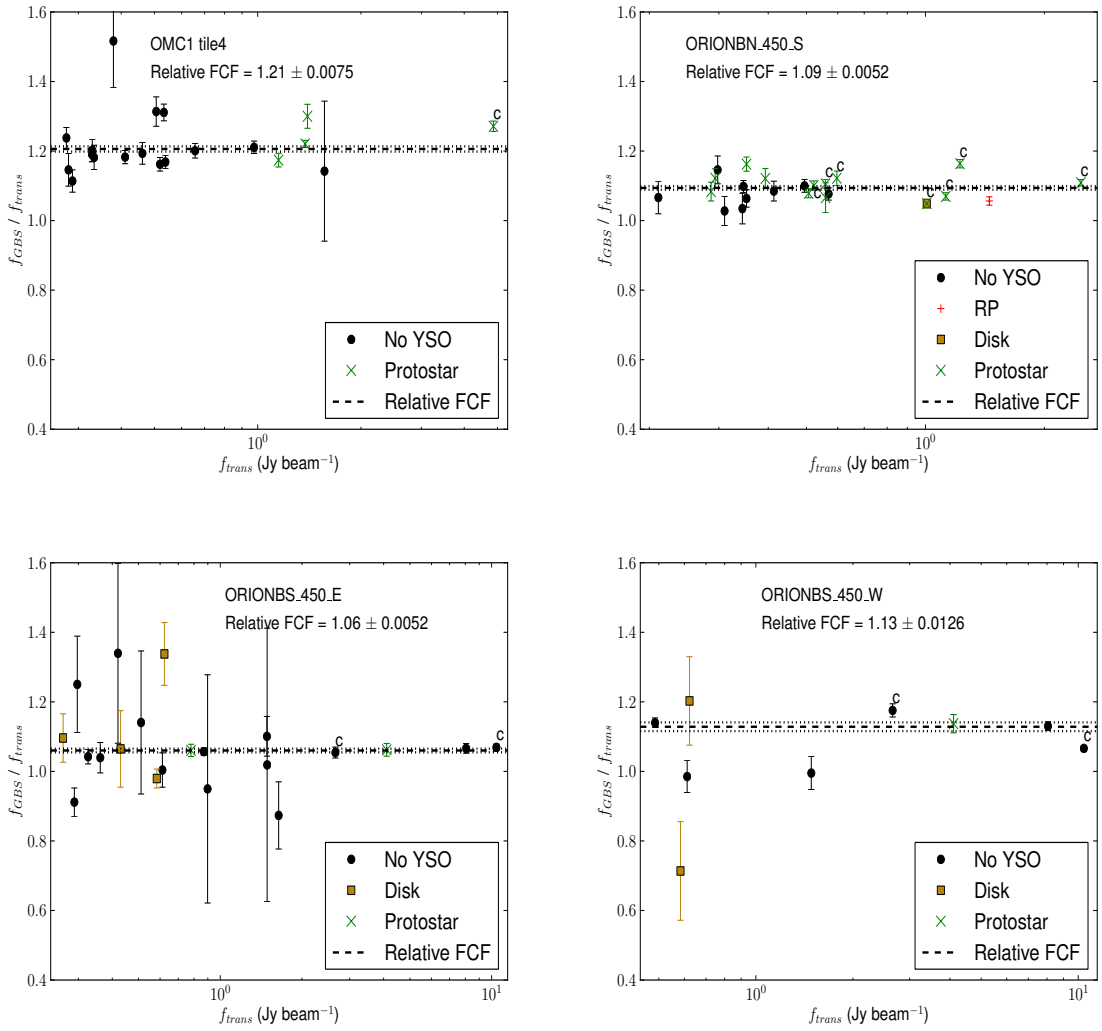

Figure 6.2 Same as Figure 6.1 for the Orion A and B Molecular Cloud fields.

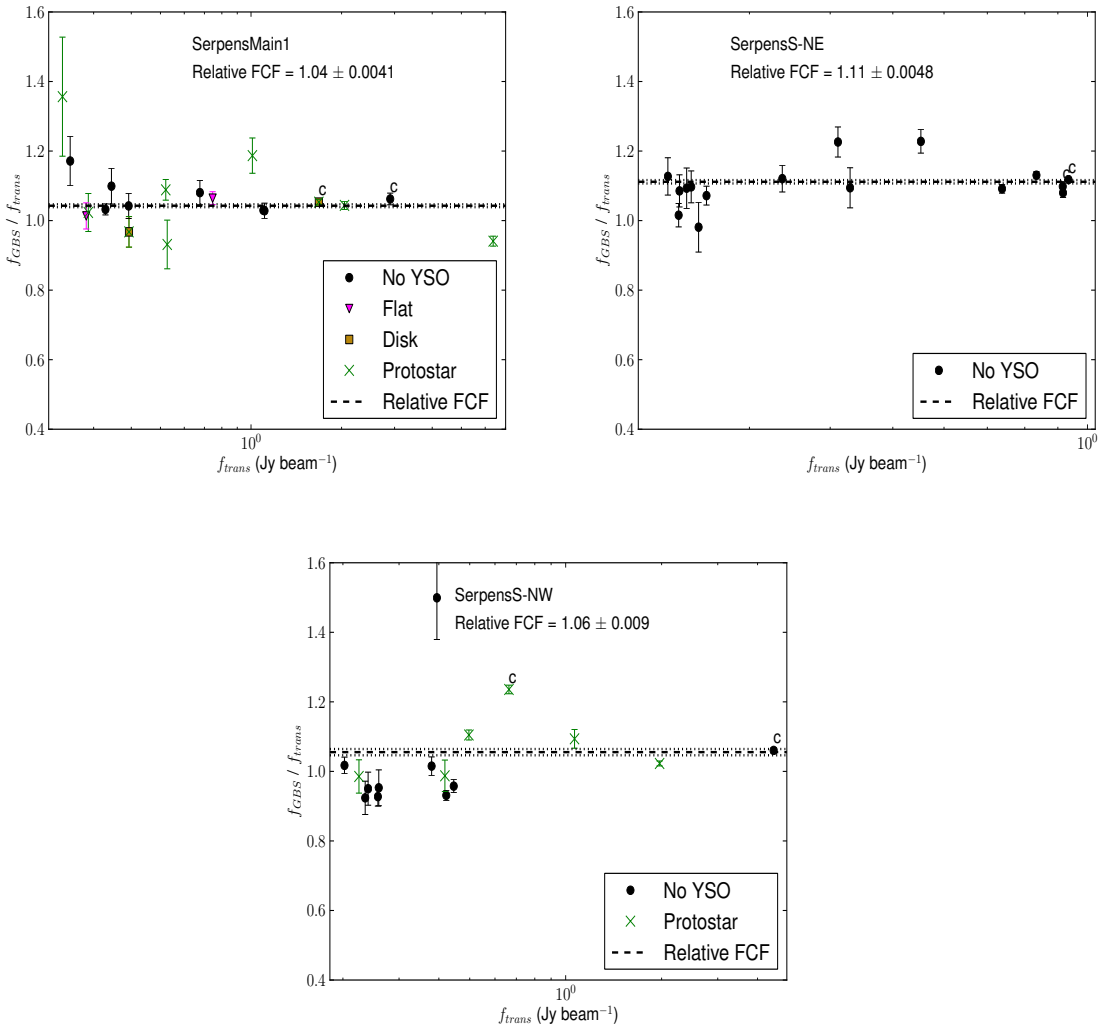

Figure 6.3 Same as Figure 6.1 for the Serpens Molecular Cloud fields.

and dividing the result by the square root of the number of observations that were included in the calculation (see Table 6.2).

We calculate a calibration factor using the measured source brightnesses by dividing the $f_{\rm GBS}$ values by their corresponding $f_{\rm trans}$ values. For the i^{th} source, we label this ratio R_i and we propagate the uncertainties, $\sigma_{R,i}$, in order to calculate the weighted mean, $\bar{R}$,

$$\bar{R} = \frac{\sum_{i=1}^{n} R_i w_i}{\sum_{i=1}^{n} w_i}, \tag{6.1}$$

where n is the number of sources and the weights are the inverse square of the propagated uncertainties,

$$w_i = \sigma_{R,i}^{-2}. \tag{6.2}$$

The uncertainty in the weighted mean, $\sigma_{\bar{R}}$, is given by

$$\sigma_{\bar{R}} = \sqrt{\frac{1}{\sum_{i=1}^{n} w_i}}. \tag{6.3}$$

Next, we calculate the difference, δ, between each peak brightness ratio and the weighted mean by subtracting the latter from the former and dividing by the uncertainty associated with that source added in quadrature to the uncertainty in the weighted mean,

$$\sigma_{{\rm tot},i} = \sqrt{\sigma_{R,i}^2 + \sigma_{\bar{R}}^2} \tag{6.4}$$

$$\delta_i = \frac{R_i - \bar{R}}{\sigma_{{\rm tot},i}}. \tag{6.5}$$

We consider all sources with $|\delta| > 3$ to be deviant outliers that might skew the weighted mean. Therefore, we remove these sources from the calculation and recompute the weighted mean. This refined weighted mean (that excludes outliers) represents the initial approximation of the relative flux calibration factor between overlapping average GBS and Transient Survey images.

To explore how the peak brightness uncertainties in each data set ($\sigma_{f_{\rm GBS}}$ and $\sigma_{f_{\rm trans}}$) affect the refined weighted mean, we use a Monte Carlo analysis. We fix $\sigma_{f_{\rm GBS}}$ and $\sigma_{f_{\rm trans}}$ for each source and randomly draw new peak brightness measurements from normal distributions with mean values equal to $f_{\rm GBS}$ and $f_{\rm trans}$ and standard

deviations equal to $\sigma_{f_{\rm GBS}}$ and $\sigma_{f_{\rm trans}}$. In this way, we calculate a new peak brightness ratio for each source, R_i, that is within the derived measurement uncertainties. Then, we calculate a new weighted mean (Equation 6.1) based on these values, discard outliers in the same manner as before, and compute a refined weighted mean. We repeat this process 10,000 times.

Of these 10,000 refined weighted mean values, we adopt the average as the relative flux calibration factor, or, *relative FCF*. This is the number by which we divide the GBS image to bring it into relative calibration with the Transient Survey image. The standard deviation in refined weighted mean values is the uncertainty in the relative FCF, $\sigma_{\rm FCF}$.

We plot the results in Figures 6.1 through 6.3. The colours represent a source's association with known YSOs. In these figures, to be associated with a protostar, flat spectrum source, protostellar candidate, or disk, the peak position of the source must be within $10''$ of the YSO location (to match the radius of the largest compact source we consider). Points labelled with a "c" are *Family Members* in both the GBS and Transient Surveys, i.e. they appear to have stable peak brightnesses in each dataset independently but not necessarily when compared over several year timescales. The FCF values are indicated by the dashed lines and $\sigma_{\rm FCF}$ is indicated by the dotted lines. As the noise is relatively constant across a map and large scale modes have been mostly removed in the data reduction procedure, we expect the relative FCF value to remain constant across the full field of any single image.

The GBS images were all originally calibrated at a level that is slightly brighter than their respective Transient Survey images obtained prior to March 1^{st}, 2017. This is the result of several factors that affect the nominal flux calibration performed at the JCMT, before we apply the relative flux calibration presented above. For instance, the nominal flux calibration values are based on data obtained between 2011 and 2012 (Dempsey et al., 2013), the water vapour monitor was replaced in 2015, and SCUBA-2 had a filter upgrade in late 2016. The combination of these factors have led to differences in the original calibration of the data obtained in the GBS and the Transient Survey eras. These effects are corrected for by our relative flux calibration.

6.5 Results

In Section 6.4.2, above, we described how we bring the mean GBS data and the mean Transient Survey data into relative flux calibration with one another by using the

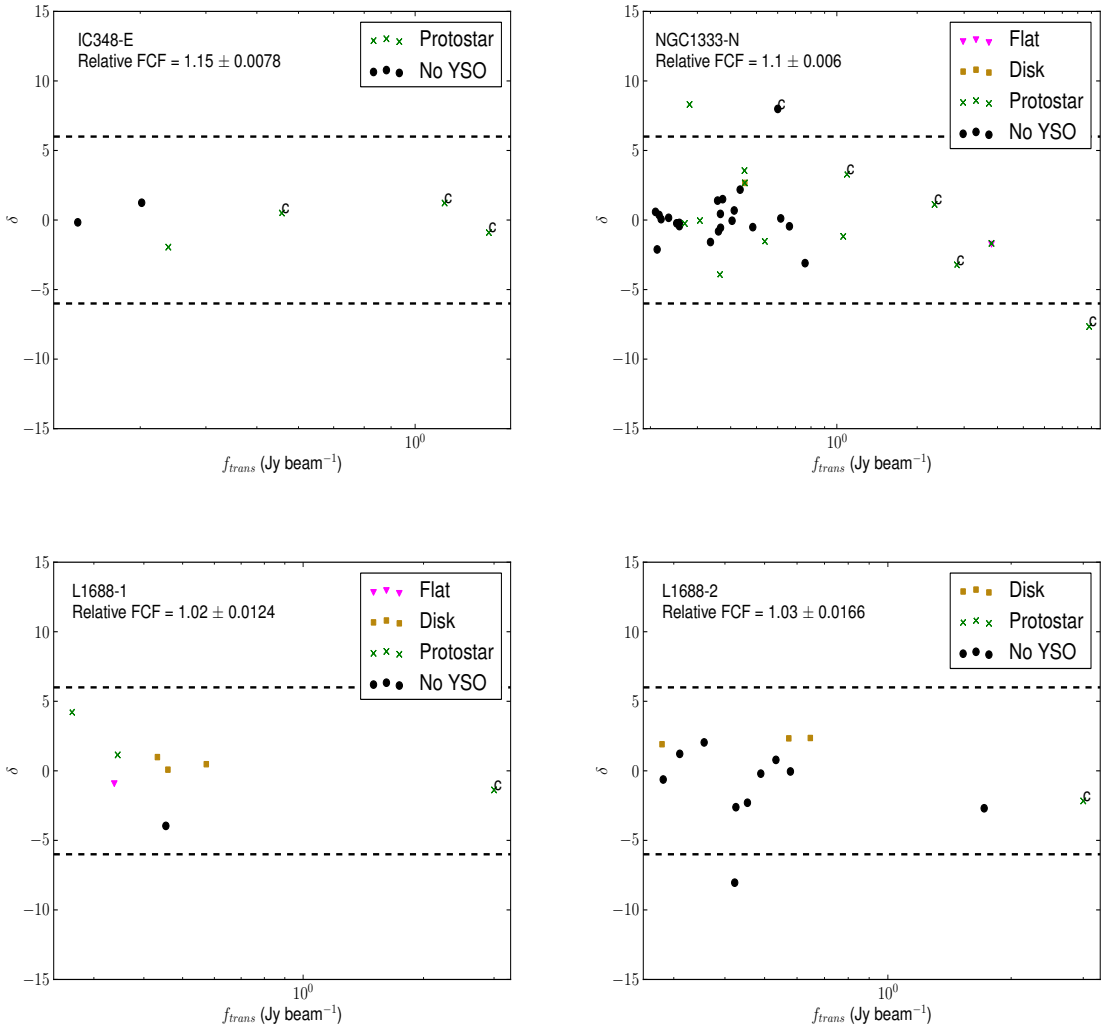

Figure 6.4 The deviation from the FCF for all sources brighter than 200 mJy beam^{-1} with radii $< 10''$ in the Perseus (top) and Ophiuchus (bottom) Molecular Cloud fields. The ratios are plotted against their mean peak brightness as measured across the Transient Survey. Points labeled with a "c" are chosen to be calibrators (*Family members*) in both the GBS and Transient Survey data independently. Each point is coloured according to its association with YSOs (see text and legend). Dashed lines are drawn at ±6 to highlight sources defined to be significant outliers.

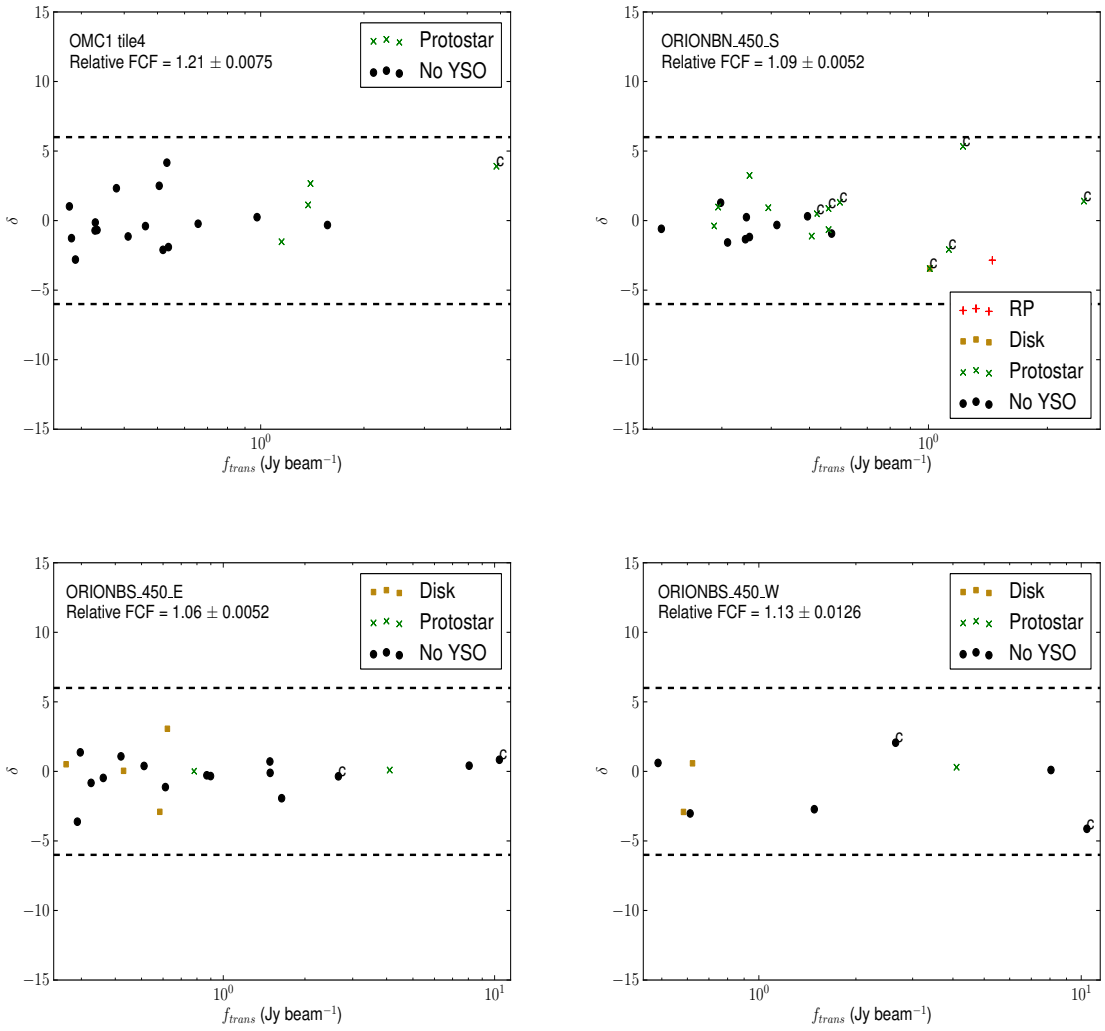

Figure 6.5 Same as Figure 6.4 for the Orion A and B Molecular Cloud fields.

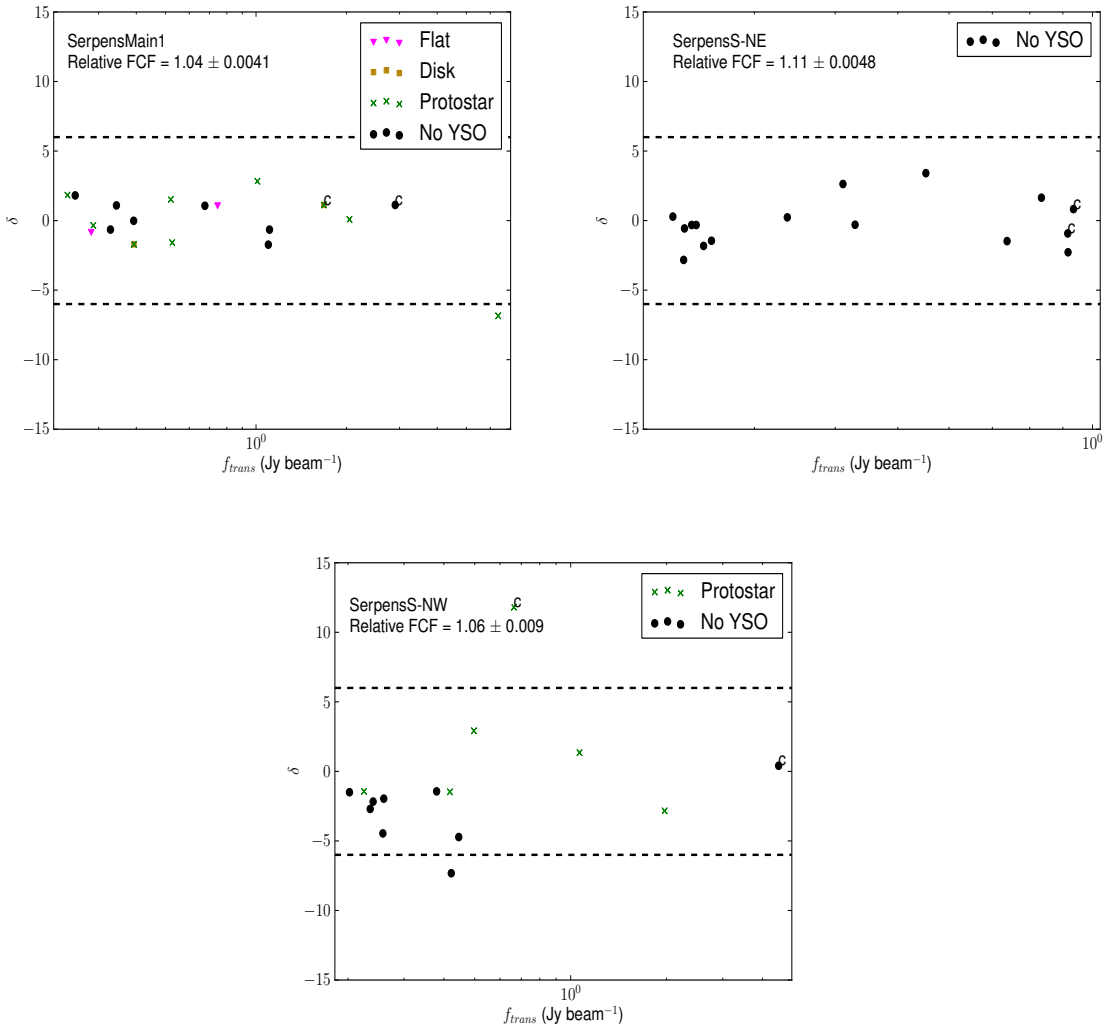

Figure 6.6 Same as Figure 6.4 for the Serpens Molecular Cloud fields.

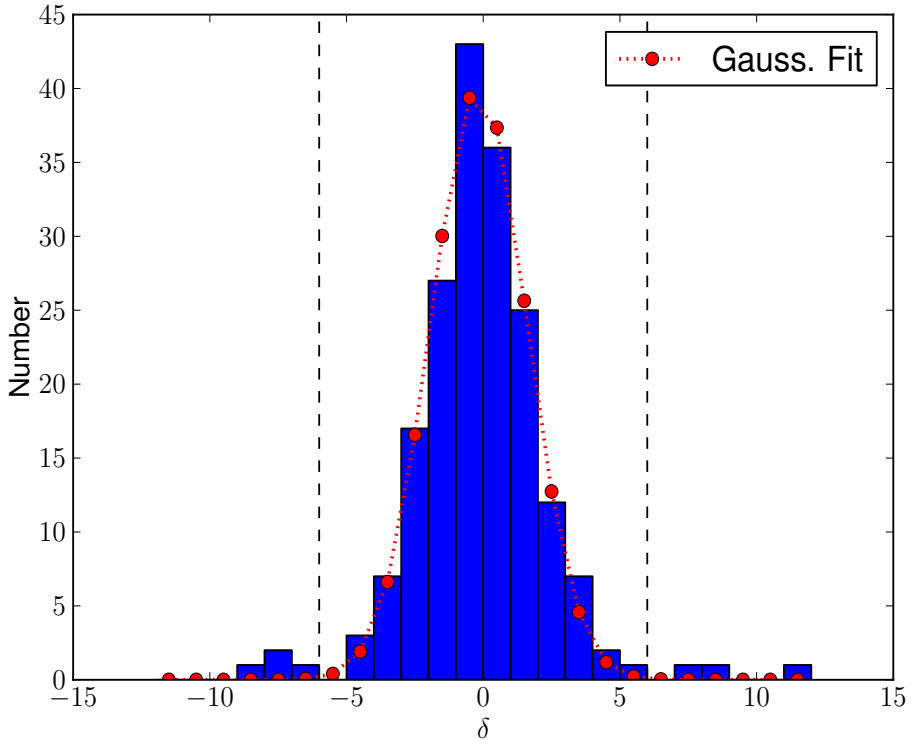

Figure 6.7 The distribution of δ values for all sources. The red points represent a Gaussian fit to the histogram. The vertical dashed lines indicate the threshold for a significant detection of a variable candidate.

Table 6.2 Summary of the variable candidate source properties.

GBS Field	ID	Other Name[a]	R.A. (J2000)	Dec (J2000)	$f_{\rm trans}$ [b]	$\frac{\sigma_{f_{\rm trans}}}{f_{\rm trans}}$ [c]	$f_{\rm GBS}$ [b]	$\frac{\sigma_{f_{\rm GBS}}}{f_{\rm GBS}}$ [c]	$\lvert\delta\rvert$	$\frac{\dot{f}}{f_{\rm trans}}$ [d]	$\sigma_{\dot{f}/f}$	Cat.[e]
NGC1333-N	PER-1	IRAS4A[f]	3:29:10.42	31:13:30.63	8.83	1.0	8.10	0.4	7.66	2.09	0.28	S
NGC1333-N	PER-10	Bolo 40[g]	3:28:59.86	31:21:33.09	0.60	1.0	0.67	0.7	7.99	-3.03	0.36	S
NGC1333-N	PER-34	[LAL96] 213[h]	3:29:07.66	31:21:54.05	0.28	2.8	0.38	1.2	8.31	-8.64	0.87	S
SerpensMain1	SER-1	[KOB2004] 258b[i]	18:29:49.80	1:15:19.33	6.38	1.5	5.76	0.4	6.85	2.37	0.39	S
SerpensS-NW	SER-10	IRAS 18270-0153[j]	18:29:37.99	-1:51:04.66	0.66	0.8	0.78	0.6	11.81	-4.05	0.35	S
L1688-2	OPH-14	–	16:26:24.95	-24:24:23.92	0.42	1.9	0.32	2.7	8.04	6.10	0.78	E
SerpensS-NW	SER-21	SerpS-MM15[k]	18:30:02.69	-2:01:09.33	0.42	0.9	0.37	1.3	7.32	2.82	0.38	E
OMC1 tile4	ORA-36	HOPS 383[l]	5:35:29.67	-4:59:37.25	0.53	0.9	0.58	1.6	4.17	-2.66	0.64	Pos.

[a]Reference name from literature. YSO name where possible.
[b]$f_{\rm x}$ is the mean source peak brightness measured across the Transient Survey ($x = trans$) or GBS ($x = GBS$) in Jy beam^{-1}.
[c]The standard deviation in f divided by the square root of the number of observations, normalised by f. In units of %.
[d]Units of % yr^{-1}
[e]Category: "S" is *Strong*, "E" is *Extended*, and "Pos." is *Possible*.
[f]Jennings et al. (1987)
[g]Enoch et al. (2006)
[h]Lada et al. (1996)
[i]Kaas et al. (2004)
[j]Connelley et al. (2007)
[k]Maury et al. (2011)
[l]Safron et al. (2015)

bright, compact sources in each overlapping field. Once the relative FCF has been computed, we repeat our calculation to search for significant outliers by replacing the individually calculated weighted mean of the source peak ratios, $\bar{R}$, with the mean FCF and $\sigma_{\bar{R}}$ with $\sigma_{\rm FCF}$ in Equation 6.5. Here, we define the significance of outliers based on the distribution of these newly calculated δ values.

Figures 6.4 to 6.6 show the δ value of every source. In Figure 6.7, we show the distribution of δ values for all sources fit with a Gaussian curve. The fitted Gaussian has a standard deviation of $\sigma_{GaussFit} = 1.76$. The measured δ values significantly deviate from the fitted Gaussian profile beyond a threshold of $\delta = \pm 6$. Therefore, we define sources that have $|\delta| > 6$ as noteworthy outliers. The probability of detecting a source with $|\delta| > 6$ from the Gaussian distribution of values is 0.06%. Over all 11 GBS fields that overlap with the Transient Survey data, however, we find that 7 out of 175 independent sources[2] brighter than 200 mJy beam^{-1} with radii $<10''$ exceed this threshold. Thus, 96% of the identified sources show no sign of variation between the average GBS data and the average Transient data to our sensitivity, while the remaining 4% are considered variable candidates and form the basis of all further investigation. We summarise the properties of the variable candidates in Table 6.2.

In order to discern the quality of each of the variable candidates, we construct difference maps, subtracting the GBS co-add from the Transient co-add for each region, and perform a visual analysis on each map to note sources with extended features in confused regions as well as larger-scale differences between the maps which can complicate our measurements (see Figures 6.18 and 6.19 in Appendix 6.8).

While we were investigating the difference maps, we were also able to look for any indication of compact sources that were present only in the GBS data and not in the Transient Survey data (or vice versa) in case an object had varied such that it fell below the detection threshold (200 mJy beam^{-1}) in one dataset but not in the other. No significant objects of this type were identified.

Through our visual inspection of each source in their respective difference maps, we define 2 categories of variable candidate:

Strong Candidates (S): The source exceeds the significance threshold ($|\delta| > 6$), has an average Transient Survey peak brightness measurement of $f_{\rm trans} > 200$ mJy beam^{-1}, and has a radius less than $10''$. There is an obvious indication of significant compact structure at the location of the source in the difference map.

[2]Sources that appear in multiple GBS fields as well as a Transient Survey field are only counted once.

Table 6.3 Associations between variable candidate and YSOs.

GBS Field	ID	Other Name	N_{proto} [a]	$Dist_{proto}$ [b]	Category
NGC1333-N	PER-1	IRAS4A	2	2.64	S
NGC1333-N	PER-10	Bolo 40	0	–	S
NGC1333-N	PER-34	[LAL96] 213	1	2.56	S
SerpensMain1	SER-1	[KOB2004] 258b	1	3.16	S
SerpensS-NW	SER-10	IRAS 18270-0153	1	6.22	S
L1688-2	OPH-14	–	0	11.31	E
SerpensS-NW	SER-21	SerpS-MM15	0	–	E
OMC1 tile4	ORA-36	HOPS 383	0	13.49[c]	Pos.

[a]The number of protostars within 10″ of the source peak.

[b]The distance, In units of ″, between the source peak and the nearest protostar within 15″. – indicates no nearby objects.

[c]The extracted 2D Gaussian traces an extended structure, slightly shifting the peak of this emission source away from HOPS 383 but a brightness change associated with a compact feature containing the Class 0 protostar is apparent in the constructed difference maps (see Section 6.6.1 and Figure 6.18).

Table 6.4 Associations between 850 μm emission sources and YSOs.

	# 850 μm Sources[a]	# With Proto (10″)[b]	# With Disk (10″)[c]	# With no known YSO
Total	175	54	13	108
Strong Var. Can.	5 (3%)	4 (7%)	0 (0%)	1 (1%)
All Var. Can.	7 (4%)	4 (7%)	0 (0%)	3 (3%)

[a]Number of robust, bright, compact sources extracted using the GAUSSCLUMPS algorithm.

[b]Number of sources with a protostar within 10″ of their peak location (also expressed as a percentage of the total number of sources in this category).

[c]Number of sources with a disk (Class II YSO) within 10″ of their peak location (also expressed as a percentage of the total number of sources in this category).

Extended Candidates (E): The source exceeds the significance threshold ($|\delta| > 6$), has an average Transient Survey peak brightness measurement of $f_{\rm trans} > 200\,{\rm mJy\,beam^{-1}}$, and a radius less than $10''$. There is little indication of compact structure present at the location of the source in the difference map; surrounding extended structures complicate the measurements.

We find 5 *Strong* sources and 2 *Extended* sources. *Extended* variable candidates display very little evidence of real compact emission changing brightness between the GBS and Transient Survey datasets. It is likely that we are underestimating the uncertainty for these objects due to the uncertainty in the background subtraction computed by the GAUSSCLUMPS algorithm in confused areas. Both of these remain interesting sources, though they are less robust candidates for variability than those classified as *Strong*. The *Extended* source OPH-14 traces part of the larger scale structure around the prototypical Class 0 source VLA 1623 (Andre et al., 1993), though we see no significant evidence that the deeply embedded protostar itself is undergoing a significant brightness change at 850 μm. In addition to the *Strong* and *Extended* candidates, one *Possible* candidate (HOPS 383; Safron et al. 2015) is also identified in Tables 6.2 and 6.3 and is discussed further in Section 6.6.1.

In general, we expect the presence of a disk to influence the accretion rate of material onto the central protostar. Of the 5 *Strong* variable candidates, 4 are associated with a known protostar (and likely, therefore, a young circumstellar disk) and none are associated with a known evolved disk object (see $N_{\rm proto}$ in Table 6.3; see also Table 6.4). To be associated with a protostar or a disk, the peak position of the source must be within $10''$ of the YSO location. Recall that the presence of a dusty envelope increases the likelihood of detecting variability at submillimetre wavelengths due to the reprocessing of the light emitted by a burst event. Generally, the envelope is weak for known, more evolved disk candidates seen at infrared wavelengths.

In total, out of the 175 independent sources identified across all 8 Transient Survey fields and their 11 associated GBS fields, we find 54 protostars and 13 disk objects within $10''$ of source peaks. Therefore, to the sensitivity achieved across these surveys, we find approximately 7% of known protostars associated with an 850 μm emission source to be potentially varying. One of the *Strong* variable candidates, IRAS4A (PER-1), has two protostars associated with its peak. Another, SER-1 displays an elongated structure that may indicate multiple embedded sources or some outflow activity. Only 3% of the sources not known to be associated with a YSO show signs

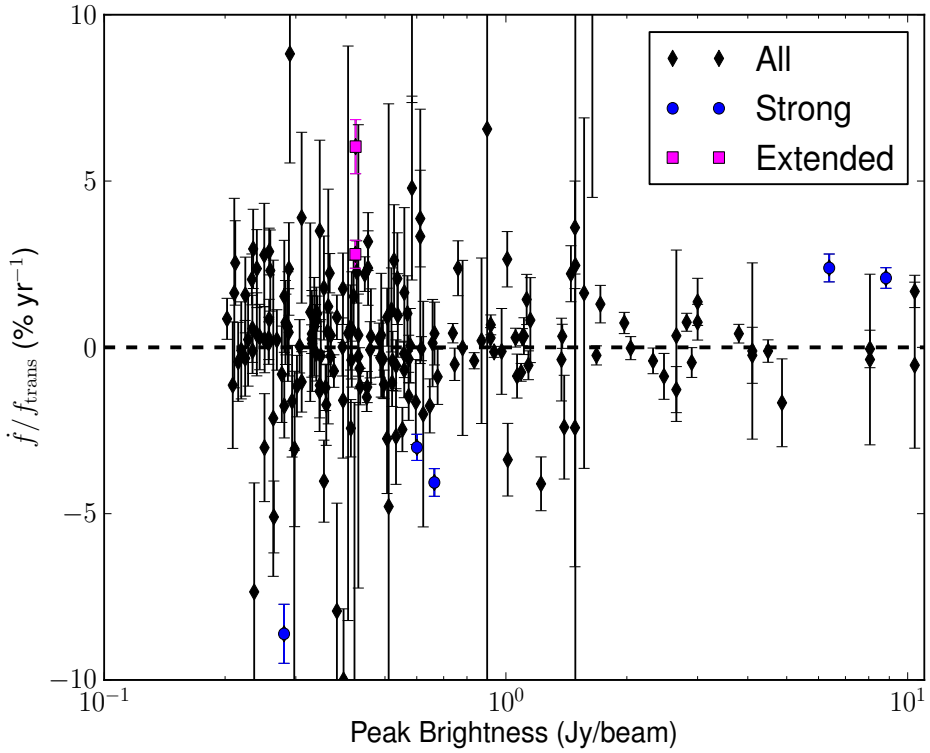

Figure 6.8 The change in peak brightness divided by the difference between the average GBS and Transient Survey observation dates, normalised to the average Transient Survey peak brightness ($(\dot{f}/f_{\rm trans})$, Equation 6.6). *Strong* variable candidates are indicated by blue circles. *Extended* variable candidates are indicated by magenta squares. All other sources are indicated by black diamonds. Variable candidates are intermixed with non-variable sources as the detection sensitivity varies from field to field (see Table 6.5).

of variability. Excluding the *Extended* sources, which are less robust detections, only one source without a known protostar or disk shows signs of variability. We do not expect starless cores to be variable. Therefore, the *Strong* variable candidate without a known embedded YSO, Bolo 40 (Enoch et al., 2006), is a good target for follow-up studies to identify signatures of very faint, deeply embedded protostars that have yet to be detected.

The GBS data and the Transient Survey data were obtained 2-4 years apart depending on the field (see Table 6.1) which allows us to characterise the apparent, significant submillimetre brightness changes in terms of a fractional change per year (averaged over both datasets) assuming a linear change throughout the GBS/Transient

Survey time lag,

$$\frac{\dot{f}}{f_{\rm trans}} = \frac{f_{\rm trans} - f_{\rm GBS}}{f_{\rm trans}} \times \left(\frac{1}{\bar{t}_{\rm trans} - \bar{t}_{\rm GBS}} \right), \tag{6.6}$$

where $\bar{t}_{\rm GBS}$ is the mean GBS observation date for that field and $\bar{t}_{\rm trans}$ is the mean Transient Survey observation date for that field (the parenthetical term in the denominator is the same as Δt in Table 6.1). We choose to normalise the result to the mean Transient Survey observation to express the brightness change as a percentage of the (near) current source peak brightness. The associated error, $\sigma_{\dot{f}/f}$, is the combination of the Transient Survey average peak brightness error (see Section 6.4.2 and Table 6.2), the GBS peak brightness error, and the error in the weighted mean.

Table 6.5 Current $\dot{f}/f_{\rm trans}$ sensitivity limits.

GBS Field	Δf Sensitivity Limit (%yr^{-1})	Typical Δf Sensitivity (%yr^{-1})
IC348-E	2.2	2.9
L1688-1	3.3	5.0
L1688-2	2.9	4.8
NGC1333-N	1.4	3.6
OMC1 tile4	2.0	4.3
OrionBN_450_S	3.7	7.4
OrionBS_450_E	3.8	17.7[3]
OrionBS_450_W	2.4	4.7
SerpensMain1	1.1	5.0
SerpensS-NE	1.0	4.6
SerpensS-NW	1.5	3.8

We plot $\dot{f}/f_{\rm trans}$ as a function of the Transient Survey average peak brightness in Figure 6.8, coloured according to category. A typical, *Strong* variable candidate has an averaged brightness change per year of $|4.0|\%\,{\rm yr}^{-1}$ with a standard deviation of $2.7\%\,{\rm yr}^{-1}$. The *Extended* variable candidates are grouped in a similar area of parameter space. This grouping is primarily the result of poor background flux subtraction performed by the GAUSSCLUMPS algorithm in these more confused regions. This strengthens the notion that the uncertainties in these measurements are likely underestimated. Every calibrated GBS field includes a distribution of sources that appear slightly brighter and slightly fainter than their Transient Survey counterparts. The brightest *Strong* candidates all display a positive $\dot{f}/f_{\rm trans}$, while the fainter *Strong*

candidates all show significant brightness decreases between the GBS and Transient Survey eras. This may indicate an intrinsic difference in the underlying accretion process for different types of protostars. This trend, however, is only based on small number statistics.

Three factors contribute to the sensitivity of $|\dot{f}/f_{\rm trans}|$: the uncertainties in the GBS and Transient Survey peak brightness measurements, the uncertainty in the calibration, and the time lag between the two data sets for each field (see Δt in Table 6.1). In Table 6.5, we present both the sensitivity limit and the typical sensitivity in $|\dot{f}/f_{\rm trans}|$ for each field. To calculate the sensitivity limit for each field, we set Equation 6.5 (replacing $\bar{R}$ with the mean FCF and σ_R with $\sigma_{\rm FCF}$) equal to 6 (the threshold at which we define a source to be a variable candidate) and solve for the GBS peak brightness in terms of the Transient Survey peak brightness. Then, we substitute the result into Equation 6.6 for each source and find the minimum allowed $|\dot{f}/f_{\rm trans}|$ for a variable candidate in each field. For the typical $|\dot{f}/f_{\rm trans}|$ sensitivity, we report the median $|\dot{f}/f_{\rm trans}|$ value calculated in this fashion. As the Transient Survey continues and we are able to observe longer time separations, our sensitivity will improve.

6.6 Discussion

The relative flux calibration agreement between GBS fields associated with the same Transient Survey field is robust. There are 13 sources in total that overlap two GBS fields and a Transient Survey field. There are no cases where a source is considered to be a variable candidate in one GBS field and not the other. In total, we find 7 sources with significantly discrepant GBS to Transient Survey peak brightness ratios, indicating they are candidates for variability. These sources are distributed around $\dot{f}/f_{\rm trans} = 0\%\,{\rm yr}^{-1}$ (Figure 6.8). Though we do not necessarily expect linear changes over 2-4 year timescales, assuming linearity, the average $|\dot{f}/f_{\rm trans}|$ of the *Strong* variable candidates over several year timescales using co-added, well calibrated maps is $|4.0|\%\,{\rm yr}^{-1}$ with a standard deviation of $2.7\%\,{\rm yr}^{-1}$ (see Table 6.2 and Figure 6.8). We are not sensitive to short timescale, small fluctuations that may average out the signal over time (see Section 6.6.2 for a further example of the limitations of time averaging), so we expect there to be more variable candidates in these fields that can be identified at higher time resolutions and sensitivities. An analysis of variability within the Transient Survey data alone is addressed by Johnstone et al., (in preparation).

The observed difference in the submillimetre flux of an embedded protostar undergoing a change in accretion rate is determined by the heating or cooling of the dusty envelope. As long as the dust temperature remains above ∼25 K, the sub-mm response will be approximately linear to this change in temperature. When the dust temperature is lower, the submillimetre response becomes much stronger. In equilibrium, the dust temperature, $T_{\rm dust}$, in most of the envelope is expected to vary with accretion luminosity, $L_{\rm acc}$, as $T_{\rm dust} \propto L_{\rm acc}^{1/4}$ (Johnstone et al., 2013). As Johnstone et al. (2013) note, however, this relationship will break down in the very outer envelope where significant heating comes from the external radiation field and therefore the temperature of the dust remains relatively fixed.

For small fractional changes in temperature, the accretion luminosity is approximated by

$$\frac{\Delta L_{\rm p}}{L_{\rm p}} \propto 4 \times \frac{\Delta T_{\rm dust}}{T}. \tag{6.7}$$

Assuming the submillimetre response is roughly proportional to the dust temperature which itself is determined primarily by the accretion luminosity, a 4% change in the observed submillimetre flux corresponds to a ∼16% change in the accretion luminosity (accretion rate) of the central protostar. If the envelope temperature drops below ∼25 K, then the submillimetre response will be closer to one-to-one (i.e. a 4% change in the observed submillimetre flux corresponds to ∼4% change in accretion luminosity). Much work is still required to fully understand the relationship between the observed submillimetre flux and the accretion luminosity (see, for example, Johnstone et al. 2013).

We find 7% of the known protostars in our observed fields display a typical 16% accretion variability over ∼3 years (using Equation 6.7). In Figure 3 of Herczeg et al. (2017), the authors summarise expectation values of accretion variability over specific timescales, taking into consideration a model in which the variability is driven by large-scale gravitational instabilities in the disk (Vorobyov & Basu, 2010) and a model in which smaller-scale magneto-rotational instabilities are included Bae et al. (2014). The models of Vorobyov & Basu (2010) predict that ∼7% of protostars will undergo a 7%-8% change in accretion luminosity over 3 years of observations. Bae et al. (2014), however, predict that ∼ 7% of protostars will undergo a 40% change in accretion luminosity over this same timeframe. Under the simple assumption that submillimetre brightness varies linearly as dust temperature, Equation 6.7 predicts our results to lie between the two models. We note, however, that this result is

tempered by uncertainties in the relationship between changes in the submillimetre flux due to the protostellar luminosity, the reliability expected from the models of protostellar episodic accretion over few year timsescales (as a detailed investigation relies on accurately tracing the physics of the inner disk), and the sensitivity of our source detection methods.

Future surveys studying accretion variability onto deeply embedded protostars would benefit from working in the far infrared, near the peak of the protostellar envelope spectral energy distribution in order to have a more linear relationship between observed brightness changes and the underlying accretion luminosity variation (see Johnstone et al., 2013). These surveys are likely to be undertaken by space observatories such as the *Space Infrared Telescope for Cosmology and Astrophysics* (*SPICA*; Roelfsema et al., submitted) or the *Origins Space Telescope* (*OST*; Meixner et al. 2016) which will further benefit from the stability of space-based observations, provided that the calibration and dynamic range of the instruments is excellent. As these missions are still a decade or more away, an obvious first undertaking will be to use *Herschel Space Observatory* observations of nearby star-forming regions as a previous epoch, yielding a multi-decade delta in time. As this paper shows, however, there are significant challenges in collating two disparate data sets and thus care will need to taken in order to reach relative uncertainties at the $1\% - 2\%$ level.

6.6.1 Previously Known Signatures of Variability

Nearly all of the submillimetre emission sources in Table 6.2 are detected in previous surveys (see, for example, Johnstone et al., 2000b, 2001; Skrutskie et al., 2006; Kirk et al., 2006b; Di Francesco et al., 2008b), and many have been associated with outflows. Two *Strong* sources have previously-known indicators of variability from outflow knots or inferences from spectroscopic diagnostics: IRAS4A (PER-1) and IRAS 18270-0153 (SER-10).

In the case of IRAS4A, the evidence is in the form of outflowing jets with compact knots (Choi, 2001), a phenomenon that has been characterised around protostellar and Herbig-Haro objects for many years (see, for examples, Reipurth, 1989; Cernicharo & Reipurth, 1996; Reipurth et al., 2004, and references therein). These jets may be caused by episodic outbursts (Choi, 2001) that increase the density of the ejected material for a short period of time, leaving some indication of the history of activity around the source. Other evidence, however, points to jet precession as the source of

the knots (Choi et al., 2006; Santangelo et al., 2015).

IRAS 18270-0153 (Connelley et al., 2007) has been classified as an "FU Orionis-like" object, owing to its deep CO and water vapour absorption bands and lack of clearly defined photospheric absorption lines (Greene & Lada, 1996; Connelley & Greene, 2010). These features indicate the presence of a very hot, optically thick inner disk, which is a signpost for an ongoing FUor accretion outburst (Zhu et al., 2007). In addition, this protostar has a notable bipolar outflow in H_2 (Zhang et al., 2015). We observe a decrease in brightness at the rate of 4.3% yr^{-1}, assuming a linear change.

In addition to these *Strong* candidates, we highlight one further source of interest, ORA-36 (HOPS 383; Safron et al. 2015), which we list as a *Possible* variable candidate in Tables 6.2 and 6.3. HOPS 383 is a source that contains the youngest known Class 0 protostar that has shown evidence of an outburst in both infrared and submillimetre data (Safron et al., 2015). Mid- and far-infrared photometric data indicate that the source underwent a strong outburst between 2004 and 2012. By comparing 450 μm Submillimetre Common-User Bolometre Array (SCUBA) data from 1998 to 350 μm Submillimetre APEX Bolometer Camera (SABOCA) data in 2011, Safron et al. (2015) found that the source had doubled in brightness in the submillimetre. We expect that an accretion outburst would be much brighter in the infrared (Johnstone et al., 2013). Here, we see a clear indication of a compact emission source closely associated with HOPS 383. We do not consider it a robust variable candidate as its δ value is less than 6 ($\delta = 4.17$; see Table 6.2), though it appears to be undergoing a brightness decrease between the GBS and Transient Survey data at the level of -2.66 ± 0.64% yr^{-1}. Fischer & Hillenbrand 2017 have also noted a recent brightness decrease in the H and K-bands for this source. The extracted 2D Gaussian source traces an extended structure in which the compact feature is embedded (see Figure 6.18), causing the peak of the identified source to artificially shift further from the protostar it contains.

In addition to the variables, some non-varying sources are also of interest. Our observations coincide with 2 long-term radio (cm wavelength) variable sources in IC 348 (VLA 2 and VLA 3; Forbrich et al. 2011), but neither are significantly variable at 850 μm. VLA 2 was found to decrease in brightness from 0.09 mJy in 2001 (Avila et al., 2001) to 0.04 mJy in 2008, In this work, we have found no significant brightness change between the GBS and Transient Survey observations ($\delta = 0.81$) for the associated 850 μm emission source. Similarly, we find no 850 μm emission source to coincide with VLA 3, which increased in radio brightness from 0.41 mJy in 2001 Avila

et al. (2001) to 0.542 mJy in 2008, It is important to recognise that radio and submillimetre variability arise from different phenomena. In the former case, magnetic flares and synchrotron radiation dominate while in the latter case we are tracing accretion events.

6.6.2 The Submillimetre Variable EC 53

One prominent source in the Serpens Main Transient Survey field, EC 53 (Eiroa & Casali, 1992), is identified as a sub-mm variable in a companion paper (Yoo et al., 2017) and has previously been identified as a periodic variable in near-IR (K-band) photometry (Hodapp et al., 2012). The periodicity is thought to be driven by accretion instabilities triggered by a nearby companion (Hodapp et al., 2012). We do not detect it as a variable candidate in this paper ($\delta = 2.83$) because EC 53's periodicity is timed such that the difference between the GBS measurement and the average Transient measurement is only moderate. In addition, the uncertainty (standard deviation) in EC 53's time averaged brightness across the Transient Survey data is high, because the brightness change over one period is significant (see Johnstone et al., in prep. for an analysis performed at a higher time resolution). To make this more clear, the source's 850 μm light curve presented in Figure 6.9 (see also, Yoo et al. 2017). In the top panel, the GBS and Transient peak brightness data are plotted against the dates of observation. The red (upward) triangle represents the average, calibrated GBS data, the blue circles represent Transient Survey data included in the investigation presented in this paper (obtained between February 2^{nd}, 2016 and February 22^{nd}, 2017), and the black squares represent Transient Survey data obtained between March 1^{st}, 2017 and July 5^{th}, 2017. The Transient Survey error bars represent the standard deviation of the normalised peak brightnesses across the *Family* of calibrator sources for each epoch (whereas the uncertainty of the GBS data point includes all 4 GBS observations taken over two nights, see Table 6.1).

In the bottom panel, we shift the calibrated GBS data from its original observation date until it reasonably aligns with the Transient Survey observation dates. We find that a shift of 1700 days from the original observation date agrees well with the rise of the peak brightness (red, upward triangle) with a range of acceptable values from 1605 days to 1795 days (horizontal, red errorbars). A shift of 1700$\pm$95 days corresponds to 3 full periods of 567 $\pm$ 32 days at 850 μm. To this accuracy, we independently confirm the 850 μm periodicity is consistent with the 543 day K-band periodicity

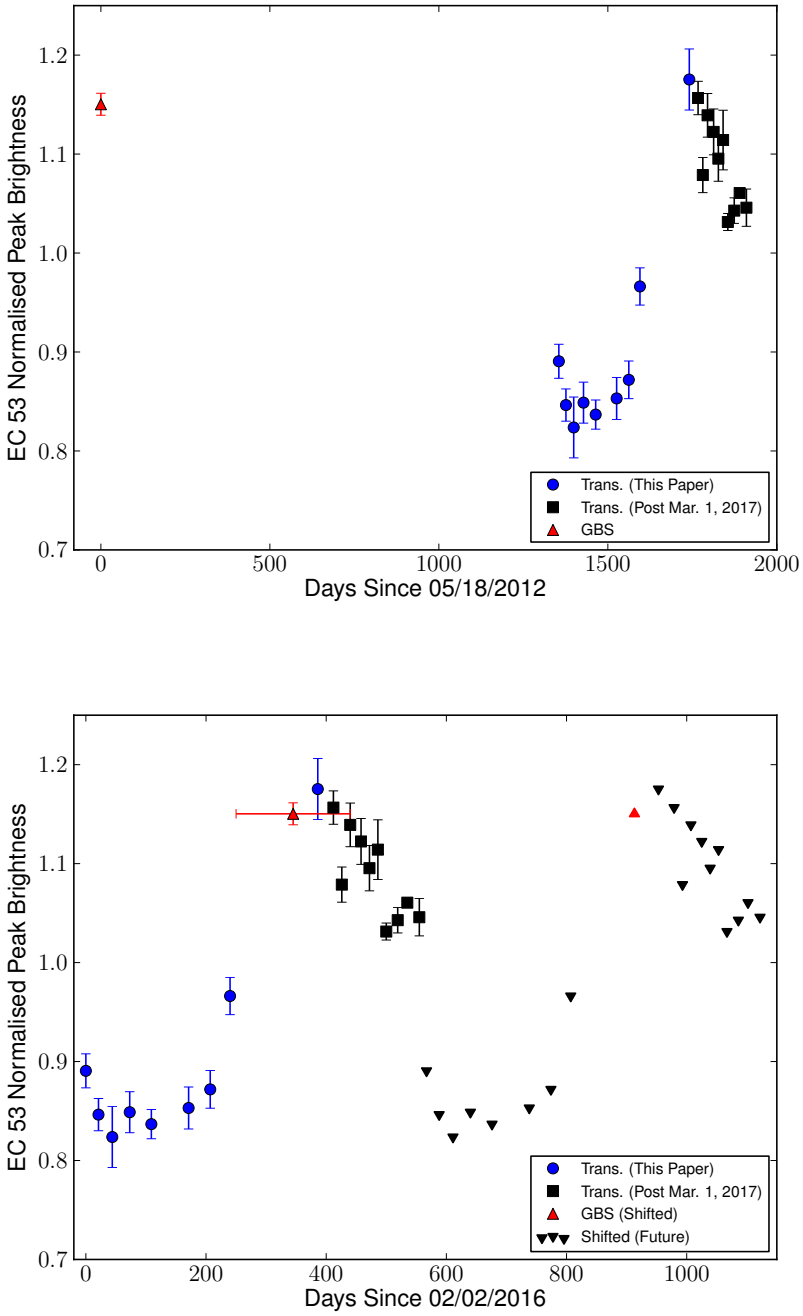

Figure 6.9 The 850 μm light curve of EC 53 (see also, (Yoo et al., 2017)). *Top*: The red (upward) triangle represents the average, calibrated GBS data, the blue circles represent data analysed in this paper, and the black squares represent data that has been collected between March 1^{st}, 2017 and July 5^{th}, 2017. *Bottom*: The black (downward) triangles represent all obtained Transient Survey data shifted one period (567 days) into the future. The GBS data presented in this Figure has been shifted three and then four increments of 567 days until it matched the current and next periodic cycles. The error bars in the GBS dates suggest a reasonable range of values that agree with the rise in the light curve.

(Hodapp et al., 2012). In order to show the periodic nature of EC 53, we assume the cycle is continuously repeating and we display all of the obtained Transient Survey observations shifted by 567 days (black, downward triangles), once again including the average GBS data in this future cycle.

6.7 Summary and Conclusions

In this paper, we investigate signatures of 850 μm submillimetre variability by comparing archival GBS fields, observed between 2012 and 2014, to JCMT Transient Survey fields, observed between December 2015 and March 1$^{\rm st}$ 2017. We follow the data reduction and calibration procedures presented in Mairs et al. (2017) to self-consistently align and calibrate each set of observations from the two surveys individually before bringing the co-added GBS images into relative flux calibration with the co-added Transient Survey images (see Section 6.4 and Figures 6.1 through 6.3). Using the source extraction algorithm GAUSSCLUMPS (Stutzki & Guesten, 1990), we identify 175 independent bright (>200 mJy beam^{-1}), compact (effective radius <10″) compact emission objects that were well fit with Gaussian profiles, correlate them with known protostars (Class 0+I, Flat spectrum sources; see Section 6.3.3) and disks (Class II sources), and identify objects that are significant outliers in their GBS to Transient Survey average peak brightness ratio with respect to the other sources in the field (see Figures 6.4 through 6.6, Figure 6.7 and Equation 6.5). Based on a visual inspection for compact structure present around the area of each outlying source in calibrated difference maps (the Transient Survey co-add subtracted from the GBS co-add), we define two categories for the quality of each variable candidate.

Our main results are summarised as follows:

1. We have developed methods to robustly analyze repeated observations of an area of the sky for signatures of submillimeter variability. We identify 11 archival GBS fields that can be self-consistently flux calibrated and have significant overlap with the 8 Transient Survey fields (see Appendix 6.8).

2. Out of 175 independent compact, 850 μm emission sources, we find a total of 7 variable candidates, 4 of which are associated with known protostars.

3. We classify 5 of the variable candidates as *Strong* and 2 as *Extended* (see Section 6.5), and we highlight one additional source, HOPS 383, as a *Possible* detection

of variability. Two *Strong* sources (IRAS4A, IRAS 18270-0153) along with HOPS 383 have previously noted signatures of variability. There is one *Strong* variable candidate without a known protostellar or disk association (Bolo 40/PER-10). This is a good target for follow-up studies to identify signatures of very faint, deeply embedded protostars (see Table 6.2).

4. The average flux change for the strong variable candidates is $|4.0|\%\,\mathrm{yr}^{-1}$ with a standard deviation of $2.7\%\,\mathrm{yr}^{-1}$ over 2-4 year timescales. Assuming the heating of the envelope is responsible for the changing luminosity, this corresponds to a change in accretion rate of $\sim 16\%$ (see Section 6.6). The observed changes in flux for all sources are distributed around $0\%\,\mathrm{yr}^{-1}$.

5. Using the archival GBS data, we strengthen the detection of the submillimetre variable source EC 53 by adding a critical data point to its periodic light curve and determine its 850 μm period to be 567 ± 32 days. This value is consistent with the 543 day period perviously reported in the K-band (see Figure 6.9, Yoo et al. 2017, and Hodapp et al. 2012).

Throughout this work, we have developed methods to robustly analyse repeated observations of an area of the sky for signatures of submillimetre variability. The JCMT Transient Survey will continue through at least January, 2019 and as more data are collected we will have the opportunity to continue this investigation to fainter sources and smaller levels of variability over longer timescales. Future directions include periodically co-adding sets of Transient Survey observations to construct very precise light curves (sacrificing temporal resolution for higher sensitivity), improving the flux calibration procedures such that more archival data can be included, comparing these observations with the simultaneous 450 μm datasets once the latter can be robustly reduced and calibrated, and applying these observational constraints to current simulations of variable protostellar accretion.

6.8 Appendix: Source Extraction and Comparison

For maximum consistency in relative flux calibration across all the regions, we select individual GBS fields and compare each one to its respective Transient Survey field independently. For a given GBS field to be useful for this work, it must: 1) have enough bright, compact sources to undergo self calibration and 2) have significant

overlap with a Transient field such that they share at least three sources of interest and a flux calibration between the two datasets can be performed. It is the first criterion that generally causes GBS fields with some Transient field overlap to fail. In order for a specific GBS field to undergo relative flux calibration, it must have at least two compact sources brighter than 0.5 Jy beam^{-1} that are observed to have consistent peak brightnesses with respect to one another across all observations. If two potential calibrator sources are noted, but display discordant flux calibration factors, it is unclear which, if either, of the sources represents the more correct value without further investigation. Where we lack robust sources, we discard the field. Similarly, if only one potential calibrator source is noted, it is unclear whether or not that source is intrinsically variable and, again, we discard the field. A self-calibration failure is generally encountered when the field is very sparse, or when a field is inundated with complex, extended emission without isolated, well-defined point-like sources. In the latter case, the GAUSSCLUMPS algorithm has difficulties in defining source boundaries and properly subtracting background emission (see, for example, the "Integral Shaped Filament" in the OMC 2-3 region in Figure 6.12; two GBS fields with the southern extension of the filament present along the noisy edge of their field of view were discarded).

Note that a clear example of GAUSSCLUMPS having difficulty subtracting the background is in the ORIONBS_450_E field. The error bars for many sources in Figure 6.2 (bottom left) are large due to the inconsistency of the identified source boundaries. To appear in Figures 6.1 through 6.3, a source must be consistently observed in at least 2 GBS observations and at least 2 Transient Survey observations. Recall that we apply minimum peak brightness and maximum radius thresholds. Sources that have sizes that are near this threshold may be culled from many observations, yet detected in two or three as the extraction algorithm fits a slightly different Gaussian model to the same region on different dates, attempting to separate clustered structure. The lack of robust observations increases the uncertainty of the peak measurement but this is mitigated by well-defined, well recovered sources in conjunction with the calculation of a weighted mean to derive the relative FCF.

Source recovery in particularly confused and blended emission regions is also complicated by the fact that the recovery of extended background emission can vary from observation to observation, especially near the edges of the map. Reducing SCUBA-2 data is a complex process. Best practices for the GBS data reduction were developed by Mairs et al. (2015) and extended to the Transient Survey by Mairs et al. (2017).

Adopting the methodology of Mairs et al. (2017) in this paper, we robustly recover compact structure in exchange for less information at extended scales. As discussed in Section 6.4.1, we perform a two-stage reduction where we employ an external mask in the final stage to help constrain MAKEMAP's solution. These external masks are created individually for each field in the GBS and Transient surveys, due to the different central coordinates of the overlapping fields. Where the fields from the two surveys overlap (see Figures 6.10 through 6.17), the masked structures are nearly identical. Outside of these regions, however, the fields have their own structure that can slightly affect how astronomical signal across the rest of the recovered image grows in the final iteration of MAKEMAP. This effect is generally insignificant across the majority of the image but can cause slight differences near the edges of the fields where the noise levels are higher.

In many instances, the edges of GBS fields overlap with the centre of their associated Transient Survey field and the small differences in extended structure recovery create flux pedestals and negative bowling, which add to the uncertainty of a measured source in those regions (see Mairs et al., 2015, for more information). Since the telescope has to slow down and speed up near the edges, the time domain filtering has a different effect on structure near the edge of the map with respect to that at the centre of the map. We have addressed this by inspecting each of the variable candidate sources in Table 6.2 in difference maps we constructed (see Figures 6.18 and 6.19), looking for indications of larger-scale residual structures. We expect that compact, truly varying sources would show significant, point-like structure even in the midst of these extended regions.

In Figures 6.18 and 6.19, we present thumbnail images extracted from the constructed difference maps (the GBS co-added data subtracted from the Transient Survey co-added data) for all variable candidates in Table 6.2. All of the *Strong* variable candidates show significant, compact structure in their respective difference maps.

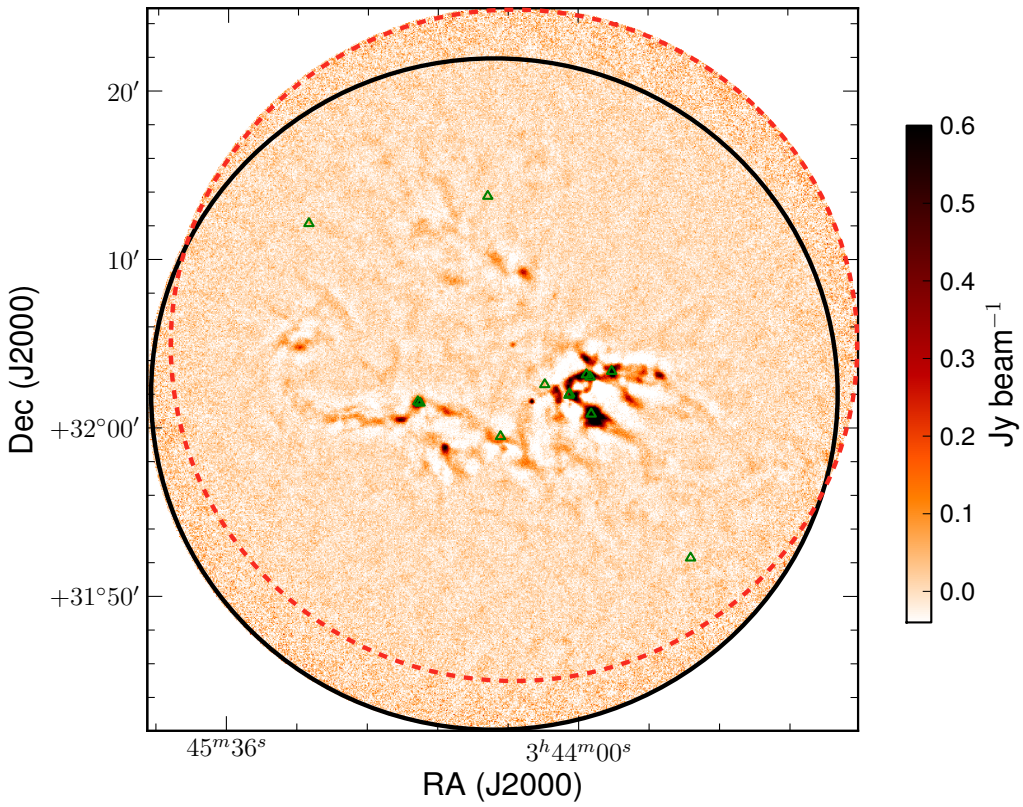

Figure 6.10 The Transient Survey field IC348 mosaicked with its corresponding archival GBS fields at 850 μm. The area of each observed GBS and Transient Survey field included in the mosaic is bounded by a circle. The solid black circle is the Transient Survey field. The red (dashed) circle shows the boundary of the IC348-E GBS field. The green triangles represent the positions of known protostars taken from the *Spitzer Space Telescope* catalogue of Dunham et al. (2015).

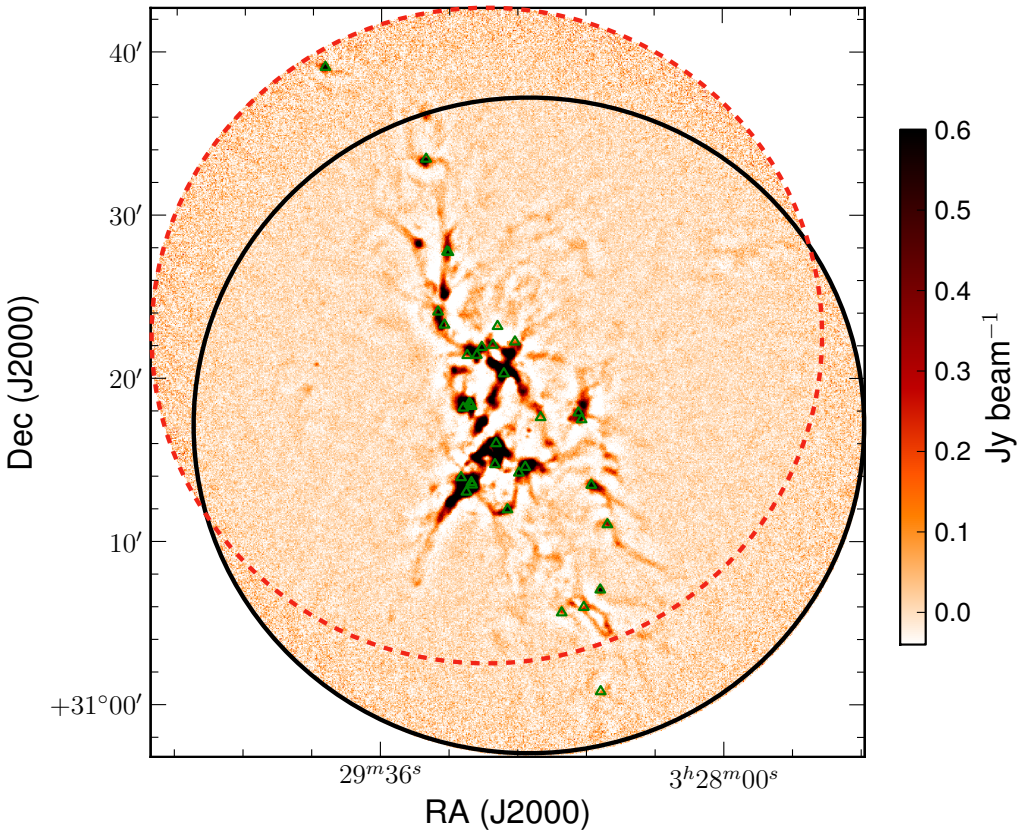

Figure 6.11 Same as Figure 6.10, but showing the NGC1333 field with its corresponding archival GBS field. The red (dashed) circle shows the NGC1333-N GBS field.

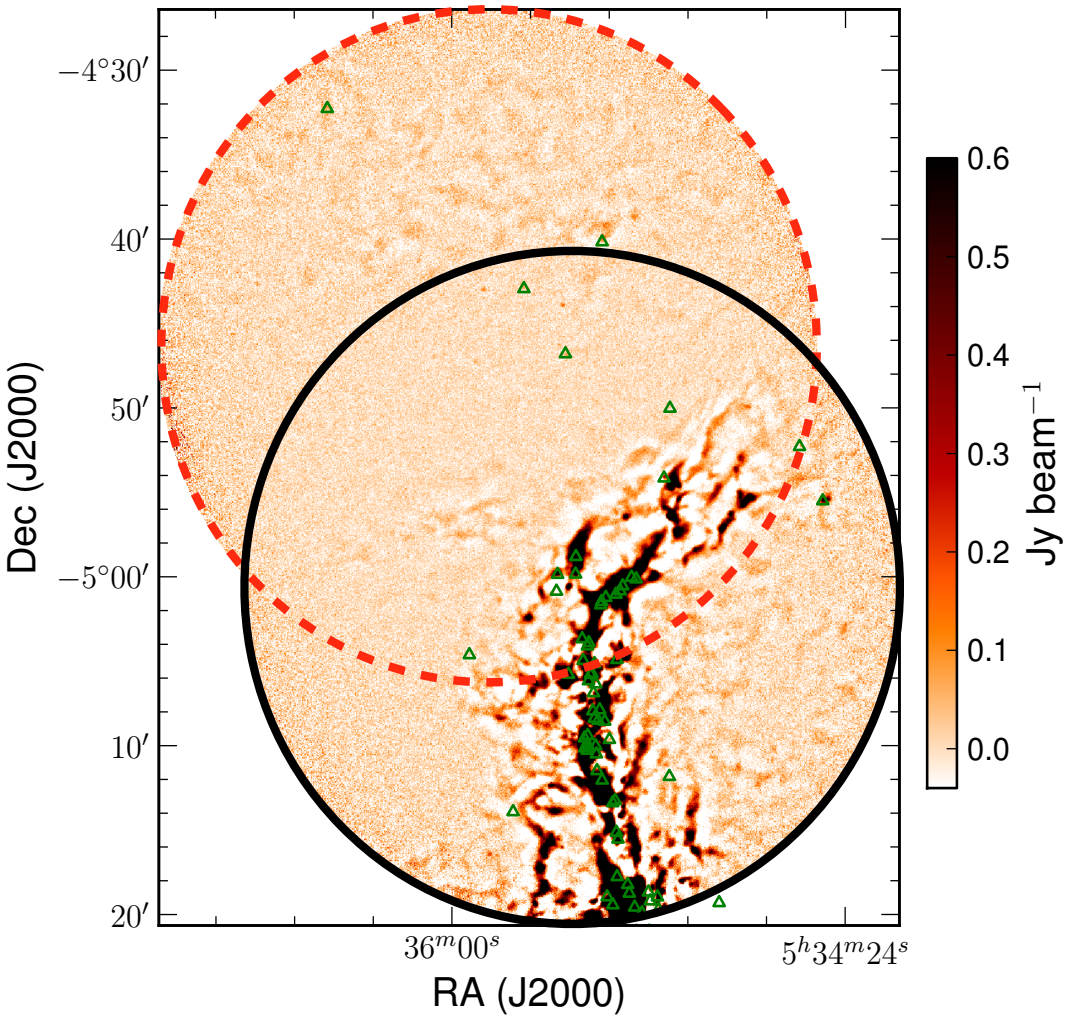

Figure 6.12 Same as Figure 6.10, but showing the OMC 2-3 field with its corresponding archival GBS fields. The red (dashed) circle shows the OMC1 tile4 GBS field. The green triangles represent the positions of known protostars taken from the *Spitzer Space Telescope* and *Herschel Space Observatory* catalogues of Megeath et al. (2012) and Stutz et al. (2013), respectively.

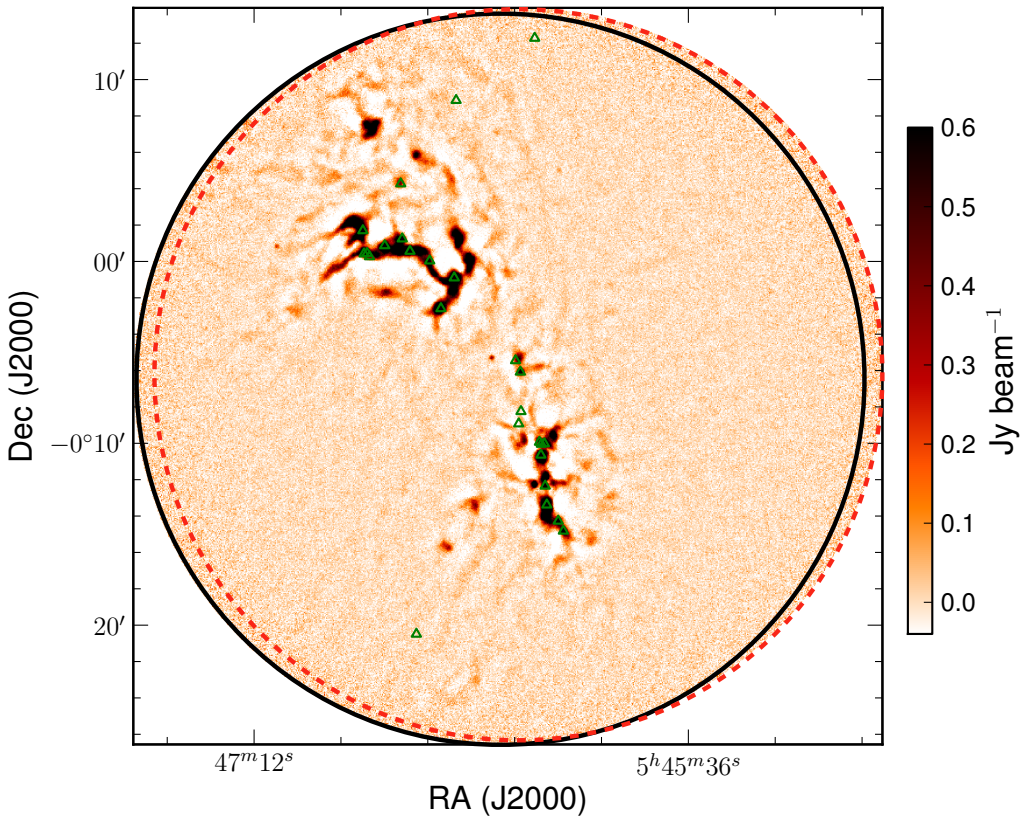

Figure 6.13 Same as Figure 6.10, but showing the NGC2068 field with its corresponding archival GBS field. The red (dashed) circle shows the ORIONBN_450_S GBS field. The green triangles represent the positions of known protostars taken from the *Spitzer Space Telescope* and *Herschel Space Observatory* catalogues of Megeath et al. (2012) and Stutz et al. (2013), respectively.

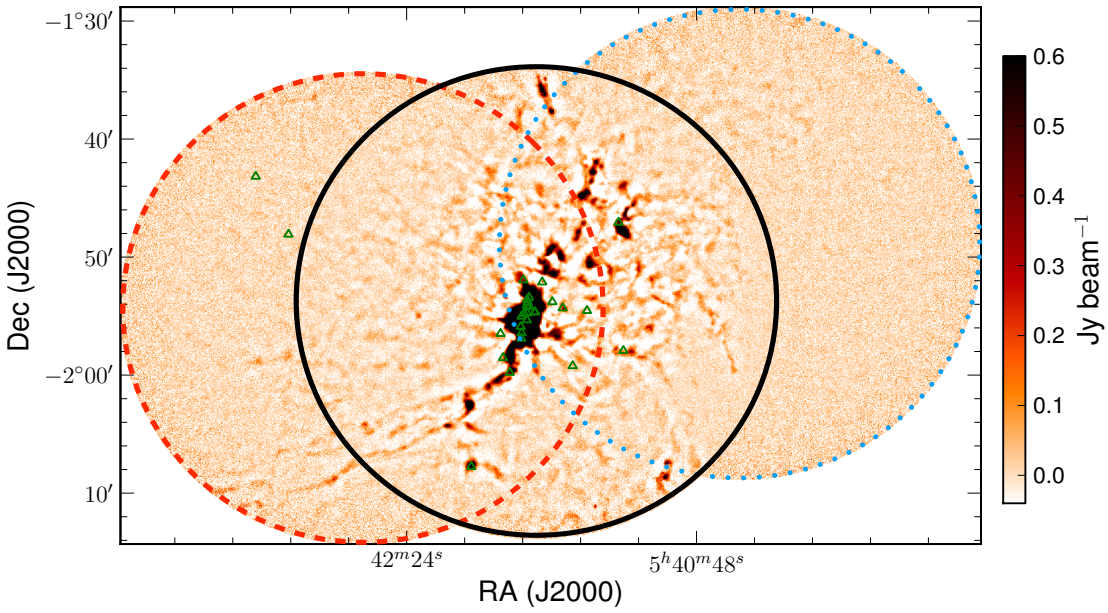

Figure 6.14 Same as Figure 6.10, but showing the NGC2024 field with its corresponding archival GBS fields. The red (dashed) circle shows the ORIONBS_450_E GBS field while the blue (dotted) circle shows the ORIONBS_450_W GBS field. The green triangles represent the positions of known protostars taken from the *Spitzer Space Telescope* and *Herschel Space Observatory* catalogues of Megeath et al. (2012) and Stutz et al. (2013), respectively.

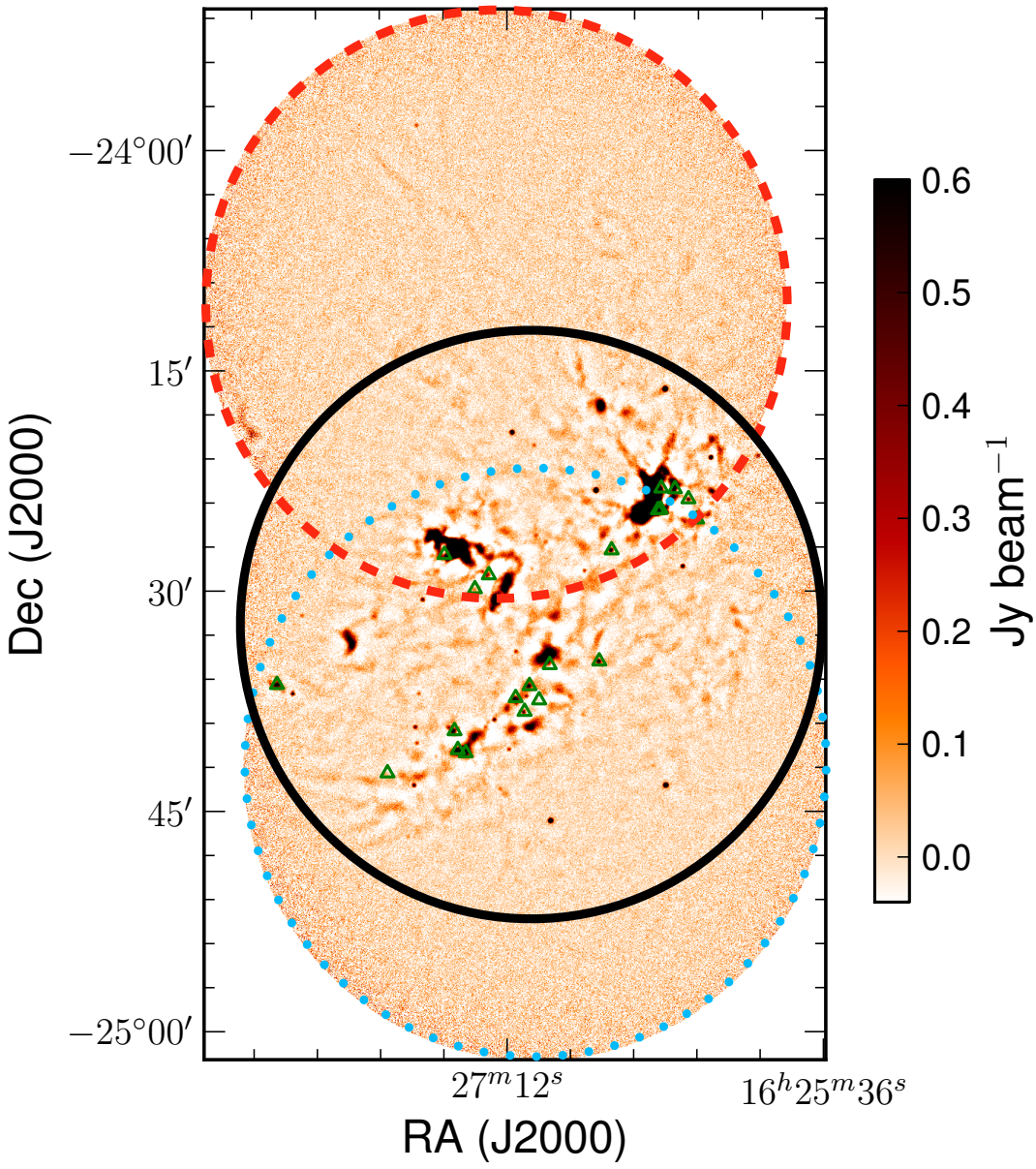

Figure 6.15 Same as Figure 6.10, but showing the Oph Core field with its corresponding archival GBS field. The red (dashed) circle shows the L1688-2 GBS field while the blue (dotted) circle shows the L1688-1 GBS field.

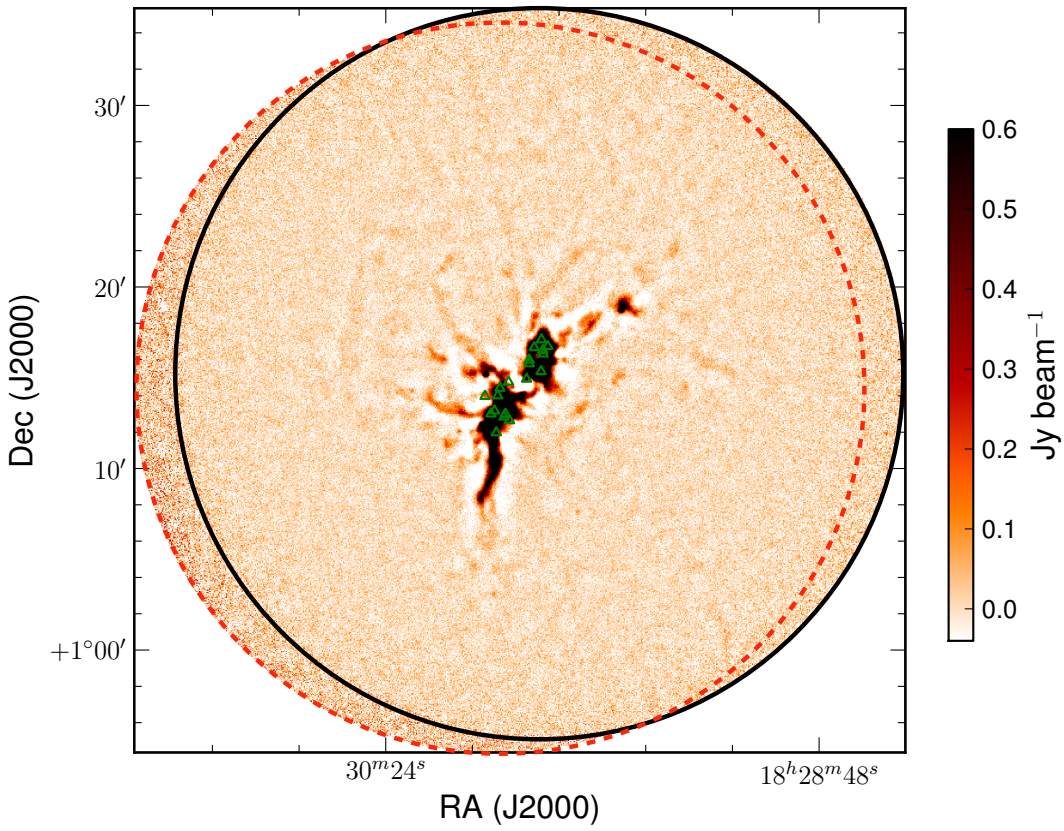

Figure 6.16 Same as Figure 6.10, but showing the Serpens Main field with its corresponding archival GBS field. The red (dashed) circle shows the SerpensMain1 GBS field.

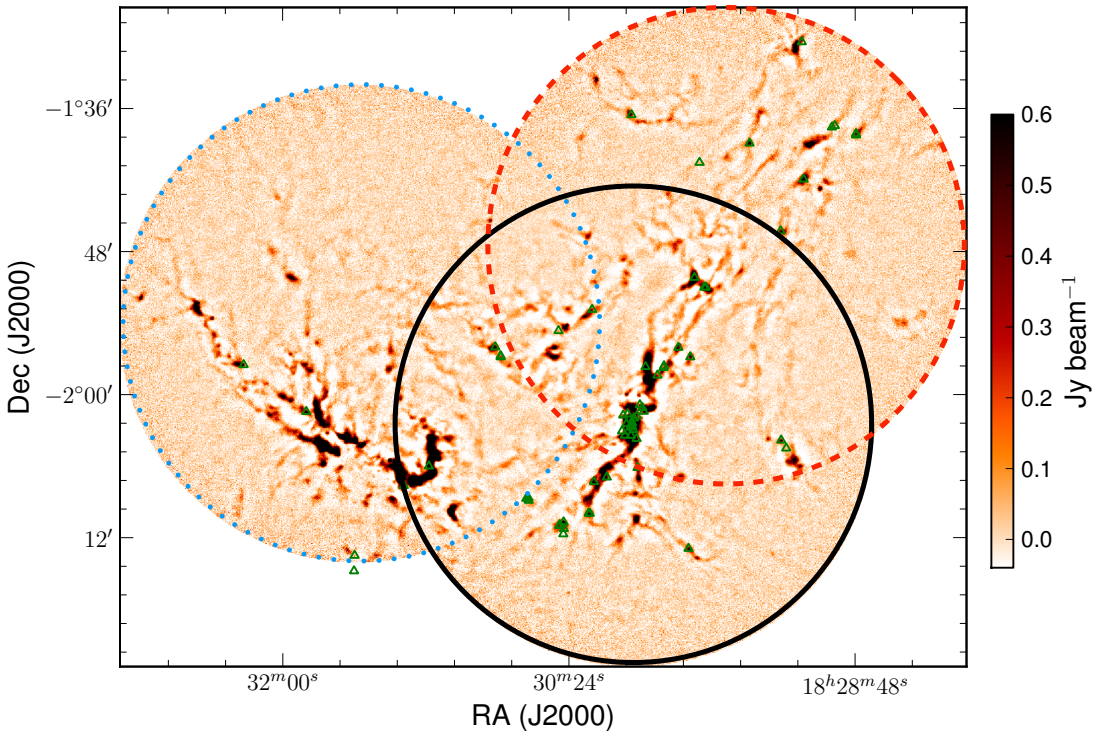

Figure 6.17 Same as Figure 6.10, but showing the Serpens South field with its corresponding archival GBS fields. The red (dashed) circle shows the SerpensSouthS-NW GBS field while the blue (dotted) circle shows the SerpensSouthS-NE GBS field.

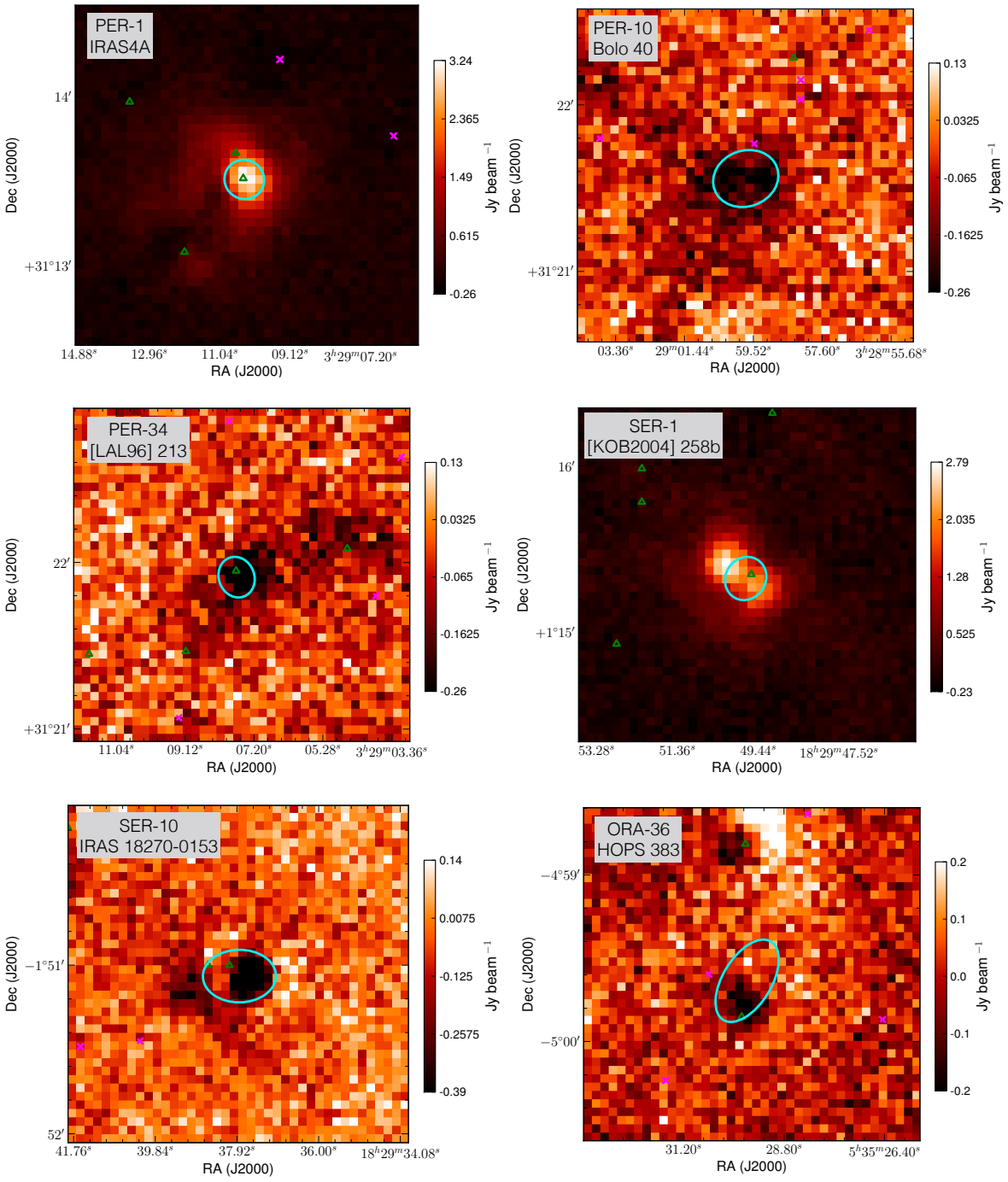

Figure 6.18 The 5 *Strong* variable candidates and the 1 *Possible* variable candidate (ORA-36/HOPS 383) extracted from difference maps where the GBS co-add has been subtracted from the Transient Survey co-add. Green triangles represent known protostars and magenta crosses represent known disk sources taken from the catalogues of Megeath et al. (2012), Stutz et al. (2013), and Dunham et al. (2015). Cyan boundaries show the fitted 2D Gaussian truncated at the level of $0.5\sigma_{rms}$.

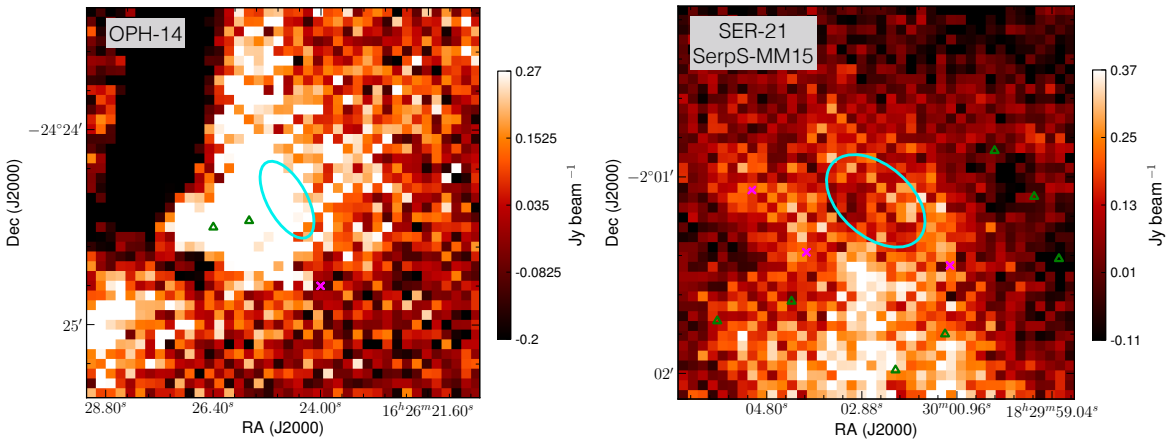

Figure 6.19 Same as Figure 6.18, but for *Extended* variable candidates.

Chapter 7

Summary and Future Directions

"Can you bind the chains of the Pleiades?
Can you loosen Orion's belt?
Can you bring forth the constellations in their seasons
or lead out the Bear with its cubs?"
-Job 38:31-32, Bible: NIV

Stars form in the complex environments of molecular clouds. Material flows from the largest scales, tens of parsecs across, down to individual dense cores through a combination of gas kinematics, gravity, and magnetic fields. Intermediary mass reservoirs such as filaments are formed with a variety of morphologies depending on stellar feedback, magnetic fields, turbulence, and large-scale flows. When mass finally accretes onto a protostar, the process is non-steady owing to gravitational and magnetorotational instabilities in the protoplanetary disc. Since most stars form in clusters, interactions with companions further complicate the story of stellar birth.

In order to study the earliest stages of protostellar assembly, we primarily use a combination of submillimetre and infrared wavelengths. Submillimetre data reduction and image reconstruction is an inherently complicated procedure due to the nature of the detectors and the atmospheric signal that must be subtracted from the total power received. Large-scale astronomical features are unavoidably subtracted along with the atmospheric signal. Therefore, in order to understand the robustness of the final dataset used for a specific science goal, the best practices for reducing the data and constructing images must first be derived. To study star formation holistically and to be sensitive to all of the different scales involved in this complex problem, a variety

of different telescope facilities operating at different wavelengths (such as the *Spitzer Space Telescope*, the *Herschel Space Observatory*, the James Clerk Maxwell Telescope, the Combined Array for Research in Millimeter-wave Astronomy, the Submillimetre Array, and the Atacama Large Millimeter/submillimeter Array) must be employed.

Throughout this dissertation, I have provided new insights on the connection between the large and small scales of star formation in nearby molecular clouds, unveiled the first systematic study on protostellar variability over several year timescales using submillimetre wavelengths, and constructed and analysed the optimum data reduction and image processing techniques for two large surveys. Below, I recap the main results of each project and provide ideas for future research directions.

7.1 Synthetic Observations of a Simulated Turbulent, Star-forming Region

In this paper (Mairs et al., 2014), my collaborators ran a simulation of a turbulent molecular cloud and I applied the same analysis techniques as I would use on data obtained using a telescope to investigate the nature of the dense structures produced. I was originally motivated to see if the simulation produced the recently observed highly super-Jeans cores without any signatures of embedded star formation (Sadavoy et al., 2010b), but I continued the investigation further to connect the larger scale structures to the simulated stars produced. The main results of this project can be summarised as follows:

1. The masses and densities of the simulated cores I detected are very similar to "real" cores in the Perseus Molecular Cloud, a typical example of a star forming region the simulation may represent. I found many more sub-Jeans cores than super-Jeans, in terms of their mass and size, which is consistent with Sadavoy et al. (2010a). In addition, nearly all cores that I detected eventually went on to form simulated protostars. This suggests that observed cores detected following my analysis procedures are probably "real" as well; that is, they will likely go on to form protostars in the future.

2. The mass of the observed envelope does not appear to be a good tracer of the eventual protostellar mass. This has implications for comparing the core mass function with the stellar initial mass function. Note, however, that the simulation does

not include magnetic fields or outlfows, which could provide additional support that may inhibit a core from collapsing.

3. Nearly all cores I identified are associated with filamentary structures. This is consistent with the ubiquity of filaments recently observed using the *Herschel Space Observatory* (André et al., 2014). Mass appears to flow through these filaments from larger scale reservoirs down to individual cores.

4. Single dish observations such as those with the JCMT as well as previous-generation interferometers like CARMA appear to miss substructures within individual cores due to flux averaging. These facilities are instead useful for characterising intermediate scale structures. High resolution interferometric observations with ALMA are necessary to recover the smallest scales.

7.1.1 Future Directions

Over the past five years, there have been major improvements in simulations of star forming regions (see, for examples, Bate & Keto, 2015; Offner et al., 2016; Vázquez-Semadeni et al., 2017) such that it is now becoming possible to include stellar feedback, magnetic fields, and post-processed chemical networks in larger-scale environments. As simulations continue to improve, synthetic observations and comparisons to data obtained using telescopes is only becoming more relevant. Furthering the work presented here, I would like to spend time investigating the differences between several major simulations currently addressing the connection between large and small scales in star formation such that I could synthetically observe (with the JCMT and ALMA) a robust set that employ different prescriptions for stellar feedback, radiative transfer, and magnetic fields. By characterising the differences between the "observed" structures and comparing them to the molecular cloud features observed on sky, useful insights could undoubtedly be gained on the dominant physics governing the flow of material in these complex environments.

A study like this could have revolutionary implications about the core mass function and its connection with the stellar initial mass function, the relative importance of turbulence and magnetic fields in forming and supporting structures such as filaments and cores, and the role of stellar feedback in dense environments of cluster formation. One of the benefits of this future project is that all the necessary data are already available. Consistently comparing multiple simulations from different groups

in a fair manner, however, would take careful consideration.

7.2 Investigating Data Reduction Methods for the Gould Belt Survey

In this paper (Mairs et al., 2015), I investigated the best practices for SCUBA-2 data reduction by comparing two test cases (the GBS Legacy Release 1 and the JCMT Legacy Reduction) and I characterised the robustness of the JCMT Gould Belt Survey images that went on to inform more than ten independent studies to date (see the Foreword of Chapter 3). To do this, I input artificial Gaussian sources of differing sizes and peak intensities into the raw signal received, performed multiple data reduction procedures using a variety of different parameters, and then recovered those artificial sources to quantify the effect of each reduction. Through this study, I was able to offer suggestions to improve the data reduction procedures for further Gould Belt Survey data releases. The main results can be summarised as follows:

1. Both the GBS LR1 and the JCMT LR1 reductions recover the peak intensities of bright compact sources (sources with FWHMs of 3 beams or less and a peak brightness of at least 7 σ_{rms}) to within 10-20% of the true value. The GBS LR1 reduction also accurately recovers the peak intensities of the larger Gaussians whereas the peaks produced by the JCMT LR1 reduction are diminished because of its stringent spatial filtering parameters. In general, more accurate results are obtained for objects which are both brighter and more compact.

2. Although the JCMT LR1 reduction only recovers compact emission present in a given region and the GBS LR1 reduction recovers the extended structure, the two reduction methods trace the same general areas of significant signal very closely. The JCMT LR1 reduction's diminished extended structure, however, causes structure identification algorithms to break up large areas into many smaller objects. Conversely, the GBS LR1 reduction draws out these locations of extended emission and, thus, much more emission can be recovered.

3. For faint objects larger than a point source, only a fraction of the true size (and, therefore, total flux density) originally present in an artificial Gaussian is recovered without an external masking procedure. The larger the object, the brighter it must

be for an automask detection. In the GBS LR1 automask data reduction, Gaussians with a FWHM of 7 beams must have a peak brightness of 5 σ_{rms} for the peak intensity to be measured to within ∼20%. To measure the total flux density to within 20% of the nominal value, a peak brightness of greater than 25 σ_{rms} is required. For a Gaussian with a FWHM of 7 beams, the JCMT LR1 reduction will never result in a measurement of a source's peak intensity or total flux density to within 20% accuracy of the nominal value due to the inherent filtering of large spatial scales.

4. When identifying objects with the automask employed in the GBS LR1 automask reduction, the most accurate Gaussian parameters are measured when nearby pixels are incorporated by extending to lower flux values. For improved reductions, e.g. GBS Legacy Release 2 (GBS LR2), I recommend setting the *ast.zero_snrlo* parameter to a value of 2. Similarly, the *ast.zero_snr* parameter should be set to 3. See Section 3.6.1 for details. One must, however, be cautious when extending the AST mask around significant peaks down to a lower flux threshold as artificial structure could be introduced around noise spikes. Fortunately, in the variety of automask tests performed, there was no significant evidence of any artificial structure outside of the Gaussians being included in the AST model.

5. The external mask used in the GBS LR1 reduction can increase or decrease the brightness of compact peaks depending on the surrounding region. Thus, in some cases where an incorrect external mask size is used, the JCMT LR1 reduction and the GBS LR1 reduction can even differ a little on compact scales. Artificial structure in the data caused by a poorly sized external mask can act as pedestals and bowls, affecting the peak intensity, the size, and the total flux density measured for a given object. A mask that is too small will only highlight compact regions embedded within larger extended emission. A mask that is too large will include noise variations in the AST mask. A reasonable external mask should cover a given source in its entirety and extend a small distance into the noise. It should, however, be less than a factor of 2 larger than a source which was reliably recovered by the automask reduction in order to achieve 20% accuracy in total flux density. I have found that this is possible even for faint, large sources.

7.2.1 Future Directions

Although I was successful in quantifying the robustness of Gould Belt Survey images and deriving improvements for future data releases, there is still much work that can be done to better characterise the effects of data reduction. Signal is lost in the noisy edges of maps, artificial structures can be introduced to the final images if noise features are included in the external mask, and negative bowling around bright sources is difficult to reduce in bright, extended regions. I have already made significant improvements to the pointing accuracy and the relative flux calibration of repeated SCUBA-2 observations (see Chapter 5 and Section 7.4) but these have not yet been automatically implemented for future Gould Belt Survey data releases. This would require deriving a more precise absolute flux calibration, however.

To further this work, I would like to test a larger variety of artificial sources such that they have irregular shapes and better represent the real structures we see in the sky. I would insert these sources in amongst other, real signal to better test the differences between recovering astronomical signal in isolated areas of a given map in comparison to more clustered areas of the map. I would also like to thoroughly test a more realistic set of external masks and to investigate how small changes can reduce negative bowling and provide a more optimal image for analysis. Ideally, I would like to construct an automated routine that would make use of this method of introducing and extracting artificial sources with known properties and iteratively modifying data reduction parameters to produce the best image possible. This, however, would be very computationally expensive.

The next generation of JCMT instrumentation is looking very promising with planned SCUBA-2 upgrades and the introduction of new heterodyne receivers (Dempsey et al., 2016). Therefore, I would like to build on the infrastructure I have already created and continue to derive best practices for data reduction at the JCMT in the coming era.

7.3 The First Look at Southern Orion A with SCUBA-2

In this paper (Mairs et al., 2016), I performed the first look analysis on the southern extent of the Orion A Molecular Cloud. Building on the previous two projects, I investigated the connection between larger and smaller scale structures by analysing

an infrared extinction map and YSO locations in conjunction with SCUBA-2 data. I performed an analysis on the fragmentation of intermediate scale structures I label as *islands*, I noted several interesting candidates for follow-up studies, and I constructed a simple model to recreate the locations of YSOs assuming they were gravitationally ejected from presently observed dust structures. The main results can be summarised as follows:

1. There are emission structures with a variety of sizes, flux levels, and morphologies present in Southern Orion A. As expected from local Jeans lengths, many large islands are often subdivided into multiple localised fragments. There are, however, several objects which require further study.

2. The fragments I identified and characterised are significant sites of star formation. We find that those fragments that are Jeans unstable tend to have higher concentrations than those fragments that appear stable.

3. The most Jeans unstable, monolithic structures show the most evidence for ongoing star formation due to their associations with protostars near the peak brightness location. This is in contrast to fragments extracted from complex islands (i.e., they have siblings in their parent cloud). Starting at an M/M_J ratio of 1, these latter objects do not necessarily show more evidence of star formation at higher degrees of instability implying clustered star formation may be more drawn out.

4. Class 0+I and flat-spectrum YSOs have higher associated 850 μm brightness values and are closer to the nearest fragment's peak emission than their more-evolved disc counterparts. I find a similar result as Heiderman & Evans (2015) in that only $\sim$72% of the objects defined as Class 0+I and flat-spectrum protostars are above a significant flux threshold, suggesting that some of the protostars identified in previous surveys may be misclassified.

5. The observed spatial distribution of disc sources across Southern Orion A has a "clustered" population and a "distributed" population. I am able to reproduce the projected distances between protostars and their nearest fragment reasonably well by using a simple toy model. Assuming a Maxwell-Boltzmann velocity distribution for these objects, I derived a range of most probable velocity values, $v_p = 0.2-0.5$ km

s^{-1}, which reasonably fit the spatial distribution of protostars observed by Megeath et al. (2012) and Stutz et al. (2013). The model disc source locations, however, do not recreate the distributed population in Southern Orion A using the same v_p values. I found that the Class II objects (the disc sources) require a v_p value of 0.7 km s^{-1}, indicating an apparent trend in velocity with respect to YSO classes.

7.3.1 Future Directions

I have already begun a follow-up study on the continuum first look at Southern Orion A by obtaining data on dense-gas molecular tracers in order to investigate the kinematics of the region. In the work presented in this dissertation, I identified the main gravitationally unstable regions in the southern extent of the Orion A Molecular Cloud. Using this dataset, I compiled a representative sample of 7 interesting islands with similar sizes and densities but different fragmentation and star formation properties. I submitted a proposal to collect ^{13}CO and C^{18}O (J=3$\rightarrow$2 transitions) data on these sources using the Heterodyne Array Receiver Program (HARP; Buckle et al. 2009) at the JCMT The proposal was highly ranked and awarded time in semester 16B.

To truly understand whether and how these sources of interest are fragmented, I seek to measure the velocity (in)coherence with ^{13}CO and C^{18}O, which both trace dense gas. I aim to uncover velocity field variations and multiple velocity components within the 7 individual islands observed. As well, I will be able to correct overestimates in the masses of continuum objects by disentangling line of sight coincidences (see, for example, Kainulainen et al. 2016). Smaller-scale fragments that appear blended in continuum images may also be separated into independent velocity components. ^{13}CO and C^{18}O provide information on the interesting molecular gas in the transition zone (10^4 cm^{-3}) between the more diffuse bulk cloud and the densest parts of the cores (where CO freezes-out).

The sample of islands I selected for this project were those I calculated to be significantly Jeans unstable and that provide a good sample of monolithic, fragmented, starless, and protostellar emission regions. To construct a larger sample of targets, l will combine these new heterodyne observations with existing CARMA and GBS HARP observations (Buckle et al., 2012) taken over a small portion of our larger SCUBA-2 map such that I can examine the effect of (in)coherent motions such as turbulence, stellar outflows, bulk flows, and shock fronts on the fragmentation of

massive structures in the Orion A molecular cloud and compare the kinematic morphologies directly against numerical models (as in Chapter 2). Making use of these additional datasets will require me to expand my continuum analysis presented here to include the extreme conditions in the integral shaped filament such that I can cross-compare more targets in a consistent manner throughout all of Orion A.

In addition to the kinematic study, I am also helping advise an undergraduate student (James Lane) on repeating this island and fragment analysis on all of the regions observed by the Gould Belt Survey. In this way, we will be able to consistently compare different star forming environments and note general trends in the properties of continuum sources. As investigations continue using data collected by the Gould Belt Survey, multi-cloud comparisons will be fundamental in understanding the universality of observed star forming structures.

7.4 The JCMT Transient Survey: Data Reduction and Calibration Methods

In this paper (Mairs et al., 2017), I constructed the default data reduction and post-reduction calibration pipeline used for the JCMT Transient Survey. Building on the work I presented in Chapter 3, I produced robust images optimised for studying the variability of bright, compact sources and significantly improved the inherent JCMT pointing and relative flux uncertainties. The calibration uncertainties I was able to derive are unprecedented for single dish submillimetre data and these methods can be bootstrapped to other SCUBA-2 projects such at the Gould Belt Survey. The main results can be summarised as follows:

1. I thoroughly tested four different data reduction methods and found the most robust set of parameters for the Transient Survey's scientific goals.

2. I achieve a sub-pixel alignment uncertainty of $\sim 1''$, improving on the pointing error of the telescope by a factor of ~ 4.

3. I achieve a relative flux calibration factor uncertainty of $2-3\%$ for bright sources, improving on the native, absolute flux calibration uncertainty by a factor of ~ 3.

4. These calibrations have already resulted in variable detections that would have otherwise not been possible (see Chapter 6).

7.4.1 Future Directions

The work presented in this dissertation is the first iteration of the data reduction and calibration procedures for the Transient Survey. As the survey matures, I will continue to develop these methods to further reduce the uncertainties in relative flux calibration. My more immediate goals involve automating the relative flux calibration such that it can be run at the East Asian Observatory headquarters (like the spatial alignment algorithm currently is), characterising and correcting how the fluctuating beam profile affects the results, and building more robust infrastructure to flux calibrate the 450 μm data to the same level as the 850 μm data. This will include using artificial sources (as in Chapter 3) to better quantify the uncertainties introduced by extended emission structures and perhaps deriving multiple correction factors for different areas of a given map depending on how much emission is recovered in the vicinity of interesting sources.

Already, Transient Survey team members are working on calibration strategies based on cross-correlating repeated observations in order to take into consideration more flux information than individual Gaussian sources provide (see Section 5.10). The initial spatial alignment results look promising, but the analysis working toward deriving relative flux calibration corrections using cross-correlation is still in its infancy.

7.5 The JCMT Transient Survey: Hunting for Variability Over Several Year Timescales

In this final project, I relied on the data reduction and calibration procedures presented in Chapters 2 and 5 to investigate 850 μm variable sources in 8 star forming regions over 2-4 year timescales. Processing the raw Gould Belt Survey and Transient Survey data in the same way, I self-consistently aligned and flux calibrated each dataset. Then, using all the overlapping sources, I calibrated the average GBS images to their corresponding average Transient Survey images and robustly compared the peak brightnesses of all identified, overlapping sources using a Monte Carlo method. This is the first time two submillimetre data sets have been systematically used to

identify variability across such a large sample. The main results can be summarised as follows:

1. I have developed methods to robustly analyze repeated observations of an area of the sky for signatures of submillimetre variability. I identify 11 archival GBS fields that can be self-consistently flux calibrated and have significant overlap with the 8 Transient Survey fields (see Appendix 6.8).

2. Out of 175 independent compact, 850 μm emission sources, I find a total of 7 variable candidates.

3. I classify 5 of the variable candidates as *Strong* and 2 as *Extended*, and I highlight one additional source, HOPS 383, as a *Possible* detection of variability. Two *Strong* sources (IRAS4A, IRAS 18270-0153) along with HOPS 383 have previously noted signatures of variability. There is one *Strong* variable candidate without a known protostellar or disk association (Bolo 40/PER-10). This is a good target for follow-up studies to identify signatures of very faint, deeply embedded protostars (see Table 6.2).

4. The average flux change for the strong variable candidates is $|4.0|\%\,\mathrm{yr}^{-1}$ with a standard deviation of $2.7\%\,\mathrm{yr}^{-1}$ over 2-4 year timescales.

5. Using the archival GBS data, I strengthen the detection of the submillimetre variable source EC 53 by adding a critical data point to its periodic light curve and determine its 850 μm period to be 567 ± 32 days. This value is consistent with the 543 day period perviously reported in the K-band (see Figure 6.9, Yoo et al, submitted, and Hodapp et al. 2012).

7.5.1 Future Directions

The Transient Survey will continue through at least January, 2019, allowing for deeper analyses to take place over longer time lags. In this dissertation, I have broadly addressed the signatures of variability in bright, compact sources in all regions but there is a wealth of fainter structure that requires further investigation. There are many different methods of searching for a variable source signal I would like to employ, from well calibrated difference maps and aperture photometry to source extraction using a variety of different algorithms (see, for examples, Williams et al., 1994; Rosolowsky

et al., 2008; Men'shchikov et al., 2012; Berry, 2015) and co-adding sets of data over time, sacrificing temporal resolution for better sensitivity.

In addition, the comparison between data obtained at other wavelengths will be fundamental to understanding the physics at the smallest scales. Submillimetre variable observations need to be understood in the context of infrared, radio and even x-ray variability (Forbrich et al., 2011). Each signal has a different expected timescale and different physical processes related to the forming protostar. I look forward to investigating the synergy of publicly available radio data in combination with new observing programs at facilities like the Green Bank Telescope and the Jansky Very Large Array. Further in the future, I aim to be a part of collaborations using infrared capable spacecrafts such as the *James Webb Space Telescope* (JWST) and the *Space Infrared Telescope for Cosmology and Astrophysics* (SPICA), which will enhance our understanding of variable YSOs by orders of magnitude.

"You -
you alone will have the stars as no one else has them...
In one of the stars I shall be living.
In one of them I shall be laughing.
And so it will be as if all the stars were laughing,
when you look at the sky at night...
You -
only you -
will have stars that can laugh..."
-Antoine de Saint-Exupéry, The Little Prince

"The heavens declare the glory of God;"
the skies proclaim the work of his hands.
Day after day they pour forth speech;
night after night they reveal knowledge.
They have no speech, they use no words;
no sound is heard from them.
Yet their voice goes out into all the earth,
their words to the ends of the world."
-Psalm 19:1-4, Bible: NIV

Appendix A

Glossary of Terms and Acronyms

The Atacama Large Millimetre/Submillimetre Array (ALMA): An interferometric array of telescopes located at Chajnantor plateau, Chile, at an elevation of 5,000 metres. The array consists of sixty-six 12-metre and 7-metre dishes.

Bolometer: A type of detector able to measure the power of incident light based on changes in electrical resistance. In the context of this dissertation, the bolometers employed at the James Clerk Maxwell Telescope are detectors constructed of a Molybdenum/Copper alloy cooled to ~ 60 mK. When submillimetre radiation is absorbed by these devices, their resistance dramatically changes and the corresponding change in output current is converted into a power received based on calibration images taken nightly.

Bonnor-Ebert Spheres: A family of solutions to the spherical Lane-Emden equation for a self-gravitating, isothermal gas that describes a sequence of equilibria ranging from stable, low central concentration to unstable, high concentration.

Clump: A significant region of submillimetre emission that is much smaller than a molecular cloud but may be tens to hundreds of solar masses. Clumps may fragment into smaller components or they can behave as transient, dissipating objects depending on their virial state.

Core: Smaller than a clump, a core is the fundamental unit of low-mass star formation. This significant region of submillimetre emission is expected to be the birth site of at most one to a few low-mass stars. Cores can be subdivided into three types

depending on their evolutionary stage and virial state:

Starless: A starless core has no visible signatures of ongoing star formation. Depending on the density of the structure and the relative strengths of the support pressures counteracting gravity, a starless core may or may not go on to eventually form stars.

Prestellar: A prestellar core is gravitationally bound and expected to collapse and form one to a few low mass stars.

Protostellar: A protostellar core is gravitationally bound and has evidence of at least one embedded protostar.

Core Mass Function (CMF): Similar to the **Initial Mass Function**, the Core Mass Function is the distribution of observed prestellar core masses. The universality of the CMF and its connection to the IMF are still debated.

EXors: Ex Lupi objects. A pre-main sequence (T Tauri) star that exhibits dramatic changes in brightness on timescales of days to months. These events are thought to be a result of sudden changes in the accretion rate from the circumstellar disc to the central, forming star. See also **FUors**.

Filament: A ubiquitous, cylindrical intermediary structure in a **molecular cloud** that has shown evidence of transporting mass and connecting the flow of material from the largest to the smallest scales.

First Hydrostatic Core: A short-lived stage of stellar evolution that occurs just before the birth of a protostar. A First Hydrostatic Core occurs when the central density of a collapsing **core** becomes high enough to halt the collapse until the temperature rises to approximately 2000 K, when H_2 molecules dissociate. As the temperature continues to rise, Hydrogen and Helium atoms begin to ionise and the core continues to collapse to higher densities in order to form a protostar.

FUors: FU Orionis objects. These pre-main sequence (T Tauri) stars exhibit dramatic changes in luminosity and spectral type over several year to decade timescales. These events are thought to be a result of sudden changes in the accretion rate from the circumstellar disc to the central, forming star. See also **EXors**.

JCMT Gould Belt Survey (GBS): The James Clerk Maxwell Telescope Gould Belt Survey is a large-scale survey dedicated to understanding low-mass star formation in nearby **molecular clouds**. The GBS focuses on 450 and 850 μm continuum data taken using **SCUBA-2** and spectroscopic data of three CO isotopologues (12CO, 13CO, and C18O, J = 3-2) transitions) observed using the Heterodyne Array Receiver (HARP) instrument.

Jeans Mass (Length): The maximum mass (size) that can be thermally supported in a spherical configuration before undergoing gravitational collapse.

Gould Belt: A ring of bright, young stars 700 pc in diameter. Its centre is approximately 200 pc from the Sun and the ring is inclined to the Galactic plane by approximately 20°. This belt is home to many well known star-forming molecular clouds within 500 pc of the Sun such as Orion, Perseus, Serpens, Lupus, Ophiuchus, Taurus, and Serpens.

Initial Mass Function (IMF): The observed mass distribution of stars as they join the main sequence of the Hertzsprung-Russell diagram.

Interstellar Radiation Field (ISRF): The electromagnetic energy occupying the space between the stars (the radiation throughout the **Interstellar Medium**). In a broad sense, the dominant contributions to the ISRF consist of 21-cm emission, cosmic microwave background radiation, thermal emission of dust grains, radiation from stellar feedback, and gamma rays.

Interstellar Medium (ISM): The dynamic mixture of gas and dust that exists between the stars. The ISM is mainly comprised of hot Hydrogen and Helium gas with **molecular clouds** constituting $<1\%$ by volume. Hydrogen can exist in ionised, atomic, or molecular forms depending on the temperatures and densities influenced by the **Interstellar Radiation Field**.

James Clerk Maxwell Telescope (JCMT): At present, the JCMT is the largest single dish submillimetre telescope in the world. Situated on Maunakea, Hawaii, USA, this 15-metre dish is operated by the East Asian Observatory.

Luminosity Problem, The: The discrepancy between the measured, median pro-

tostellar luminosity and the expected median protostellar luminosity assuming the seminal steady state accretion model. Observed protostars are found to be approximately an order of magnitude fainter than the steady-state accretion model predicts.

Magnetorotational Instabilities: Magnetohydrodynamic simulations predict that when gas in a protoplanetary disc is coupled to a magnetic field, the differential rotation of the disc is expected to give rise to instabilities that are linked to turbulence and angular momentum transport in the innermost regions. These instabilities may significantly contribute to the frequency and amplitude of episodic accretion onto forming protostars.

Molecular Cloud: The coldest and densest regions of the **Interstellar Medium**, these clouds of gas and dust are the birth places of stars. Molecular clouds can be thousands to millions of solar masses and span tens to hundreds of parsecs in size.

Pong Observation: The primary mode of observation employed throughout this dissertation using **SCUBA-2** and the **JCMT**. The telescope continuously scans across a circular region of the sky. Whenever it reaches the boundary of its footprint, it changes direction, scanning across the same areas of the sky from multiple position angles until the desired region is consistently sampled to a required depth. This scan pattern is called a Pong observation after the video game which its motion resembles. A typical Pong observation presented throughout this work is $30'$ in diameter.

Protoplanetary Disc: Protoplanetary discs form around an accreting protostar. This is the result of a combination of magnetic fields and rotation which cause anisotropies in the otherwise symmetrically infalling material. Therefore, a majority of the mass will first accrete onto the disc before being transferred to the protostar. This leftover material will eventually go on to form planets.

Stellar Jets: Highly collimated, bi-polar outflows thought to be caused by the magnetic fields present in a forming star in combination with infalling, rotating material. Jets allow for the dissipation of angular momentum as the protostar continues to collapse.

Submillimetre Common User Bolometer Array 2 (SCUBA-2): The work horse, 10,000 pixel, continuum observation instrument in operation at the **JCMT**. SCUBA-2 collects continuum data at 450 and 850 μm simultaneously with half-power bandwidths of 32 and 85 μm, respectively.

Spectral Energy Distribution (SED): The measured flux density of an object as a function of wavelength or frequency.

Water Vapour Radiometer (WVM): This device measures three points of the 183 GHz water line (the peak and the two wings of the profile) in order to fit the broad feature and characterise the amount of precipitable water vapour in the atmosphere. It is used to derive the atmospheric extinction correction necessary to reduce **SCUBA-2** data.

Young Stellar Object (YSO): Stars in their earliest stages of evolution, before they arrive on the main sequence of the Hertzsprung-Russell diagram. Though the original definition of different classes of YSOs was based on the overall shape of the **SED**, it is now common practice to separate each class by the steepness of the slope of their SED (plotted logarithmically) at infrared frequencies. The SED of a YSO is a power law at infrared frequencies, so it can be characterised by the spectral index, α. There are four commonly used classes of YSOs:

Class 0+I: $\alpha \geq 0.3$. The youngest, most embedded YSOs.

Flat Spectrum: $-0.3 \leq \alpha < 0.3$. The transitionary stage between deeply embedded, young YSOs and more evolved disc sources.

Class II: $-1.6 \leq \alpha < -0.3$. More evolved YSOs that have developed a disc and continue accreting material from their surroundings.

Class III: $\alpha < -1.6$. The most evolved YSOs with very little envelope left in the final stages of their mass accretion.

Bibliography

Aguirre, J. E. et al. 2011, ApJS, 192, 4

Alencar, S. H. P., Johns-Krull, C. M., & Basri, G. 2001, AJ, 122, 3335

Alexander, R., Pascucci, I., Andrews, S., Armitage, P., & Cieza, L. 2014, Protostars and Planets VI, 475

Ali, B. & Noriega-Crespo, A. 2004, ApJ, 613, 374

Allen, L. E. & Davis, C. J. 2008, Low Mass Star Formation in the Lynds 1641 Molecular Cloud, ed. B. Reipurth (in Handbook of Star Forming Regions, Volume I. ASP Monograph Publications), 621

ALMA Partnership et al. 2015, ApJL, 808, L3

Alves, J., Lombardi, M., & Lada, C. J. 2007, A&A, 462, L17

André, P. 2002, in EAS Publications Series, Vol. 3, EAS Publications Series, ed. J. Bouvier & J.-P. Zahn, 1–38

André, P., Di Francesco, J., Ward-Thompson, D., Inutsuka, S.-I., Pudritz, R. E., & Pineda, J. E. 2014, Protostars and Planets VI, 27

André, P. et al. 2010a, A&A, 518, L102

— 2010b, A&A, 518, L102

Andre, P., Ward-Thompson, D., & Barsony, M. 1993, ApJ, 406, 122

Appenzeller, I. & Mundt, R. 1989, A&ARv, 1, 291

Armitage, P. J., Livio, M., & Pringle, J. E. 2001, MNRAS, 324, 705

Aspin, C. & Reipurth, B. 2000, MNRAS, 311, 522

Audard, M. et al. 2014, Protostars and Planets VI, 387

Avila, R., Rodríguez, L. F., & Curiel, S. 2001, RevMexAA, 37, 201

Bae, J., Hartmann, L., Zhu, Z., & Nelson, R. P. 2014, ApJ, 795, 61

Bae, J., Nelson, R. P., & Hartmann, L. 2016, ApJ, 833, 126

Bally, J. 2016, ARA&A, 54, 491

Bally, J., Langer, W. D., Stark, A. A., & Wilson, R. W. 1987, ApJL, 312, L45

Bate, M. R. & Keto, E. R. 2015, MNRAS, 449, 2643

Beckwith, S. V. W., Sargent, A. I., Chini, R. S., & Guesten, R. 1990, AJ, 99, 924

Bell, G. S. et al. 2014, in Proc. SPIE, ed. T. G. Phillips & J. Zmuidzinas, Vol. 9152, 2. SPIE, Bellingham, WA

Bell, K. R. & Lin, D. N. C. 1994, ApJ, 427, 987

Belloche, A. et al. 2011, A&A, 527, A145

Benson, P. J. & Myers, P. C. 1989, ApJS, 71, 89

Berné, O., Marcelino, N., & Cernicharo, J. 2014, ApJ, 795, 13

Berry, D. S. 2015, Astronomy and Computing, 10, 22

Berry, D. S., Reinhold, K., Jenness, T., & Economou, F. 2007, in Astronomical Society of the Pacific Conference Series, Vol. 376, Astronomical Data Analysis Software and Systems XVI, ed. R. A. Shaw, F. Hill, & D. J. Bell, 425

Berry, D. S., Reinhold, K., Jenness, T., & Economou, F. 2013, CUPID: Clump Identification and Analysis Package, Astrophysics Source Code Library

Bintley, D. et al. 2014, in Proc. SPIE, ed. T. G. Phillips & J. Zmuidzinas, Vol. 9153, 3. SPIE, Bellingham, WA

Blinova, A. A., Romanova, M. M., & Lovelace, R. V. E. 2016, MNRAS, 459, 2354

Bodenheimer, P. & Sweigart, A. 1968, ApJ, 152, 515

Bonnor, W. B. 1956, MNRAS, 116, 351

Borys, C. J. K. 2002, PhD thesis, The University of British Columbia (Canada)

Bourke, T. L. et al. 2006, ApJL, 649, L37

Bouvier, J., Alencar, S. H. P., Harries, T. J., Johns-Krull, C. M., & Romanova, M. M. 2007, Protostars and Planets V, 479

Bradshaw, C., Offner, S. S. R., & Arce, H. G. 2015, ApJ, 802, 86

Buckle, J. V. et al. 2012, MNRAS, 422, 521

— 2015, MNRAS, 449, 2472

— 2009, MNRAS, 399, 1026

Cernicharo, J. & Reipurth, B. 1996, ApJL, 460, L57

Chandrasekhar, S. 1939, An introduction to the study of stellar structure

Chapin, E. L., Berry, D. S., Gibb, A. G., Jenness, T., Scott, D., Tilanus, R. P. J., Economou, F., & Holland, W. S. 2013, MNRAS, 430, 2545

Chen, H., Ohashi, N., & Umemoto, T. 1996, AJ, 112, 717

Chen, M. C.-Y. et al. 2016, ApJ, 826, 95

Choi, M. 2001, ApJ, 553, 219

Choi, M., Hodapp, K. W., Hayashi, M., Motohara, K., Pak, S., & Pyo, T.-S. 2006, ApJ, 646, 1050

Clarke, S. D., Whitworth, A. P., Duarte-Cabral, A., & Hubber, D. A. 2017, MNRAS, 468, 2489

Cody, A. M., Hillenbrand, L. A., David, T. J., Carpenter, J. M., Everett, M. E., & Howell, S. B. 2017, ApJ, 836, 41

Commerçon, B., Hennebelle, P., & Henning, T. 2011, ApJL, 742, L9

Connelley, M. S. & Greene, T. P. 2010, AJ, 140, 1214

Connelley, M. S., Reipurth, B., & Tokunaga, A. T. 2007, AJ, 133, 1528

Contreras, Y., Garay, G., Rathborne, J. M., & Sanhueza, P. 2016, MNRAS, 456, 2041

Costigan, G., Vink, J. S., Scholz, A., Ray, T., & Testi, L. 2014, MNRAS, 440, 3444

Cottaar, M. et al. 2014, ApJ, 794, 125

Coudé, S. et al. 2016, MNRAS, 457, 2139

Cuadrado, S., Goicoechea, J. R., Pilleri, P., Cernicharo, J., Fuente, A., & Joblin, C. 2015, A&A, 575, A82

Currie, M. J., Berry, D. S., Jenness, T., Gibb, A. G., Bell, G. S., & Draper, P. W. 2014, in Astronomical Society of the Pacific Conference Series, Vol. 485, Astronomical Data Analysis Software and Systems XXIII, ed. N. Manset & P. Forshay, 391

Curry, C. L. 2000, ApJ, 541, 831

Davis, C. J. et al. 2009, A&A, 496, 153

Dempsey, J. T. & Friberg, P. 2008, in Proc. SPIE, Vol. 7012, Ground-based and Airborne Telescopes II, 70123Z

Dempsey, J. T. et al. 2013, MNRAS, 430, 2534

Dempsey, J. T., Ho, P. T. P., Walther, C., Friberg, P., Bintley, D., & Chen, M.-T. 2016, in Proc. SPIE, Vol. 9908, Ground-based and Airborne Instrumentation for Astronomy VI, 990807

Di Francesco, J., Evans, II, N. J., Caselli, P., Myers, P. C., Shirley, Y., Aikawa, Y., & Tafalla, M. 2007a, Protostars and Planets V, 17

— 2007b, Protostars and Planets V, 17

Di Francesco, J., Johnstone, D., Kirk, H., MacKenzie, T., & Ledwosinska, E. 2008a, ApJS, 175, 277

— 2008b, ApJS, 175, 277

Dobashi, K., Uehara, H., Kandori, R., Sakurai, T., Kaiden, M., Umemoto, T., & Sato, F. 2005, PASJ, 57, S1

Dobbs, C. L. et al. 2014, Protostars and Planets VI, 3

Dodds, P., Greaves, J. S., Scholz, A., Hatchell, J., Holland, W. S., & JCMT Gould Belt Survey Team 2015, MNRAS, 447, 722

Donati, J.-F. et al. 2013, MNRAS, 436, 881

Dowell, C. D. et al. 2003, in Proc. SPIE, Vol. 4855, Millimeter and Submillimeter Detectors for Astronomy, ed. T. G. Phillips & J. Zmuidzinas, 73–87. SPIE, Bellingham, WA

Drabek, E. et al. 2012, MNRAS, 426, 23

Duarte-Cabral, A. & Dobbs, C. L. 2016, MNRAS, 458, 3667

Dunham, M. M. et al. 2015, ApJS, 220, 11

— 2013, AJ, 145, 94

Dunham, M. M., Chen, X., Arce, H. G., Bourke, T. L., Schnee, S., & Enoch, M. L. 2011, ApJ, 742, 1

Dunham, M. M., Crapsi, A., Evans, II, N. J., Bourke, T. L., Huard, T. L., Myers, P. C., & Kauffmann, J. 2008, ApJS, 179, 249

Dunham, M. M., Evans, II, N. J., Terebey, S., Dullemond, C. P., & Young, C. H. 2010, in Astronomical Society of the Pacific Conference Series, Vol. 432, New Horizons in Astronomy: Frank N. Bash Symposium 2009, ed. L. M. Stanford, J. D. Green, L. Hao, & Y. Mao, 197

Dunham, M. M. et al. 2016, ApJ, 823, 160

— 2014, Protostars and Planets VI, 195

Dunham, M. M. & Vorobyov, E. I. 2012, ApJ, 747, 52

Ebert, R. 1955, ZAP, 37, 217

Economou, F. et al. 2015, Astronomy and Computing, 11, 161

Eiroa, C. & Casali, M. M. 1992, A&A, 262, 468

Emerson, D. T. 1995, in Astronomical Society of the Pacific Conference Series, Vol. 75, Multi-Feed Systems for Radio Telescopes, ed. D. T. Emerson & J. M. Payne, 309–317

Enoch, M. L., Evans, II, N. J., Sargent, A. I., & Glenn, J. 2009, ApJ, 692, 973

Enoch, M. L., Evans, II, N. J., Sargent, A. I., Glenn, J., Rosolowsky, E., & Myers, P. 2008, ApJ, 684, 1240

Enoch, M. L., Glenn, J., Evans, Neal J., I., Sargent, A. I., Young, K. E., & Huard, T. L. 2007, ApJ, 666, 982

Enoch, M. L., Lee, J.-E., Harvey, P., Dunham, M. M., & Schnee, S. 2010, ApJL, 722, L33

Enoch, M. L. et al. 2006, ApJ, 638, 293

Evans, N. J. et al. 2009a, VizieR Online Data Catalog, 218, 10321

Evans, II, N. J. et al. 2003, PASP, 115, 965

— 2009b, ApJS, 181, 321

Fischer, W. J. & Hillenbrand, L. 2017, The Astronomer's Telegram, 9969

Fischer, W. J. et al. 2017, ApJ, 840, 69

— 2012, ApJ, 756, 99

Fischera, J. & Martin, P. G. 2012a, A&A, 547, A86

— 2012b, A&A, 542, A77

Forbrich, J., Osten, R. A., & Wolk, S. J. 2011, ApJ, 736, 25

Forgan, D. & Rice, K. 2010, MNRAS, 402, 1349

Foster, J. B. et al. 2015, ApJ, 799, 136

Freundlich, J., Jog, C. J., & Combes, F. 2014, A&A, 564, A7

Friesen, R. K., Bourke, T. L., Di Francesco, J., Gutermuth, R., & Myers, P. C. 2016, ApJ, 833, 204

Friesen, R. K., Johnstone, D., Naylor, D. A., & Davis, G. R. 2005, MNRAS, 361, 460

Friesen, R. K., Medeiros, L., Schnee, S., Bourke, T. L., Di Francesco, J., Gutermuth, R., & Myers, P. C. 2013, ArXiv e-prints

Frimann, S., Jørgensen, J. K., & Haugbølle, T. 2016, A&A, 587, A59

Fukui, Y., Sugitani, K., Takaba, H., Iwata, T., Mizuno, A., Ogawa, H., & Kawabata, K. 1986, ApJL, 311, L85

Geach, J. E. et al. 2013, MNRAS, 432, 53

Gibb, A. G., Jenness, T., & Economou, F. 2013, PICARD - A PIpeline for Combining and Analyzing Reduced Data, Starlink User Note 265, Joint Astronomy Centre, Hilo, HI.

Gong, H. & Ostriker, E. C. 2011, ApJ, 729, 120

Górski, K. M., Hivon, E., Banday, A. J., Wandelt, B. D., Hansen, F. K., Reinecke, M., & Bartelmann, M. 2005, ApJ, 622, 759

Gould, B. G. 1879, Impr. de P.E. Coni, 1, 32

Greene, T. P. & Lada, C. J. 1996, AJ, 112, 2184

Greene, T. P., Wilking, B. A., Andre, P., Young, E. T., & Lada, C. J. 1994, ApJ, 434, 614

Hacar, A. & Tafalla, M. 2011, A&A, 533, A34

Hacar, A., Tafalla, M., Kauffmann, J., & Kovács, A. 2013, A&A, 554, A55

Hansen, C. E., Klein, R. I., McKee, C. F., & Fisher, R. T. 2012, ApJ, 747, 22

Haro, G. 1952, ApJj, 115, 572

— 1953, ApJ, 117, 73

Hartmann, L. 2002, ApJ, 578, 914

Hartmann, L., Ballesteros-Paredes, J., & Bergin, E. A. 2001, ApJ, 562, 852

Hartmann, L., Calvet, N., Gullbring, E., & D'Alessio, P. 1998, ApJ, 495, 385

Hartmann, L., Herczeg, G., & Calvet, N. 2016, ARAA, 54, 135

Hartmann, L., Hewett, R., Stahler, S., & Mathieu, R. D. 1986, ApJ, 309, 275

Hartmann, L. & Kenyon, S. J. 1985, ApJ, 299, 462

— 1996, ARA&A, 34, 207

Hatchell, J., Richer, J. S., Fuller, G. A., Qualtrough, C. J., Ladd, E. F., & Chandler, C. J. 2005, ArXiv Astrophysics e-prints

Hatchell, J. et al. 2013, MNRAS, 429, L10

Haubois, X. et al. 2012, A&A, 540, A41

Heiderman, A. & Evans, II, N. J. 2015, ApJ, 806, 231

Heitsch, F. 2013, ApJ, 769, 115

Hennemann, M. et al. 2012, A&A, 543, L3

Henriksen, R., Andre, P., & Bontemps, S. 1997, A&A, 323, 549

Herbig, G. H. 1951, ApJ, 113, 697

— 1960, ApJS, 4, 337

— 1977, ApJ, 217, 693

Herbig, G. H. 1989, in European Southern Observatory Conference and Workshop Proceedings, Vol. 33, European Southern Observatory Conference and Workshop Proceedings, ed. B. Reipurth, 233–246

Herczeg, G. J. et al. 2016, ApJ, 831, 133

— 2017, ApJ, 849, 43

Herschel, Sir, J. F. W. 1847, Results of astronomical observations made during the years 1834, 5, 6, 7, 8, at the Cape of Good Hope; being the completion of a telescopic survey of the whole surface of the visible heavens, commenced in 1825

Hildebrand, R. H. 1983, QJRAS, 24, 267

Hillenbrand, L. A. 2008, Physica Scripta Volume T, 130, 014024

Hodapp, K. W., Chini, R., Watermann, R., & Lemke, R. 2012, ApJ, 744, 56

Holland, W. S. et al. 2013, MNRAS, 430, 2513

— 1999, MNRAS, 303, 659

Hubber, D. A. 2014, in Astrophysics and Space Science Proceedings, Vol. 36, The Labyrinth of Star Formation, ed. D. Stamatellos, S. Goodwin, & D. Ward-Thompson, 95

Hunter, T. R. et al. 2017, ApJL, 837, L29

Inutsuka, S.-I. & Miyama, S. M. 1992, ApJ, 388, 392

— 1997, ApJ, 480, 681

Jeans, J. H. 1902, Royal Society of London Philosophical Transactions Series A, 199, 1

Jenness, T., Chapin, E. L., Berry, D. S., Gibb, A. G., Tilanus, R. P. J., Balfour, J., Tilanus, V., & Currie, M. J. 2013, SMURF: SubMillimeter User Reduction Facility, Astrophysics Source Code Library.

Jenness, T., Holland, W. S., Chapin, E., Lightfoot, J. F., & Duncan, W. D. 2000, in Astronomical Society of the Pacific Conference Series, Vol. 216, Astronomical Data Analysis Software and Systems IX, ed. N. Manset, C. Veillet, & D. Crabtree, 559

Jennings, R. E., Cameron, D. H. M., Cudlip, W., & Hirst, C. J. 1987, MNRAS, 226, 461

Johns, C. M. & Basri, G. 1995, ApJ, 449, 341

Johnstone, D. & Bally, J. 1999, ApJl, 510, L49

— 2006, ApJ, 653, 383

Johnstone, D. et al. 2017, ApJ, 836, 132

Johnstone, D., Fich, M., Mitchell, G. F., & Moriarty-Schieven, G. 2001, ApJ, 559, 307

Johnstone, D., Hendricks, B., Herczeg, G. J., & Bruderer, S. 2013, ApJ, 765, 133

Johnstone, D., Wilson, C. D., Moriarty-Schieven, G., Giannakopoulou-Creighton, J., & Gregersen, E. 2000a, ApJS, 131, 505

Johnstone, D., Wilson, C. D., Moriarty-Schieven, G., Joncas, G., Smith, G., Gregersen, E., & Fich, M. 2000b, ApJ, 545, 327

— 2000c, ApJ, 545, 327

Jørgensen, J. K., Johnstone, D., Kirk, H., & Myers, P. C. 2007, ApJ, 656, 293

Jørgensen, J. K., Johnstone, D., Kirk, H., Myers, P. C., Allen, L. E., & Shirley, Y. L. 2008, ApJ, 683, 822

Kaas, A. A. et al. 2004, A&A, 421, 623

Kackley, R., Scott, D., Chapin, E., & Friberg, P. 2010, in Proc. SPIE, ed. T. G. Phillips & J. Zmuidzinas, Vol. 7740, 1. SPIE, Bellingham, WA

Kainulainen, J., Hacar, A., Alves, J., Beuther, H., Bouy, H., & Tafalla, M. 2016, A&A, 586, A27

Kainulainen, J., Ragan, S. E., Henning, T., & Stutz, A. 2013, A&A, 557, A120

Kauffmann, J., Bertoldi, F., Evans, II, N. J., & C2D Collaboration 2005, Astronomische Nachrichten, 326, 878

Kawamura, A. et al. 2009, ApJS, 184, 1

Kenyon, S. J., Hartmann, L. W., Strom, K. M., & Strom, S. E. 1990, AJ, 99, 869

Kirk, H. et al. 2016a, ApJ, 817, 167

— 2016b, ApJ, 817, 167

— 2017, ApJ, 838, 114

Kirk, H., Johnstone, D., & Di Francesco, J. 2006a, ApJ, 646, 1009

— 2006b, ApJ, 646, 1009

Kirk, H. et al. 2016c, ApJ, 821, 98

Kirk, H., Johnstone, D., & Tafalla, M. 2007, ApJ, 668, 1042

Kirk, H., Klassen, M., Pudritz, R., & Pillsworth, S. 2015, ApJ, 802, 75

Kirk, H., Myers, P. C., Bourke, T. L., Gutermuth, R. A., Hedden, A., & Wilson, G. W. 2013a, ApJ, 766, 115

— 2013b, ApJ, 766, 115

Kirk, J. M., Ward-Thompson, D., & André, P. 2005, MNRAS, 360, 1506

Klassen, M., Pudritz, R. E., & Kirk, H. 2017, MNRAS, 465, 2254

Klein, R. I. 1999, Journal of Computational and Applied Mathematics, 109, 123

Klessen, R. S. & Hennebelle, P. 2010, A&A, 520, A17

Koda, J. et al. 2009, ApJL, 700, L132

Könyves, V. et al. 2015, A&A, 584, A91

— 2010, A&A, 518, L106

Kounkel, M. et al. 2017, ApJ, 834, 142

Kovács, A. 2006, PhD thesis, California Institute of Technology.

Krumholz, M. R. et al. 2014, Protostars and Planets VI, 243

Krumholz, M. R., Matzner, C. D., & McKee, C. F. 2006, ApJ, 653, 361

Krumholz, M. R., McKee, C. F., & Klein, R. I. 2004, ApJ, 611, 399

Kryukova, E., Megeath, S. T., Gutermuth, R. A., Pipher, J., Allen, T. S., Allen, L. E., Myers, P. C., & Muzerolle, J. 2012, AJ, 144, 31

Lada, C. J. 1978, Moon and Planets, 19, 157

Lada, C. J. 1987, in IAU Symposium, Vol. 115, Star Forming Regions, ed. M. Peimbert & J. Jugaku, 1–17

Lada, C. J., Alves, J., & Lada, E. A. 1996, AJ, 111, 1964

Lada, C. J. & Lada, E. A. 2003, ARAA, 41, 57

Lane, J. et al. 2016, ApJ, 833, 44

Larson, R. B. 1969, MNRAS, 145, 271

Li, D., Velusamy, T., Goldsmith, P. F., & Langer, W. D. 2007, ApJ, 655, 351

Lombardi, M. 2009, A&A, 493, 735

Lombardi, M., Alves, J., & Lada, C. J. 2011, A&A, 535, A16

Lombardi, M., Bouy, H., Alves, J., & Lada, C. J. 2014, A&A, 566, A45

Lorenzetti, D. et al. 2012, ApJ, 749, 188

Mairs, S. et al. 2016, MNRAS, 461, 4022

— 2015, MNRAS, 454, 2557

Mairs, S., Johnstone, D., Offner, S. S. R., & Schnee, S. 2014, ApJ, 783, 60

Mairs, S. et al. 2017, ApJ, 843, 55

Malinen, J., Juvela, M., Collins, D. C., Lunttila, T., & Padoan, P. 2011, A&A, 530, A101

Mamajek, E. E. 2009, in American Institute of Physics Conference Series, Vol. 1158, American Institute of Physics Conference Series, ed. T. Usuda, M. Tamura, & M. Ishii, 3–10

Matzner, C. D. & McKee, C. F. 2000, ApJ, 545, 364

Maury, A. J., André, P., Men'shchikov, A., Könyves, V., & Bontemps, S. 2011, A&A, 535, A77

McCutcheon, W. H., Roger, R. S., & Dickman, R. L. 1982, ApJ, 256, 139

McKee, C. F. & Offner, S. R. R. 2011a, in IAU Symposium, Vol. 270, Computational Star Formation, ed. J. Alves, B. G. Elmegreen, J. M. Girart, & V. Trimble, 73–80

McKee, C. F. & Offner, S. R. R. 2011b, in IAU Symposium, Vol. 270, Computational Star Formation, ed. J. Alves, B. G. Elmegreen, J. M. Girart, & V. Trimble, 73–80

McKee, C. F. & Ostriker, E. 2007a, ARA&A, 45, 565

McKee, C. F. & Ostriker, E. C. 2007b, ARAA, 45, 565

Megeath, S. T. et al. 2012, AJ, 144, 192

— 2016, AJ, 151, 5

Meidt, S. E. et al. 2015, ApJ, 806, 72

Meixner, M. et al. 2016, in Proc. SPIE, Vol. 9904, Space Telescopes and Instrumentation 2016: Optical, Infrared, and Millimeter Wave, 99040K

Men'shchikov, A., André, P., Didelon, P., Motte, F., Hennemann, M., & Schneider, N. 2012, A&A, 542, A81

Merello, M., Evans, II, N. J., Shirley, Y. L., Rosolowsky, E., Ginsburg, A., Bally, J., Battersby, C., & Dunham, M. M. 2015, ApJS, 218, 1

Mezger, P. G. 1990, in IAU Symposium, Vol. 139, The Galactic and Extragalactic Background Radiation, ed. S. Bowyer & C. Leinert, 63–73

Miettinen, O. 2012, A&A, 540, A104

Miura, R. E. et al. 2012, ApJ, 761, 37

Molinari, S. et al. 2010, PASP, 122, 314

Motte, F., Andre, P., & Neri, R. 1998, A&A, 336, 150

Mowat, C. et al. 2017, MNRAS, 467, 812

Muench, A., Getman, K., Hillenbrand, L., & Preibisch, T. 2008, Star Formation in the Orion Nebula I: Stellar Content, ed. B. Reipurth, 483

Murray, N. 2011, ApJ, 729, 133

Myers, P. C. 2009a, ApJ, 700, 1609

— 2009b, ApJ, 700, 1609

Narayan, R. & Nityananda, R. 1986, ARA&A, 24, 127

Nayakshin, S. & Lodato, G. 2012, MNRAS, 426, 70

Nutter, D. & Ward-Thompson, D. 2007, MNRAS, 374, 1413

Offner, S. S. R., Bisbas, T. G., Viti, S., & Bell, T. A. 2013, ApJ, 770, 49

Offner, S. S. R., Capodilupo, J., Schnee, S., & Goodman, A. A. 2012, MNRAS, 420, L53

Offner, S. S. R., Clark, P. C., Hennebelle, P., Bastian, N., Bate, M. R., Hopkins, P. F., Moraux, E., & Whitworth, A. P. 2014, Protostars and Planets VI, 53

Offner, S. S. R., Dunham, M. M., Lee, K. I., Arce, H. G., & Fielding, D. B. 2016, ApJL, 827, L11

Offner, S. S. R., Klein, R. I., McKee, C. F., & Krumholz, M. R. 2009a, ApJ, 703, 131

— 2009b, ApJ, 703, 131

Offner, S. S. R., Kratter, K. M., Matzner, C. D., Krumholz, M. R., & Klein, R. I. 2010, ApJ, 725, 1485

Ossenkopf, V. & Henning, T. 1994, A&A, 291, 943

Ostriker, J. 1964, ApJ, 140, 1056

Padoan, P. & Nordlund, Å. 2002, ApJ, 576, 870

Panopoulou, G. V., Psaradaki, I., & Tassis, K. 2016, MNRAS, 462, 1517

Patanchon, G. et al. 2008, ApJ, 681, 708

Pattle, K. 2016, MNRAS, 459, 2651

Pattle, K. et al. 2015, MNRAS, 450, 1094

Penston, M. V. 1969, MNRAS, 144, 425

Pierce-Price, D. P. I. 2002, PhD thesis, Cavendish Astrophysics Group, University of Cambridge

Pineda, J. E. et al. 2011, ApJ, 743, 201

Pineda, J. E., Rosolowsky, E. W., & Goodman, A. A. 2009a, ApJL, 699, L134

— 2009b, ApJL, 699, L134

Planck Collaboration et al. 2015, ArXiv e-prints

Polychroni, D. et al. 2013, ApJL, 777, L33

Pon, A., Johnstone, D., & Heitsch, F. 2011, ApJ, 740, 88

Pon, A., Johnstone, D., & Kaufman, M. J. 2012a, ApJ, 748, 25

Pon, A., Toalá, J. A., Johnstone, D., Vázquez-Semadeni, E., Heitsch, F., & Gómez, G. C. 2012b, ApJ, 756, 145

Pudritz, R. E. & Kevlahan, N. K.-R. 2013, Philosophical Transactions of the Royal Society of London Series A, 371, 20120248

Ragan, S. et al. 2012, A&A, 547, A49

Reipurth, B. 1989, A&A, 220, 249

Reipurth, B. 1990, in IAU Symposium, Vol. 137, Flare Stars in Star Clusters, Associations and the Solar Vicinity, ed. L. V. Mirzoian, B. R. Pettersen, & M. K. Tsvetkov, 229–251

— 2008, Handbook of Star Forming Regions, Volume I: The Northern Sky (ASP Monograph Publications. ISBN: 978-1-58381-670-7)

Reipurth, B., Bally, J., Aspin, C., Connelley, M. S., Geballe, T. R., Kraus, S., Appenzeller, I., & Burgasser, A. 2013, AJ, 146, 118

Reipurth, B., Heathcote, S., Morse, J., Hartigan, P., & Bally, J. 2002, AJ, 123, 362

Reipurth, B., Rodríguez, L. F., Anglada, G., & Bally, J. 2004, AJ, 127, 1736

Ribas, Á., Bouy, H., & Merín, B. 2015, A&A, 576, A52

Rice, W. K. M., Mayo, J. H., & Armitage, P. J. 2010, MNRAS, 402, 1740

Richer, J. S. 1992, MNRAS, 254, 165

Romanova, M. M., Toropina, O. D., Toropin, Y. M., & Lovelace, R. V. E. 2003, ApJ, 588, 400

Rosolowsky, E. W., Pineda, J. E., Kauffmann, J., & Goodman, A. A. 2008, ApJ, 679, 1338

Rumble, D. et al. 2015, MNRAS, 448, 1551

— 2016, MNRAS, 460, 4150

Sadavoy, S. I. et al. 2010a, ApJ, 710, 1247

Sadavoy, S. I., Di Francesco, J., & Johnstone, D. 2010b, ApJL, 718, L32

Sadavoy, S. I. et al. 2013, ApJ, 767, 126

Safier, P. N., McKee, C. F., & Stahler, S. W. 1997, ApJ, 485, 660

Safron, E. J. et al. 2015, ApJL, 800, L5

Salji, C. J. et al. 2015a, MNRAS, 449, 1782

— 2015b, MNRAS, 449, 1769

Santangelo, G. et al. 2015, A&A, 584, A126

Schnee, S., Di Francesco, J., Enoch, M., Friesen, R., Johnstone, D., & Sadavoy, S. 2012a, ApJ, 745, 18

Schnee, S., Sadavoy, S., Di Francesco, J., Johnstone, D., & Wei, L. 2012b, ApJ, 755, 178

Schneider, N., Csengeri, T., Bontemps, S., Motte, F., Simon, R., Hennebelle, P., Federrath, C., & Klessen, R. 2010, A&A, 520, A49

Schneider, S. & Elmegreen, B. G. 1979a, ApJS, 41, 87

— 1979b, ApJS, 41, 87

Scholz, A., Froebrich, D., & Wood, K. 2013, MNRAS, 430, 2910

Scott, K. S. et al. 2008, MNRAS, 385, 2225

Shu, F. H. 1977, ApJ, 214, 488

Shu, F. H., Adams, F. C., & Lizano, S. 1987, ARA&A, 25, 23

Shu, F. H., Galli, D., Lizano, S., Glassgold, A. E., & Diamond, P. H. 2007, ApJ, 665, 535

Skrutskie, M. F. et al. 2006, AJ, 131, 1163

Smith, R. J., Shetty, R., Beuther, H., Klessen, R. S., & Bonnell, I. A. 2013, ApJ, 771, 24

Smith, R. J., Shetty, R., Stutz, A. M., & Klessen, R. S. 2012, ApJ, 750, 64

Soderblom, D. R., Hillenbrand, L. A., Jeffries, R. D., Mamajek, E. E., & Naylor, T. 2014, Protostars and Planets VI, 219

Stahler, S. W. 1988, ApJ, 332, 804

Stanke, T., McCaughrean, M. J., & Zinnecker, H. 2002, A&A, 392, 239

Stanke, T. et al. 2010, A&A, 518, L94

Stodólkiewicz, J. S. 1963, Acta Astron., 13, 30

Stutz, A. M. & Gould, A. 2015, ArXiv e-prints

Stutz, A. M. et al. 2013, ApJ, 767, 36

Stutzki, J. & Guesten, R. 1990, ApJ, 356, 513

Terebey, S., Shu, F. H., & Cassen, P. 1984, ApJ, 286, 529

Thomas, H. S. & Currie, M. J. 2014, The SCUBA-2 Data Reduction Cookbook, Vol. 21 (Joint Astronomy Center, Hilo, HI)

Truelove, J. K., Klein, R. I., McKee, C. F., Holliman, II, J. H., Howell, L. H., & Greenough, J. A. 1997, ApJL, 489, L179+

Truelove, J. K., Klein, R. I., McKee, C. F., Holliman, II, J. H., Howell, L. H., Greenough, J. A., & Woods, D. T. 1998, ApJ, 495, 821

Vaillancourt, J. E. et al. 2008, ApJL, 679, L25

van Boekel, R. 2004, PhD thesis, University of Amsterdam

van Kempen, T. A., van Dishoeck, E. F., Salter, D. M., Hogerheijde, M. R., Jørgensen, J. K., & Boogert, A. C. A. 2009, A&A, 498, 167

Vázquez-Semadeni, E., González-Samaniego, A., & Colín, P. 2017, MNRAS, 467, 1313

Venuti, L. et al. 2017, A&A, 599, A23

Vorobyov, E. I. & Basu, S. 2005, ApJL, 633, L137

— 2006, ApJ, 650, 956

— 2010, ApJ, 719, 1896

— 2015, ApJ, 805, 115

Ward-Thompson, D., André, P., Crutcher, R., Johnstone, D., Onishi, T., & Wilson, C. 2007a, Protostars and Planets V, 33

— 2007b, Protostars and Planets V, 33

Ward-Thompson, D. et al. 2007c, PASP, 119, 855

Williams, J. P., de Geus, E. J., & Blitz, L. 1994, ApJ, 428, 693

Wilson, B. A., Dame, T. M., Masheder, M. R. W., & Thaddeus, P. 2005, A&A, 430, 523

Wilson, C. D. et al. 1999, ApJl, 513, L139

Wright, E. L., Hinshaw, G., & Bennett, C. L. 1996, ApJl, 458, L53

Yoo, H. et al. 2017, ApJ, 849, 69

Young, C. H. et al. 2004, ApJS, 154, 396

Zhang, M., Fang, M., Wang, H., Sun, J., Wang, M., Jiang, Z., & Anathipindika, S. 2015, ApJS, 219, 21

Zhu, Z., Hartmann, L., Calvet, N., Hernandez, J., Muzerolle, J., & Tannirkulam, A.-K. 2007, ApJ, 669, 483

Zhu, Z., Hartmann, L., & Gammie, C. 2009, ApJ, 694, 1045